Connecting the coherent and stochastic X-ray variability of accreting millisecond pulsars

Bult, P.M.

Publication date
2015

Document Version
Final published version

Connecting the coherent and stochastic X-ray variability of accreting millisecond pulsars

Connecting the coherent and stochastic X-ray variability of accreting millisecond pulsars

Peter Bult

Peter Bult

Connecting the coherent and stochastic X-ray variability of accreting millisecond pulsars

ACADEMISCH PROEFSCHRIFT

ter verkrijging van de graad van doctor
aan de Universiteit van Amsterdam
op gezag van de Rector Magnificus
prof. dr. D.C. van den Boom
ten overstaan van een door het College voor Promoties ingestelde
commissie, in het openbaar te verdedigen in de Agnietenkapel
op dinsdag 15 september 2015, te 10:00 uur

door

Petrus Michael Bult

geboren te Hilversum

Promotiecommissie:

Promotor:	prof. dr. M.B.M. van der Klis	Universiteit van Amsterdam
Copromotor:	dr. A. Patruno	Universiteit Leiden
Overige leden:	prof. dr. W. Hermsen	Universiteit van Amsterdam, SRON
	prof. dr. A.R. King	University of Leicester
	prof. dr. M. Méndez	Rijksuniversiteit Groningen
	prof. dr. R.A.J.M. Wijers	Universiteit van Amsterdam
	dr. J.W.T. Hessels	Universiteit van Amsterdam, ASTRON
	dr. R.A.D. Wijnands	Universiteit van Amsterdam

Faculteit der Natuurwetenschappen, Wiskunde en Informatica

Het hier beschreven onderzoek is gefinancierd door de Nederlandse Organisatie voor Wetenschappelijk Onderzoek (NWO) en uitgevoerd aan het Anton Pannekoek Instituut voor Sterrenkunde van de Universiteit van Amsterdam.

Contents

1 Introduction

Neutron stars are among the most extreme objects in the universe. With masses of around 1.5 to 2 times that of the Sun and radii on the order of 10 km, neutron stars are exceedingly compact objects, with an internal structure that greatly exceeds the nuclear density (10^{14} g cm^{-3}).

The properties of matter in the high density and low temperature environment of a neutron star core remains unknown. It is not clear which fundamental particles occur in such an extreme environment, nor what their state will be. As such, the relation between a neutron star's internal density, pressure and temperature, summarized with the equation of state, cannot be uniquely predicted. Understanding of this regime of nuclear physics can only come from the study of neutron stars.

Due to their large mass and small radius, neutron stars are relativistic objects, exerting a strong gravitational force on their surroundings. General relativity predicts that the space-time around these objects will be strongly curved, giving rise to various exotic effects, such as light-bending, dragging of inertial frames and relativistic precession. Consequently, investigating neutron stars and their environment provides a direct means to study the, as of yet untested, strong-field regime of general relativity.

These links to fundamental physics are accessible by studying the flow of matter under influence of gravity in vicinity of neutron stars. Such flows arise in low-mass X-ray binaries: systems in which matter is transferred from a low mass ($\leq 1\ M_\odot$) companion star to a compact object such as a black hole or a neutron star. As the accretion process naturally produces X-ray emission, the observation and study of the variations in the X-ray intensity gives a probe of these extreme objects and their environment.

This thesis deals with the study of the X-ray variability of accreting neutron stars, focussing on accreting millisecond pulsars, a special sub-class for which the stellar rotation rate is precisely known. In this chapter the context of this study is presented, with the following sections discussing some of the basic theory of accretion and the magnetic interaction of the accreting material with the neutron star. Then a brief overview is given of the methodology used to study these objects, followed by a short outline of the chapters in this work.

1.1 Neutron stars in low-mass X-ray binaries

In X-ray binaries a companion star is transferring material into the gravitational potential well of a compact object, be it a black hole or neutron star. While intermediate or special configurations are possible, the bulk of the known X-ray binaries belong to two distinct groups: high-mass X-ray binaries and low-mass X-ray binaries (see e.g. Tauris & van den Heuvel 2006). If the companion is a high mass star ($\gtrsim 10 M_\odot$), it may shed material through its stellar wind, which is then swept up by the compact object. For a low mass companion ($\lesssim 1 M_\odot$) the configuration of the binary may be such that the extent of the companion star's Roche lobe, its gravitational sphere of influence, is smaller than the star. The outer layers of the companion are then no longer bound to the star, and can flow into the gravitational well of the neutron star, leading to mass transfer through so-called Roche-Lobe overflow.

Due to their very different configurations, these two binary classes differ in many other aspects as well. Most notably, those with a high-mass companion are linked to the lifetime of the massive star and evolve on comparatively short timescales of $10^5 - 10^7$ years. Neutron stars found in such high-mass X-ray binaries are strongly magnetized (10^{12} G). Those binaries with a low-mass companion, on the other hand, evolve on much longer timescales of $10^7 - 10^9$ years. Neutron stars in low-mass X-ray binaries are weakly magnetized neutron stars (10^8 G) and show fast variability in their X-ray emission that can reach the millisecond timescale associated with the innermost surroundings of the neutron star (van der Klis et al. 2000). For this reason the neutron star low-mass X-ray binary systems are the focus of this work.

1.1.1 Accretion disks

Matter that is transferred from the companion star to the neutron star through Roche-lobe overflow has a specific angular momentum, J, that is of the same order as the specific angular momentum of the binary orbit. Due to this initial angular momentum the transferred matter cannot fall straight down the gravitational potential well of the neutron star, and will instead settle into an orbit around the star as an accretion disk. If the structure of the disk is dominated by the gas pressure, it will form a geometrically thin and optically thick disk (Shakura & Sunyaev 1973; Ghosh & Lamb 1978) that rotates differentially at a near Keplerian frequency

$$\nu_K(r) = \frac{1}{2\pi}\sqrt{\frac{GM}{r^3}}, \tag{1.1}$$

where G is the gravitational constant, M the mass of the neutron star and r the radius in the disk.

For the gas in the accretion disk to move closer to the neutron star it must first shed its energy and angular momentum. While the precise mechanism by which this occurs is not

yet definitively established, the most likely candidate is a turbulent viscosity mechanism due to the magneto-rotational instability (Balbus & Hawley 1991). Through turbulent viscosity an accretion disk may lose energy by means of thermal emission, and simultaneously transport angular momentum outwards, thus allowing the accreting material to spiral in toward the neutron star.

As the gas moves closer to the neutron star, gravitational potential energy is released. The total luminosity released due to accretion down to the neutron star is then approximately

$$L = \frac{GM\dot{M}}{R}, \tag{1.2}$$

where $\dot{M}$ gives the mass accretion rate and R the neutron star radius. The bulk of this energy is released within a few tens of km from the neutron star, where the gravitational potential is steepest. Since the gas in this region has been heated to $\sim 10^7$ K, the emerging thermal emission peaks in X-ray band. The Keplerian timescale in this region is on the order of milliseconds, and hence the dynamical properties of the accretion flow close to the neutron star are expected to be accessible through the variations in the X-ray emission on a millisecond timescale.

1.1.2 Magnetospheric interaction

Because neutron stars are magnetized objects, and the accreting material consists of ionized plasma, the dynamics of the flow are influenced by the stellar magnetic field. This becomes increasingly important as the accreting material approaches the neutron star. The radius at which magnetic effects dominate is usually called the *magnetospheric radius*, and is roughly estimated as the radius at which the material and magnetic stresses balance (Pringle & Rees 1972; Lamb et al. 1973)

$$r_m = \gamma_B^{2/7} \left(\frac{\mu^4}{GM\dot{M}^2} \right)^{1/7}, \tag{1.3}$$

Here $\gamma_B \sim 0.1-1$ is a dimensionless magnetospheric boundary parameter, which captures the uncertainties in the topology of the magnetic field, the geometry of the accretion flow, and the many uncertainties in the detailed physics of the flow's coupling to the stellar magnetic field (Ghosh & Lamb 1979a,b, see also Chapter 7). Additionally, μ gives the dipolar magnetic moment of the neutron star, with

$$B = 2\frac{\mu}{R^3}. \tag{1.4}$$

the surface dipolar magnetic field at the stellar poles.

When the accreting plasma couples to the field, the structure and orbital motion of the disk are disrupted. The accretion flow will be forced to move along with the

magnetosphere at the rotation rate of the star, and depending on the relative rate of rotation between the star and the disk this leads to different accretion scenarios. If the Keplerian orbital frequency of the disk is *higher* than the rotation rate of the star, the plasma will decelerate and move along the magnetic field lines until it collides with the neutron star surface in a confined region near the stellar magnetic poles. This creates a local emission region on the neutron star surface (the hotspot), which through periodic aspect variations gives rise to coherent X-ray pulsations at the stellar spin frequency. If the disk orbital frequency is *lower* than the spin frequency of the star, the magnetic coupling causes the gas to accelerate, giving rise to a centrifugal force that inhibits accretion. The *co-rotation radius*, the radius at which the Kepler frequency and stellar spin frequency are equal, therefore has special significance, and is expressed as

$$r_c = \left(\frac{\sqrt{GM}}{2\pi\nu_s} \right)^{2/3}, \tag{1.5}$$

with ν_s the spin frequency of the neutron star. Thus a funneled accretion flow occurs when $r_m < r_c$ and a centrifugal barrier is expected when $r_m > r_c$. If $r_m \geq 2^{1/3} r_c$ the centrifugal force is strong enough to accelerate the inflowing matter to above the escape velocity, and may drive an outflow like a propeller (Illarionov & Sunyaev 1975; Spruit & Taam 1993). The situation for $r_m \simeq r_c$ is less clear.

At radii just outside r_m a boundary layer is expected, where the magnetic field will not yet disrupt the disk, but will still be strong enough to affect its dynamics. The extent and behavior of this boundary region is subject to considerable uncertainty (see, e.g. Uzdensky 2004). Nonetheless, it is clear that the coupling between the stellar magnetosphere and the accretion disk leads to a magnetic torque that transfers angular momentum between the disk and the star, causing a number of physical processes that affect both.

The angular momentum exchange between the disk and the star consists of several contributions. First, for $r_m < r_c$, when accretion can proceed normally, the flow of matter from a disk adds angular momentum to the neutron star

$$\dot{J}_{\rm acc} = \dot{M}\sqrt{GMr_m}. \tag{1.6}$$

Second, the differential rotation between the neutron star spin and the Keplerian orbital frequency in the magnetospheric boundary region applies a magnetic torque (Ghosh & Lamb 1979a,b; Rappaport et al. 2004). This term is highly uncertain as it depends on the specifics of the magnetic field configuration, the geometry of the accretion and the width of the interaction region, Δr, but can be estimated as (e.g. Patruno & Watts 2012, and references therein)

$$\dot{J}_{\rm mag} \simeq n(\omega)\frac{\mu^2}{9r_m^3}, \tag{1.7}$$

where $n(\omega)$ is a dimensionless transition function that depends on the fastness parameter $\omega = (r_m/r_c)^{3/2}$. Third, for $r_m > r_c$, a possible outflow driven by the rotation of the

magnetosphere can carry away angular momentum of the star

$$\dot{J}_{\rm ej} = 2\pi\nu_s \dot{M}_{\rm ej} r_m^2. \tag{1.8}$$

If the accretion disk extends to inside the co-rotation radius ($r_m < r_c$) these effects will transfer angular momentum from the disk to the star, thus causing the star to spin-up. Inversely, if the magnetosphere truncates the disk well outside the co-rotation radius ($r_m > r_c$) these effects will extract angular momentum from the star, causing it to spin-down. As the spin frequency of the star increases or decreases, r_c will respectively become smaller or larger, narrowing the difference between r_m and r_c. So, over time, the system is expected to evolve toward an equilibrium state where $r_m \sim r_c$ and the spin period of the star is linked to its magnetic field strength.

The magnetic interaction also greatly affects the accretion disk, and various potentially observable variability mechanisms have been predicted to originate in the magnetospheric boundary layer. For instance, the disk-magnetosphere interface may show an interchange instability (Arons & Lea 1976; Spruit et al. 1995; Romanova et al. 2008), in which screening currents allow the plasma to slip between the magnetic field lines and accrete transversely onto the neutron star. When $r_m \sim r_c$ the accretion flow might proceed episodically (Spruit & Taam 1993; D'Angelo & Spruit 2010; Lii et al. 2014). Alternatively, a magnetic field that is slightly misaligned with respect to the stellar rotation may introduce a warp in the disk (Lai 1999), or could excite density or bending waves (Lovelace & Romanova 2007; Lai & Zhang 2008; Romanova et al. 2013). While none of these predictions have been uniquely linked to observed variability phenomena in accreting neutron stars, their diversity stresses the importance of understanding the physics that governs the magnetic coupling between the neutron star and the accretion flow.

1.2 Spin-period evolution

The angular momentum exchange between the neutron star and the accretion disk affects the dynamics of the accreting flow and has important consequences for the spin-period evolution of the neutron star. The latter is directly evident when considering the larger population of (not accreting) neutron stars.

Most of the known neutron stars are radio pulsars, rotating magnetized neutron stars that show radio emission powered by the loss of rotational kinetic energy. The characteristic feature of a pulsar is a sequence of pulses in its radio emission that reveals the spin period of the neutron star (see e.g. Lorimer 2008 for a review). Based on their spin periods these objects are roughly divided in two populations. One group is formed by the regular pulsars, which have rotation periods of about one second and are steadily slowing down at a rate of $\dot{P} \sim 10^{-15}$ s s^{-1}. The other group are the millisecond pulsars, which show a faster rotation of about five milliseconds and slow down at a much slower rate of $\dot{P} \sim 10^{-20}$ s s^{-1} (see Figure 1.1). More often than not these millisecond pulsars are part of a binary system.

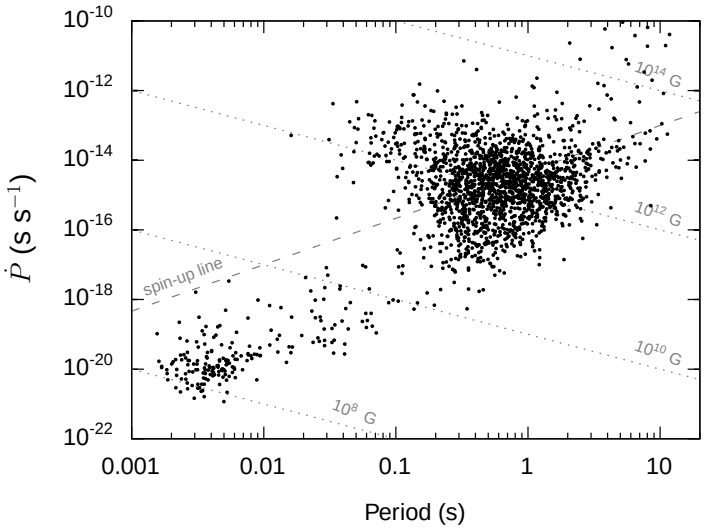

Figure 1.1: P-$\dot{P}$-diagram, showing the pulsar spin period against it period derivative. The dashed 'spin-up line' gives the lowest attainable spin period through accretion, assuming Eddington-rate accretion and a 1.4 $M_\odot$ neutron star (Tauris et al. 2012). Dotted lines mark the magnetic field strength assuming the spin-down is due to magnetic dipole emission.

The difference between regular and millisecond pulsars is commonly explained with the *recycling scenario* (Bisnovatyi-Kogan & Komberg 1974; Alpar et al. 1982; Radhakrishnan & Srinivasan 1982), which proposes that neutron stars attain their high rotation rates through a prolonged period of accretion in low-mass X-ray binaries. This scenario was confirmed with the discovery of the first accreting millisecond X-ray pulsar in a low-mass X-ray binary (Wijnands & van der Klis 1998a) and further reinforced with the detection of a series of millisecond pulsars that are transitioning between an accretion powered and rotation powered state (Archibald et al. 2009, 2015; Papitto et al. 2013a, 2015).

In spite of the observational confirmation that low-mass X-ray binaries can produce millisecond radio pulsars, many uncertainties on the details of the recycling process remain. Because the highest attainable spin period is limited by the magnetic field strength (Srinivasan & van den Heuvel 1982), the magnetic field of millisecond pulsars must have somehow decayed by several orders of magnitude. The cause of this field decay remains undetermined, although a candidate mechanism is the accretion process itself (Bisnovatyi-Kogan & Komberg 1974; van den Heuvel et al. 1986). Additionally, differences in the distribution of spin frequencies, estimated ages and magnetic fields between the population of accretion powered and rotation powered millisecond pulsar are not yet confidently explained (Tauris 2012). Such questions might be answered by studying the spin-period evolution of accreting millisecond pulsars in low-mass X-ray binaries.

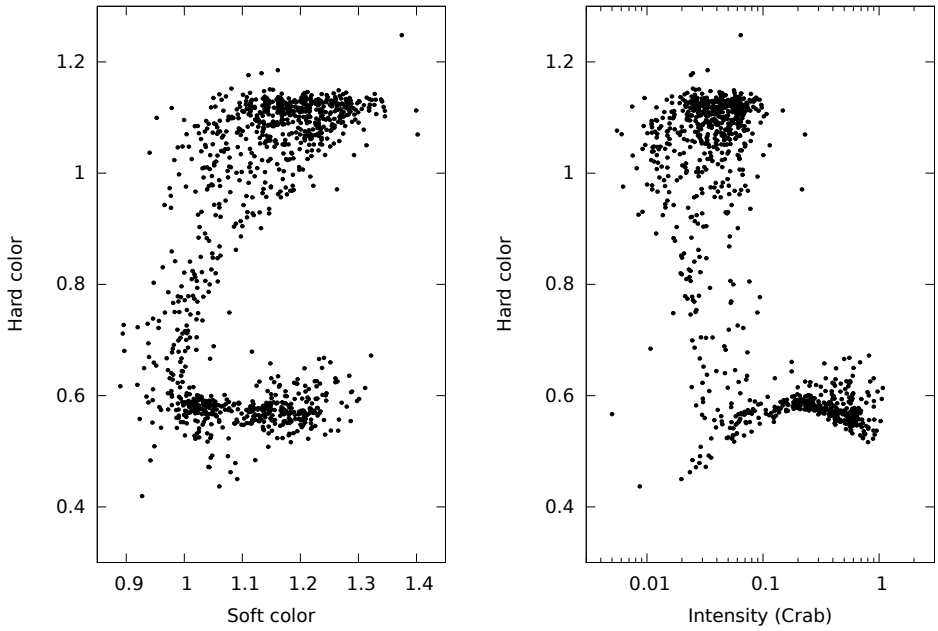

Figure 1.2: Example color-color diagram (left) and hardness-intensity diagram (right) for the atoll source 4U 1608–52

1.3 Observing accreting neutron stars

Neutron star low-mass X-ray binaries are a diverse class of systems. Observationally they are broadly divided in Z sources and atoll sources (Hasinger & van der Klis 1989), based on their luminosity and their different timing and spectral properties. The Z sources are the more luminous class, with intensities on the order of $\sim 10^{38}$ erg s^{-1}, whereas the atoll sources are somewhat less bright and move through a broad range of luminosities of $\sim 10^{36-38}$ erg s^{-1}. Special cases are known that can move between these states, and further subclasses exist, such as the accreting millisecond pulsars that are studied in this thesis, which are relatively dim ($\sim 10^{36}$ erg s^{-1}) and appear 'stuck' on a narrow region of the atoll track.

Some of these X-ray binaries appear as persistent sources, showing some level of X-ray emission at all times. Others are transient sources, they go through outbursts of X-ray emission lasting several weeks, separated by months-to-years long periods of quiescence. Either way, all types show recurring patterns in their timing and spectral properties, which are thought to reflect qualitatively different states of the accretion flow.

The spectral characteristics are usually categorized based on broad-band spectroscopy using color analysis. In this approach the X-ray spectrum is divided in four broad energy

bands, from which a soft color is calculated as the ratio between the X-ray count rate in the 3.5–6.0 keV band and the 2.0–3.5 keV band, and a hard color is calculated as the ratio between the 9.7–16.0 keV band and the 6.0–9.7 keV band. Plotting the hard color against the soft color (color-color diagram, CD), or the hard color against X-ray intensity (hardness-intensity diagram, HID) then reveals the systematic recurring patterns that form the basis of source classification. In Figure 1.2 the CD and HID of the atoll source 4U 1608–52 are shown as example.

1.3.1 Coherent timing

The periodic variability of accreting millisecond X-ray pulsars (AMXPs) can be studied through coherent timing. This method comes from the analysis of radio pulsars, where the arrival times of a fiducial point in the pulse waveform is measured for succeeding pulses. These arrival times are then transformed to the pulsar's reference frame by first adjusting the measured times to the Solar System barycenter and then removing the modulation due to the binary orbit. The corrected arrival times should then be determined only by the rotation of the neutron star, and, owing to the stability of its rotation, advance in a highly stable and predictable fashion.

As the pulsations of AMXPs are too weak to be detected in a single rotation, the signal must be reconstructed by folding $\sim 10^2$ seconds of data on the pulse period. With the resulting pulse waveform one can measure the average amplitude and phase of the pulsating signal during the considered observation.

The pulsations of AMXPs are typically highly sinusoidal, with only little harmonic content. Their shape, however, is not constant and both the pulse amplitude and harmonic content may show abrupt and gradual changes throughout an outburst. Such variability of the pulse shape complicates the analysis as it introduces shifts between the expected and measured arrival times that are not related to the rotation of the neutron star. To overcome this difficulty, the pulse waveform is decomposed into its harmonic components

$$p(t) = a_0 + \sum_{k=1}^{K} a_k \cos\left(2\pi(k\nu_{\mathrm{p}}t - \phi_k)\right), \tag{1.9}$$

where $p(t)$ gives the measured waveform, ν_{p} the pulsar spin frequency, a_0 the non-pulsed emission and a_k and ϕ_k are the amplitude and phase of the k-th harmonic. The phase of each harmonic then provides a well-defined fiducial point that can be traced from profile to profile. While this approach provides no special insight on how the pulse shape changes relate to the underlying neutron star rotation, it does provide an empirical method by which the pulse changes can be characterized that does not rely on model-dependent assumptions of how that pulsed emission arises.

To establish the rotational properties of the neutron star, the measured harmonic

phase is compared with the expected phase based on a timing model as

$$\phi(t) = \int_{t_0}^{t} \nu(\tau) d\tau. \tag{1.10}$$

Here t_0 gives the epoch to which the parameters of the model refer and $\nu(\tau)$ the time variable frequency function it predicts. By expressing this frequency function as a Taylor expansion around t_0, the expected phase can be expressed as

$$\phi(t) = \phi_0 + \nu\left(t - t_0\right) + \frac{1}{2}\frac{\partial \nu}{\partial t}\left(t - t_0\right)^2 + \ldots \tag{1.11}$$

which may be fitted to the measurements through standard χ^2 minimization methods. Then, by analyzing the phase residuals for systematic patterns, one can refine the parameters of the binary orbit, the measured pulse frequency and their derivatives.

It should be stressed that measured parameters are the *pulse* frequency and its derivatives, which are not necessarily equal to the frequency and derivatives of the *neutron star spin*. As the pulsations are due to aspect variations of the hotspot on the stellar surface, changes of that region or its location introduce variations in the pulse profile that are not related to the neutron star. An example of such an effect was was demonstrated by Patruno et al. (2009e), who show that the phase residuals of many AMXPs show a strong correlation with the X-ray flux. If this correlation is interpreted as variations in the instantaneous mass accretion rate influencing the position or beaming of the hotspot, the variations in flux introduce a systematic trend in the phase residuals. While such a shift cannot be more than a cycle, the introduced trend will be absorbed by the timing model, causing it to yield a pulse frequency that is offset from the spin frequency.

1.3.2 Stochastic timing

In contrast to the strictly periodic oscillations discussed in the previous section, the aperiodic variability observed in X-ray binaries is stochastic and can only be studied through its averaged phenomenology. The dominant approach is to study the power spectral density as estimated through Fourier analysis (van der Klis 1989).

A time series x_j of N evenly spaced samples may be transformed to the frequency domain using the discrete Fourier transform

$$X_k = \sum_{j=0}^{N-1} x_j \exp\left(-2\pi i t_j \nu_k\right), \tag{1.12}$$

where $t_j = j\delta t$ is the time of the j-th bin and $\nu_k = k\delta\nu$ the k-th Fourier frequency bin, such that X_k is a complex vector with $k = -\frac{N}{2}, \ldots, \frac{N}{2} - 1$. Because X-ray time series are strictly real-valued, the Fourier spectrum will have the Hermitian symmetry $X_k = X^*_{-k}$, such that it can be completely defined using only its positive frequency domain, which

runs from zero (the DC component) to the Nyquist frequency ($\nu_{\rm Nyquist} = 1/2\delta t$). The power density estimate can then be calculated as the squared amplitude of the normalized Fourier spectrum

$$P_k = \frac{2}{N_\gamma} \left|X_k\right|^2, \tag{1.13}$$

where

$$N_\gamma = \sum_{j=0}^{N-1} x_j, \tag{1.14}$$

gives the total number of events in the time series. This normalization is chosen such that a time series due to a Poisson noise process produces a power spectrum with its elements distributed as a χ^2-distribution with 2 degrees of freedom (Leahy et al. 1983), which allows the statistical properties of combined powers to be straightforwardly calculated. Usually the resulting power spectrum is subsequently renormalized in terms of the squared rms amplitude as a fraction of the mean count-rate per unit frequency (van der Klis 1995), such that the integrated power directly measures the variance of the X-ray light curve. This normalization is given by

$$P_k = \frac{2T}{N_\gamma^2} \left(\frac{B+S}{S}\right)^2 \left|X_k\right|^2, \tag{1.15}$$

where the factor $(B+S)^2/S^2$ serves to correct the power for the expected background count rate, B, by expressing the rms amplitude as a fraction of the source count rate, S, rather than the observed count rate, $N_\gamma/T = (B+S)$.

The usual frequency range in which statistically significant power is detected is between millihertz and kilohertz. Although X-ray binaries also show variability on longer time scales, such slow variability is more conveniently diagnosed in the time domain directly. The power spectral density consists of several components (see e.g. Figure 1.3), showing broad features at low frequency with superimposed sharp peaks at higher frequency. Traditionally the broad features are called noise components and the narrow peaks are called quasi-periodic oscillations (QPOs).

The power spectrum can be presented in a multitude of ways: with a linear or logarithmic scale, with the Poisson noise subtracted or not, multiplied with frequency or not. The latter is of particular interest, as the power versus frequency representation (P_ν) shows the straightforward power density which draws attention to the noise components, whereas the frequency times power versus frequency representation (νP_ν) gives a direct impression of each component's contribution to the total variance, which is useful to illustrate the higher frequency QPOs.

In the absence of a physical model describing the power spectral components it has been standard practice to fit the power spectrum with the sum of several Lorentz func-

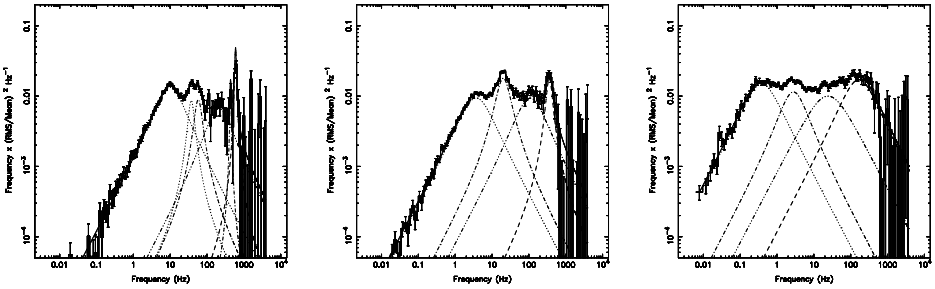

Figure 1.3: Shown here are three example power spectra in the νP_ν representation for three different source states. See, for instance, Chapter 4 for a discussion on the shapes, naming and evolution of the different power spectral components.

tions (Nowak 2000; Belloni et al. 2002). The Lorentz function is given as

$$L\left(\nu \mid \nu_0, W, r\right) = \frac{2Wr^2}{\pi} \frac{1}{W^2 + 4\left(\nu - \nu_0\right)^2}, \tag{1.16}$$

with ν_0 the centroid frequency, W the full-with-at-half-maximum and r the fractional rms, that is, the surface below the Lorentzian function integrated from $-\infty$ to $+\infty$. Because the characteristic frequency of this function is different for broad and narrow features (i.e. for a broad feature the characteristic frequency is dominated by W, whereas for a narrow feature the characteristic frequency is dominated by ν_0) the Lorentzian function is often parameterized as $L\left(\nu \mid \nu_{\max}, Q, r\right)$, where the characteristic frequency

$$\nu_{\max} = \sqrt{\nu_0^2 + \left(\frac{W}{2}\right)^2}, \tag{1.17}$$

gives the frequency at which the power density times frequency reaches a maximum and the quality factor $Q = \nu_0/W$ describes the coherence of the component. This description has the advantage of describing both broad and narrow components with the same characteristic frequency and applying smoothly to intermediate cases.

The Lorentzian function gives the power density of a sinusoidal oscillation at frequency ν_0 with an exponentially damped amplitude. While this gives a reasonably good description of the power spectral shape from an empirical point of view, it may not be the actual process of underlying variability. Occasionally a Lorentzian profile fails to provide a statistically satisfactory description of the data, usually in the low-frequency regime. Sometimes this can be solved by using multiple Lorentzians for a single feature (see e.g. Chapter 4), but for others an alternative function is required. An example is seen in Chapter 3, in which case a Schechter function (Hasinger & van der Klis 1989; Dotani et al. 1989) is used. This function is given by an exponentially cut-off power-law

$$S(\nu) \propto \nu^{-\alpha} \exp\left(-\nu/\nu_{\text{cut}}\right), \tag{1.18}$$

with power-law index α and cut-off frequency ν_{cut}.

1.4 Outline

In this thesis the X-ray variability of accreting millisecond pulsars is investigated. Special attention is given to the canonical accreting millisecond pulsar SAX J1808.4–3658, which thanks to a comparatively short and stable recurrence time is the best sampled source of its class. Through the coherent timing method the pulsations are used to study the characteristics and long-term spin and orbital evolution of these accreting neutron stars. Through stochastic timing methods the aperiodic variability is studied, with the aim of understanding the variable accretion flow that drives the X-ray emission and the coherent pulsations. Finally, both the coherent and aperiodic variability are considered together, such that the accuracy and diagnostic power of the coherent pulsations are used to shed light on the physical connection between these two phenomena: the magnetic coupling between the neutron star and its surrounding accretion flow.

In Chapter 2 the outburst of SAX J1808.4–3658 observed in 2011 is analyzed using the coherent timing method. This analysis yielded precise measurements of the pulsar's spin frequency and spin-down rate. Additionally, thanks to the 14-year observational baseline, the orbital period is measured to great precision, allowing its derivative and second derivative to be measured. These measurements suggest that the angular momentum of the companion star is coupling to the binary orbital period through its mass quadrupole.

In Chapter 3 the discovery of a peculiar aperiodic flaring variability at high luminosity is reported for SAX J1808.4–3658. Through careful study of the periodic pulsations during the episodes of flaring it is shown that the amplitude of the pulsations correlates with flux changes due to the flaring, in such a way that the fractional pulse amplitude remains constant. This provides strong evidence that the flaring originates from an accretion rate variability of the magnetospheric boundary that is modulating the intensity of the pulsed emission. Based on this work, the detection of such a flaring phenomenon in other low-mass X-ray binaries then provides a new method of demonstrating the existence of a magnetosphere in the absence of coherent pulsations.

In Chapter 4 the aperiodic variability observed in SAX J1808.4–3658 across five outbursts spread over 14 years of observation is analyzed in detail. This systematic study catalogues the rich variability seen in this source, offers new detections of twin kHz QPOs, and the first in-depth analysis of the enigmatic $\sim$ 410 Hz QPO, which has only been observed in this accreting pulsar. Interpreting the 410 Hz QPO as a beat with the 401 Hz pulse signal, it is suggested it may be due to the same mechanism as the low-frequency QPO, which would then have to be retrograde with respect pulsar's rotation direction.

In Chapter 5 a direct relation between the kHz QPOs and the coherent pulsations is discovered in SAX J1808.4-3658. By simultaneously measuring these two probes of the inner accretion flow it is shown that the kHz QPO has a direct effect on the amplitude of the pulsations: as the QPO frequency drifts through the spin frequency, the brightness of the pulsar systematically jumps by a factor of two. This strongly suggests that the upper

kHz QPO is due to an azimuthal motion at the inner edge of the accretion disk that, depending on whether it is faster or slower than the spin, is interacting differently with the stellar magnetosphere.

In Chapter 6 the coherent pulsations of the accreting millisecond pulsar NGC 6440 X-2 are considered. Among the accreting millisecond pulsars this peculiar source is unique in its outburst pattern, showing a recurrence time of one to a few months and outbursts lasting only a few days. Through coherent timing analysis the spin and orbital parameters of this source are measured. The possibility of coherently connecting the spin-phase across all outbursts is investigated, but shown not to have a unique solution.

In Chapter 7 the entire population of accreting millisecond pulsars detected with the *Rossi X-ray Timing Explorer* is studied. Based on an accretion disk-magnetosphere interaction model, the luminosity range over which pulsations are detected is used to estimate the strength of the stellar magnetic field. This approach offers an estimate of the field strength that can be applied consistently across all accreting millisecond pulsars, allowing for a robust comparison of field strengths within the population and with other millisecond pulsars, as needed to study the evolution process of these rapidly rotating neutron stars.

2 Accelerated orbital expansion and secular spin-down of the accreting millisecond pulsar SAX J1808.4–3658

A. Patruno, P. Bult, A. Gopakumar, J. M. Hartman, R. Wijnands,
M. van der Klis & D. Chakrabarty

The Astrophysical Journal Letters, 2012, 746, L27

Abstract

The accreting millisecond pulsar SAX J1808.4–3658 has shown a peculiar orbital evolution in the past with an orbital expansion much faster than expected from standard binary evolutionary scenarios. Previous limits on the pulsar spin frequency derivative during transient accretion outbursts were smaller than predicted by standard magnetic accretion torque theory, while the spin evolution between outbursts was consistent with magnetic dipole spin-down. In this Letter, we present the results of a coherent timing analysis of the 2011 outburst observed by the *Rossi X-Ray Timing Explorer* and extend our previous long-term measurements of the orbital and spin evolution over a baseline of 14 years. We find that the expansion of the 2-hr orbit is accelerating at a rate of $\ddot{P} \simeq 1.6\times10^{-20}$ s s^{-2} and we interpret this as the effect of short-term angular momentum exchange between the mass donor and the orbit. The gravitational quadrupole coupling due to variations in the oblateness of the companion can be a viable mechanism for explaining the observations. No significant spin frequency derivatives are detected during the 2011 outburst $\left(|\dot{\nu}| \lesssim 4\times10^{-13}\ \text{Hz s}^{-1}\right)$ and the long-term spin-down remains stable over 14 years with $\dot{\nu} \simeq -10^{-15}$ Hz s^{-1}.

2.1 Introduction

The transient X-ray binary SAX J1808.4–3658 is the first accreting millisecond X-ray pulsar (AMXP) discovered (Wijnands & van der Klis 1998a) among the 15 systems currently known. It is also the best sampled AMXP thanks to its relatively short recurrence time (1.6–3.3 years) and the continuous coverage of the *Rossi X-ray Timing Explorer* (*RXTE*), which has extensively monitored all outbursts since 1998. The presence of pulsations reveal the spin of the accreting pulsar ($\sim$ 401 Hz) and allow the study of torques that act upon the neutron star. This is particularly valuable because the spin evolution reveals details of the recycling mechanism that transforms a newly born slowly rotating neutron star into a millisecond pulsar via accretion (Alpar et al. 1982; Radhakrishnan & Srinivasan 1982). In our previous works (Hartman et al. 2008, 2009) we reported upper limits on the spin-up of the pulsar due to accretion torques (during outbursts) with a pulsar spin frequency derivative of $|\dot{\nu}| \lesssim 2.5\times10^{-14}$ Hz s^{-1}. This value is smaller than predicted by accretion theory (Ghosh & Lamb 1979b) if the spin frequency of SAX J1808.4–3658 substantially differs from the equilibrium spin frequency at the accretion rate close to the peak of the outburst. The long term spin evolution of the pulsar reveals a constant spin-down of magnitude $-5.5\pm1.2\times10^{-16}$ Hz s^{-1} possibly due to magnetic-dipole radiation acting during quiescence, for a surface magnetic field of the pulsar $B \simeq 1.5\times10^{8}$ G, in line with the expected field strength of millisecond radio pulsars.

SAX J1808.4–3658 is undergoing an unexpectedly fast orbital evolution with the orbital period increasing on a timescale of $\sim$ 70 Myr (Hartman et al. 2008,di Salvo et al. 2008). The binary has an orbital period of 2.01 hours (Chakrabarty & Morgan 1998) and the donor star is a $0.05-0.1\ M_{\odot}$ brown dwarf (Bildsten & Chakrabarty 2001; Deloye et al. 2008) suggesting that the orbital evolution should be dominated by angular momentum loss via gravitational waves and possibly by magnetic braking (Tauris & van den Heuvel 2006). The timescale of the orbital evolution is, however, too fast to be explained with such a scenario, and non-conservative processes with large mass loss from the system have been invoked (di Salvo et al. 2008, Burderi et al. 2009). Hartman et al. (2008, 2009) suggested instead that interchanges of angular momentum between the companion and the orbit can dominate the short-term orbital evolution as seen in several binary millisecond pulsars (Arzoumanian et al. 1994; Nice et al. 2000).

On October 31, 2011 *Swift*-BAT detected a new outburst of SAX J1808.4-3658 (Markwardt et al. 2011; Papitto et al. 2011a). This is the seventh outburst observed since its discovery (in 't Zand et al. 1998) and the sixth monitored with *RXTE*. We present a coherent pulsation analysis of the outburst and we complete the study of the spin and orbital evolution of SAX J1808.4–3658 over a baseline of fourteen years.

2.2 X-ray observations and coherent analysis

We use all *RXTE* Proportional Counter Array (PCA; Jahoda et al. 2006) public data for the 2011 outburst (Program ID 96027). We construct the 2–16 keV X-ray light-curve with PCA Standard-2 data averaging the flux for each observation and normalizing it in Crab units (see for example van Straaten et al. 2003). One burst is detected at MJD 55873.9 and all data with a flux more than twice the pre burst level are removed from the light curve.

For the timing analysis we use all photons (excluding the burst interval) in the energy band $\sim 2-16$ keV (5–37 absolute channels) in Event 122 μs mode. The data are barycentered with the FTOOL *faxbary* by using the optical position (Hartman et al. 2008) and the JPL DE405 Solar System ephemeris. We fold $\sim$ 500 s long data segments in pulse profiles of 32 bins, keeping only those with signal-to-noise (S/N) $> 3.3\sigma$, giving < 1 false pulse detection for the entire outburst. The S/N is defined as the ratio between the pulse amplitude and its 1σ statistical error. The folding procedure uses the preliminary ephemeris reported in Papitto et al. (2011a). A fundamental (ν) and a first overtone (2ν) are detected in the pulse profiles. The Time of Arrivals (TOAs) are measured separately for each harmonic to avoid that pulse shape variability affects the fiducial point defining the pulse TOA (see Hartman et al. 2008 for details).

To follow the evolution of the orbit and the pulsar spin we fit separately the two sets of TOAs (fundamental and first overtone) with the software TEMPO2 (Hobbs et al. 2006). The initial model used is a Keplerian circular orbit and a constant pulse frequency. We then repeat the folding procedure with the new timing solution until we reach convergence to the final orbital and pulse parameters. To calculate the errors on the rotational parameters we use Monte Carlo (MC) simulations, that account for the presence of long-timescale correlations in the pulse TOAs (Hartman et al. 2008; Arzoumanian et al. 1994). To verify the presence of a spin frequency derivative we fit a pulse frequency and its time derivative to the TOAs and run 10^4 MC simulations to estimate the significance of the measurements (see Hartman et al. 2008 and Patruno et al. 2010b for further details).

2.3 Results of the 2011 outburst

2.3.1 X-ray light curve and pulse profiles

The first *RXTE* pointed observation was taken on November 4, $\sim$ 5 days after the beginning of the outburst (Markwardt et al. 2011). The X-ray flux shows a peak at $\sim$ 80 mCrab, remarkably higher than the peak luminosity in 2005 and 2008 and similar to the 1998 and 2002 values (Wijnands 2004). Since the observations started five days after the onset of the outburst, the true outburst peak at MJD 55868 (observed by *Swift*-BAT) has been missed by *RXTE*. The *RXTE* PCA light-curve of the 2011 outburst is shown in Figure 2.1.

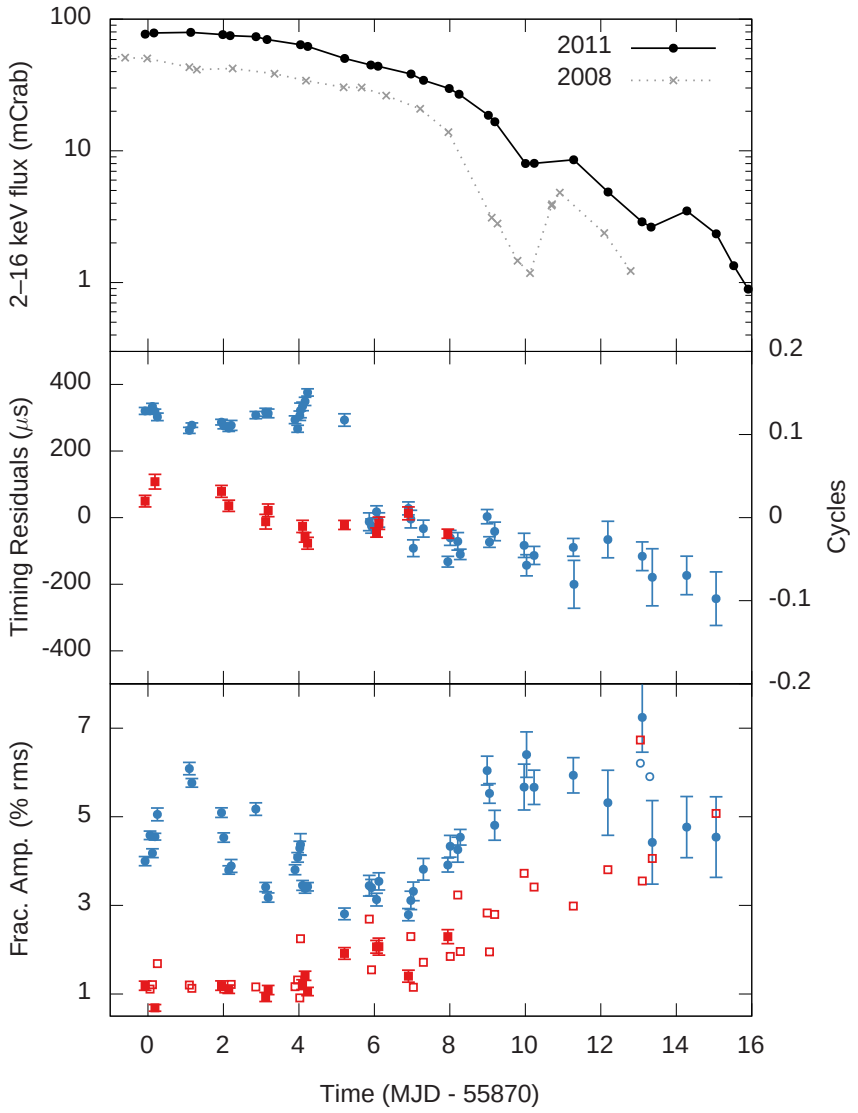

Figure 2.1: Top panel: X-ray light-curve (2–16 keV) of the 2011 outburst (solid line) compared to the 2008 outburst (dotted curve). The data points are *RXTE* observations-long averages. Middle Panel: timing residuals for fundamental (blue dots) and first overtone (red squares) for a ν = const model. Each data point is an *RXTE* orbit-long average. The fundamental has a jump of ~ 0.15 at MJD ~ 55875. Bottom Panel: Fractional amplitude of the fundamental (blue dots) and first overtone (red squares). The 95% c.l. upper limits are indicated with open symbols.

Table 2.1: SAX J1808.4–3658 Timing Solution for the 2011 Outburst

Parameter	Value	Stat. Error	Syst. Error
ν (Hz)	400.97520981	7×10^{-8}	10^{-7}
$\lvert\dot{\nu}\rvert$ (Hz s^{-1})	$< 4 \times 10^{-13}$	(95% c.l.)	
P_b (s)	7249.162	0.003	
$A_x \sin(i)$ (lt-ms)	62.798	0.005	
$T_{\rm asc}$ (MJD)	55896.895635	0.00002	
e	$< 10^{-4}$	(95% c.l.)	

The flux is observed to slowly decay over the entire duration of the main outburst, reaching a minimum flux of 8 mCrab on MJD 55880. The flux then keeps decreasing with two bumps at MJD 55881 and 55884, which might possibly be associated with the flaring-tail stage, when quasi periodic bumps are observed at low flux level (Wijnands et al. 2001; Hartman et al. 2008; Patruno et al. 2009d). However, differently from the 2000 through 2008 outbursts, this phase is poorly sampled and difficult to characterize. During the tail a strong 1 Hz modulation was reported for several outbursts (2000, 2002, 2005; van der Klis et al. 2000; Patruno et al. 2009d) but it is not detected in any of the 2011 observations.

The source became undetectable on MJD 55885.9 (November 20) and the monitoring abruptly ended on November 27, due to solar constraints. These also prevented to establish whether at the time of the last observation SAX J1808.4–3658 was in quiescence or in one of the faint ($\sim 10^{32}$ erg s^{-1}) states observed in the past with *Swift* and *XMM-Newton* observations (Wijnands et al. 2003; Campana et al. 2008).

The pulse profiles are very sinusoidal until MJD 55874 and then change becoming skewed with a more evident first overtone peaking on the right part of the profile. At MJD 55880, during the possible flaring stage, the pulse profiles become very sinusoidal again, a phenomenon never observed in the previous outbursts. This is reflected in the rms amplitude of the two harmonics (see Figure 2.1).

2.3.2 Timing noise and error estimation

The timing solution of the 2011 outburst is displayed in Table 2.1 while a previous analysis of the five outbursts observed with *RXTE* is available in Hartman et al. (2008, 2009). The authors found strong timing noise operating on the same timescales over which the pulse frequency and its time derivative were measured. The 2011 TOA residuals of a ν = const model, show the typical behavior observed in the previous outbursts in both harmonics.

We detect a strong phase jump in the fundamental with magnitude of 0.15 cycles (0.3 ms) at MJD ∼55874–55876. This behaviour is similar to what was previously seen during the 2002 and 2005 outbursts, with phase jumps of 0.2 cycles observed when the flux reached the transition from slow to fast decay (Burderi et al. 2006, Hartman et al.

2008, Patruno et al. 2009d). The first overtone instead has no phase jump but displays a short timescale (few minutes to ~ 1 day) scattering slightly in excess of that expected from measurement errors alone.

We use the phase information of the first overtone to phase connect across the phase jump of the fundamental (see Hartman et al. 2008 for details of the procedure). A net spin frequency derivative (i.e., measured over the entire outburst length) is not detected, with upper limits of $|\dot{\nu}| \lesssim 8.8 \times 10^{-13}$ Hz s^{-1} at the 95% confidence level. By removing the TOAs of the first observation in both harmonics (when timing noise is strong) and the 0.15 cycle phase jump for the fundamental, we obtain similar results with a more stringent constraint on the spin frequency derivative: $|\dot{\nu}| \lesssim 4 \times 10^{-13}$ Hz s^{-1} (95% c.l.).

The errors on the orbital parameters measured with the fundamental are only marginally affected by timing noise since they are measured on timescales (2 hr) different than the timing noise one ($\sim$ days). This is verified by calculating a power spectrum of the TOA residuals and comparing the Poissonian level to the power at the orbital frequency $1/P_b$. The excess power at $1/P_b$ is about 1.5 and 3 times the Poissonian level for fundamental and first overtone respectively. We therefore rescale the statistical errors on the orbital parameters by the same factor.

2.3.3 X-ray flux / pulse phase correlation

In 2009, Patruno et al. (2009e) proposed an alternative method to partially account for the timing noise in the TOAs of AMXPs. X-ray flux variations were found to be linearly correlated or anti-correlated with the pulse phases. Instead of minimizing the rms of the TOA residuals, Patruno et al. (2009e) minimized the χ^2 of a linear fit to the phase-flux correlation, finding slightly different spin frequencies than those measured with rms minimization methods. The reason of this difference is that instead of treating timing noise as a red noise process of unknown origin, the variations of the X-ray flux are assumed to instantaneously affect the pulse phases. We found that while the fundamental frequency always follows a correlation, the first overtone in some cases behaves differently and we exclude it from our 2011 analysis. By repeating the same procedure outlined in Patruno et al. (2009e) for the 2011 outburst, we find a pulse frequency of $\nu = 400.97520981(7)$ Hz, where 1σ errors have been rescaled by a factor 2.5 such that $\chi^2/\mathrm{dof} = 1$ (Bevington & Robinson 2003; Patruno et al. 2009c). The difference between this value and the pulse frequency $\nu_{\rm rms}$ obtained with standard rms minimization of the TOA residuals is $\nu - \nu_{\rm rms} = -0.15 \pm 0.08$ μHz.

2.4 The long term evolution of SAX J1808.4–3658

2.4.1 Long term spin frequency evolution

We first fit the change of the six constant pulse frequencies (from 1998 to 2011) of SAX J1808.4–3658 using the values reported in Patruno et al. (2009e) and the 2011 frequency obtained from the flux-phase correlation technique. We rescale the errors of each spin frequency to give a $\chi^2/\mathrm{dof} = 1$ and we fit a linear relation to the data. The fit gives a $\chi^2 = 5.4$ for 4 dof, and a spin-down of $\dot{\nu} = -1.65(20) \times 10^{-15}$ Hz s^{-1} (Figure 2.2). This is in agreement with the value reported in Patruno et al. (2009e). A spin frequency second derivative is not required by the fit, and we can place upper limits of $|\ddot{\nu}| \lesssim 10^{-24}$ Hz s^{-2} (95% c.l.).

We also fit the 2011 outburst pulse frequency with the rms minimization method (i.e., TEMPO2 plus MC errors), together with the previous five spin frequency measurements obtained with the same technique (Hartman et al. 2009). The χ^2 is high, 19.5 for 4 dof and we ascribe this almost exclusively to the 2000 outburst spin frequency (see Hartman et al. 2009). If we remove the 2000 data, the fit returns a $\chi^2 = 3.57$ for 3 dof. The spin-down is constrained to be $\dot{\nu} = -7.4(4) \times 10^{-16}$ Hz s^{-1}. This estimate is within 2σ from the value previously reported by Hartman et al. (2009) and within 1σ when removing the 2000 outburst data.

Since both fits of the long-term spin frequency evolution are statistically acceptable, we cannot decide which of the two values reported is closer to the true $\dot{\nu}$. The differences in the ν and long term $\dot{\nu}$ found with the rms minimization and with the phase-flux correlation reflect a systematic uncertainty of ~ 0.1 μHz that needs to be considered until the exact mechanism behind timing noise is identified.

2.4.2 Long term orbital evolution

To detect variations of the orbital period we use the procedure explained in Hartman et al. (2008, 2009) that requires estimates for the times of passage through the ascending node T_{asc} at various outbursts. We choose as a reference point the $T_{\mathrm{asc,ref}}$ value in Table 1 of Hartman et al. (2009), and we calculate the residuals $\Delta T_{\mathrm{asc}} = T_{\mathrm{asc},i} - \left(T_{\mathrm{asc,ref}} + N\ P_b\right)$, where $T_{\mathrm{asc},i}$ is the i^{th} outburst and N is the closest integer to $\left(T_{\mathrm{asc},i} - T_{\mathrm{asc,ref}}\right)/P_b$. The chosen P_b is also reported in Table 1 of Hartman et al. (2009).

In a previous work (Hartman et al. 2008, 2009) we detected a $\dot{P}_b = (3.80 \pm 0.06) \times 10^{-12}$ s s^{-1} (see also di Salvo et al. 2008 and Burderi et al. 2009). When including the 2011 data, a parabolic fit gives a $\chi^2 = 62.8$ for 3 dof, thus suggesting that a constant increase of the orbital period is not the correct model for SAX J1808.4–3658. We then add an orbital period second derivative $\left(\ddot{P}_b\right)$ and fit a cubic polynomial to the data. The fit is statistically acceptable, with $\chi^2 = 5.4$ for 2 dof and parameters $\dot{P}_b = 3.5(2) \times 10^{-12}$ s s^{-1} and $\ddot{P}_b = 1.65(35) \times 10^{-20}$ s s^{-2} (see Figure 2.2).

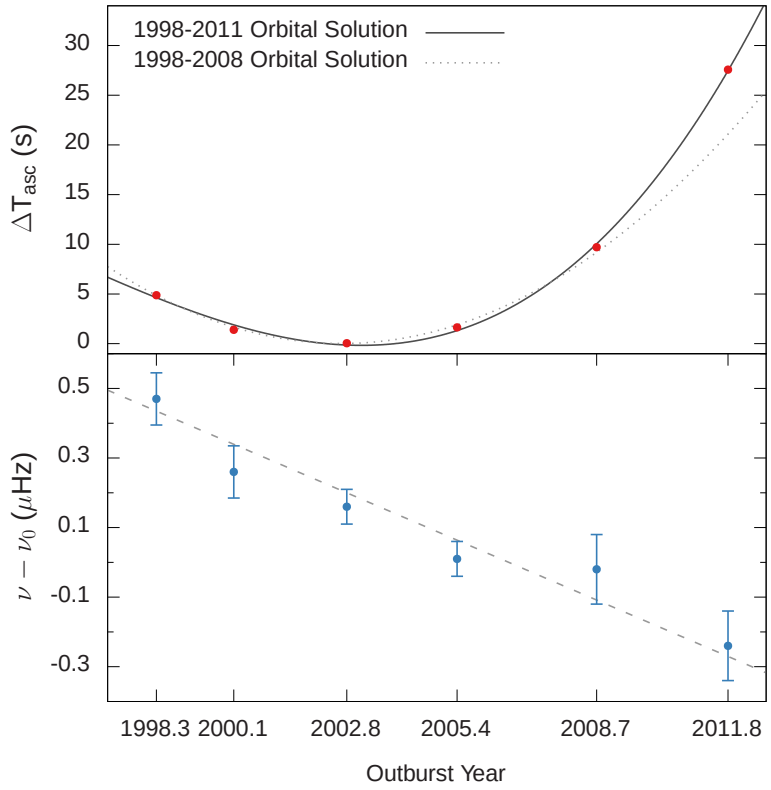

Figure 2.2: Orbital (top panel) and spin frequency evolution (bottom panel) over 14 years of observations. The $T_{\rm asc}$ residuals cannot be fitted with a parabola (dotted line) and they need a cubic fit suggesting an acceleration of the orbital period $\ddot{P}_b = 1.65 \times 10^{-20}$ s s^{-2}. The spin-down of the pulsar is stable and proceeds at a rate of -10^{-15} Hz s^{-1}. The reference frequency is $\nu_0 = 400.975210$ Hz.

A third time derivative or a sinusoidal model are not required by the data. We also tried to fix the P_b and $\dot{P}_b$ at the values observed up to 2008 and add a sinusoidal fit to the data to investigate the possibility of apsidal motion. The fit is statistically unacceptable and the periodicity found is of the order of 10^3 yr, which is already orders of magnitude larger than the expected general relativistic effect alone.

2.5 Discussion

2.5.1 Pulsar spin evolution

The long term spin-down continues with a constant rate comparable to what has been measured between 1998 and 2008. The only plausible explanation for the spin-down in SAX J1808.4–3658 requires magnetic-dipole radiation with a surface magnetic field of the neutron star at the poles $B \simeq (1.5-2.5)\times 10^8$ G (for a radius $R = 10$ km) for a magnetic-dipole moment $\mu = (0.7-1.5)\times 10^{26}$ G cm^3. This range includes the different spin-down measurement methods reported in Sections 2.3.2 and 2.3.3 and is close to the B field obtained with Fe line spectral fitting (Cackett et al. 2009; Papitto et al. 2009) and accretion disk modeling (Ibragimov & Poutanen 2009).

The remarkably constant long term spin-down places stringent constraints on any ongoing spin-up during an outburst. If spin frequency variations were larger than the upper limit reported by Hartman et al. (2008) ($|\dot{\nu}| \lesssim 2.5\times 10^{-14}$ Hz s^{-1}), they would produce a scatter in the observed spin frequencies of the order of $0.1-0.4$ μHz (for $\dot{\nu} \simeq 5-10\times 10^{-14}$ Hz s^{-1}). This scatter is not observed with statistical errors of $\sim 0.05-0.1$ μHz (see Figure 2.2), and suggests that the net spin-up during an outburst is at best very small in magnitude for SAX J1808.4–3658.

2.5.2 Orbital period evolution

The orbital period P_b indicates that the orbit of SAX J1808.4–3658 is expanding and accelerating at a very fast rate. The timescale for the acceleration is:

$$\tau_{\rm acc} \simeq \frac{2\dot{P}_b}{\ddot{P}_b} \sim 10 \text{ yr} \tag{2.1}$$

suggesting that the identified $\dot{P}_b$ might not represent the secular evolution of the orbital period. If we assume that the measured acceleration is constant, then SAX J1808.4–3658 has changed sign of $\dot{P}_b$ about 25 years ago. There is, however, no reason for $\ddot{P}_b$ to be constant, since we are not sensitive to higher order derivatives and both $\dot{P}_b$ and $\ddot{P}_b$ might be part of long timescale variations similar to those observed in binary millisecond pulsars (Nice et al. 2000). Until the 2008 outburst, when only a constant $\dot{P}_b$ was detected, two interpretations were given: a secular orbital evolution due to non-conservative mass transfer (di Salvo et al. 2008, Burderi et al. 2009) and a short-term evolution associated with exchange of angular momentum between the donor star and the orbit (Hartman et al. 2008, 2009).

If SAX J1808.4–3658 has increased its mass loss due to an enhancement of the donor ablation, then the wind loss from the companion ($\dot{M}_w$) needs to increase at a rate comparable with that of the orbital period, since $\dot{P}_b \propto \dot{M}_w$. The mass loss is related to $\dot{E}_{\rm abl} = 0.25\,(R/A)^2\,\dot{E}$, where $\dot{E}_{\rm abl}$ is the ablation power, $\dot{E}$ is the pulsar rotational spin-

down power and R and A the donor radius and the semi-major axis of the binary. To explain the acceleration $\ddot{P}_b$, the energy loss of the pulsar $\dot{E}$ needs to have increased (in absolute value) in the last 14 years by a factor of ~ 5. Since $\dot{E} \propto \nu\dot{\nu}$, the spin-down $\dot{\nu}$ needs to vary at a rate $\ddot{\nu} \simeq -10^{-23}$ Hz s^{-2} to reach the energy loss required. By using the long-term spin evolution presented in the previous section we can put constraints on $|\ddot{\nu}| \lesssim 10^{-24}$ Hz s^{-2}. We conclude that the enhanced ablation scenario is not supported by the observations.

A dynamically induced period derivative in the gravitational potential well of a third body can also be excluded. The effect of a potential well is identical on the orbital and spin frequencies and derivatives

$$f^{(n)} = -f\frac{\boldsymbol{a}^{(n-1)} \cdot \hat{\boldsymbol{n}}}{c} \tag{2.2}$$

where $f^{(n)}$ is the n^{th} time derivative of the orbital or spin frequency, $\boldsymbol{a}$ is the acceleration due to the third body, $\hat{\boldsymbol{n}}$ is a unit vector along the line of sight and c the speed of light. To explain the observed $\ddot{P}_b$ we need $\dot{a} \sim 10^{-15} - 10^{-16}$ m s^{-3} and $|\ddot{\nu}| \sim 10^{-21}$ Hz s^{-1}, which is not observed.

If the measured orbital evolution is a short-term event, then one explanation can be found with the donor spin-orbit coupling model. A coupling between the pulsar rotational energy loss (in form of winds or fields) and the orbital angular momentum (Damour & Taylor 1991) is ruled out by the small magnitude of the effect produced by the tiny $\dot{E}$ of SAX J1808.4–3658. A mass quadrupole variation of the donor star is a more promising possibility. A change ΔQ in the mass quadrupole leads to a change in orbital period (Richman et al. 1994; Applegate & Shaham 1994; Applegate & Patterson 1987):

$$\frac{\Delta P_b}{P_b} = -2\left(\frac{R}{A}\right)^2 \frac{\Omega^2 R^3}{GM}\frac{M_s}{M}\frac{\Delta\Omega}{\Omega} \tag{2.3}$$

where M and R are the donor mass and radius, M_s is a thin shell of mass generating the quadrupole, and Ω the angular velocity of the star. If we assume that the angular velocity of the donor is almost synchronous with the orbital angular velocity, then the variation $\Delta P_b \simeq 0.004$ s observed in the last 14 years gives:

$$\frac{\Delta\Omega}{\Omega} \sim 10^{-4}\frac{M}{M_s} \tag{2.4}$$

The observed orbital period variations in the eclipsing millisecond pulsar PSR J2051–0827 and PSR B1957+20 are likely to be caused by changes in the quadrupole moment of the companion (Arzoumanian et al. 1994; Doroshenko et al. 2001; Lazaridis et al. 2011). Applegate (1992) proposed a magnetic activity cycle that leads to a deformation of the star at the origin of this behavior. The donor star of SAX J1808.4–3658 is also in Roche lobe contact, whereas binary millisecond pulsars are detached systems. If the orbital period of SAX J1808.4–3658 has decreased in the past for some time, then the Roche lobe

has moved across the outer envelope of the brown dwarf enhancing the mass transfer rate. A detailed discussion of this effect is beyond the scope of this letter, but we can speculate that SAX J1808.4–3658 has gone through periodic episodes (each lasting $\tau_{\rm acc} \sim$ 10 yr) of enhanced accretion in the past. This effect is opposite during the accelerated orbital expansion, with the mass transfer being less than in the non-accelerated case. The quadrupolar moment change has also the effect of heating the star, providing an explanation for the large entropy content of the donor (Deloye et al. 2008).

3 Discovery of 1–5 Hz flaring at high luminosity in SAX J1808.4–3658

P. Bult & M. van der Klis

The Astrophysical Journal, 2014, 789, 99

Abstract

We report the discovery of a 1–5 Hz X-ray flaring phenomenon observed at > 30 mCrab near peak luminosity in the 2008 and 2011 outbursts of the accreting millisecond X-ray pulsar SAX J1808.4–3658 in observations with the *Rossi X-ray Timing Explorer*. In each of the two outbursts this high luminosity flaring is seen for $\sim$3 continuous days and switches on and off on a timescale of 1–2 hours.

The flaring can be seen directly in the light curve, where it shows sharp spikes of emission at quasi-regular separation. In the power spectrum it produces a broad noise component, which peaks at 1–5 Hz. The total 0.05–10 Hz variability has a fractional rms amplitude of 20–45 percent, well in excess of the 8–12 percent rms broad-band noise usually seen in power spectra of SAX J1808.4–3658.

We perform a detailed timing analysis of the flaring and study its relation to the 401 Hz pulsations. We find that the pulse amplitude varies proportionally with source flux through all phases of the flaring, indicating that the flaring is likely due to mass density variations created at or outside the magnetospheric boundary. We suggest that this 1–5 Hz flaring is a high mass accretion rate version of the 0.5–2 Hz flaring which is known to occur at low luminosity (< 13 mCrab), late in the tail of outbursts of SAX J1808.4–3658. We propose the dead-disk instability, previously suggested as the mechanism for the 0.5–2 Hz flaring, as a likely mechanism for the high luminosity flaring reported here.

3.1 Introduction

The accreting millisecond X-ray pulsar (AMXP) SAX J1808.4–3658 (henceforth SAX J1808), was the first X-ray binary to show pulsations in the millisecond domain (Wijnands & van der Klis 1998a). Since its discovery with the *BeppoSax* satellite in 1996 (in 't Zand et al. 1998), SAX J1808 has shown regular outbursts with a recurrence time of 2–3.5 years. Between 1998 and 2012 a total of 6 outbursts have been detected, all of which were extensively monitored with the *Rossi X-ray Timing Explorer* (*RXTE*). The light curves of these outbursts show a remarkably similar morphology (Hartman et al. 2008), consistently starting with a 2–5 day steep rise in flux (*fast rise*), followed by a flattening that lasts for a few days (*peak*). After reaching its peak X-ray luminosity, the light curve shows a slow exponential decay over a time span of several days (*slow decay*), followed by faster linear decay (*fast decay*) which typically lasts for 3 to 5 days (Hartman et al. 2008). After the fast decay, the source enters a prolonged, low luminosity state (*outburst tail*), during which ∼5 day long episodes of increased X-ray emission are seen (Patruno et al. 2009d), causing the luminosity to vary between 5×10^{32} and 5×10^{35} erg s^{-1} (Wijnands 2004; Campana et al. 2008). After several weeks to months, the outburst tail ends and the source returns to a quiescent luminosity of $\sim 5 \times 10^{31}$ erg s^{-1} (Heinke et al. 2009).

Several types of variability are seen in SAX J1808. The 401 Hz coherent pulsations can be detected throughout the outburst, including the outburst tail (Hartman et al. 2008, 2009; Patruno et al. 2012), and are thought to be caused by thermal emission from a localized region on the neutron star surface heated by the impact of plasma coming down the accretion funnel. This so-called hotspot revolves with the neutron star spin, modulating the observed X-ray flux at the spin frequency. The pulsations thus offer a physical tracer of the innermost accretion flow.

In addition to the pulsations, type I X-ray bursts (in 't Zand et al. 1998) and twin kHz QPOs (Wijnands et al. 2003) have also been detected in SAX J1808. The stochastic variability of the 1998 and 2002 outbursts of SAX J1808 has been studied by van Straaten et al. (2005), who find that the power spectral characteristics are similar to those of a typical atoll source.

A peculiar type of variability in SAX J1808 is the strong 0.5–2 Hz flaring often seen in the outburst tail at luminosities < 13 mCrab. This phenomenon has frequently been designated as the '1 Hz QPO', however, in this paper we refer to it as the 'low luminosity flaring'. The low luminosity flaring was first reported by van der Klis et al. (2000) and found to occur sporadically throughout the outburst tails of 2000 and 2002 (Wijnands 2004). An in-depth study by Patruno et al. (2009d) showed that it was also present in the tail of the 2005 outburst, but not in the tail of the 2008 outburst. In the later 2011 outburst the low luminosity flaring was again not detected (Patruno et al. 2012, see Chapter 2), although due to Solar constraints only the onset of the tail could be observed.

The large luminosity variations in the outburst tails of SAX J1808 have been proposed to be caused by an intermittent propeller effect (Campana et al. 2008). In the propeller regime the inner edge of the accretion disk rotates slower than the neutron star magnetosphere and in-falling matter is no longer able to accrete onto the neutron star, but instead is blown out of the system as by a propeller (Illarionov & Sunyaev 1975). Considering the 0.5–2 Hz low luminosity flaring in the context of the propeller onset, Patruno et al. (2009d) propose the Spruit-Taam instability (Spruit & Taam 1993) as the most likely origin. An open problem with this interpretation, however, is the sporadic nature of this flaring in the 2000, 2002 and 2005 outburst tails as well as its complete absence in the 2008 and 2011 outbursts. As noted by Patruno et al. (2009d) other mechanisms such as an interchange instability (Arons & Lea 1976) can not be strictly ruled out.

In the present work we report on the detection of strong 1–5 Hz flaring observed in the 2008 and 2011 outbursts of SAX J1808 that is similar to the 0.5–2 Hz low luminosity flaring, but occurs at much higher luminosities, near the peak of the outburst. We present the timing properties of this high luminosity flaring and discuss its nature. In Section 3.2 we outline our data reduction procedure and our timing analysis methods. In Section 3.3 we present the results we obtained and in Section 3.4 we explore potential mechanisms for the high luminosity flaring and discuss our results in the context of the previously observed low luminosity flaring. Our conclusions are summarized in Section 3.5.

3.2 X-ray observations

We used data collected with the *RXTE* Proportional Counter Array (PCA, see Jahoda et al. 2006, for technical details). For the timing analysis we used the pointed observations of all observed outbursts of SAX J1808, excluding the outburst tail, selecting only data taken in GoodXenon or 122 μs Event mode. All data were binned to a time resolution of 1/8192 s prior to further analysis.

Additionally, we used the 16 second time-resolution Standard-2 data to construct 2–16 keV X-ray light curves normalized to Crab and calculate the standard Crab-normalized soft (3.5–6.0 keV / 2.0–3.5 keV) and hard (9.7–16 keV / 6.0–9.7 keV) colors (see e.g. van Straaten et al. 2003, for the detailed procedure).

3.2.1 Stochastic timing analysis

To study the stochastic time variability we calculated Fourier transforms of 256 second data segments, giving a frequency resolution of $\sim 4 \times 10^{-3}$ Hz and a Nyquist frequency of 4096 Hz. To optimize the signal-to-noise we selected only the events in channels 5–48 ($\sim$2–20 keV). No background subtraction or dead-time correction was applied prior to the Fourier transform. We used the transforms to compute Leahy normalized power spectra and subtracted the Poisson level using the formula of Zhang et al. (1995) according to the method described by Klein-Wolt et al. (2004).

Power spectra computed using segments of the same ObsID were averaged to improve statistics. Additionally, power spectra of consecutive ObsIDs were sometimes averaged to improve statistics further, but only if their flux and color properties were consistent with being the same and the power spectra were similar.

Finally, we normalized the averaged power spectra to source fractional rms amplitude squared per Hz (van der Klis 1995) while correcting for the background count rate as estimated using the FTOOL *pcabackest*. In this normalization the fractional rms contribution, r, of a given frequency band is

$$r^2 = \int_{\nu_1}^{\nu_2} P(\nu) d\nu, \tag{3.1}$$

where $P(\nu)$ is the power density in the described units.

We describe the power spectra by fitting a function consisting of the sum of several Lorentzians plus a Schechter function for the flaring component (see Section 3.3). We characterize each Lorentzian by its centroid frequency and full-width-at-half-maximum (FWHM). The strength, or power, of the Lorentzian is obtained by integrating it over frequency from 0 to ∞ and reported in terms of the corresponding fractional rms as defined in equation 3.1.

The Schechter function is an exponentially cut-off power law and is given by $P(\nu) \propto \nu^{-\alpha} e^{-\nu/\nu_{\rm cut}}$ (Hasinger & van der Klis 1989; Dotani et al. 1989), with power-law index α and cut-off frequency $\nu_{\rm cut}$. We can define a 'centroid' frequency $\nu_0 = -\alpha\nu_{\rm cut}$ as the frequency at which the Schechter function reaches is maximum in $P(\nu)$.

3.2.2 Coherent timing analysis

We correct the photon arrival times to the Solar System barycenter with the FTOOL *faxbary* using the source coordinates of Hartman et al. (2008). This tool also applies the *RXTE* fine clock corrections, allowing for high precision (∼4 μs) timing analysis (Rots et al. 2004). Selecting only the events in the channel range 5–37 (∼2–16 keV, Patruno et al. 2012), we fold the data to produce folded pulse profiles. For the timing solution we use the ephemeris of Hartman et al. (2009) for the 2008 outburst and that of Patruno et al. (2012) for the 2011 outburst. The length of the folded data segments varies depending on purpose; typically we fold ∼3000 s of continuous *RXTE* observations to obtain high signal-to-noise pulse profiles. Alternatively we take ∼256 s segments to obtain better time resolution when following the outburst evolution. In both cases we allow the segment length to vary such that we use the entire observed time series.

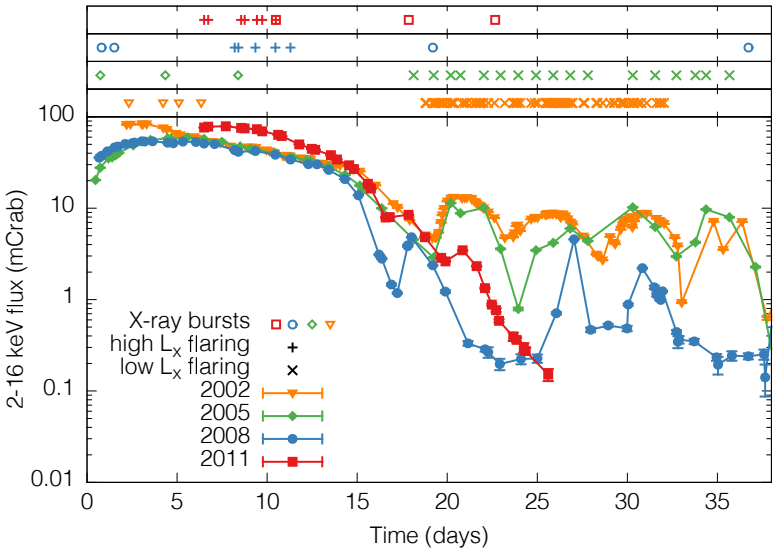

Figure 3.1: Light curves in the 2–16 keV X-ray band of the 2002 (orange triangles), 2005 (green diamonds), 2008 (blue circles) and 2011 (red squares) outbursts. The symbols in the top bars show the times of type I X-ray bursts and observations with high luminosity flaring (pluses, this paper) and low luminosity flaring (crosses, Patruno et al. 2009d). The light curves have been shifted in time such that the transition from slow to fast decay is at day 15, using a shift in MJD of 52553.6, 53522.3, 54731.2 and 55863.4 for the outbursts 2002 through 2011, respectively.

3.3 Results

The outbursts of SAX J1808 show very similar light curves. In Figure 3.1 we show the four outbursts that occurred between 2002 and 2011. Since the 1998 outburst does not show either flaring component and in 2000 only the outburst tail could be observed, we do not show these outbursts and exclude them from further analysis.

In Figure 3.1 the light curves where shifted in time such that the transition from the slow decay to the fast decay occurs on day 15. The top panels indicate the times of confirmed and suspected X-ray bursts (removed from the data prior to the analysis), detections of the low luminosity flaring (Patruno et al. 2009d) and detections of the high luminosity flaring (below).

Like the light curves, the power spectra of SAX J1808 are similar. The power spectra can usually be described with 4 Lorentzians (van Straaten et al. 2005); a broad noise 'break' component at ∼4 Hz, a 'hump' component in the range ∼20–80 Hz, a hectoHz component in the range ∼100–200 Hz, and the upper kHz QPO with a frequency in the range ∼300–700 Hz.

Both in 2008 and 2011 we find an interval spanning ∼3 days during which the power spectrum deviates significantly from its standard shape. The power density between

Table 3.1: High Luminosity Flaring Observation Information

ObsID	Length (s)	Start MJD	Flux (mCrab)	rms (%)[a]
		2008		
A-07	3000	54739.40	43.2	28.5
A-09	2300	54739.60	41.4	29.0
A-02	6100	54740.54	42.2	27.0
A-08	6100	54741.65	38.5	29.0
B-00[b]	1280	54742.49	34.1	38.7
		2011		
C-01	2800	55869.83	76.3	21.9
C-00	12000	55870.16	78.2	21.7
C-02	6100	55871.13	78.8	11.1
C-03	5400	55871.98	75.7	22.4
C-04	6100	55872.18	74.7	22.1
C-05	3100	55872.86	73.2	18.9
C-06	6100	55873.16	69.5	22.3

Note. A = ObsID 93027-01-02, B = ObsID 93027-01-03, C = ObsID 96027-01-01.
[a] 0.05–10Hz fractional rms.
[b] Using only the first of three observation files in the ObsID.

0.05 Hz and 10 Hz is much higher and rather than showing the usual horizontal plateau in $P(\nu)$, the power density shows a peak around ∼3 Hz (see Figure 3.2). Lorentzian and Gaussian functions fail to provide statistically acceptable fits to the power spectra as they are not steep enough at low frequencies. We find that replacing the Lorentzian break component with a Schechter function does provide a satisfactory fit to the data. The observations in which we see this behavior are marked with pluses in Figure 3.1 and their ObsIDs are given in Table 3.1. We combined the 12 observations showing this new phenomenon into 8 intervals and give all power spectrum fit parameters for those intervals in Table 3.2.

The centroid frequency of the best-fit Schechter function, as defined in Section 3.2.1, varies between 1 and 5 Hz. The amplitude of the flaring varies between 26 and 34% rms, and shows a clear anti-correlation with ν_0 (see Figure 3.3). The power-law index α shows some scatter, but no correlation with frequency.

The morphology of this new component is very different from the regular broad band noise, but quite similar to that of the low luminosity flaring seen in the outburst tails. Because the power spectrum returns to its normal shape outside the reported ∼3 day intervals, we suggest that this new high luminosity flaring phenomenon dominates over the Lorentzian break component normally seen in the same frequency range. During the 2008 outburst the amplitude of this new component briefly reaches ∼45% rms (see Section 3.3.1). In the bottom panel of Figure 3.4 we show a small selection of the light

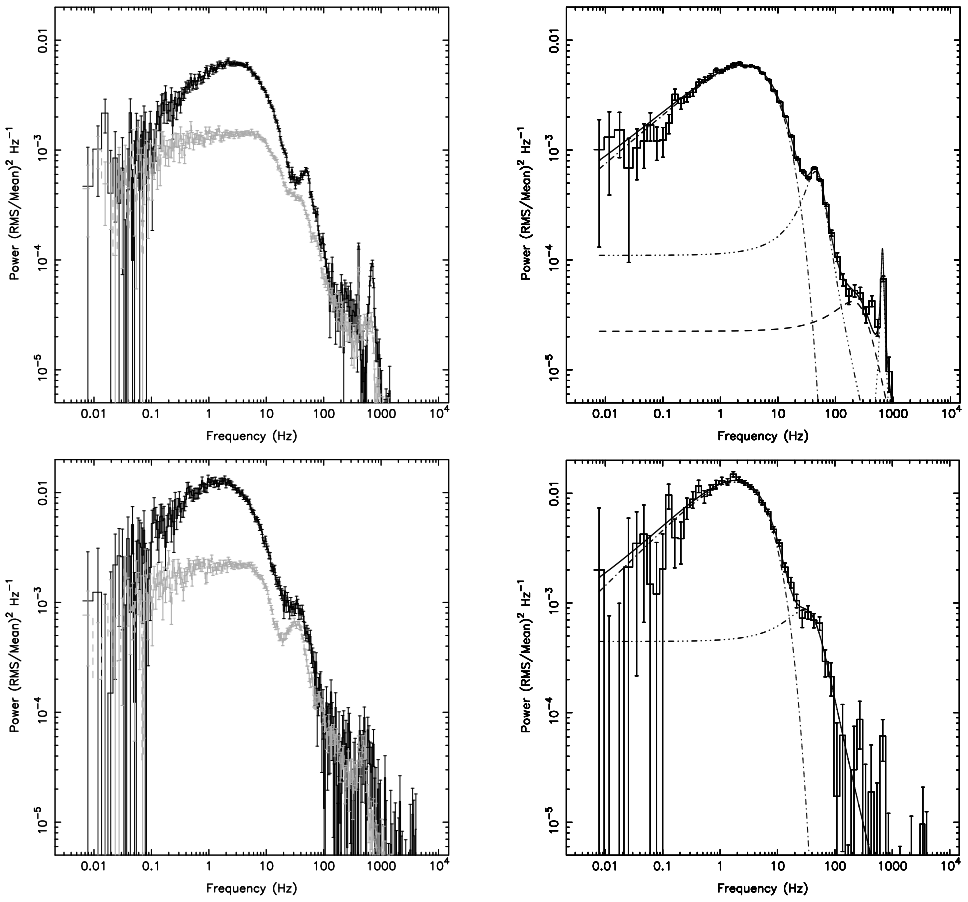

Figure 3.2: Power spectra of the high luminosity flaring. The left column compares the high luminosity flaring (average of all ObsIDs reported Table 3.1) of 2011 (top, black) and 2008 (bottom, black) with the broad band noise in the 2002 (top, gray) and 2005 (bottom, gray) outbursts in similar outburst stages and spectral states. The right column shows the Schechter function fit to power spectra for the 2011 (top) and 2008 (bottom) outbursts. Note that all power spectra show power density versus frequency.

curve during this time. The ∼3 Hz variability is directly visible and indeed has a flaring morphology, showing relatively sharp spikes of emission at quasi-regular separation. Contrary to the 0.5–2 Hz *low luminosity flaring*, which is seen only in the outburst tail for luminosities < 13 mCrab, the 1–5 Hz flaring, reported here for the first time, occurs near the peak of the outburst at luminosities > 30 mCrab and is therefore called the *high luminosity flaring*.

Table 3.2: Power Spectrum Fit Parameters

	high L_x flaring	Hump	hHz	upper kHz	
Group	α $\nu_{\rm cut}$ r	FWHM ν_0 r	FWHM ν_0 r	FWHM ν_0 r	χ^2/dof
			2008		
A-07, A-09	-0.69 ± 0.04 2.54 ± 0.12 28.03 ± 0.43	45.6 ± 4.9 21.4 ± 2.8 29.1 ± 1.8	... ...	404 ± 196 496 ± 56 19.5 ± 3.1	173/118
A-02	-0.41 ± 0.02 4.21 ± 0.15 28.72 ± 0.29	46.7 ± 4.1 34.1 ± 1.7 26.0 ± 1.0	... ...	147 ± 103 618 ± 31 12.1 ± 2.3	148/121
A-08	-0.51 ± 0.05 3.59 ± 0.24 30.78 ± 0.66	60.1 ± 9.7 29.2 ± 6.5 28.6 ± 2.7	... ...	... ...	76.8/121
B-00	-1.94 ± 0.25 1.40 ± 0.19 34.4 ± 1.6	14.1 ± 3.2 9.1 ± 1.6 25.7 ± 2.7	... ...	... ...	102/75
			2011		
C-01, C-00	-0.45 ± 0.01 5.63 ± 0.09 25.48 ± 0.10	40.8 ± 3.1 44.64 ± 0.52 20.20 ± 0.92	427 ± 232 199 ± 164 $16.7^{+11.2}_{-2.3}$	72 ± 23 656.1 ± 2.3 11.54 ± 0.76	172/141
C-02	-0.79 ± 0.15 5.65 ± 0.95 15.4 ± 1.3	58 ± 18 24 ± 13 13.7 ± 3.3	... ...	494 ± 430 466 ± 118 12.9 ± 3.8	58.9/65
C-03, C-04	-0.55 ± 0.02 5.29 ± 0.11 26.75 ± 0.15	52.0 ± 3.3 46.4 ± 1.1 21.48 ± 0.54	151 ± 50 321 ± 24 8.8 ± 1.2	95 ± 17 716.0 ± 4.6 13.34 ± 0.64	228/123
C-05, C-06	-0.59 ± 0.02 5.80 ± 0.13 27.31 ± 0.18	31.3 ± 4.6 50.04 ± 0.82 16.0 ± 1.4	472 ± 255 0 (fixed) 21.6 ± 1.9	61 ± 37 709.3 ± 3.3 12.60 ± 0.74	140/124

Note. A = ObsID 93027-01-02, B = ObsID 93027-01-03, C = ObsID 96027-01-01. Frequencies ν_0 and $\nu_{\rm cut}$ and FWHM are in units of Hz, and fractional rms, r, is expressed as a percentage.

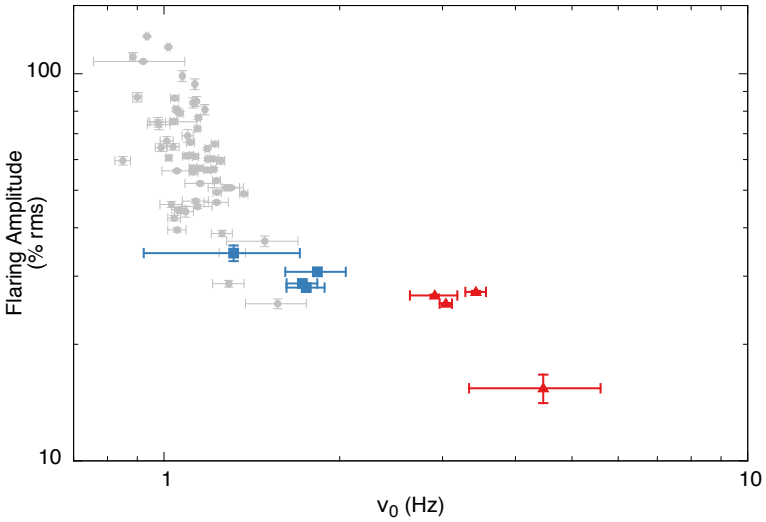

Figure 3.3: Correlation between the fractional rms and the high and low luminosity flaring centroid frequencies. We show the 2008 (blue squares) and 2011 (red triangles) high luminosity flaring frequency obtained in this work along with the low luminosity flaring frequencies (grey) from (Patruno et al. 2009d) against their respective fractional rms.

In order to study the evolution of the high luminosity flaring on short time scales we compute power spectra of 256 second data segments. Fitting a Schechter function to these short segment power spectra does not provide meaningful results, so instead we characterize the high luminosity flaring power by integrating the power spectrum between 0.05 and 10 Hz, the range in which we observe the bulk power in excess of the expected break component. These frequency bounds are identical to those used by Patruno et al. (2009d), allowing a comparison of the low luminosity flaring results with the results we obtain for the high luminosity flaring. The power estimates obtained in this way are described below. They match with the power measured by fitting a Schechter function to power spectra of longer observations.

We also study the relation of the high luminosity flaring with the 401 Hz pulsations by constructing pulse profiles for the same data segments and considering the joint behavior of the flaring rms amplitude and the phase and amplitude of the pulsations. We now discuss these results in detail for each outburst.

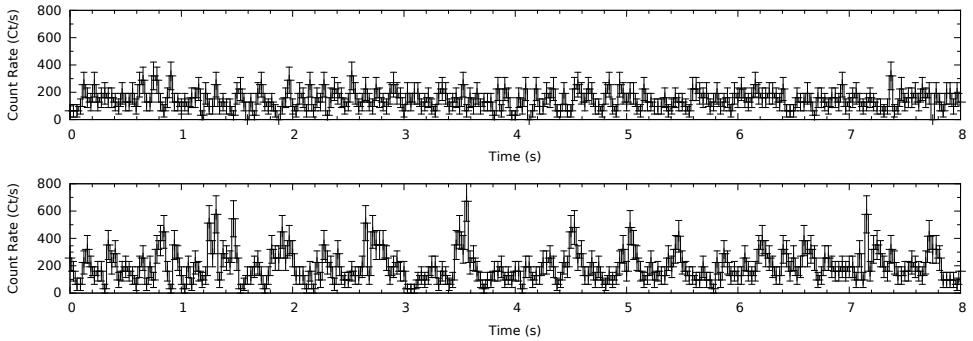

Figure 3.4: Light curve segments of the 2008 outburst at a time resolution of 0.035 s. The top panel shows a segment of ObsID 93027-01-03-02 which shows the regular broad band noise in the power spectrum. The bottom panel shows a segment of ObsID 93027-01-03-00, during the time that the high luminosity flaring shows an amplitude of 45% rms.

3.3.1 2008

In 2008 the high luminosity flaring is seen at the onset of the slow decay. The flaring is present for ∼3.1 days between MJD 54739 and MJD 54742, during which the flux decays from 43 to 34 mCrab. In Figure 3.5 we present the source evolution during this interval showing, from top down, the 2–16 keV light curve, hard (orange) and soft (purple) colors, 0.05–10 Hz rms amplitude, and the phase and amplitude for the fundamental (blue) and second harmonic (red) of the 401 Hz pulsations. In the left column we averaged the data segments per ∼ 3000 second *RXTE* observations and the right column uses the full 256 second resolution. We describe the evolution as a function of days using the time shift of Figure 3.1.

The flaring is first observed at day 8.3 with a fractional rms of 28%. The previous observation ∼1.1 days earlier, showed a fractional rms of 8%. Assuming this level of fractional variability due to the break component persists incoherently during the flaring interval, an rms amplitude of 27% is deduced for the flaring.

Between day 8.3 and 10.3 the flaring amplitude varies between 25–28% rms, showing a weak anti correlation with flux on a day-to-day timescale. In the same period the soft color slowly decreases while the hard color remains roughly constant. Since these color trends extend beyond the flaring interval, and are also seen in the same stage in the other outbursts (van Straaten et al. 2005), they are most likely not related to the presence of flaring. During the flaring interval the pulse amplitude and phase show complicated variations, again also seen outside the flaring interval and in the other outbursts (see e.g. Hartman et al. 2008), which relate to the flux variations rather than the presence of flaring (Patruno et al. 2009e).

At day 11.3 we see the flaring at an amplitude of 45% before it switches off. During the switch-off we see the flaring rms drop dramatically over the course of 5 consecutive

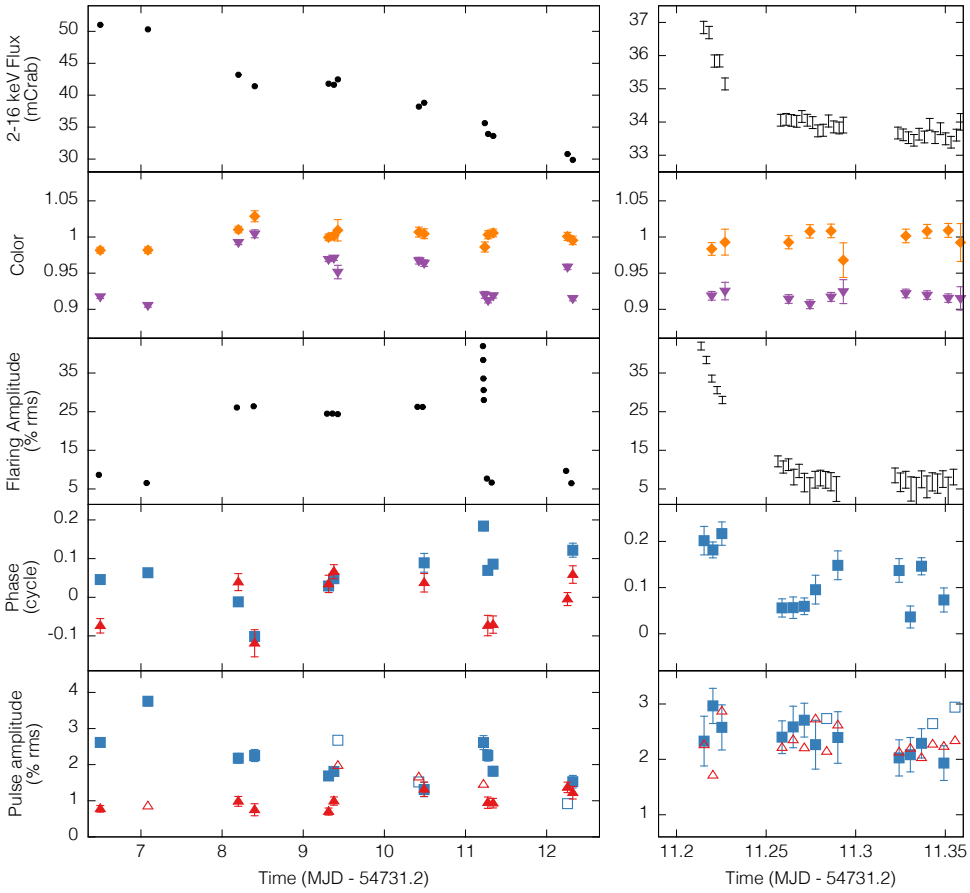

Figure 3.5: Evolution of the high luminosity flaring in the 2008 outburst, showing in the left column: the 2–16 keV light curve (top panel); soft (purple triangle) and hard (orange diamond) colors (second panel); 0.05–10 Hz high luminosity flaring fractional rms (middle panel); the pulse phases (fourth panel) and finally the pulsed fractional rms (bottom panel). Amplitude and phase measurements of the pulsations are given for the fundamental (blue squares) and the second harmonic (red triangles). Open symbols give 95% confidence upper limits. The right column shows the same data, but zoomed in on the flaring switch-off.

data segments, showing a strong correlation with a small drop in flux. A zoom-in of this entire episode is shown in the right column of Figure 3.5. Assuming the flaring started to switch off at the highest observed fractional rms and completely turned off at day 11.27, we obtain a switch-off time of 1.2 hours. Since the decay could have set in prior to the observed peak this is a lower limit.

While the flaring rms amplitude drops rapidly, the pulse fundamental remains steady in amplitude and phase. Yet, at day 11.27, just as the fractional rms returns to the 8%

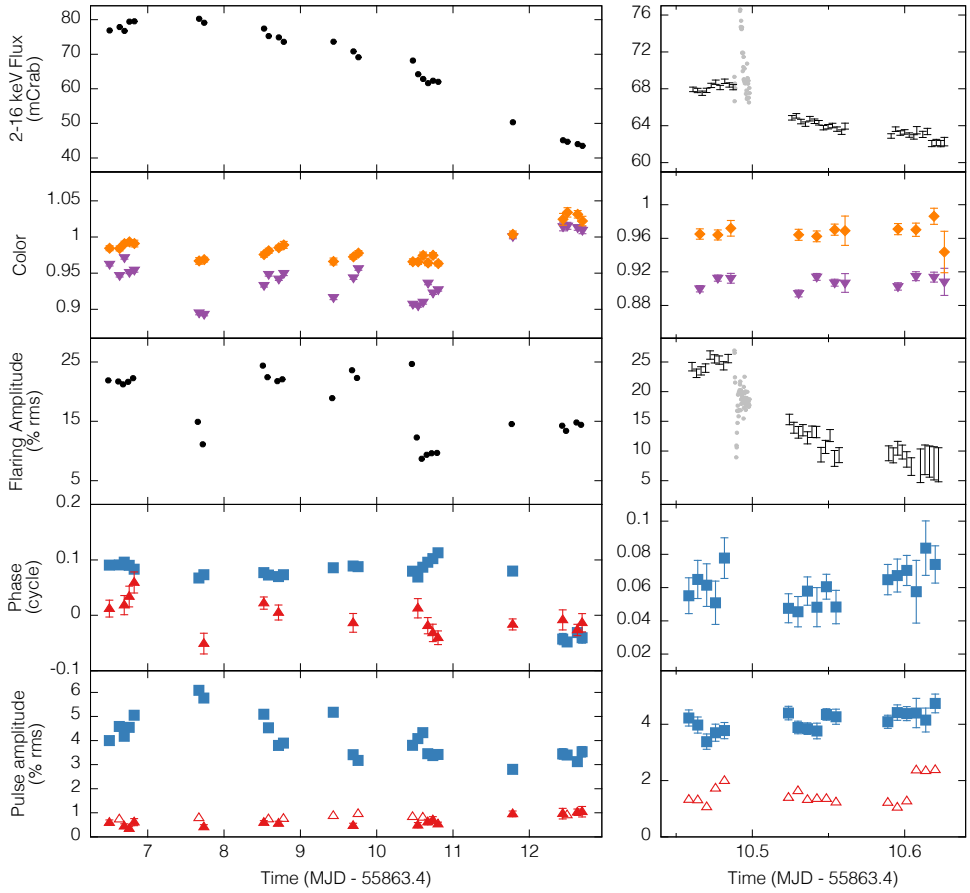

Figure 3.6: Evolution of the high luminosity flaring in the 2011 outburst in comparison to the 401 Hz pulsations. The grey bullets in the right column show the flux and 0.05–10 Hz fractional rms if 16 second data segments during a type I X-ray burst interval. For a detailed view see Figure 3.7. For details on the remaining data see Figure 3.5.

base level, there is a systematic drift in the fundamental phase of about 0.1 cycles, which does not relate to a flux variation and might be a response to the flaring mechanism.

3.3.2 2011

In Figure 3.6 we show the outburst evolution during the flaring interval of the 2011 outburst. In the first observation of the 2011 outburst, at MJD 55869.9, the flaring is already present with a 0.05–10 Hz rms of $\sim$ 23%. The flaring stays active for the following 4 days, during which the flux decays from 76 to 69 mCrab.

At day 7.9 the flaring decreases in strength, with the amplitude dropping consecutively to ∼ 15% and ∼ 9% rms. The rms drop coincides with the outburst peak luminosity, and an unexpected drop in soft color. At the same time the pulsations show a drop in the second harmonic phase and an increase in the fundamental amplitude, however, this could again be related to the flux rather than the flaring.

Over the entire flaring interval, between days 6.5 and 10.5, the flaring rms varies between 17–26%, showing a correlation with flux on a 3000 s timescale and an anti-correlation on the longer day-to-day timescale.

At day 10.49 a bright type I X-ray burst occurs (in 't Zand et al. 2013). Prior to the X-ray burst the flux is constant and the flaring amplitude holds steady at 25% rms (see Figures 3.6 and 3.7). During the X-ray burst peak flux (∼ 7 Crab) there is no significant variability in the 0.05–10 Hz frequency band above the Poisson noise level, giving a 95% confidence level upper limit on the flaring amplitude of 2% rms. As the burst flux decays, the 0.05–10 Hz fractional rms slowly increases, such that the absolute rms is consistent with the pre-burst level. At 550 seconds after the X-ray burst went off, just before the end of the *RXTE* observation, the flux returns to its pre-burst level, but at 18% rms the flaring amplitude does not.

In the next *RXTE* observation, at day 10.52, the flaring amplitude is 15% rms, and shows a steady decrease until it reaches the 8% rms of the broad band noise on day 10.6. Outside the X-ray burst interval, the switch-off is again strongly correlated with a small drop in flux. Assuming the switch-off started when the X-ray burst occurred, we obtain a switch-off time of ∼ 2 hours. Like in the 2008 outburst, the pulse fundamental phase shows a systematic drift of 0.1 cycles after the flaring switched off, although for the 2011 outburst this drift is much slower.

3.3.3 Summary of observed correlations

The sharp decrease in flaring amplitude when the flaring switches off in both outbursts and the rms drop at peak flux in 2011 suggest the flaring only occurs in a specific flux range with a sharp upper and lower bound which differs between the two outbursts. The flaring switch-off takes place on a timescale of 1–2 hours and is strongly correlated with flux. In one outburst the start of the flaring switch-off coincides with a bright type I X-ray burst.

Directly after the flaring switches off and the 0.05–10 Hz rms returns to the 8% rms of the broad band noise, the pulse phase of the fundamental shows a systematic drift of 0.1 cycles for both outbursts.

For both outbursts the flaring fractional amplitude correlates with flux on a 3000 s timescale, while on a longer day-to-day timescale the flaring fractional amplitude is anti-correlated with flux. If we consider the relation of the 0.05–10 Hz fractional rms versus mean flux in the 2002 and 2005 outbursts, we find that the broad band noise follows similar trends, but with different correlation factors, indicating the observed relations

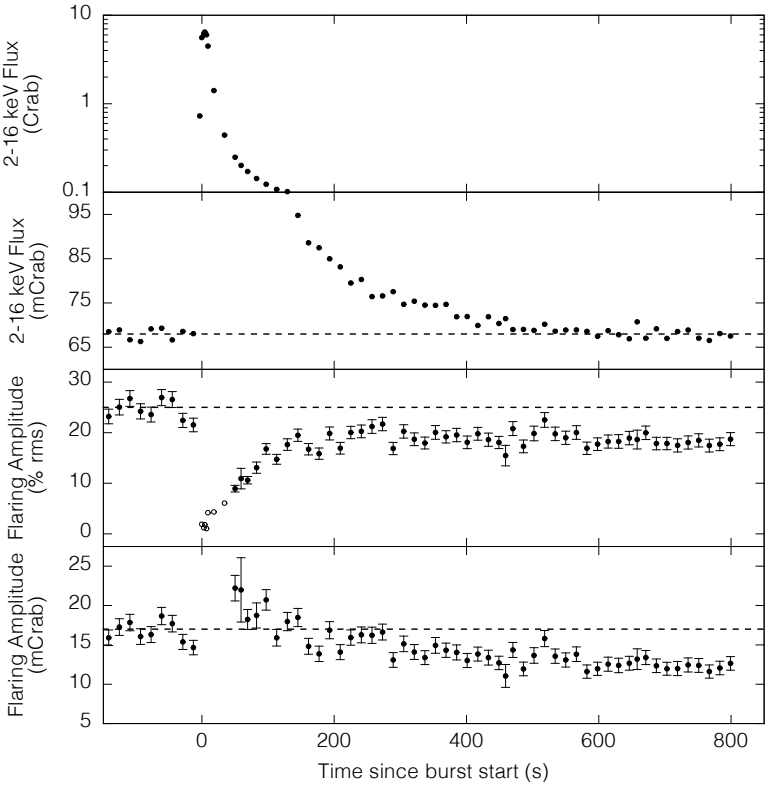

Figure 3.7: Evolution of the 2–16 keV X-ray flux (top, second) the 0.05–10 Hz fractional rms (third) and absolute rms (bottom) of the 2011 type I X-ray burst in seconds since the start of the burst. The open symbols in the third panel give 95% C.L. upper limits on the fractional rms. The corresponding upper limits on the absolute rms where greater than 50 mCrab and have been omitted for clarity. Horizontal dashed lines show the respective averaged pre-burst levels.

between flux and flaring rms are not due the underlying broad band noise. This supports our assumption that the flaring is a distinct component that is added onto the broad band noise.

3.3.4 Relation of the flaring phase with pulsations

In ObsID 93027-01-03-00 (day 11.2 of the 2008 outburst) the flaring reached an rms of 45% and was directly visible in the light curve (Figure 3.4). This allows us to investigate the pulsations as a function of the flux variations at the flaring timescale.

We construct a light curve at 1/32 s time resolution and sort the light curve in flux quartiles. To account for longer timescale variations in flux we apply the quartile selection on short 8 s segments containing 256 flux estimates. We then construct 4 pulse profiles

Table 3.3: Pulse Parameters for Quartile Selection

Count rate (ct/s)	Pulse Amplitude (% rms)	Error	Phase	Error
70.6	2.55	0.83	0.27	0.05
138.3	2.09	0.57	0.30	0.04
193.1	2.53	0.39	0.26	0.02
314.8	2.93	0.33	0.30	0.02

corresponding to the the 4 flux quartiles. We find that the pulse phases in different quartiles are statistically consistent. The absolute amplitude of the pulsations is found to be proportional to flux ($\chi^2/\mathrm{dof} = 0.6$), such that the fractional amplitudes are the same within the errors (see Table 3.3).

3.3.5 Energy dependence

Figure 3.8 shows the energy dependence of the high luminosity flaring fractional rms as measured in the 0.05–10 Hz band. We consider the fractional rms, which means the rms spectrum is divided by the energy spectrum of the mean flux. If the flaring has the same energy dependence as the mean flux, then we expect the fractional rms to be constant in energy at the level of the fractional rms of the full energy band. We find that the rms energy spectrum deviates from the average spectrum by contributing more between 6–16 keV and less below 6 keV.

This harder-than-average spectrum suggests that the high luminosity flaring does not originate from the soft disk emission, but instead comes from a harder spectral component, possibly the neutron star surface or boundary layer (Gilfanov et al. 2003).

We observe the same fractional rms spectral shape for the flaring during both the 2008 and 2011 outbursts. More importantly, in this frequency range the same rms spectral shape is also found for observations where the flaring is not seen, which suggests that the broad band noise in the 0.05–10 Hz range and the flaring share a similar origin. Since the broad band noise is believed to be caused by mass accretion rate variations in the inner accretion disk, this suggests that the high luminosity flaring is an accretion rate variation as well.

3.4 Discussion

We have found two intervals of unusual 1–5 Hz flaring occurring at high luminosity ($>$ 30 mCrab) in the 2008 and 2011 outbursts of SAX J1808 as observed with *RXTE*. This high luminosity flaring is characterized by spikes of emission in the light curve at quasi-regular intervals, which result in a broad noise component in the power spectrum. It is only seen for 3–4 days per outburst in a narrow $\sim$10 mCrab wide flux window at a

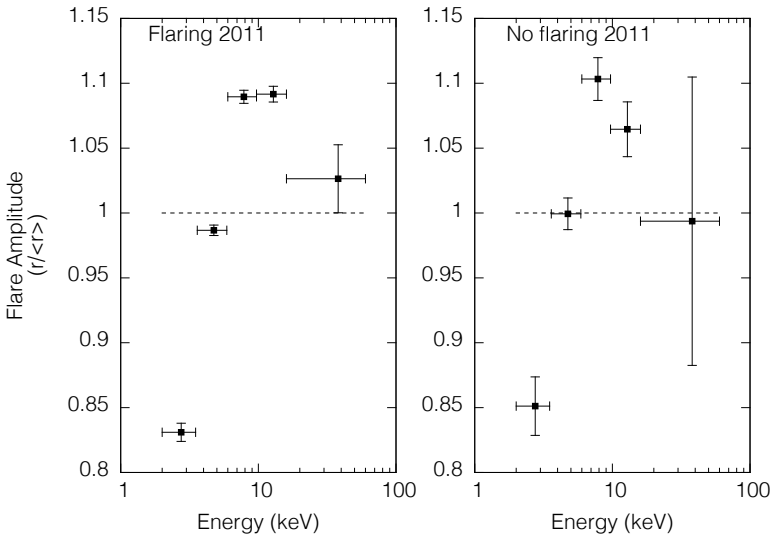

Figure 3.8: Fractional rms spectra for flaring (right) and non-flaring (left) intervals in the 2011 outburst. We show the fractional rms divided by the mean fractional rms of the full energy band (22.1% and 13.3%, respectively).

different flux for 2008 and 2011, and only in those 2 (of 6) outbursts.

The characteristics of the high luminosity flaring are reminiscent of those of the low luminosity (< 13 mCrab) flaring previously detected in the tail of the of 2000, 2002 and 2005 outbursts (Patruno et al. 2009d). The low luminosity flaring also produces a broad noise component in the power spectrum and is also seen exclusively in a narrow $\sim$ 10 mCrab wide flux window, which, however, is at the same flux for all three outbursts. The high and low luminosity flaring also differ in a number of other ways. Specifically, the high luminosity flaring is seen at $\sim$35 and $\sim$75 mCrab, with centroid frequency, ν_0, of 1–5 Hz and rms amplitudes of 20–45%. The low luminosity flaring, on the other hand, is seen between 2 and 13 mCrab, with ν_0 of 0.5–2 Hz and rms amplitudes between 40% and 120%. As seen in Figure 3.3 the trend in fractional rms against frequency of the high and low luminosity flaring match at $\sim$40% rms, but the relation is different for the two types of flaring. Additionally, the absolute rms increases with frequency.

The similarities between the high and low luminosity flaring suggest they could be caused by the same mechanism, however, the large discrepancy in the luminosity at which they are detected might indicate the opposite. We therefore first consider mechanisms that can explain the properties we observe for the high luminosity flaring alone, then we consider models that could explain them commonly with the low luminosity flaring.

3.4.1 Flaring origin

The observed flaring can either be caused by an extra emission component from the accretion disk or neutron star; or by periodic obscuration along the line of sight or a variation in the accretion flow.

3.4.1.1 An isolated component

In both the 2008 and 2011 outbursts the flaring switched off smoothly, showing a strong correlation between a drop in flux and the decreasing flaring amplitude. This correlation might suggest that the flaring is due to some isolated emission component that is added to the mean flux. For such a process, we can estimate an upper limit on fractional rms of the total signal by assuming the extra component is 100% modulated. We consider a signal of the form $f(t) = a + p(t)$, such that a gives the unperturbed flux and $p(t)$ the added flaring signal. The average of $f(t)$ is $\mu_f = a + \mu_p$ with μ_p the average of $p(t)$. The fractional rms of the total signal is defined as

$$r = \frac{\text{rms}}{\mu_f} = \frac{\sqrt{\int_0^T (f(t) - \mu_f)^2 dt/T}}{\mu_f}, \tag{3.2}$$

with T the average period of a single flare. For simplicity we take p(t) to be a square wave with duty cycle D, such that wave amplitude is μ_p/D. The enumerator now reduces drastically, giving

$$r = \sqrt{D^{-1} - 1}\,\frac{\mu_p}{\mu_f}. \tag{3.3}$$

For μ_f we can use the observed flux prior to switch-off, which is 37 and 68 mCrab for 2008 and 2011 respectively. The flux drop during the switch-off gives μ_p, which is 3 mCrab in both outbursts. To calculate the minimum required duty cycle we use the maximum observed fractional rms (45% and 26%, respectively) and find that a duty cycle of ~ 0.03 is needed. This is much higher than the $D \simeq 0.25$ that is apparent in the light curve (see e.g. Figure 3.4), so the flaring cannot be produced by an isolated emission process.

3.4.1.2 Surface processes

In Section 3.3.4 we found that the pulse amplitude responds to flux variations due to individual flares. This might suggest that the flaring originates from the neutron star surface, for instance from quasi-periodic oscillations on the nuclear burning timescale in the hotspot (see e.g. Bildsten 1998b; Heger et al. 2007).

Marginally stable nuclear burning occurs in the transition between stable and unstable burning. It therefore occurs only in a narrow range of mass accretion rates, naturally

explaining the narrow flux window observed for the high luminosity flaring. Furthermore, a transition to unstable burning, a type I X-ray burst, should stop the flaring, which is indeed observed during the 2011 flaring switch-off.

The predicted oscillation timescale of marginally stable burning depends on the thermal and accretion timescale of the burning region and is $\sim$ 100 s (Heger et al. 2007), which is too slow to account for the observed flaring. Furthermore, the flux variation due to the oscillations is limited by the fraction of nuclear energy and gravitational energy released per accreted nucleon. This fraction is of the order of a few percent, resulting in a fractional rms of $\sim 5-10\%$ (depending on duty cycle, see equation 3.3), far too low to account for the large fractional amplitude of the high luminosity flaring. Nuclear burning therefore is an unlikely candidate.

3.4.1.3 Obscuration

Another possibility is that the flaring is caused by periodic obscuration of the neutron star. Dipping low-mass X-ray binaries show QPOs in the ∼0.5–2.5 Hz range at rms amplitudes up to 12% (Homan et al. 1999; Jonker et al. 1999, 2000). These QPOs were proposed to be caused by a nearly opaque medium orbiting at the radius where the orbital frequency matches the observed QPO frequency. This argument is supported by the flat rms spectrum of the QPO, the high inclination angle of the binaries, and constant fractional rms amplitude during short term luminosity variations like dips and type I X-ray bursts, which are all characteristics of obscuration.

The frequency range of the dipping QPO is similar to that of the high luminosity flaring, but all other characteristics differ. SAX J1808 does not show dips in the light curve and at an inclination of 60° (Cackett et al. 2009; Ibragimov & Poutanen 2009; Kajava et al. 2011) is unlikely to show obscuration. The rms spectrum of the flaring is not flat, and the flaring fractional rms is diluted by the increased flux on a type I X-ray burst. An obscuration origin for the high luminosity flaring can therefore be ruled out.

3.4.1.4 Accretion flow variations

The rms spectrum (Section 3.3.5) suggests the high luminosity flaring may be due to variations in the accretion flow. If this is the case, flaring variability is present in the accretion flow channeled to the hotspot, and should therefore affect both the persistent emission and the pulsed emission in a similar fashion. This relation between the flares and the pulsations was indeed observed (see Section 3.3.4). As, therefore, the accretion flow is the most plausible origin for the high luminosity flaring, we consider a number of such mechanisms in greater detail.

3.4.2 Disk length- and timescales

We discuss instabilities in the accretion flow within the framework of the interplay between the corotation and magnetospheric radius. The corotation radius, r_c, is defined as the radius where the disk Keplerian frequency matches the neutron star spin frequency and the magnetospheric radius, r_m, as the radius where magnetic stresses equal the material stresses of the accreting plasma. For specificity we note that r_c can be written as

$$r_c \simeq 31 \text{ km } \left(\frac{\nu_s}{400 \text{ Hz}}\right)^{-2/3} \left(\frac{M}{1.4 M_\odot}\right)^{1/3}, \tag{3.4}$$

with ν_s the spin frequency and M the neutron star mass. Additionally we write r_m as (Spruit & Taam 1993; D'Angelo & Spruit 2010)

$$r_m \simeq 20 \text{ km } \left(\frac{M}{1.4 M_\odot}\right)^{-1/10} \left(\frac{B}{10^8 \text{ Gauss}}\right)^{2/5} \left(\frac{R}{10 \text{ km}}\right)^{6/5} \times \left(\frac{\dot{M}}{4 \times 10^{-10} M_\odot \text{yr}^{-1}}\right)^{-1/5} \left(\frac{\nu_s}{400 \text{ Hz}}\right)^{-3/10}, \tag{3.5}$$

where B is the magnetic field strength, R the neutron star radius and $\dot{M}$ the mass accretion rate.

In 2008 the high luminosity flaring is seen at an average flux of $F = 41$ mCrab. Relating flux to mass accretion rate as $4\pi d^2 F = GM\dot{M}/R$, for a distance $d = 3.5(1)$ kpc (Galloway & Cumming 2006), and bolometric correction factor of 2.14 (Galloway et al. 2008), the mass accretion rate was $3 \times 10^{-10} M_\odot$ yr^{-1} during the high luminosity flaring in the 2008 outburst. In 2011 the high luminosity flaring appears at an average flux of 75 mCrab, giving a mass accretion rate of $5 \times 10^{-10} M_\odot$ yr^{-1}. For a canonical accreting neutron star ($M = 1.4 M_\odot$, $R = 10$ km and $B = 10^8$ Gauss), we find an r_m of $\sim$21 km and $\sim$19 km for 2008 and 2011, respectively.

As a second estimate of the inner disk radius we can assume the upper kHz QPO frequency (see Table 3.2) to be a proxy for the inner disk Kepler frequency. This way we obtain radii of 21–28 km. All these estimates are consistent with an inner disk cut off by the magnetosphere near the corotation radius.

3.4.3 Magnetic reconnection

Magnetic reconnection has been proposed by Aly & Kuijpers (1990) as the origin of QPOs that occur in the Rapid Burster at frequencies similar to those in SAX J1808 discussed here. In their magnetic reconnection model the stellar magnetic field threads the inner disk. The differential rotation between the accretion disk and the magnetosphere shears the field lines, building up magnetic energy. This energy is periodically released in reconnection events that occur a few times per beat period between the inner edge of the

accretion disk and the neutron star spin. The reconnection events break up the accretion flow into blobs, which results in the observed flaring behavior.

Because in this model the QPO frequency depends on the beat between the inner disk radius and the neutron star spin, it will be a function of mass accretion rate. An increasing mass accretion rate pushes the disk inward. For $r_m > r_c$ this causes a decreasing QPO frequency, at $r_m = r_c$ the QPO frequency passes through zero, and for $r_m < r_c$ the frequency will increase with mass accretion rate. For the high luminosity flaring we found $r_c \simeq r_m$, so the frequency is in the correct range. The higher frequency and mass accretion rate in 2011 with respect to 2008 then implies $r_m \lesssim r_c$, so that centrifugal inhibition is not an issue. However, the frequency and flux change between the outbursts, $\nu(F)$, is inconsistent with predictions.

The QPO amplitude predicted by Aly & Kuijpers (1990) for an inner disk radius inside r_c is only a few percent, whereas our observed amplitudes are at a few tens of precent. This instability is therefore unlikely to be the cause of the high luminosity flaring.

3.4.4 Interchange instabilities

Interchange instabilities can occur at the boundary between the neutron star magnetosphere and the accretion disk. In the case of stable accretion, the accretion disk structure cannot be maintained within the magnetosphere. At the magnetospheric boundary matter is forced to move along the magnetic field lines, forming an accretion funnel to the neutron star surface. An interchange instability can occur if it is energetically more favorable for the accreting matter to be inside the magnetosphere rather than outside (Arons & Lea 1976). Plasma screening currents allow some of the matter to slip between the magnetic field lines and form long narrow accretion streams directly to the neutron star equatorial plane.

Numerical simulations of interchange instabilities in the context of accretion onto a weakly magnetized neutron star have been done by Romanova et al. (2008). Such simulations confirmed the formation of equatorial accretion tongues and showed that they can co-exist with a stable accretion funnel (Romanova et al. 2008; Kulkarni & Romanova 2008). Kulkarni & Romanova (2008) further showed that a small number of accretion tongues can remain coherent for short periods of time, producing a QPO in the light curve.

Kulkarni & Romanova (2009) found that accretion tongues create a QPO with the rotation frequency at the inner disk radius. The expected frequency of such a QPO is therefore much too high to explain the high luminosity flaring. Alternatively, the frequency at which the tongues are formed and disappear may also lead to a QPO. However, then the flux modulation of an individual flare would not affect the mean flux and the pulsed emission similarly, rather the opposite might be expected. Since we observed the pulse amplitude to change proportionally with flux variations due to the flaring, an interchange instability origin can also be ruled out.

3.4.5 Unstable dead disk

When r_m approaches r_c, the centrifugal force at the inner edge of the disk can prevent accretion onto the neutron star (Illarionov & Sunyaev 1975). When the inner disk radius remains smaller than $\sim 1.3 r_c$, the centrifugal force is not strong enough to accelerate matter beyond the escape velocity (Spruit & Taam 1993) and matter will accumulate at the magnetospheric radius (Spruit & Taam 1993; Rappaport et al. 2004). The inner accretion disk can then be described with the dead-disk solution (Sunyaev & Shakura 1977), which has been shown to be subject to an accretion instability (D'Angelo & Spruit 2010).

The instability arises when the mass accretion onto the neutron star is suppressed and a mass reservoir builds up in the inner accretion disk. As the reservoir grows in mass it exerts more pressure on the magnetosphere, forcing the inner disk radius to move inwards. Once a critical radius is reached, the disk can overcome the centrifugal barrier and the reservoir empties in an episode of accretion.

In the simplest form of this model, the inner edge of the accretion disk oscillates near the corotation radius. While the reservoir builds up mass, the accretion onto the neutron star, and as such the pulsed emission, stops. Although we find $r_m \sim r_c$, the second characteristic is in conflict with our observation of pulsations during the flux minima of the high luminosity flaring.

Recent investigations by D'Angelo & Spruit (2010, 2012) show that the range of mass accretion rates at which the instability can occur is much larger than initially suggested by Spruit & Taam (1993). By parameterizing the uncertainties in the disk/magnetosphere interaction in terms of a length scale over which the accretion disk boundary moves during the instability, and a length scale that gives the size of the disk/magnetic-field coupling region, D'Angelo & Spruit (2010) find that the Spruit-Taam instability can occur in two regions of parameter space. One region covers the original regime studied by Spruit & Taam (1993), while the other region, which they call RII, extends to higher mass accretion rates. This RII region was shown to occur together with continuous accretion (D'Angelo & Spruit 2012) and is a plausible candidate for the high luminosity flaring.

The mass accretion rates explored by D'Angelo & Spruit (2012) are parameterized in terms of a characteristic mass accretion rate

$$\dot{m}_c \simeq 0.5 \times 10^{-10} M_\odot \ \mathrm{yr}^{-1} \left(\frac{M}{1.4 M_\odot}\right)^{-5/3} \left(\frac{B}{10^8 \ \mathrm{Gauss}}\right)^2 \times \left(\frac{R}{10 \ \mathrm{km}}\right)^6 \left(\frac{\nu_s}{400 \ \mathrm{Hz}}\right)^{7/3}. \tag{3.6}$$

which is the mass accretion rate at which $r_m = r_c$. The instability is found to occur at

mass accretion rates of 0.1–10$\dot{m}_c$, with periods of 0.01–0.1τ_ν, where

$$\tau_\nu \simeq 40 \text{ s} \left(\frac{\alpha}{0.1}\right)^{-4/5} \left(\frac{\dot{M}}{4\times10^{-10} M_\odot \text{yr}^{-1}}\right)^{-3/10} \times \left(\frac{M}{1.4 M_\odot}\right)^{1/4} \left(\frac{R_{\text{in}}}{20 \text{ km}}\right)^{5/4}, \tag{3.7}$$

is the viscous timescale at the inner edge of the accretion disk, R_{in}, with α the disk viscosity parameter. This means the instability can occur at the $3-5\times10^{-10} M_\odot \text{yr}^{-1}$ at which we observed the flaring, and the frequency of the instability is 0.25–2.5 Hz, which agrees well with the observed flaring frequency.

The RII instability region is bounded by a lower and an upper mass accretion rate, which can explain why the high luminosity flaring is seen in a narrow flux window and why that window has the same width in 2008 and 2011. The difference in flux at which the window is located in the two flaring instances is more difficult to understand. Possibly this difference could be explained by a change in the relative size of the two length scales governing the model, which is predicted to change the mean mass accretion rate of the instability window. This could also explain why the high luminosity flaring is not observed in 2002 and 2005 outbursts. However, why these length scales would change between outbursts is unclear, especially as SAX J1808 is otherwise very homogeneous in its outburst phenomenology.

The dead-disk accretion instability can naturally explain both the high and low luminosity flaring if the latter is caused by the low mass accretion rate instability region as proposed by Patruno et al. (2009d). Owing to the lower luminosity, the flaring in the outburst tail has τ_ν ∼60–100 s (equation 3.7), giving a frequency range of 0.1–1.7 Hz, which agrees with the observed low luminosity flaring frequency range.

3.5 Conclusions

We have reported on the discovery of a 1–5 Hz flaring phenomenon with ∼20–45% fractional rms appearing at the peak of the 2008 and 2011 outbursts of SAX J1808. We have performed a detailed timing study of this high luminosity flaring and found that it is similar to the previously reported low luminosity flaring, which is observed in the prolonged outburst tail. We found that pulse amplitude changes proportionally to flux variations in individual flares, such that the pulse fractional amplitudes are the same within errors, implying that the flaring is most likely present in the accretion flow prior to matter entering the accretion funnel.

We have considered multiple candidate mechanisms for the high luminosity flaring and find that the dead-disk accretion instability of D'Angelo & Spruit (2012) provides the most plausible explanation. This model was previously proposed to explain the very similar low luminosity flaring seen in other outbursts of SAX J1808.

If both the observed high and low luminosity flaring are indeed caused by the dead-disk accretion instability like we suggest, then the observation of this type of variability is a new observational indicator of a magnetosphere in the system, accessible over a wide range of accretion rates. It would therefore be very interesting to search for this type of flaring in other, non-pulsating, LMXB sources.

4 The aperiodic X-ray variability of the accreting millisecond pulsar SAX J1808.4–3658

P. Bult & M. van der Klis

The Astrophysical Journal, 2015, 806, 90

Abstract

We have studied the aperiodic variability of the 401 Hz accreting millisecond X-ray pulsar SAX J1808.4–3658 using the complete data set collected with the *Rossi X-ray Timing Explorer* over 14 years of observation. The source shows a number of exceptional aperiodic timing phenomena that are observed against a backdrop of timing properties that show consistent trends in all five observed outbursts and closely resemble those of other atoll sources. We performed a detailed study of the enigmatic ∼410 Hz quasi-periodic oscillation (QPO), which has only been observed in SAX J1808.4–3658. We find that it appears only when the upper kHz QPO frequency is less than the 401 Hz spin frequency. The difference between the ∼410 Hz QPO frequency and the spin frequency follows a similar frequency correlation as the low frequency power spectral components, suggesting that the ∼410 Hz QPO is a retrograde beat against the spin frequency of a rotational phenomenon in the 9 Hz range. Comparing this 9 Hz beat feature with the low-frequency QPO in SAX J1808.4–3658 and other neutron star sources, we conclude that these two might be part of the same basic phenomenon. We suggest that they might be caused by retrograde precession due to a combination of relativistic, classical and magnetic torques. Additionally we present two new measurements of the lower kHz QPO, allowing us, for the first time, to measure the frequency evolution of the twin kHz QPOs in this source. The twin kHz QPOs are seen to move together over 150 Hz, maintaining a centroid frequency separation of $(0.446 \pm 0.009)\nu_{\rm spin}$.

4.1 Introduction

The transient X-ray source SAX J1808.4–3658 (SAX J1808) was discovered with the *BeppoSax* satellite in September, 1996 (in 't Zand et al. 1998). It remained in quiescence for 1.6 years after the discovery, until the *Rossi X-ray Timing Explorer* (*RXTE*) detected renewed X-ray activity with the Proportional Counter Array (Marshall et al. 1998). The initial *RXTE* observations revealed coherent pulsations at 401 Hz, making SAX J1808 the first known accreting millisecond X-ray pulsar (AMXP; Wijnands & van der Klis 1998a).

From extrapolating the recurrence time between the 1996 and 1998 outbursts, SAX J1808 was expected to show a new cycle of activity around November, 1999. Unfortunately, Solar constraints prevented observations until late January, 2000, at which time SAX J1808 was observed to be in a low luminosity state at roughly a tenth of the typical flux of the 1998 outburst (van der Klis et al. 2000). It is generally assumed that the main outburst occurred when the Solar constraints prevented observation (Wijnands et al. 2001). The low luminosity state persisted for $\sim$ 114 days (Wijnands et al. 2001), showing dramatic changes in luminosity. On a timescale of $\sim$5 days the luminosity would drop below a detection limit of $\sim 10^{32}$ erg s^{-1} and then increase again to $\sim 10^{35}$ erg s^{-1}. During these episodes of increased emission the 401 Hz pulsations were detected along with a sporadic strong modulation at about 1 Hz (van der Klis et al. 2000). Campana et al. (2008) proposed that the 5-day episodic variations of luminosity were caused by an intermittently active propellor effect (Illarionov & Sunyaev 1975), periodically inhibiting accretion onto the neutron star. The 1 Hz flaring remained unique to SAX J1808 until a similar feature was discovered in the AMXP NGC 6440 X-2 (Patruno et al. 2010d; Patruno & D'Angelo 2013).

The fourth outburst of SAX J1808 was detected in October 2002, some 2.8 years after the 2000 outburst, triggering an extensive monitoring campaign with *RXTE*. Twin kHz quasi-periodic oscillations (QPOs) were detected early in the outburst (Wijnands et al. 2003), for the first time in a source for which the spin frequency was precisely known. An additional QPO was unexpectedly detected at 410 Hz, which so far is unique to SAX J1808 and whose nature remains a mystery. After the main outburst, which lasted several weeks, the source entered a low luminosity state showing the same $\sim$5 day episodes of increased emission and 1 Hz flaring seen in 2000 (Wijnands 2004).

Since its 2002 outburst, SAX J1808 has been observed in outburst another three times; in 2005, 2008 and 2011. For both the 2005 and 2008 outbursts a low-luminosity prolonged outburst tail was observed, again showing luminosity variations on a $\sim$ 5 day timescale. During these episodes the 1 Hz flaring was again observed in 2005 but not in 2008 (Patruno et al. 2009d). Observations of the 2011 outburst were cut short by Solar constraints, such that only the onset of the low-luminosity outburst tail was seen, where again, no 1 Hz flaring was detected (Patruno et al. 2012, see Chapter 2). The 2008 and 2011 outbursts were later found to show a 1–5 Hz flaring which shares many of the characteristics of the 1 Hz flaring, but occurred at luminosities an order of magnitude

higher, near the peak of the outburst (Bult & van der Klis 2014, see Chapter 3).

SAX J1808 showed several thermonuclear X-ray bursts in each outburst. Using the X-ray bursts of the 1998, 2002 and 2005 outbursts Galloway & Cumming (2006) derived a distance estimate of 3.5 ± 0.1 kpc.

The literature contains a large body of work on the coherent pulsations of SAX J1808 (Wijnands & van der Klis 1998a; Poutanen & Gierliński 2003; Burderi et al. 2006; Hartman et al. 2008, 2009; Leahy et al. 2008; Ibragimov & Poutanen 2009; Patruno et al. 2012). The study of the stochastic variability of SAX J1808, on the other hand, remains incomplete, with all work constrained to the earlier outbursts. Specifically, Wijnands & van der Klis (1998b) studied the broadband power spectrum of the 1998 outburst and Menna et al. (2003) considered the coupling between the broad band noise and the coherent pulsations. The 2002 outburst power spectrum was studied by Wijnands et al. (2003), but only the high frequency region, in the context of the kHz QPOs. A more general analysis of the 1998 and 2002 outbursts was done by van Straaten et al. (2005), who compared the timing behavior of AMXPs with non-pulsating low-mass X-ray binaries. The stochastic variability of the 2005, 2008 and 2011 outbursts remains unaddressed.

With the demise of *RXTE*, its 14 year monitoring campaign of SAX J1808 has now been completed. We use this remarkable dataset to provide a complete overview of the stochastic time variability of SAX J1808. In this work we analyze all outbursts in a consistent approach, but do not consider the low luminosity outburst tail, which has been studied in-depth by Patruno et al. (2009d). We provide the first in-depth analysis of the broadband power spectra of the 2005, 2008 and 2011 outbursts and characterize the rich variability phenomenology observed in this accreting millisecond X-ray pulsar.

4.2 Data reduction

We used all *RXTE* pointed observations of SAX J1808's outbursts (see Table 4.1 for ObsIDs), selecting only observations with stable pointing, source elevation above 10° and pointing offset less than 0.02°.

Using the Standard-2 data we created Crab normalized 2–16 keV light curves. We also calculated the Crab normalized soft color as the count rate in the 3.5–6.0 keV band divided by the count rate in the 2.0–3.5 keV band. Similarly, the Crab normalized hard color is calculated by dividing the 9.7–16 keV band count rate by the count rate in the 6.0–9.7 keV band (see e.g. van Straaten et al. 2003, for the detailed procedure).

The timing analysis was done using high time resolution (122 μs) Event and GoodXenon data, selecting all events in the 2–20 keV energy band. Data obtained in GoodXenon mode were binned to 122 μs prior to further analysis. We calculate Fourier transforms using 256 s segments at full time resolution, yielding power spectra with a frequency resolution of $\sim$0.004 Hz and a Nyquist frequency of 4096 Hz. No background subtraction or dead-time correction has been applied prior to the Fourier transform.

Table 4.1: Interval Listing

Interval	State	Start MJD	ObsID
		1998 Outburst	
1	IS	50914.9	A-01-03S
2	EIS	50919.8	A-03-00
3	EIS	50920.1	A-04-00
4	EIS	50921.3	A-05-00
5	EIS	50921.5	A-06-01
6	EIS	50921.7	A-06-000
7	EIS	50921.9	A-06-00
8	EIS	50923.9	A-07-00
9	EIS	50926.8	A-08-00
10	EIS	50927.7	A-09-01, A-09-02
11	EIS	50928.6	A-09-03, A-09-04
12	EIS	50929.8	A-09-00
13	EIS	50930.6	A-10-02, A-10-01, A-10-00
		2002 Outburst	
1	IS	52562.1	B-03-04-00
2	LLB	52562.3	B-01-01-000
3	LLB	52563.1	B-01-01-03, B-01-01-04
4	LLB	52563.4	B-01-01-01
5	LLB	52564.3	B-01-01-020, B-01-01-02
6	IS	52565.0	B-01-02-01, B-01-02-000, B-01-02-00
7	IS	52566.0	B-01-02-02, B-01-02-03, B-01-02-04
8	IS	52567.1	B-01-02-05, B-01-02-06, B-01-02-07
9	IS	52568.1	B-01-02-10, B-01-02-08
10	IS	52569.0	B-01-02-20
11	IS	52569.2	B-01-02-09
12	IS	52569.4	B-01-02-19, B-01-02-23
13	IS	52570.0	B-01-02-21, B-01-02-11
14	IS	52570.4	B-01-02-18, B-01-02-12, B-01-02-22
15	IS	52571.0	B-01-02-13, B-01-02-15, B-01-02-14, B-01-02-16
16	IS	52572.0	B-01-02-17, B-01-03-00, B-01-03-04, B-01-03-05
17	IS	52572.2	B-01-03-000
18	IS	52572.9	B-01-03-06, B-01-03-07, B-01-03-010, B-01-03-01
19	IS	52573.4	B-01-03-08, B-01-03-09, B-01-03-10, B-01-03-11, B-01-03-12, B-01-03-13
20	IS	52574.1	B-01-03-02
21	IS	52574.8	B-01-03-14, B-01-03-03, B-03-05-00, B-02-01-04
22	IS	52577.1	B-02-01-000, B-02-01-00
		2005 Outburst	
1	IS	53523.0	C-01-01
2	IS	53523.5	C-01-02, C-01-03, C-01-04, C-01-05, C-02-00
3	IS	53524.9	C-02-01
4	IS	53525.8	C-02-02
5	IS	53526.8	C-02-030
6	IS	53527.0	C-02-03
7	LLB	53527.8	C-02-04, C-02-05, C-02-06
8	IS	53530.8	C-02-08
9	IS	53531.3	C-03-03, C-03-02, C-03-00, C-03-01
10	IS	53533.6	C-03-05, C-03-04, C-03-07, C-03-08
11	IS	53535.7	C-03-06, C-03-09, C-03-11, C-03-10

Note. Table continues on next page.

Table 4.1: Interval Listing (*continued*)

		2008 Outburst	
1	IS	54731.9	D-01-01, D-01-00, D-01-02
2	IS	54732.7	D-01-080, D-01-08, D-01-03
3	IS	54733.7	D-01-04, D-01-07, D-01-06, D-01-05, D-01-10, D-02-00, D-02-01
4	IS	54736.5	D-02-05, D-02-06, D-02-03, D-02-04
5	IS/F	54739.4	D-02-07, D-02-09, D-02-02, D-02-08
6	IS	54742.5	D-03-00, D-03-01, D-03-08, D-03-02
7	IS	54745.5	D-03-03, D-03-10, D-03-05, D-03-04
		2011 Outburst	
1	IS/F	55869.9	E-01-01, E-01-00
2	IS/F	55871.1	E-01-02
3	IS/F	55872.0	E-01-03, E-01-04
4	LLB/F	55872.9	E-01-05, E-01-06
5	LLB	55874.0	E-01-070, E-01-07
6	IS	55875.2	E-01-08, E-01-09, E-02-00
7	IS	55877.0	E-02-01, E-02-02
8	IS	55878.0	E-02-03, E-02-04
9	EIS	55879.0	E-02-05, E-02-06, E-02-07, E-02-08
10	EIS	55881.3	E-02-09, E-02-10, E-03-00, E-03-01, E-03-04

Note. *RXTE* ObsIDs grouped together in intervals for all outbursts. ObsIDs are chronologically ordered from left to right and top to bottom. Source states are abbreviated as: EIS – extreme island state; IS – island state; LLB – lower-left banana, F – high luminosity flaring present. A = '30411-01'; B = '70080', C = '91056-01', D = '93027-01', E = '96027-01'.

The power spectra were calculated using the standard Leahy normalization (Leahy et al. 1983). Following the method of Klein-Wolt et al. (2004) we inspected the high frequency region (> 1500 Hz) for anomalous features. Since none were found we subtracted a Poisson noise power spectrum calculated using the analytical formula of Zhang et al. (1995) and shifted to fit the > 1500 Hz power. All power spectra were averaged per ObsID. If necessary, multiple consecutive ObsIDs were averaged into *intervals* to improve statistics, but only if the power spectra showed similar morphology and the corresponding colors and intensities were consistent with being the same. Details of the intervals used are given in Table 4.1. Finally we estimated the background count rate using the FTOOL *pcabackest* and used it to renormalize the power spectra to units of source fractional rms squared per Hz (van der Klis 1995).

The power spectra are described in terms of a sum of Lorentzian profiles (see e.g. Nowak 2000; Belloni et al. 2002). Each profile, $L(\nu|\nu_{\max}, Q, r)$, is a function of Fourier frequency ν and determined by three parameters: the characteristic frequency $\nu_{\max} = \sqrt{\nu_0^2 + (\mathrm{FWHM}/2)^2}$, the quality factor $Q = \nu_0/\mathrm{FWHM}$ and its fractional rms amplitude squared $r^2 = P = \int_0^\infty L(\nu)d\nu$. Here ν_0 is the Lorentzian centroid frequency and FWHM the full-width-at-half-maximum. A feature is called a QPO if $Q > 2$. Features with $Q < 2$ are called noise components. We consider a component to be significant if the ratio of the integrated power to its single trial negative error is greater than three; $P/\sigma_P \geq 3$. Boundary cases with $P \simeq 3\sigma_P$ for which we deviate from this rule are explicitly discussed in Section 6.3.

In the 2008 and 2011 outbursts we previously found a broad noise component centered at 1–5 Hz (Bult & van der Klis 2014, see Chapter 3), which we call *high luminosity flaring*. This flaring component cannot be fitted with a Lorentzian profile, but instead is well described by a Schechter function, which is a power-law with an exponential cut-off, $S(\nu) \propto \nu^{-\alpha} e^{-\nu/\nu_{\rm cut}}$ (Hasinger & van der Klis 1989; Dotani et al. 1989), with power law index α and cut-off frequency $\nu_{\rm cut}$. To compare the Schechter function with Lorentzian components, and by analogy to the definitions used for Lorentzian components, we define the Schechter "centroid" frequency, $\nu_0 = -\alpha\nu_{\rm cut}$, as the frequency of maximum power in $S(\nu)$. Alternatively, we can define a characteristic frequency, $\nu_{\rm max} = (1-\alpha)\nu_{\rm cut}$, as the frequency of the maximum in $\nu S(\nu)$.

4.3 Source state identification

Atoll sources are named after the shape they trace out in the color-color diagram (Hasinger & van der Klis 1989; van der Klis 2006). At high luminosities they exhibit a banana shaped pattern, which is divided into three regions corresponding to three source states (*upper, lower* and *lower-left banana*). At lower luminosities the hard color increases and the observations cluster in the *island state*. In the hardest, lowest luminosity states a change in variability distinguishes another source state; the *extreme island* state. Depending on the source state, atoll sources show a different number of power spectral features and have a different morphology (see van der Klis 2006 for a detailed overview).

SAX J1808 is a low luminosity atoll source (van Straaten et al. 2005) and has shown only three source states: the extreme island state, the island state and the lower-left banana. We discuss the power spectral shapes relevant to these source states.

In the *extreme island state* three to four broad Lorentzians are needed to fit the power spectrum. The components with the lowest and second lowest characteristic frequencies are respectively called the break (b) and hump (h) Lorentzians (Belloni et al. 2002). The highest frequency component is usually found at 100–200 Hz and is identified as "u" to represent the widely held idea that this component evolves into the upper kHz QPO found in the island state and the lower-left banana (Psaltis et al. 1999). An additional component is usually present between the upper kHz and hump Lorentzian, which is proposed to evolve into the lower kHz QPO (Psaltis et al. 1999), but that identification is debated (van Straaten et al. 2003). In this work we follow van Straaten et al. (2005) and label this feature as a separate "ℓow" component. The relation between the ℓow component and the lower kHz QPO is further discussed in Section 4.5.1.2

In the *island state* three or four Lorentzian profiles are needed. These components tend to be less broad, while covering a higher frequency range with respect to the Lorentzians seen in the extreme island state. The lowest frequency noise components are again called the break and hump Lorentzians. The highest frequency component is now a QPO, and identified as the upper kHz QPO (Wijnands et al. 2003). Often an

additional Lorentzian is needed at $\nu_{\max} \sim 100 - 200$ Hz, which is called the hectohertz (hHz) component (Ford & van der Klis 1998; van Straaten et al. 2002). This component is usually observed as a broad noise component with a quality factor below 0.5. Occasionally it becomes more peaked, but it always has $Q \lesssim 2$. A characteristic property of the hHz component is that it does not show a systematic trend in frequency. It stays roughly constant in the hectohertz range. A ℓow component is not usually observed in the island state, but given their similar frequencies, the ℓow and hHz components may be difficult to disentangle. We simply always label the noise component below the upper kHz QPO as the hHz component and discuss this issue further in Section 4.5.1.3.

In the *lower-left banana* the power spectra show a complex morphology and can require up to seven different Lorentzians. In contrast to the two island states, the lower-left banana may show two breaks in the broad band noise, "b" and "$b2$", with $b2$ being the lower frequency component. As in the island state, higher frequency features are called the hump and hectohertz components. Finally, at the highest frequencies a lower (ℓ) and upper (u) kHz QPO is seen. If both kHz QPOs are detected in SAX J1808, the upper kHz QPO is always the most prominent feature, so if only one QPO is present, it is identified as the upper kHz QPO (Wijnands et al. 2003; van Straaten et al. 2005). Because the lower kHz QPO always appear as a very sharp, weak QPO it can be easily distinguished from the much broader hHz component that may be present at a lower frequency.

In some atoll sources the hump feature occasionally shows two discernible peaks, or a complex morphology requiring two Lorentzian profiles for an acceptable fit. In such cases the narrow Lorentzian is called the low-frequency (LF) component, while the broader Lorentzian is called the hump (h) component. In SAX J1808 the two components are sometimes both narrow QPOs, in which case we call the lower frequency component LF and the higher frequency component the hump.

Following Belloni et al. (2002) we refer to each Lorentzian profile as L_i, where subscript $i = \{b2, b, \mathrm{LF}, h, \ell\mathrm{ow}, \mathrm{hHz}, \ell, u\}$ represents the name of the specific component (e.g. L_b refers to the break component). We may further use ν_i to refer to characteristic frequency and $\nu_{0,i}$ for the centroid frequency. Similarly, the quality factor and fractional rms are referred to as Q_i and r_i.

4.4 Results

We briefly discuss the timing and color evolution of SAX J1808 for each individual outburst. We make use of Figure 4.1, which shows the 2–16 keV light curves, and the soft and hard color evolution for all outbursts. Additionally, we refer to Figure 4.2, which shows a sample of representative power spectra for each outburst, and Tables 4.2, 4.3, 4.4 and 4.5 which list the full set of fit parameters obtained for SAX J1808.

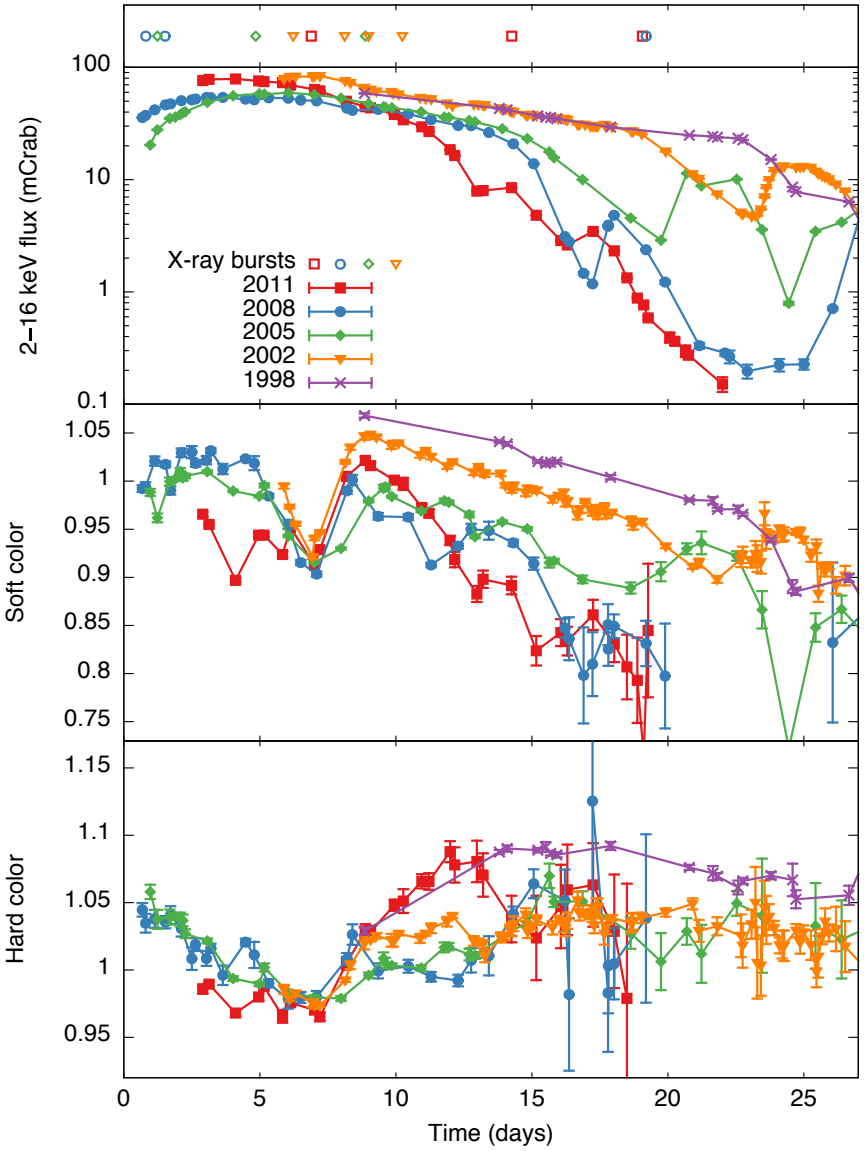

Figure 4.1: Evolution of the outbursts of SAX J1808. The top panel gives the times of type I X-ray bursts. The second panel gives the 2–16 keV light curves, while the third and fourth panel give the evolution of the soft and hard colors, respectively. Color measurements with large uncertainties have been omitted for clarity. Each light curve has been shifted in time by: 2011 MJD 55867.03; 2008 MJD 54731.20; 2005 MJD 53521.79; 2002 MJD 52556.19; and 1998 MJD 50906.03, such that their color minima approximately match on day 7.0. Each point in this figure corresponds to an ObsID in Table 4.1.

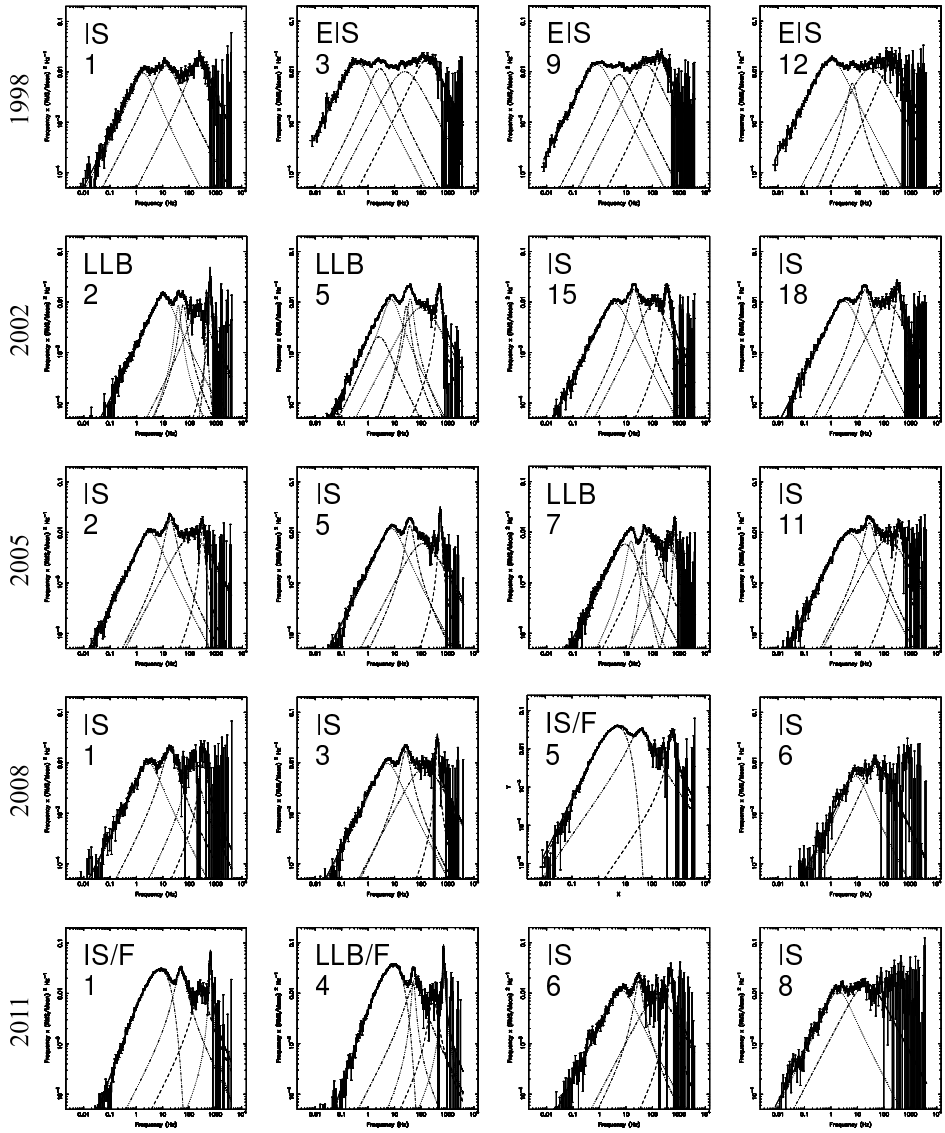

Figure 4.2: Selected power spectra of each outburst of SAX J1808. Every row represents a separate outburst as indicated. Each power spectrum has been marked with the number of the interval in its respective outburst and its associated source state (see Table 4.1 for details). Parameters of the fitted curves are given in Tables 4.2–4.5.

Table 4.2: Characteristic Frequency; $\nu_{\max}$ (Hz)

Interval	L_{b2}	L_b	L_h	$L_{\rm LF}$	$L_{\ell \rm ow}$	$L_{\rm hHz}$	L_ℓ	L_u
				1998 Outburst				
1	...	1.83 ± 0.08	13.3 ± 0.5	...	...	...	...	236 ± 14
2	...	0.408 ± 0.013	2.89 ± 0.08	...	26 ± 2	...	...	155 ± 7
3	...	0.381 ± 0.018	2.79 ± 0.10	...	24 ± 4	...	...	167 ± 13
4	...	0.363 ± 0.012	2.62 ± 0.07	...	21.9 ± 1.8	...	...	150 ± 6
5	...	0.38 ± 0.03	2.39 ± 0.16	...	22 ± 3	...	...	162 ± 20
6	...	0.347 ± 0.013	2.57 ± 0.09	...	28 ± 3	...	...	177 ± 11
7	...	0.359 ± 0.014	2.63 ± 0.09	...	21 ± 3	...	...	164 ± 11
8	...	0.37 ± 0.02	2.80 ± 0.17	...	27 ± 6	...	...	159 ± 16
9	...	0.81 ± 0.04	5.5 ± 0.3	...	54 ± 8	...	...	213 ± 14
10	...	1.31 ± 0.07	7.6 ± 0.4	...	52 ± 8	...	...	199 ± 19
11	...	2.01 ± 0.08	13.1 ± 0.8	...	...	...	...	170 ± 14[a]
12	...	1.03 ± 0.03	6.5 ± 0.4	...	32 ± 10	...	...	193 ± 34
13	...	0.93 ± 0.03	...	...	37 ± 4	...	...	...
				2002 Outburst				
1	...	10.4 ± 0.5	43.9 ± 2.1	...	...	179 ± 26	...	567 ± 25
2	...	9.9 ± 0.2	57.8 ± 2.2	37.4 ± 1.1	...	212 ± 34	435 ± 12	599 ± 5
3	7.9 ± 1.5	15.4 ± 0.4	78.2 ± 2.0	47.2 ± 1.8	...	257 ± 35	...	698 ± 6
4	10.0 ± 1.0	15.9 ± 0.2	75.7 ± 1.0	47.4 ± 0.7	...	355 ± 43	504 ± 3	686 ± 5
5	2.6 ± 0.5	7.6 ± 0.2	39.3 ± 1.1	28.1 ± 1.1	...	101 ± 13	...	497 ± 8
6	...	3.14 ± 0.05	18.01 ± 0.15	...	...	122 ± 9	...	352 ± 5
7	...	3.08 ± 0.05	18.53 ± 0.19	...	...	122 ± 11	...	339 ± 5
8	...	3.00 ± 0.05	18.40 ± 0.19	...	...	127 ± 12	...	332 ± 6
9	...	2.26 ± 0.05	13.6 ± 0.3	...	...	112 ± 12	...	294 ± 7
10	...	4.6 ± 0.2	24.4 ± 1.0	...	...	98 ± 48	...	389 ± 21
11	...	5.00 ± 0.12	25.4 ± 0.3	...	...	113 ± 14	...	393 ± 5
12	...	4.9 ± 0.2	25.1 ± 0.6	...	...	100 ± 25	...	381 ± 10
13	...	4.26 ± 0.11	23.0 ± 0.3	...	...	120 ± 19	...	370 ± 7
14	...	3.41 ± 0.17	19.3 ± 0.5	...	...	89 ± 28	...	332 ± 11
15	...	3.71 ± 0.10	20.2 ± 0.3	...	...	109 ± 10	...	358 ± 10
16	...	3.53 ± 0.19	23.2 ± 0.7	...	...	88 ± 7	...	336 ± 17
17	...	3.41 ± 0.10	20.9 ± 0.4	...	...	127 ± 22	...	326 ± 10
18	...	3.15 ± 0.07	19.2 ± 0.3	...	...	139 ± 27	...	340 ± 11
19	...	3.49 ± 0.14	20.8 ± 0.5	...	...	187 ± 48	...	358 ± 14
20	...	3.73 ± 0.12	21.2 ± 0.4	...	...	139 ± 18	...	332 ± 11
21	...	3.99 ± 0.15	23.1 ± 0.5	...	...	173 ± 51	...	357 ± 16
22	...	4.8 ± 0.4	28.7 ± 1.0	...	...	...	...	413 ± 143
				2005 Outburst				
1	...	2.6 ± 0.2	23.7 ± 1.9	...	...	...	...	...
2	...	3.15 ± 0.06	18.9 ± 0.2	...	...	122 ± 21	...	304 ± 10
3	...	5.51 ± 0.12	28.1 ± 0.4	...	...	90 ± 10	...	399 ± 7
4	...	7.50 ± 0.14	38.5 ± 0.6	...	...	155 ± 35	...	526 ± 8
5	...	7.63 ± 0.12	38.4 ± 0.6	...	...	121 ± 21	...	532 ± 5
6	...	6.67 ± 0.17	34.2 ± 0.7	...	...	161 ± 45	...	494 ± 14
7	8.9 ± 1.0	15.4 ± 0.3	78 ± 4	47.9 ± 0.6	...	438 ± 56[a]	...	685 ± 10
8	...	7.24 ± 0.15	36.6 ± 0.5	...	...	136 ± 12	...	498 ± 11
9	3.3 ± 0.7	7.9 ± 0.3	36.5 ± 0.4	...	...	131 ± 19	...	488 ± 9
10	...	6.70 ± 0.16	34.4 ± 0.4	...	...	127 ± 27	...	481 ± 19
11	...	5.07 ± 0.18	28.3 ± 0.6	...	...	138 ± 30	...	393 ± 25
				2008 Outburst				
1	...	2.85 ± 0.10	18.7 ± 0.8	...	...	135 ± 17	...	350 ± 36
2	...	3.66 ± 0.17	19.5 ± 0.4	...	...	118 ± 23	...	372 ± 14
3	...	5.35 ± 0.15	26.5 ± 0.5	...	...	135 ± 29	...	415 ± 5
4	...	9.2 ± 0.5	49 ± 2	...	...	...	...	524 ± 33
5	...	—[b]	37 ± 3	...	...	...	...	606 ± 44
6	...	8.7 ± 1.3	54 ± 10	...	...	...	...	...
7	...	1.72 ± 0.16	23 ± 4	...	...	...	...	...
				2011 Outburst				
1	...	—[b]	49.1 ± 1.4	...	...	291 ± 203	...	657 ± 3
2	...	—[b]	38 ± 16	...	...	...	...	527 ± 226
3	...	—[b]	52 ± 8	52.3 ± 0.7	...	343 ± 22	...	719 ± 4
4	...	—[b]	59 ± 14	51.6 ± 1.5	...	289 ± 43	...	712 ± 5
5	4.4 ± 1.1	15.3 ± 0.8	78 ± 4	48.8 ± 1.7	...	...	567 ± 9	737 ± 10
6	...	6.8 ± 0.4	30.3 ± 1.0	...	...	153 ± 71	...	478 ± 25
7	...	3.7 ± 0.3	21.1 ± 0.9	...	...	...	...	245 ± 41
8	...	1.90 ± 0.13	22 ± 3	...	...	...	...	...
9	...	0.55 ± 0.04	4.6 ± 1.2	...	...	...	...	113 ± 36
10	...	0.50 ± 0.04	10 ± 7	...	...	...	...	...

Note. [a] Uncertain identification. [b] Schechter function fit to the high luminosity flaring, see Table 4.5.

Table 4.3: Quality Factor; Q

Interval	L_{b2}	L_b	L_h	$L_{\rm LF}$	$L_{\ell \rm ow}$	$L_{\rm hHz}$	L_ℓ	L_u
				1998 Outburst				
1	...	0.37 ± 0.04	0.29 ± 0.07	...	...	...	...	0.43 ± 0.10
2	...	0.21 ± 0.03	0.34 ± 0.06	...	0.11 ± 0.14	...	...	0.35 ± 0.08
3	...	0.19 ± 0.04	0.41 ± 0.08	...	0 (fixed)	...	...	0.24 ± 0.10
4	...	0.18 ± 0.03	0.41 ± 0.06	...	0 (fixed)	...	...	0.38 ± 0.07
5	...	0.25 ± 0.06	0.43 ± 0.12	...	0 (fixed)	...	...	0.32 ± 0.16
6	...	0.22 ± 0.03	0.23 ± 0.06	...	0 (fixed)	...	...	0.30 ± 0.10
7	...	0.23 ± 0.03	0.35 ± 0.08	...	0 (fixed)	...	...	0.21 ± 0.11
8	...	0.28 ± 0.05	0.24 ± 0.12	...	0 (fixed)	...	...	0.41 ± 0.19
9	...	0.20 ± 0.03	0.28 ± 0.13	...	0.19 ± 0.16	...	...	0.8 ± 0.2
10	...	0.16 ± 0.03	0.5 ± 0.2	...	0.4 ± 0.2	...	...	0.5 ± 0.2
11	...	0.12 ± 0.02	0.57 ± 0.19	...	...	...	...	0 (fixed)[a]
12	...	0.15 ± 0.02	1.1 ± 0.5	...	0 (fixed)	...	...	0.4 ± 0.3
13	...	0.02 ± 0.03	...	...	0 (fixed)	...	...	...
				2002 Outburst				
1	...	0.35 ± 0.04	0.89 ± 0.18	...	...	1.2 ± 0.7	...	0 (fixed)
2	...	0.35 ± 0.02	1.9 ± 0.7	2.4 ± 0.6	...	0.4 ± 0.3	12 ± 113	7.7 ± 1.7
3	0.35 ± 0.06	1.3 ± 0.3	2.8 ± 0.8	2.0 ± 0.5	...	0.6 ± 0.3	...	8.2 ± 1.9
4	0.28 ± 0.02	1.3 ± 0.2	3.4 ± 0.6	2.3 ± 0.3	...	0 (fixed)	27 (fixed)	7.0 ± 1.2
5	0.36 ± 0.07	0.58 ± 0.10	1.9 ± 0.4	1.9 ± 0.3	...	0 (fixed)	...	3.0 ± 0.3
6	...	0.236 ± 0.012	0.85 ± 0.04	...	...	0.19 ± 0.08	...	2.3 ± 0.3
7	...	0.260 ± 0.014	0.83 ± 0.04	...	...	0.20 ± 0.11	...	2.3 ± 0.4
8	...	0.279 ± 0.013	0.86 ± 0.05	...	...	0.24 ± 0.12	...	2.4 ± 0.5
9	...	0.217 ± 0.016	0.65 ± 0.06	...	...	0.14 ± 0.11	...	1.9 ± 0.5
10	...	0.33 ± 0.04	1.1 ± 0.3	...	...	0 (fixed)	...	2.8 ± 1.8
11	...	0.267 ± 0.018	1.18 ± 0.10	...	...	0.15 ± 0.19	...	4.4 ± 0.6
12	...	0.30 ± 0.03	1.14 ± 0.17	...	...	0 (fixed)	...	5 ± 3
13	...	0.265 ± 0.019	0.93 ± 0.07	...	...	0.3 ± 0.2	...	2.8 ± 0.8
14	...	0.27 ± 0.04	0.98 ± 0.16	...	...	0 (fixed)	...	4 ± 2
15	...	0.240 ± 0.018	0.99 ± 0.08	...	...	0.32 ± 0.16	...	2.5 ± 0.5
16	...	0.26 ± 0.04	0.72 ± 0.10	...	...	1.4 ± 0.6	...	1.5 ± 0.4
17	...	0.255 ± 0.021	0.88 ± 0.09	...	...	0.3 ± 0.2	...	2.6 ± 0.9
18	...	0.245 ± 0.017	0.91 ± 0.07	...	...	0.18 ± 0.16	...	2.0 ± 0.7
19	...	0.25 ± 0.03	0.85 ± 0.10	...	...	0 (fixed)	...	3.7 ± 1.9
20	...	0.24 ± 0.02	1.01 ± 0.09	...	...	0.34 ± 0.19	...	3.0 ± 1.3
21	...	0.24 ± 0.03	1.04 ± 0.11	...	...	0 (fixed)	...	3.2 ± 1.6
22	...	0.21 ± 0.06	1.4 ± 0.2	...	...	...	...	0 (fixed)
				2005 Outburst				
1	...	0.49 ± 0.12	0.7 ± 0.2	...	...	...	...	...
2	...	0.315 ± 0.017	1.08 ± 0.07	...	...	0 (fixed)	...	3.4 ± 1.7
3	...	0.324 ± 0.019	1.28 ± 0.10	...	...	0.40 ± 0.16	...	4.5 ± 0.9
4	...	0.308 ± 0.016	1.31 ± 0.11	...	...	0 (fixed)	...	4.4 ± 1.5
5	...	0.319 ± 0.014	1.37 ± 0.12	...	...	0 (fixed)	...	5.8 ± 1.9
6	...	0.41 ± 0.03	1.6 ± 0.2	...	...	0 (fixed)	...	9 ± 6
7	0.26 ± 0.02	1.3 ± 0.2	0.73 ± 0.15	4.0 ± 1.0	...	0.8 ± 0.5[a]	...	7 ± 6
8	...	0.293 ± 0.018	1.63 ± 0.12	...	...	0.53 ± 0.18	...	3.8 ± 1.0
9	0.34 ± 0.04	0.69 ± 0.11	1.30 ± 0.08	...	...	0.24 ± 0.15	...	2.7 ± 0.5
10	...	0.253 ± 0.019	1.56 ± 0.12	...	...	0.3 ± 0.3	...	2.3 ± 0.9
11	...	0.18 ± 0.02	0.95 ± 0.11	...	...	0 (fixed)	...	2.1 ± 0.8
				2008 Outburst				
1	...	0.35 ± 0.04	0.79 ± 0.09	...	...	1.0 ± 0.4	...	2.4 ± 1.0
2	...	0.20 ± 0.04	1.45 ± 0.18	...	...	0 (fixed)	...	4 ± 4
3	...	0.28 ± 0.02	1.20 ± 0.11	...	...	0 (fixed)	...	6 ± 4
4	...	0.29 ± 0.03	0.67 ± 0.13	...	...	...	...	1.5 ± 0.5
5	...	—[b]	0.46 ± 0.05	...	...	...	...	2.2 ± 0.7
6	...	0.35 ± 0.17	0.3 ± 0.5	...	...	...	...	...
7	...	0 (fixed)	0 (fixed)	...	...	...	...	...
				2011 Outburst				
1	...	—[b]	1.09 ± 0.08	...	...	0.5 ± 0.5	...	9 ± 3
2	...	—[b]	0.4 ± 0.3	...	...	...	...	0.9 ± 0.9
3	...	—[b]	0.42 ± 0.10	5 ± 3	...	3.3 ± 1.3	...	7.6 ± 1.0
4	...	—[b]	0.60 ± 0.18	3.3 ± 1.3	...	1.6 ± 0.8	...	7.8 ± 1.2
5	0.50 ± 0.13	0.54 ± 0.12	1.9 ± 0.9	4 ± 4	...	...	14 (fixed)	10 ± 5
6	...	0.23 ± 0.04	1.5 ± 0.3	...	...	0 (fixed)	...	3 ± 2
7	...	0.27 ± 0.05	1.0 ± 0.2	...	...	...	...	0.4 ± 0.2
8	...	0.27 ± 0.05	0 (fixed)	...	...	...	...	...
9	...	0.20 ± 0.05	0 (fixed)	...	...	...	...	0 (fixed)
10	...	0 (fixed)	0 (fixed)	...	...	...	...	...

Note. See Table 4.2 for details.

Table 4.4: RMS Amplitudes; r (%)

Interval	L_{b2}	L_b	L_h	$L_{\rm LF}$	$L_{\ell ow}$	$L_{\rm hHz}$	L_ℓ	L_u
				1998 Outburst				
1	...	14.4 ± 0.5	17.8 ± 0.7	...	...	...	...	18.6 ± 0.7
2	...	19.0 ± 0.3	16.6 ± 0.8	...	16.8 ± 1.6	...	...	20.1 ± 1.1
3	...	19.9 ± 0.4	15.7 ± 0.9	...	17.7 ± 0.9	...	...	20.9 ± 1.2
4	...	20.5 ± 0.3	15.5 ± 0.6	...	18.9 ± 0.4	...	...	20.0 ± 0.7
5	...	20.2 ± 0.7	15.4 ± 1.3	...	19.0 ± 1.0	...	...	19.2 ± 1.5
6	...	19.6 ± 0.4	17.5 ± 0.7	...	19.1 ± 0.6	...	...	19.1 ± 1.0
7	...	20.5 ± 0.4	15.7 ± 0.9	...	18.3 ± 0.7	...	...	21.0 ± 1.1
8	...	19.3 ± 0.7	17.0 ± 1.3	...	19.1 ± 1.2	...	...	19.0 ± 1.9
9	...	19.1 ± 0.5	14.6 ± 1.5	...	19 ± 2	...	...	16 ± 2
10	...	18.6 ± 0.6	11.8 ± 1.7	...	15 ± 3	...	...	18 ± 2
11	...	18.6 ± 0.4	10.7 ± 1.1	...	...	...	...	24.2 ± 0.5[a]
12	...	21.5 ± 0.2	8.2 ± 1.6	...	19.0 ± 1.8	...	...	18 ± 3
13	...	25.4 ± 0.3	...	...	28.3 ± 0.8	...	...	...
				2002 Outburst				
1	...	17.7 ± 0.5	13.7 ± 1.0	...	...	8.4 ± 1.7	...	8.0 ± 1.2
2	...	17.4 ± 0.2	8.2 ± 1.6	7.3 ± 1.0	...	11.8 ± 1.6	4.0 ± 1.0	8.7 ± 0.6
3	9.6 ± 1.3	9.8 ± 1.3	7.1 ± 1.1	7.3 ± 0.9	...	9.9 ± 1.1	...	8.3 ± 0.7
4	12.2 ± 1.0	9.0 ± 1.1	6.0 ± 0.5	7.2 ± 0.4	...	12.8 ± 0.4	2.5 ± 0.4	7.6 ± 0.6
5	6.8 ± 1.7	14.2 ± 1.0	9.3 ± 1.4	7.8 ± 1.3	...	15.5 ± 0.5	...	9.7 ± 0.4
6	...	15.36 ± 0.12	15.3 ± 0.3	...	...	15.7 ± 0.7	...	10.1 ± 0.7
7	...	15.05 ± 0.13	15.3 ± 0.4	...	...	15.1 ± 0.9	...	10.6 ± 0.8
8	...	15.17 ± 0.12	15.6 ± 0.4	...	...	15.0 ± 0.9	...	10.0 ± 0.9
9	...	16.08 ± 0.18	14.0 ± 0.6	...	...	17.4 ± 1.1	...	10.4 ± 1.3
10	...	15.24 ± 0.4	14.1 ± 1.7	...	...	15.6 ± 1.3	...	10 ± 2
11	...	15.7 ± 0.2	14.0 ± 0.7	...	...	14.7 ± 1.2	...	9.8 ± 0.6
12	...	15.4 ± 0.3	13.7 ± 1.0	...	...	15.9 ± 0.8	...	8.9 ± 1.1
13	...	15.2 ± 0.2	15.9 ± 0.6	...	...	14.0 ± 1.7	...	10.8 ± 1.2
14	...	14.7 ± 0.3	14.5 ± 1.1	...	...	15.7 ± 0.9	...	9.2 ± 1.4
15	...	15.44 ± 0.19	15.1 ± 0.6	...	...	14.8 ± 1.1	...	10.3 ± 0.9
16	...	15.0 ± 0.4	17.5 ± 0.7	...	...	9.1 ± 1.5	...	14.2 ± 1.2
17	...	15.4 ± 0.2	15.7 ± 0.7	...	...	14.5 ± 1.5	...	9.8 ± 1.4
18	...	16.15 ± 0.18	15.3 ± 0.5	...	...	15.8 ± 1.6	...	11.0 ± 1.8
19	...	15.7 ± 0.3	15.3 ± 0.6	...	...	17.1 ± 1.3	...	8.9 ± 1.6
20	...	15.6 ± 0.2	15.6 ± 0.6	...	...	15.2 ± 1.4	...	9.2 ± 1.5
21	...	15.9 ± 0.3	15.0 ± 0.7	...	...	17.2 ± 1.3	...	8.8 ± 1.9
22	...	15.7 ± 0.5	14.3 ± 0.9	...	...	...	...	21 ± 2
				2005 Outburst				
1	...	13.5 ± 0.8	18.4 ± 1.3	...	...	...	...	...
2	...	15.28 ± 0.14	14.5 ± 0.4	...	...	16.2 ± 0.7	...	7.4 ± 1.3
3	...	14.72 ± 0.18	13.0 ± 0.6	...	...	12.4 ± 1.0	...	8.7 ± 0.7
4	...	16.47 ± 0.16	11.9 ± 0.5	...	...	13.1 ± 0.6	...	8.5 ± 0.8
5	...	16.72 ± 0.15	11.6 ± 0.6	...	...	13.8 ± 0.6	...	8.8 ± 0.5
6	...	16.6 ± 0.2	12.1 ± 0.7	...	...	14.3 ± 0.9	...	5.9 ± 1.1
7	12.1 ± 0.9	8.4 ± 1.2	11.6 ± 0.9	5.0 ± 0.7	...	9.2 ± 1.4[a]	...	6.2 ± 0.9
8	...	17.19 ± 0.17	12.9 ± 0.5	...	...	13.2 ± 1.0	...	9.5 ± 1.0
9	8.7 ± 1.9	13.2 ± 1.3	14.1 ± 0.5	...	...	12.8 ± 1.0	...	10.6 ± 0.8
10	...	15.8 ± 0.2	13.1 ± 0.6	...	...	11.9 ± 1.6	...	9.6 ± 1.4
11	...	15.9 ± 0.2	14.1 ± 0.8	...	...	14.8 ± 0.7	...	8.6 ± 1.0
				2008 Outburst				
1	...	15.0 ± 0.2	16.4 ± 0.5	...	...	11.8 ± 1.2	...	10.4 ± 1.7
2	...	15.5 ± 0.3	13.0 ± 0.7	...	...	19.1 ± 0.9	...	9.1 ± 1.6
3	...	15.4 ± 0.2	13.6 ± 0.5	...	...	15.8 ± 0.7	...	9.1 ± 0.8
4	...	15.3 ± 0.5	14.2 ± 0.8	...	...	...	...	12.3 ± 1.2
5	...	—[b]	29.2 ± 1.0	...	...	...	...	14.1 ± 1.6
6	...	11 ± 2	14 ± 3	...	...	...	...	...
7	...	17.9 ± 0.8	23.5 ± 1.1	...	...	...	...	...
				2011 Outburst				
1	...	—[b]	20.2 ± 0.9	...	...	17 ± 8	...	11.5 ± 0.8
2	...	—[b]	14 ± 3	...	...	...	...	13 ± 4
3	...	—[b]	23.7 ± 1.2	7.2 ± 1.4	...	7.3 ± 1.1	...	13.4 ± 0.6
4	...	—[b]	18.5 ± 1.7	9 ± 3	...	9.2 ± 1.9	...	13.4 ± 0.7
5	6.8 ± 1.8	14.3 ± 1.1	7.8 ± 1.4	5.3 ± 1.2	...	...	4.1 ± 0.8	7.1 ± 0.9
6	...	17.0 ± 0.5	12.3 ± 1.2	...	...	15.9 ± 1.7	...	11 ± 2
7	...	16.5 ± 0.6	15.4 ± 1.2	...	...	...	...	21.2 ± 1.8
8	...	16.4 ± 0.6	21.4 ± 0.7	...	...	...	...	...
9	...	22.0 ± 0.8	18.7 ± 1.2	...	...	...	...	28 ± 3
10	...	33.8 ± 1.1	29 ± 4	...	...	...	...	...

Note. See Table 4.2 for details.

Table 4.5: Schechter Function Fit Parameters

Interval	α	$\nu_{\rm cut}$ (Hz)	r (%)
		2008 Outburst	
5	-0.52 ± 0.02	3.33 ± 0.10	28.4 ± 0.3
		2011 Outburst	
1	-0.450 ± 0.013	5.63 ± 0.09	25.48 ± 0.10
2	-0.79 ± 0.15	5.6 ± 1.0	15.4 ± 1.3
3	-0.59 ± 0.02	4.95 ± 0.17	26.75 ± 0.15
4	-0.60 ± 0.02	5.67 ± 0.16	27.1 ± 0.3

4.4.1 1998

The first *RXTE* detection of SAX J1808 was with a scan observation on MJD 50915 (day 9 of Figure 4.1, Marshall et al. 1998), during which the source flux was 59 mCrab. At this time the source was in the island state showing a power spectrum that can be fitted with three Lorentzians (L_b, L_h and L_u).

The first pointed *RXTE* observation was five days later on MJD 50920, at which time the flux had decayed to ∼43 mCrab. The soft color was decreasing, while the hard color increased. The power spectrum shifted to lower frequencies and requires an additional $L_{\ell \rm ow}$ component, clearly showing that SAX J1808 transitioned to the extreme island state.

Over the following 14 days the flux and soft colors steadily decreased, while the hard color remained constant for 5 days before also starting to decay. The flux and soft color evolution transitioned into a faster decay on MJD 50929 (day 23). The flux decay briefly slowed down three days later. Finally the flux dropped below the detection limit on MJD 50934 (day 28), as the source returned to quiescence. During the entire decay SAX J1808 remained in the extreme island state.

4.4.2 2002

In the 2002 outburst SAX J1808 was first detected with *RXTE* on MJD 52560. When pointed *RXTE* observations commenced on MJD 52562 (day 6) the source was already close to the flux maximum. In interval 1 the power spectrum clearly reflects the island state, showing L_b, L_h, $L_{\rm hHz}$ and L_u. In interval 2 both colors decrease as SAX J1808 appears to be transitioning to the lower-left banana. The power spectrum now shows a complex morphology, requiring at least six Lorentzian components. At ∼50 Hz the $L_{\rm LF}$ component appears, and we detect a 2.8σ feature at $\nu_0 = 434 \pm 12$ Hz which we tentatively accept as the lower kHz QPO, L_ℓ, as the upper kHz QPO is seen simultaneously at $\nu_{0,u} = 597.9 \pm 5.3$ Hz.

In the following observations a flux maximum of ∼85 mCrab is reached, and main-

tained for about a day. The lower kHz QPO is detected at higher significance with $\nu_{0,\ell} = 503.5 \pm 3.1$ Hz and $\nu_{0,u} = 684.5 \pm 4.9$ Hz, and a second noise component appears near L_b, providing further evidence that the source indeed transitioned to the lower-left banana.

As the flux starts to decay on MJD 52564 (day 8), both colors increase and SAX J1808 transitions back into the island state. From interval 7 (day 9) the soft color starts to decrease once more, while the hard color remains roughly constant. The power spectrum shows very little change and remains consistent with an island state morphology.

After reaching a flux minimum on MJD 52579 (day 23), SAX J1808 entered the prolonged outburst tail (Patruno et al. 2009d), which continued for 24 days.

4.4.3 2005

Routine monitoring with *RXTE* revealed a new outburst of SAX J1808 on MJD 53521 (day 1, Markwardt et al. 2005). In the following days the flux steadily increased until a maximum of ∼60 mCrab was reached approximately five days after first detection.

While the flux increased to its maximum (intervals 1–6) the hard color showed a steady decay, whereas the soft color remained roughly constant. During this time the power spectrum is that of the island state, showing L_b, L_h, $L_{\rm hHz}$ and L_u.

The flux maximum of 60 mCrab is reached on MJD 53528 (day 6, interval 7). In this interval both colors drop sufficiently to suggest a transition to the lower-left banana. The power spectrum confirms this transition with the appearance of L_{b2} and a narrow QPO at 58 Hz, which we identify as $L_{\rm LF}$. Additionally a broad feature appears at $\nu_{\rm max} = 428$ Hz, which is difficult to identify as the low Q suggests it is $L_{\rm hHz}$, while the frequency suggests it is L_ℓ. The amplitude of 9% rms lies roughly in between $L_{\rm hHz}$ and L_ℓ. We label it as $L_{\rm hHz}$, noting that it is not a 'clean' detection.

After reaching the flux maximum, both colors increased as SAX J1808 transitioned to the island state. Over the following seven days the flux and soft color decayed, while the hard color increased. On MJD 53542 (day 20) SAX J1808 was only marginally detected, marking the end of the main outburst and the start of a 40 day prolonged outburst tail (Patruno et al. 2009d).

4.4.4 2008

On MJD 54731 (day 1) SAX J1808 was again detected in outburst with *RXTE*. As in 2005 the rise to maximum flux was well sampled, and showed the same behavior: as the flux increased, the hard color decreased and the soft color remained constant. The power spectrum is an island state one and is well described with four Lorentzians (L_b, L_h, $L_{\rm hHz}$ and L_u).

During its luminosity maximum (intervals 3–4, days 3–7) SAX J1808 reached a flux of 55 mCrab, the lowest flux maximum of all outbursts. The soft and hard colors again

show a drop prior to the onset of the flux decay. Although this drop is as deep as seen in the other outbursts, the power spectrum indicates the source does not make a state transition to the lower-left banana. A sharp feature does appear at $\nu = 283$ Hz. Given $\nu_u = 520$ Hz this is roughly where L_ℓ is expected to appear, but at 2σ it is not significant.

On MJD 54737 (day 6) both colors increase as the flux starts to decay. At this point (interval 5) the power spectrum shows an unexpected deviation from the regular island state morphology as the high luminosity flaring now dominates the power spectrum below 10 Hz (Bult & van der Klis 2014, see Chapter 3). With a fractional rms amplitude of ∼30%, the flaring overwhelms the L_b component that is normally seen in the same frequency range. We therefore cannot fit the L_b component to the data. The flaring remains present for about three days, after which the power spectrum returns to the regular island state shape.

On MJD 54748 (day 19) SAX J1808 enters the prolonged outburst tail, which lasts for 30 days.

4.4.5 2011

The first pointed *RXTE* observation of SAX J1808's seventh outburst was on MJD 55869 (day 2), roughly five days after the initial detection with *SWIFT* (Markwardt et al. 2011). The low frequency region of the power spectrum was again dominated by high luminosity flaring. In the first two intervals the mid/high frequency domain required three Lorentzians (L_h, $L_{\rm hHz}$ and L_u), which suggests that despite the low color values the source was still in the island state.

On MJD 55871 (day 4, interval 3), a maximum flux of 80 mCrab was reached, which correlated with a drop in amplitude of the flaring component. In the next interval the amplitude of the flaring increased again and the high frequency components suggested the source transitioned to the lower-left banana. The feature which is normally identified as the hump component has a central peak, but also broad wings and hence is not well described by a single Lorentzian profile, but instead requires two Lorentzians for a satisfactory fit: one to describe the sharp QPO and one for the overlapping noise component. We identify the broader noise component as L_h and the peaked QPO as $L_{\rm LF}$, but note that this identification is uncertain as the two components are not well resolved, and may be distorted by the high frequency wing of the high luminosity flaring component.

In interval 5 (day 7) the high luminosity flaring disappears, while colors remain at low values. The $L_{\rm LF}$ component is now clearly present in the power spectrum and the marginal detection (2.8σ) of the lower kHz QPO at $\nu_{0,\ell} = 566.6 \pm 9.4$ Hz with a simultaneous $\nu_{0,u} = 736.1 \pm 9.7$ Hz confirms SAX J1808 entered the lower-left banana.

In interval 6 (day 8) the colors increased as the source switched back to the island state. The power spectrum can be described with L_b, L_h, $L_{\rm hHz}$ and L_u. In the following ten days SAX J1808 showed a regular decay with the soft color decreasing with flux while the hard color increased. During this time the power spectral components smoothly move

Table 4.6: 410 Hz QPO Fit Parameters

Intervals	ν_{410} (Hz)	Q	r (%)	P/σ_P	ν_b (Hz)	ν_h (Hz)	ν_u (Hz)
2002 Outburst							
6, 7, 8	409.6 ± 0.6	80^{+29}_{-21}	2.1 ± 0.3	4.4	3.07 ± 0.04	18.30 ± 0.10	330 ± 3
10, 11	414.7 ± 0.6	70^{+28}_{-17}	3.6 ± 0.5	4.3	4.95 ± 0.11	25.3 ± 0.3	383 ± 6
12, 13, 15	410.8 ± 1.1	41^{+17}_{-12}	3.4 ± 0.5	3.6	4.02 ± 0.07	22.1 ± 0.2	349 ± 7
2005 Outburst							
3	416.6 ± 0.8	98^{+49}_{-21}	3.2 ± 0.5	4.1	5.51 ± 0.09	28.2 ± 0.3	390 ± 7
2008 Outburst							
1, 2, 3	416.5 ± 0.9	92^{+92}_{-38}	2.7 ± 0.5	3.4	4.55 ± 0.08	22.8 ± 0.4	399 ± 10

Note. Fit parameters for the 410 Hz feature, its significance (P/σ_P), and the simultaneously measured $\nu_{\max}$ of break and hump components and the upper kHz QPO.

to lower frequencies, before transitioning into the extreme island state in the last two intervals.

4.4.6 The 410 Hz QPO

In the outburst of 2002, between MJD 52565 and MJD 52573, Wijnands et al. (2003) detected a sharp QPO at ∼410 Hz with an amplitude of ∼2.5% rms in the 3–60 keV energy range. We search all outbursts for this 410 Hz QPO using our 2–20 keV band, which gives a better signal to noise ratio. Due to the small amplitude of the QPO, we nearly always have to average multiple intervals to obtain a significant detection.

We detect the 410 Hz QPO at $> 3\sigma$ significance in the outbursts of 2002, 2005 and 2008 (see Table 4.6), but not in the outbursts of 1998 and 2011, for which we obtain 95% confidence upper limits for the amplitude of ∼3%. The QPO amplitude varies between 2.1% and 3.6%, and shows no relation with ν_{410} or ν_u. The characteristic frequency varies smoothly between 409.6 and 416.6 Hz and is correlated with the upper kHz QPO frequency.

We find the 410 Hz QPO is present in all observations in which L_u has $320 \leq \nu_0 \leq 401$ Hz and the flux is higher than 40 mCrab (Figure 4.3). An exception is interval 14 of the 2002 outburst (grey point in Figure 4.3 zoom-in), for which we find a 95% confidence upper limit on r_{410} of 3.4%; comparable to the typical amplitude. Due to their lower count rates, the observations below 40 mCrab have higher upper limits on the amplitude (∼4%) and are therefore also consistent with the QPO being below the detection threshold (also see Section 4.5.1.5).

The 410 Hz QPO is only seen in the island state, but is not related to a specific stage of the outburst evolution. In 2005 the QPO was detected during the rise to outburst, in 2008 at the maximum luminosity, while in 2002 the QPO was seen during the flux decay.

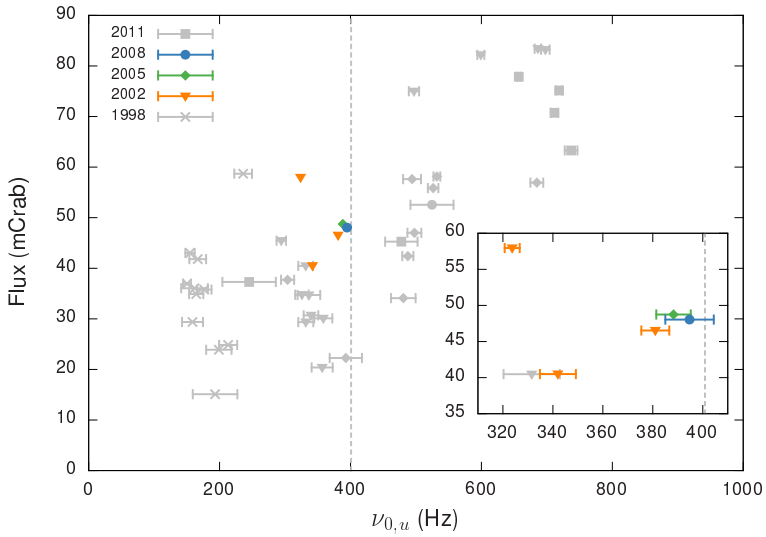

Figure 4.3: Overview of the 410 Hz QPO detections. We show flux vs. the upper kHz QPO centroid frequency for all intervals in grey. Intervals in which the 410 Hz QPO was detected are marked in yellow (2002), green (2005), and blue (2008). The vertical dashed line marks the spin frequency ($\nu_{\rm spin} = 401$ Hz). The inset shows a zoom-in of the detection region.

The proximity to the 401 Hz spin frequency suggests L_{410} may be an upper sideband of the pulsations. If this is the case then a similar feature might be present at the lower sideband frequency of ∼392 Hz. Using the same data selection for which we detected L_{410}, we searched for the lower sideband, but no significant features were found, giving a 95% confidence upper limit on the fractional rms of 1.1% to 2.3%. To improve sensitivity we use the shift-and-add method (Méndez et al. 1998) in which we shift the power spectra before averaging them, such that the frequency of the predicted lower sideband feature, $2\nu_{\rm spin} - \nu_{410}$, is expected at 390 Hz. Again, a lower sideband is not observed.

4.5 Discussion

It is common practice to study the variability properties of X-ray binaries by considering the relation between the frequencies of several components of the power spectrum. This approach is based on the success of the WK (Wijnands & van der Klis 1999) and PBK (Psaltis et al. 1999) relations, which show frequency correlations over several orders of magnitude, linking the variability components of neutron star and black hole binaries.

Applied to atoll sources the WK relation considers the correlation between the break frequency versus the $L_{\rm LF}$ or L_h frequency, whereas the PBK relation considers the correlation between the low frequency QPOs and the second highest frequency feature in

the power spectrum. For the higher luminosity lower-left banana state this would be L_ℓ, while for the lower luminosity extreme island state it is $L_{\ell\mathrm{ow}}$. In the island state it is unclear which component should be considered as neither $L_{\ell\mathrm{ow}}$ or L_ℓ are observed (also see Section 4.5.1.2).

For atoll sources van Straaten et al. (2003) suggested a scheme of correlations for the frequencies of several Lorentzian components plotted against the frequency of L_u. This scheme of correlations encompasses the WK and PBK relations and is the same across different atoll sources. AMXPs also follow this atoll correlation scheme, although they tend to be shifted in their ν_u by a constant factor of 1.1–1.6, which differs per source (van Straaten et al. 2005; Linares et al. 2005).

A complication in considering frequency relations comes from the fact that the characteristic frequency of the Lorentzian function may not be the physical frequency of the variability mechanism. In this work we used $\nu_{\max}$ as the characteristic frequency, which allows to treat QPO and noise components on the same footing, and tends to reduce the scatter on frequency correlations (Belloni et al. 2002). However, models involving resonances or beat frequencies tend to be defined in terms of the centroid frequency $\nu_0 = \nu_{\max}/\sqrt{1+1/(4Q^2)}$. For narrow QPOs (high Q) these two frequencies are almost the same, while for broad noise components (low Q) ν_0 is significantly smaller than $\nu_{\max}$. We will continue to consider the frequency relations in terms of $\nu_{\max}$ unless explicitly stated otherwise.

Further difficulty in interpreting frequency relations comes from ambiguities in the identification of the variability components. In particular when measurements deviate from a correlation, it could either indicate a break down of the relation, or a mislabeling of the considered component. It is therefore useful to distinguish between secure and more uncertain identification of the power spectral components.

4.5.1 Frequency correlations

Figure 4.4 shows the frequency relations with respect to ν_u for all outbursts of SAX J1808. Overall, the measured frequencies follow the trends of the atoll correlation scheme. We quantify the relations by fitting a set of power-laws over the full ν_u frequency range and present the fit parameters in Table 4.7. We now discuss the notable features in this figure.

4.5.1.1 Break and hump

The break and hump components are well correlated with ν_u (see Figure 4.4), but that correlation shows a break at $\nu_u \simeq 250$ Hz. This break could be due to a misidentification, however, as we are considering the three dominantly present power spectral components this is unlikely.

The break in the correlation occurs at the transition between the island state and the extreme island state and appears to affect the break and hump components in exactly the

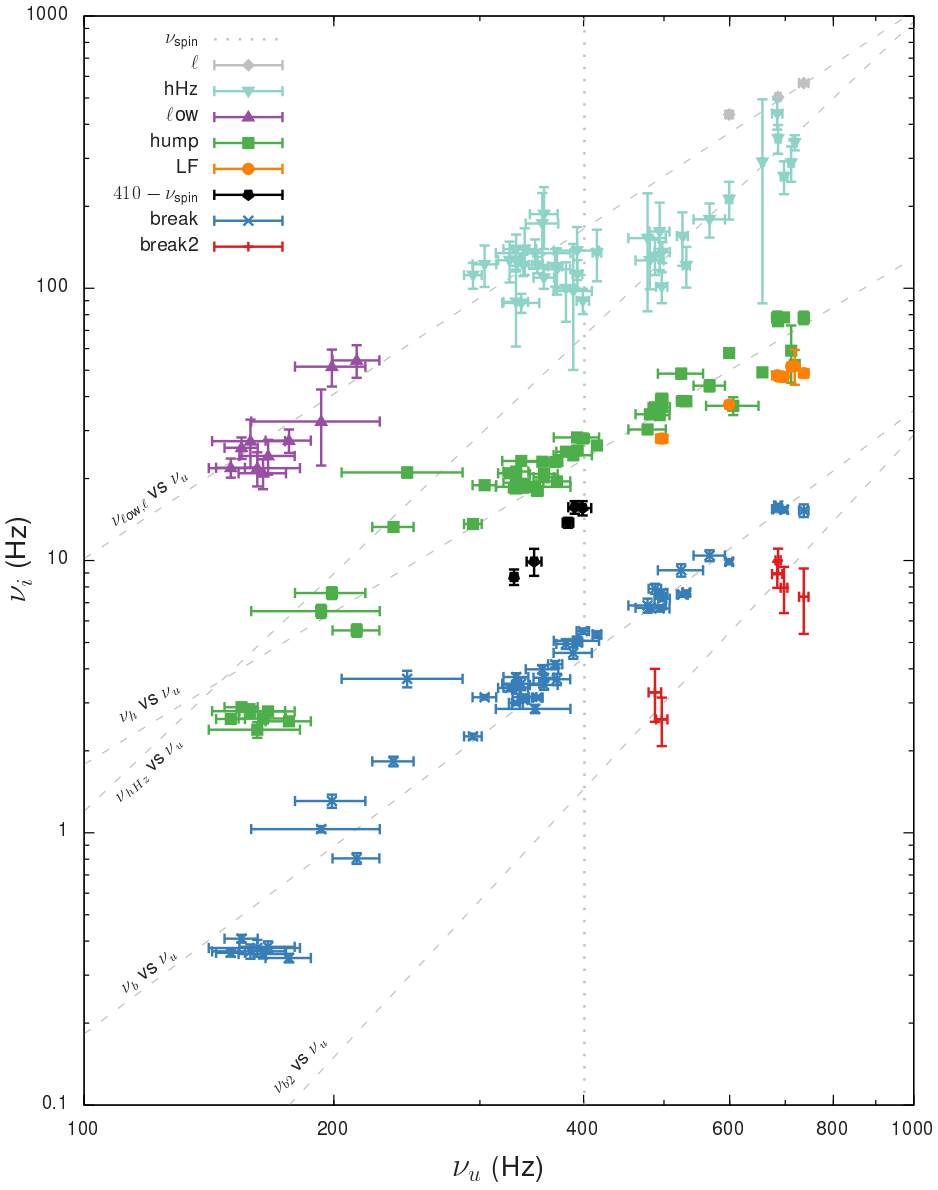

Figure 4.4: Characteristic frequencies of the power spectral components as a function of ν_u. Each point corresponds to a frequency measurement in Table 4.2. The dashed lines show the fitted power-law relations (see Table 4.7) and the vertical dotted line gives the frequency of the 401 Hz pulsations. For clarity we omitted points for which Q_u was fixed at zero, as these points have large errors in ν_u.

Table 4.7: Power-law Fit Parameters

Component	Data Selection[a]	Normalization	Index	χ^2/dof
		Atoll Scheme Relations (ν_i vs ν_u)		
break	all	$(4.8 \pm 0.7) \times 10^{-6}$	2.29 ± 0.02	225/47
hump	all	$(3.4 \pm 0.4) \times 10^{-4}$	1.86 ± 0.02	748/51
hHz	$\nu_u > 500$ Hz	$(2 \pm 5) \times 10^{-6}$	2.9 ± 0.4	6/7
LF	all	$(1.2 \pm 1.0) \times 10^{-3}$	1.62 ± 0.12	6.1/6
b2	all	$(5 \pm 14) \times 10^{-9}$	3.3 ± 0.5	5.3/4
ℓow	all	$(1 \pm 3) \times 10^{-6}$	3.4 ± 0.8	6/9
ℓow & ℓ	all	$(10 \pm 2) \times 10^{-4}$	2.01 ± 0.04	28/12
LF & (410 − 401)	all	$(1.2 \pm 0.9) \times 10^{-4}$	1.97 ± 0.11	58/11
		State Selected Relations (ν_i vs ν_u)		
break & b2	EIS & all[b]	$(7 \pm 2) \times 10^{-6}$	2.17 ± 0.05	129/15
break	IS	$(2.1 \pm 0.6) \times 10^{-5}$	2.05 ± 0.05	110/32
hump	IS	$(1.4 \pm 0.2) \times 10^{-3}$	1.64 ± 0.02	519/35
break	EIS	$(0.4 \pm 6.6) \times 10^{-19}$	8.6 ± 2.6	19/9
hump	EIS	$(0.2 \pm 3.5) \times 10^{-17}$	8.2 ± 2.5	19/9
		WK Relations (ν_i vs ν_b)		
break2	all	$(10 \pm 6) \times 10^{-2}$	1.7 ± 0.2	1.3/4
LF	all	7.9 ± 1.0	0.66 ± 0.05	6.8/4
hump	all	6.6 ± 0.1	0.88 ± 0.01	186/54
ℓow	all	44 ± 3	0.60 ± 0.09	15/9
u	all	208 ± 2	0.44 ± 0.01	231/49
LF & (410 − 401)	all	3.5 ± 0.7	0.96 ± 0.07	83/9
		PBK Relations (ν_i vs $\nu_{\ell ow/\ell}$)		
break	all	$(1.2 \pm 0.1) \times 10^{-2}$	1.15 ± 0.01	215/13
hump	all	$(1.12 \pm 0.01) \times 10^{-1}$	1.04 ± 0.01	148/12
upper kHz QPO	all	31.2 ± 1.8	0.50 ± 0.01	29/13

Notes. Results of power-law fits to the frequency-frequency relations.
[a] IS – island State, EIS – extreme island state.
[b] that is, EIS data for the break component and all data of the break2 component.

same way. Indeed, if we consider the hump frequency as a function of the break frequency (i.e. the WK relation) we find the two components are tightly correlated (Figure 4.5) and do not show state dependent behavior. This suggests that the break seen in Figure 4.4 is due to a change in ν_u that occurs when the source transitions between the island and extreme island states.

When considering centroid frequencies instead of characteristic frequencies, the break remains present. Additionally, for centroid frequencies the WK relation no longer holds, with L_h drifting in frequency faster than L_b.

If the upper kHz QPO indeed shows state dependent variations that do not occur in the other components, then considering frequency correlations against ν_u is not optimal.

In Figure 4.5 we therefore plot the frequencies of all components agains ν_b (similar to the $\nu_{\rm band}$ approach of van Straaten et al. 2002), which does not show this state dependent variation.

4.5.1.2 $L_{\ell\rm ow}$ and L_ℓ

The relation between $L_{\ell\rm ow}$ and L_ℓ is a long standing problem. The two features were proposed to be due to the same component by Psaltis et al. (1999), who suggested that like the break and hump components, $L_{\ell\rm ow}$ too becomes increasingly coherent for higher frequencies, eventually evolving into L_ℓ. Plotting the frequency of L_h against that of $L_{\ell\rm ow}$ or L_ℓ then reveals a tight correlation which can be extended over three orders of magnitude by linking black hole and neutron star data.

The uncertainty of the PBK relation comes from the fact that the transition from $L_{\ell\rm ow}$ to L_ℓ has never been observed. It has also been suggested that the two features are actually distinct components (van Straaten et al. 2003, 2005). For SAX J1808 specifically van Straaten et al. (2005) suggested the two components were not the same because each requires a different frequency shift to be compatible with the atoll correlation scheme.

Since most observations of SAX J1808 are in the island state, they do not have a $L_{\ell\rm ow}$ or L_ℓ measurement. For those observations that do have either component present we plot the measured frequencies against $\nu_{\ell\rm ow}$ and ν_ℓ in Figure 4.6. The break and hump components and the upper kHz QPO all follow a correlation with $\nu_{\ell\rm ow/\ell}$. Corresponding to the break below $\nu_u \sim 250$ Hz observed in Figure 4.4, the extreme island state L_u appears to have a relatively high frequency, resulting in a flatter correlation for L_u as compared to L_b and L_h. The very similar correlations for L_b and L_h are in accordance with the idea that the $L_{\ell\rm ow}$ and L_ℓ features are the same component, as assumed by PBK, and that it is L_u that deviates at low frequency.

Based on the PBK relation (Figure 4.6) $L_{\ell\rm ow}$ and L_ℓ could be the same, however, when considering the frequencies against ν_b (Figure 4.5) it seems more likely that $L_{\ell\rm ow}$ is somehow connected to $L_{\rm hHz}$. Whether or not the ℓow component and the lower kHz QPO are the same or different is therefore not clear from the SAX J1808 data alone.

4.5.1.3 The hHz component

The hHz component that appears in the power spectra of atoll sources is usually seen in a frequency range of 100–200 Hz and does not correlate with ν_u (Ford & van der Klis 1998). Yet in SAX J1808 it appears that this hectohertz component does depend on ν_u (Figure 4.4).

For $\nu_u \lesssim 550$ Hz $L_{\rm hHz}$ appears in the same way as it does in other atoll sources, showing a large scatter between 100 and 200 Hz, but remaining constant with ν_u (van Straaten et al. 2002, 2005). Yet from $\nu_u \simeq 550$ Hz the frequency of the hectohertz component starts to systematically increase with the upper kHz QPO frequency, in a way that is very similar to the trends seen in the other components.

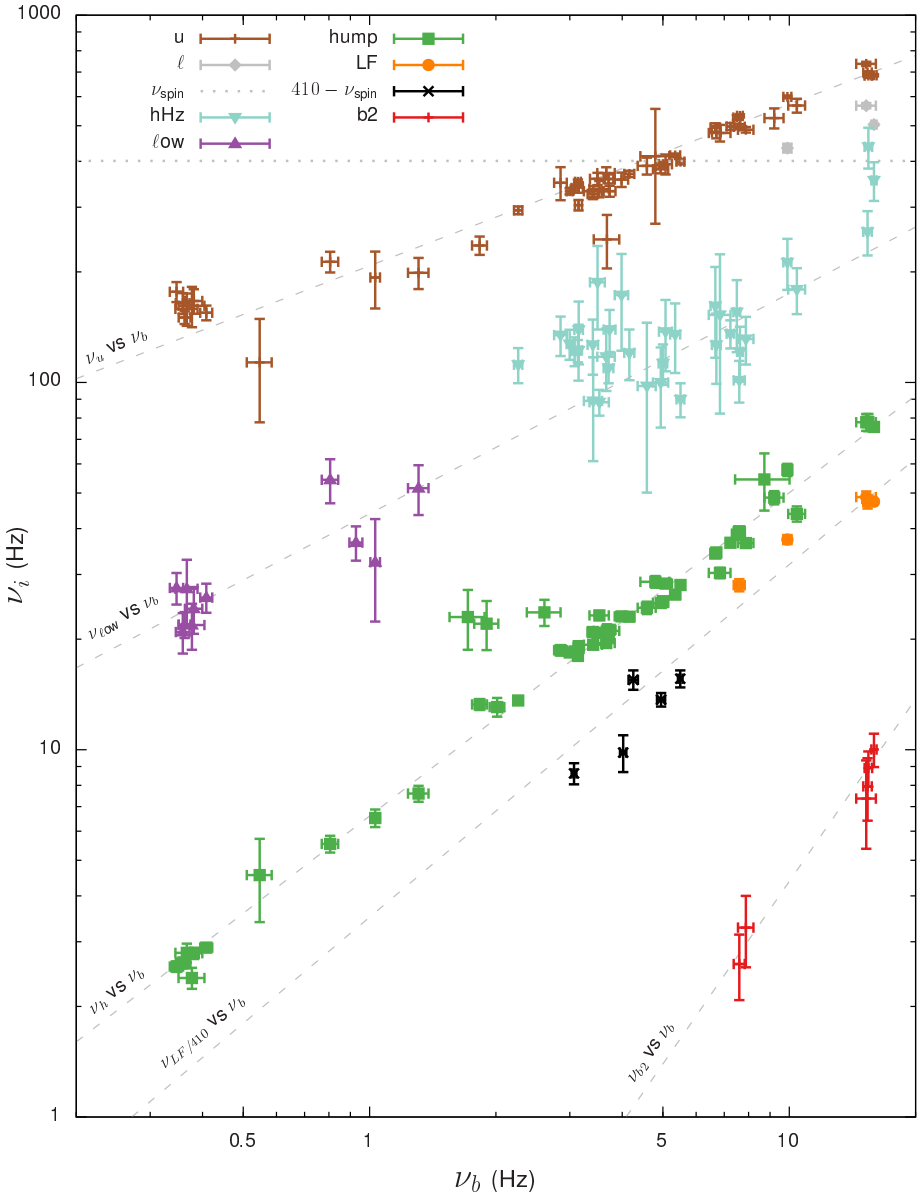

Figure 4.5: Characteristic frequencies of the power spectral components as a function of ν_b. The green squares show the hump vs. break frequency (WK relation). For further details see Figure 4.4.

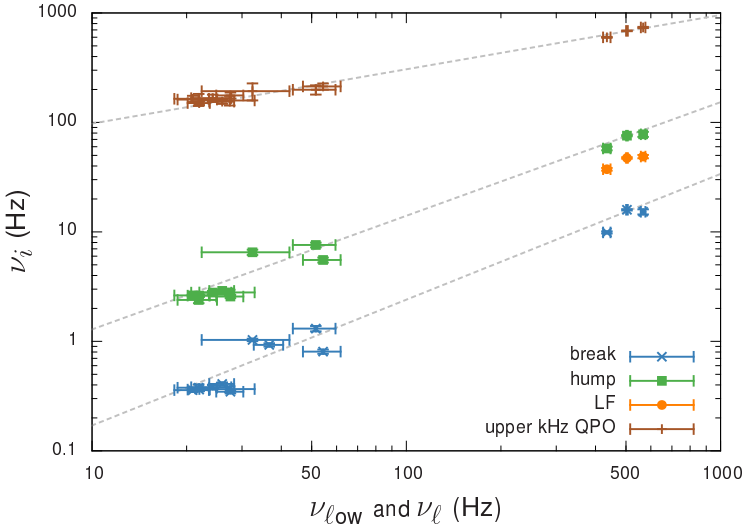

Figure 4.6: Frequency measurements plotted against the $L_{\ell ow}$ (< 100 Hz) and L_ℓ (> 100 Hz) characteristic frequencies (PBK relation). Dashed lines show fitted power-law relations (see Table 4.7).

Systematic trends of $\nu_{\rm hHz}$ have previously been reported by Altamirano et al. (2008b) who see a non-monotonic dependence of $\nu_{\rm hHz}$ on ν_u. These variations appear similarly for $\nu_u \gtrsim 550$ Hz, yet are always within the scatter of $\nu_{\rm hHz}$ seen at lower ν_u. In SAX J1808, however, the correlation extends well beyond the initial $\nu_{\rm hHz}$ scatter, suggesting the trend cannot be attributed to random variations in the frequencies.

It should be noted that $L_{\rm hHz}$ is not a dominant feature in the power spectrum. Its properties may be influenced by the position and amplitude of the nearby kHz QPOs or potentially by an unresolved ℓow component that could exist at similar frequencies.

The correlation between $L_{\rm hHz}$ and L_u was already tentatively observed by van Straaten et al. (2005), who also suggest it may be related to $L_{\ell ow}$. Indeed if the ℓow component follows the same frequency trend with ν_u as the break and hump components, then the island state observations should show a blend of $L_{\ell ow}$ and $L_{\rm hHz}$. Then, as ν_u increases, the ℓow component could become more prominent, causing the blended feature to follow the apparent correlation with ν_u.

If this interpretation is correct, it has a direct consequence for the relation between $L_{\ell ow}$ and L_ℓ. In one observation, interval 4 of 2002, the supposed ℓow/hHz blend is seen simultaneously with a lower kHz QPO, which would imply that $L_{\ell ow}$ cannot be the same component as L_ℓ. On the other hand, if $L_{\ell ow}$ and L_ℓ are in fact the same component, like the PBK relation suggests, then the observed correlation between $\nu_{\rm hHz}$ and ν_u might be intrinsic to the hectohertz component. Which of these interpretations is correct remains undecided.

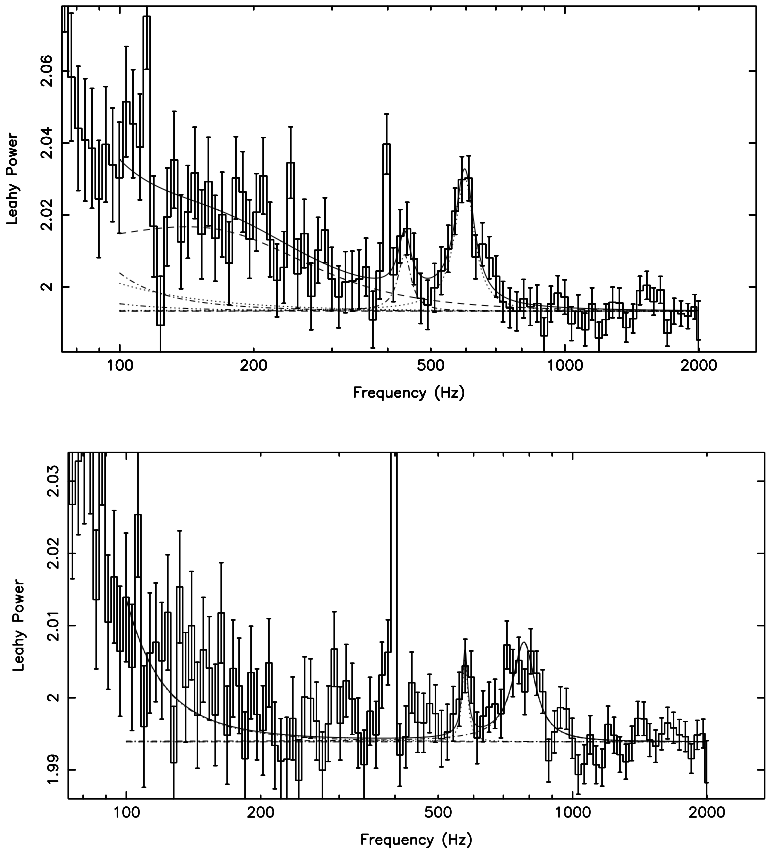

Figure 4.7: Twin kHz QPO's in SAX J1808. The top panel shows the twin kHz QPOs in interval 2 of the 2002 outburst and the bottom panel those of interval 5 in the 2011 outburst. The pulse spike at 401 Hz was excluded from the fit.

4.5.1.4 kHz QPOs

So far, twin kHz QPOs had only been reported once in SAX J1808 (Wijnands et al. 2003), from data corresponding to our interval 4 of the 2002 outburst. This frequency pair is separated by roughly half the spin frequency and is consistent with $\nu_{0,u} = |3\nu_{0,\ell} - 2\nu_{\rm spin}|$ (Wijnands et al. 2003) and a resonance at a 7:5 ratio (Kluźniak et al. 2004).

Unlike the twin kHz QPOs in most atoll sources (van der Klis 2006), for which the lower kHz QPO is the most prominent feature, in SAX J1808 it is the upper kHz that

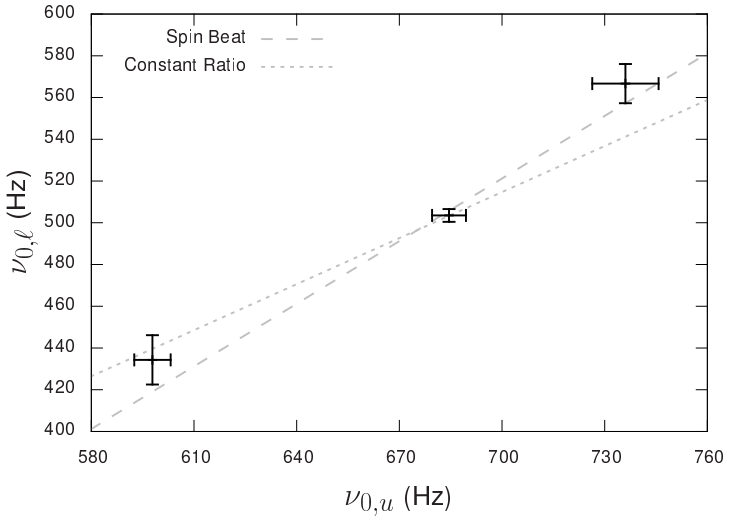

Figure 4.8: Twin kHz QPO centroid frequency trend in SAX J1808. The dashed line shows the linear relation $\nu_\ell = \nu_u - 0.446\nu_{\rm spin}$, and the dotted line gives a proportionality at the constant ratio of 1.36.

is the most prominent. This phenomenology is also seen in the AMXP XTE J1807–294 (Linares et al. 2008).

In this work we present additional detections of the twin kHz QPOs in SAX J1808 in interval 2 of the 2002 outburst and interval 5 of the 2011 outburst (Figure 4.7). The new detections of L_ℓ are only marginally significant (2.8σ), however, their phenomenology is entirely consistent with the original detection by Wijnands et al. (2003), providing additional evidence that we indeed observe the twin kHz QPO. All three observations are near the maximum luminosity of their respective outbursts, at a time when SAX J1808 has transitioned to the lower-left banana. The lower kHz QPO is very narrow and has a lower fractional rms amplitude than the upper kHz QPO.

Considering the centroid frequencies of all three detections of the lower kHz QPOs we find that the twin kHz QPOs move over a frequency range of about 150 Hz (see Figure 4.8). This trend can be fitted with a constant frequency difference of $\nu_{0,u} - \nu_{0,\ell} = (0.446 \pm 0.009)\nu_{\rm spin}$, which is *inconsistent* with being exactly half the spin frequency, but, being slightly smaller, may still be explained with a beat frequency model (Lamb & Miller 2003). Alternatively the measurements may also be explained by a constant $\nu_{0,l}/\nu_{0,u}$ ratio of 1.36 ± 0.01, close to, but inconsistent with the proposed 7:5 resonance ratio. We do note that the obtained frequency trend is tentative, as it is based on a small number of measurements and may be subject to systematic uncertainties that are not captured by the quoted errors.

4.5.1.5 The 410 Hz QPO

Returning to the frequency relations shown in Figure 4.4, we now consider the ∼410 Hz QPO. The characteristic frequency of L_{410} correlates with the upper kHz QPO, although this relation is less steep than the others. It was noted by Wijnands et al. (2003) that the difference between the 410 Hz QPO frequency and the 401 Hz spin frequency follows a quadratic trend with ν_u. In Figure 4.4 we therefore subtract the spin frequency from the measured L_{410} frequency, revealing a frequency correlation for the 410 Hz QPO that is similar to that of the other components. This correlation suggests that the 410 Hz QPO is a sideband of the pulsations caused by the beat with a low frequency disk component.

Because we consider rotation frequencies, a beat signal may appear either as lower or upper sideband, depending on the relative sense of rotation. Since L_{410} is observed as an upper sideband only, this suggests a beat with a quasi-periodic rotational low frequency disk phenomenon, $L_{410-401}$, that is retrograde (counter-rotates) with respect to the neutron star spin.

We searched for the associated low frequency $L_{410-401}$ component at 9 Hz in the power spectrum, both directly and using a shift-and-add method (Méndez et al. 1998), but did not detect it. Given that L_{410} has a very small amplitude, it is possible that the original $\sim$ 9 Hz signal is below the detection limit in this frequency region, which is dominated by the prominent L_b and L_h components. In the following we shall refer to the $L_{410-401}$ component keeping in mind that this inferred $\sim$ 9 Hz counter-rotational disk phenomenon was not, in fact, detected as a power spectral component, but seen only as a $\sim$ 410 Hz beat with the spin.

It was noticed by van Straaten et al. (2005) that the $L_{410-401}$ frequency is about half ν_h. If we fit the relation between these two characteristic frequencies we indeed obtain a proportional relation with a slope of 0.53 ± 0.03. Using this relation we can predict the frequency at which L_{410} should appear, allowing for a shift-and-add search in the observations where L_{410} is not directly observed.

In Section 4.4.6 we noted that L_{410} is detected for $320 \leq \nu \leq 401$ Hz if the source flux is greater than $\sim$ 40 mCrab. We therefore first select all the low flux observations with ν_u in this frequency range for which L_{410} was not detected. A shift-and-add search revealed a marginal feature (2.8σ) at $\nu_{\rm spin} + \nu_h/2$, suggesting L_{410} might also present below $\sim$ 40 mCrab. The observed feature has a fractional rms of 1.4% for a fixed $Q = 178$. While this quality factor is higher than the typically observed $Q \simeq 80$, it is consistent within typical errors.

A shift-and-add search for all observations with $\nu_{0,u} \geq \nu_{\rm spin}$ and a search for all observations with $\nu_{0,u} \leq 320$ Hz did not produce a detection ($< 1\sigma$), giving 95% upper limits on the fractional rms of less than 1%. We note that this could either mean that the L_{410} feature is not present those observations, is too weak to be detected, or that the proposed relation with ν_h is not correct.

4.5.1.6 The LF QPO

The narrow QPO at ~ 50 Hz, which we labeled $L_{\rm LF}$, was identified as such by van Straaten et al. (2005) based on extrapolating the $L_{\rm LF}$ versus L_h relation found in low luminosity bursters (1E 1724–3045, GS 1826–24). It was shown by Altamirano et al. (2008b) that the index of this power-law is consistent with 1, implying the relation is consistent with a simple proportionality. Extending this dataset with the additional measurements from our work we find that a proportional function performs well and that the proportionality ratio is 0.65 ± 0.02.

While the proportionality is consistent with 2/3, this small integer ratio of $L_{\rm LF}$ with L_h is only seen in SAX J1808, 1E 1724–3045, and GS 1826–24 (see Figure 4.9) and only when considering characteristic frequencies ($\nu_{\rm max}$). Relativistic resonance models (Kluzniak & Abramowicz 2001), which use centroid frequencies, are therefore not applicable.

While other atoll sources do not show a LF QPO that follows the same relation with L_h we see in SAX J1808, it has been suggested that some show a sub-harmonic ($L_{\rm LF/2}$, proportionality ratio of 0.33) rather than $L_{\rm LF}$ (van Straaten et al. 2005). However, many other sources have shown similar QPOs (e.g. Altamirano et al. 2005, 2008b) with frequencies drifting smoothly between L_{LF} and $L_{LF/2}$, crossing the frequency range of the $L_{410-401}$ component (Figure 4.9). This suggests $L_{\rm LF}$, $L_{\rm LF/2}$, and $L_{410-401}$ might be the same component.

4.5.1.7 LF and 410 Hz QPO

If $L_{\rm LF}$ and $L_{410-401}$ are the same feature then this raises the question why the LF component is seen directly in the power spectrum and $L_{410-401}$ only as a sideband of the pulsations and why $L_{\rm LF}$ and L_{410} are never seen simultaneously.

The 410 Hz QPO is only observed when the upper kHz QPO centroid frequency is below the spin frequency. We recently found that when the upper kHz QPO frequency moves above the spin frequency the pulse amplitude decreases by a factor of ~ 2 (Bult & van der Klis 2015a, see Chapter 5). If this drop in pulse amplitude also applies to the amplitude of the beat signal, then the power of the 410 Hz QPO would drop by a factor of ~ 4, putting it below the detection threshold of those observations where the upper kHz QPO frequency is above the spin frequency.

As the upper kHz QPO increases further, and presumably the inner edge of the disk moves closer to the neutron star surface, neither the LF QPO nor the 410 Hz feature are observed. Finally, when source transitions to the the lower-left banana, for the highest L_u frequencies observed in SAX J1808 and thus when the accretion disk has probably advanced closest to the neutron star surface, the LF QPO appears. If the LF QPO originates from the inner region of the accretion disk, for instance through precession, then the increased disk temperature may be the reason that the LF QPO is observed directly, while the pulsations are still too weak to power a detectable beat signal.

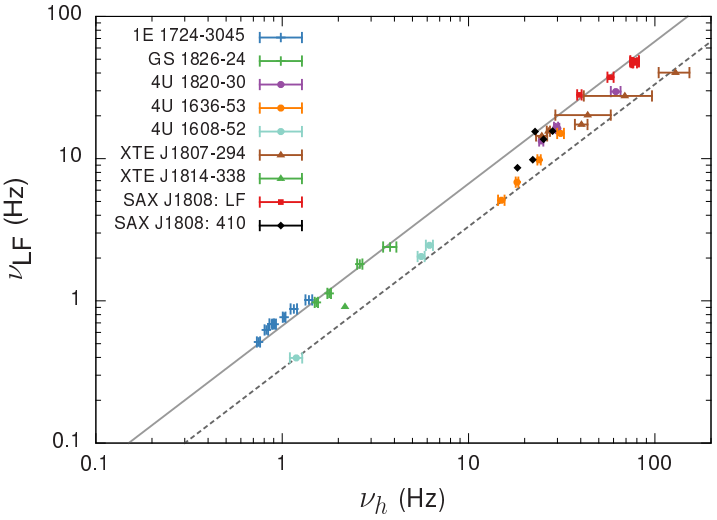

Figure 4.9: Characteristic frequency of $L_{\rm LF}$ versus L_h for SAX J1808 and several other atoll sources. The solid line show a proportionality ratio of 0.66 and the dashed line shows a proportionality ratio of 0.33.

4.5.2 Precession models

A popular interpretation of the frequency relations associates QPO frequencies with relativistic orbital and precession frequencies (Stella & Vietri 1998, 1999). In this model the LF QPO frequency corresponds to the nodal precession frequency (or its second harmonic) of a test mass orbiting at the disk inner radius as caused by relativistic frame dragging, which in the weak field approximation is known as Lense-Thirring (LT) precession. More recent versions of this model consider the LF QPO to be caused by a geometrically thick inner flow which, also due to frame dragging, precesses as a solid body (Fragile et al. 2007; Ingram et al. 2009), and produces the correct frequencies in black hole and neutron star systems (Ingram et al. 2009; Ingram & Done 2010), while naturally explaining a range of QPO properties (Ingram & Done 2012).

For atoll sources specifically the relativistic precession models attribute $L_{\rm LF}$ to LT precession. If $L_{\rm LF}$ and $L_{410-401}$ are the same component, then the interpretation that the 410 Hz QPO arises due to a retrograde beat with the neutron star spin, implies that the precession too must be retrograde. However, LT precession is always prograde with the stellar rotation (Merloni et al. 1999; Markovic 2000), excluding frame dragging as the main cause for the precession.

For neutron stars, however, frame dragging is not the only cause of precession. The neutron star oblateness and its magnetic field may also apply torques to inner accretion disk, which cause a retrograde (negative) contribution to the precession frequency (Lai 1999; Shirakawa & Lai 2002). In the magnetic precession model the stellar magnetic

field induces a warp in a geometrically thin accretion disk, which in turn undergoes retrograde precession. However, with a power-law index of ~ 4.6 (Shirakawa & Lai 2002), pure magnetic precession predicts a much steeper relation with the upper kHz QPO than we observe. Classical precession (due to the oblateness), on the other hand, predicts a power-law index of ~ 2.3, which is closer to what we observe. It would be interesting to investigate if in neutron star systems the combination of relativistic, classical and magnetic torque contributions can produce a retrograde variant of the LT thick flow precession seen by Fragile et al. (2007) in simulations of black hole disks, with all the attractive properties gained from it.

4.6 Conclusions

We have presented a complete overview of the aperiodic variability of SAX J1808 as observed with *RXTE* over the course of 14 years. We find that SAX J1808 is mainly observed as an atoll source in the island state, and sometimes transits to the lower-left banana or the extreme island state. The individual outbursts are very similar in terms of their light curve and color evolution and, aside from the 1–5 Hz high luminosity flaring observed in 2008 and 2011, show a similar evolution of the power spectra as well.

Considering the power spectra of all outbursts we find that all characteristic frequencies are correlated with ν_u, and that the correlations show a break when the accretion state changes between the island and extreme island states around $\nu_u \simeq 250$ Hz. This break disappears when considering the relations with ν_b instead, suggesting that it is ν_u that shows a state dependent relation with the other variability components.

We find that at $\nu_u \gtrsim 550$ Hz the frequency of the hectohertz component in SAX J1808 shows an unexpected correlation with ν_u, that roughly follows the frequency relations of the other components. We suggest that this correlation could be due to a blend with an unresolved ℓow component or that it could be intrinsic to the hHz component itself. We also considered the relation between extreme island state ℓow component and the lower kHz QPO, but found no definitive evidence in favor or against the two being the same.

We also presented new measurements of the lower kHz QPO, which, for the first time, allows us to probe the frequency evolution of the twin kHz QPOs in this source. Our observations are consistent with a twin kHz QPO frequency separation of $(0.446 \pm 0.009)\nu_{\rm spin}$, which is inconsistent with half the spin frequency, but tentatively so, as the fit is based on a small number of measurements.

Additionally, we presented the first detailed study of the 410 Hz QPO and found that it appears only when 320 Hz $\leq \nu_u \leq \nu_{\rm spin}$. Subtracting the spin frequency from the measured ν_{410} we find that the resulting frequency matches the overall correlation trends, which strongly suggests that the 410 Hz QPO is caused by a retrograde beat against the 401 Hz spin frequency, even though the original ~ 9 Hz signal is never seen.

Comparing the measured hump, LF and 410 Hz beat QPO with $L_{\rm LF}$ detections in other

neutron star systems we suggest that the LF and 410 Hz beat QPOs might be the same component. We suggest this QPO might be related to retrograde nodal precession caused by the (retrograde) classical and magnetic precession dominating over the (prograde) Lense-Thirring precession.

5 Pulse amplitude depends on kHz QPO frequency in the accreting millisecond pulsar SAX J1808.4–3658

P. Bult & M. van der Klis

The Astrophysical Journal Letters, 2015, 798, L29

Abstract

We study the relation between the 300–700 Hz upper kHz quasi-periodic oscillation (QPO) and the 401 Hz coherent pulsations across all outbursts of the accreting millisecond X-ray pulsar SAX J1808.4–3658 observed with the *Rossi X-ray Timing Explorer*. We find that the pulse amplitude systematically changes by a factor of ~ 2 when the upper kHz QPO frequency passes through 401 Hz: it halves when the QPO moves to above the spin frequency and doubles again on the way back. This establishes for the first time the existence of a direct effect of kHz QPOs on the millisecond pulsations and provides a new clue to the origin of the upper kHz QPO. We discuss several scenarios and conclude that while more complex explanations can not formally be excluded, our result strongly suggests that the QPO is produced by azimuthal motion at the inner edge of the accretion disk, most likely orbital motion. Depending on whether this azimuthal motion is faster or slower than the spin, the plasma then interacts differently with the neutron-star magnetic field. The most straightforward interpretation involves magnetospheric centrifugal inhibition of the accretion flow that sets in when the upper kHz QPO becomes slower than the spin.

5.1 Introduction

The low-mass X-ray binary SAX J1808.4–3658 (SAX J1808) is a 401 Hz accreting millisecond X-ray pulsar (AMXP; Wijnands & van der Klis 1998a) with a 2 hr orbital period (Chakrabarty & Morgan 1998). The system is an X-ray transient and has shown five X-ray outbursts between 1998 and 2011 (Hartman et al. 2008; Patruno et al. 2012) that were observed with the *Rossi X-ray Timing Explorer* (*RXTE*). The pulsations of SAX J1808 are near-sinusoidal with amplitudes of 2–7% (Hartman et al. 2008, 2009; Patruno et al. 2012, see Chapter 2). They are produced by thermal hotspots, emission regions near the stellar magnetic poles, undergoing periodic aspect variations due to the stellar spin (Davidson & Ostriker 1973; Ghosh & Lamb 1978). The hotspots, which may cover a large fraction of the surface (Lamb et al. 2009), are heated by the impact of plasma channeled by the magnetic field towards the poles. The pulsations therefore offer a direct probe of the inner accretion flow and specifically of the magnetic threading of the accretion disk.

SAX J1808 was the first AMXP discovered (Wijnands & van der Klis 1998a), and also the first pulsar to show the twin kHz quasi-periodic oscillations (QPOs; Wijnands et al. 2003) now known to be ubiquitous among accreting low-magnetic field neutron stars (van der Klis 2006). In SAX J1808 usually only the higher-frequency of the twin peaks is observed (Wijnands et al. 2003; van Straaten et al. 2005), at frequencies up to 700 Hz, and it is this upper kHz QPO we report on here. The lower kHz QPO is seen only on rare occasions (Wijnands et al. 2003, also see Chapter 4).

Some kHz QPO models explain the upper kHz QPO with orbital motion of short-lived inhomogeneities at some preferred radius in the accretion flow (van der Klis et al. 1996; Strohmayer et al. 1996; Miller et al. 1998; Stella & Vietri 1999; Kluźniak et al. 2004; Alpar & Psaltis 2008), others invoke alternative mechanisms (Lai 1998; Kato 2004; Zhang 2004; Bachetti et al. 2010), but for lack of observational clues the correct interpretation has remained elusive.

Although both the plasma channeling responsible for the X-ray pulsations and the mechanism producing the kHz QPOs are believed to probe the inner accretion flow of AMXPs, no direct relation between pulsations and kHz QPOs has been observed so far. In this Letter we show that such a direct relation does in fact exists in SAX J1808. This provides a new clue to the origin of the upper kHz QPO and the nature of the inner accretion flow towards this AMXP.

5.2 Data reduction

We consider all pointed observations of SAX J1808 with *RXTE* using the Proportional Counter Array (Jahoda et al. 2006). Each observation consists of one or multiple continuous 3 ks exposures as set by the data gaps associated with the 95 minute satellite orbit. We use the 16 s time-resolution Standard-2 data to create 2–16 keV light curves, which

we normalize to the Crab (see, e.g, van Straaten et al. 2003, for details).

For the stochastic timing analysis we use all GoodXenon and Event data in the 2–20 keV energy range. We compute Leahy normalized (Leahy et al. 1983) power spectra, using 256 s data segments binned to a 1/8192 s ($\sim$ 122 μs) time resolution, giving a frequency resolution of 1/256 Hz and a Nyquist frequency of 4096 Hz. No background subtraction or dead-time correction was done before a power spectrum was calculated. The resulting power spectra were averaged over intervals of 1–15 ks (depending on the number of active PCUs, which was higher for observations early in the *RXTE* mission) as required to significantly detect the upper kHz QPO.

We subtracted a modeled Poisson noise power spectrum (Zhang et al. 1995) from the averaged power spectra using the method of Klein-Wolt et al. (2004). Accounting for the background emission, we then renormalized the power spectra to source fractional rms squared per Hz (van der Klis 1995).

We fitted the power spectra with a set of Lorentzian profiles (Belloni et al. 2002), with each profile $L_i(\nu|\nu_{0,i}, W_i, r_i)$, a function of Fourier frequency ν, described by three parameters: the centroid frequency $\nu_{0,i}$, the full-width-at-half-maximum W_i, and the fractional rms

$$r_i = \sqrt{\int_0^\infty L_i(\nu) d\nu}. \tag{5.1}$$

The subscript i refers to the specific power spectral component; in particular, L_u represents the upper kHz QPO.

When its centroid frequency is high, L_u has good coherence and appears as a narrow peak in the power spectrum; as the frequency decreases, so does the coherence and L_u becomes a broad noise component. We only consider the observations for which L_u has good coherence (quality factor $Q \equiv \nu_0/W > 2$).

For the analysis of the coherent pulsations we use the same data selection as for the stochastic analysis. We correct the photon arrival times to the Solar System barycenter with the FTOOL *faxbary* using the optical source position of Hartman et al. (2008), and subsequently correct the data for the binary orbital ephemeris (Hartman et al. 2008, 2009; Patruno et al. 2012). The power spectra of Figure 5.1 were made from data corrected in this way, and rebinned such that the pulse fundamental occupies a single frequency bin. In our coherent analysis of the pulsations, we fold the data on the pulse period (Hartman et al. 2008) and for each pulse waveform measure the sinusoidal amplitude[1] of the fundamental and second harmonic, which we express as a fraction of the mean flux.

[1] Note that we report *sinusoidal* amplitudes, which are a factor of $\sqrt{2}$ larger than *rms* amplitudes

Table 5.1: Spin-frequency Transit Measurements

Outburst	Date (MJD)	Exposure (s)	QPO frequency (Hz)	A_1 (%)	A_2 (%)
2002	52564.18	2800	538 ± 16	3.49 ± 0.09	0.76 ± 0.09
	52564.97	3900	392 ± 10	5.63 ± 0.05	0.63 ± 0.05
2005	53524.96	17500	397 ± 7	7.10 ± 0.07	1.19 ± 0.07
	53525.72	13900	518 ± 7	4.35 ± 0.07	1.35 ± 0.07
2008	54735.69	10700	416 ± 10	6.49 ± 0.09	0.98 ± 0.09
	54736.44	12700	512 ± 18	3.33 ± 0.10	1.34 ± 0.10

Note. Listing (*left-to-right*): the time of observation, total exposure, upper kHz QPO frequency and the fundamental (A_1) and second harmonic (A_2) sinusoidal pulse amplitudes just before and after each transition for the indicated outbursts. The significances of these changes were calculated from the errors on the differences using standard error propagation.

5.3 Results

In the course of a typical two-week outburst the X-ray flux first rises to $\sim$ 70 milliCrab and then falls back down. In correlation to this, the upper kHz QPO drifts from $\sim$ 300 Hz up to $\sim$ 700 Hz and back down again, and so transits the 401 Hz spin frequency twice per outburst. We find that at these transits the amplitude of the pulsations abruptly changes by a factor $\sim$ 2: it halves when in the rise the QPO moves to above the spin frequency and then, as illustrated in Figure 5.1, doubles again on the way back.

We observed three such transitions at high signal-to-noise: two where the pulse amplitude approximately halves during the outburst rises in 2005 and 2008, and one where it approximately doubles during the decay in 2002. Figure 5.2 shows the QPO frequency (*top frames*) and the pulse amplitude (*bottom frames*) across these three transitions. In each case the pulse amplitude can be seen to systematically drop when the QPO moves to frequencies $>$ 401 Hz (*blue points*), and to be systematically higher when the QPO is at or below the spin frequency (*red points*). In 2002, the observations sample the source during the actual transition (*gray bands*). The pulse amplitude increases steadily from 3.5 to 5.6% on a timescale of hours when simultaneously the QPO frequency drifts down from $\sim$ 520 to $\sim$ 400 Hz. Both amplitude and frequency change very significantly (17σ and 8σ, respectively, see Table 5.1). In 2005 and 2008 we observe the opposite transition, with behavior that is entirely consistent with that in 2002, but time-reversed. The pulse amplitude drops from 7.1 to 4.3% (28σ) and 6.5 to 3.3% (23σ) in 2005 and 2008, respectively, when the QPO frequency increases through the 400–520 Hz range (12σ and 5σ change). In all cases, for QPO frequencies $<$ 401 Hz the pulse amplitude remains at the high level attained near 401 Hz.

The pulsations of SAX J1808 have been studied extensively (Hartman et al. 2008; Leahy et al. 2008; Hartman et al. 2009; Ibragimov & Poutanen 2009; Kajava et al. 2011;

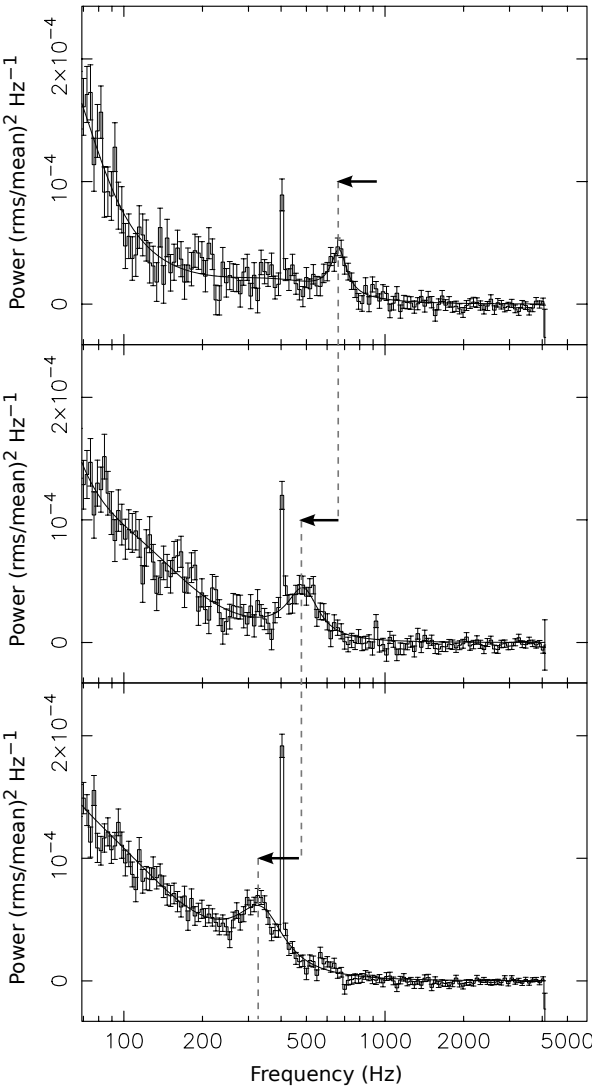

Figure 5.1: Power spectral evolution during the 2002 outburst, in chronological order (*top-down*). The frequency evolution of the kilohertz QPO (broad peak) in relation to the spike caused by the strictly periodic 401 Hz pulsations is obvious. When the kHz QPO frequency (dashed lines) moves through the spin frequency (*second to third frame*) the pulse amplitude (height of the spike) increases drastically. Arrows indicate the changes in QPO frequency and the initial spike height.

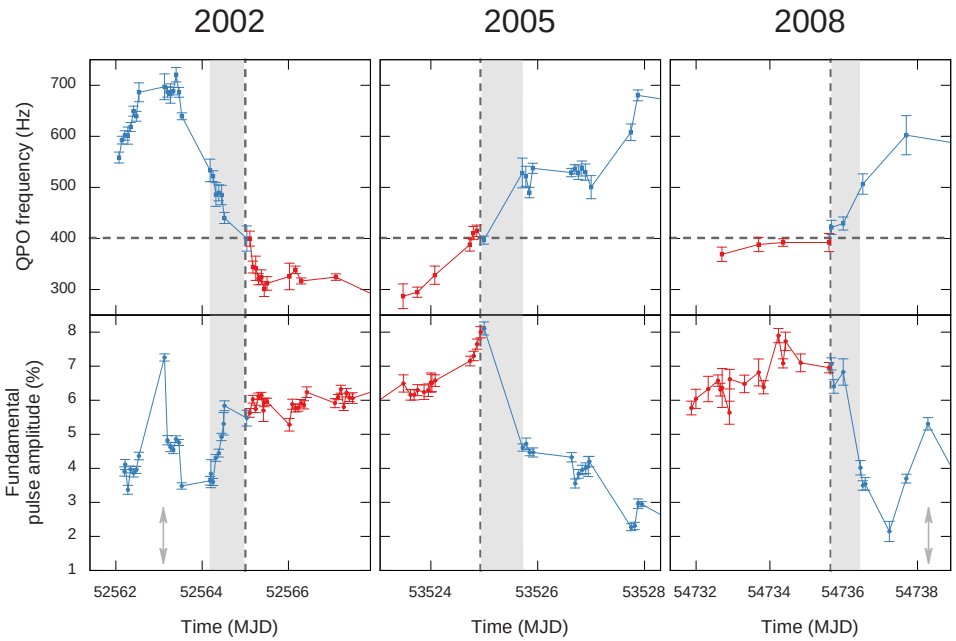

Figure 5.2: Evolution of the upper kHz QPO frequency (*top frame*) and the sinusoidal pulse amplitude (*bottom frame*) as the QPO frequency passes through the 401 Hz spin frequency during outbursts in the years indicated. Observations with the QPO frequency above and below the spin frequency are marked in blue and red, respectively. The dashed lines mark the spin-frequency passages and the gray bands indicate the full extent of the transits between the two regimes. The double-headed arrows mark pulse amplitude excursions (see text).

Morsink & Leahy 2011; Patruno et al. 2012) and are known to show brief, hour-timescale excursions in amplitude. We define an excursion as a sudden pulse amplitude increase of 50% or more directly followed by a similar amplitude decrease, such that the entire episode verifiably takes place within two days. In total there are 11 such excursions in the data, and we have marked these in Figures 5.2 and 5.3 with double-headed gray arrows.

We find that the occurrence of these brief excursions depends on QPO frequency dichotomously. The excursions only occur when the QPOs are > 401 Hz (see, e.g. Figure 5.3). While they are not limited to any particular QPO frequency, the most pronounced excursions cluster around the highest QPO frequencies of 600–700 Hz.

Figure 5.4 shows the amplitudes of the pulse fundamental (*top frame*) and second harmonic (*bottom frame*) versus upper kHz QPO centroid frequency as we measured them in all data across all outbursts. The large step in pulse amplitude taking place over a QPO frequency range of 400–500 Hz is obvious. When in this transition the fundamental amplitude drops from ~ 6 to $\sim 3\%$, the weaker second harmonic instead strengthens

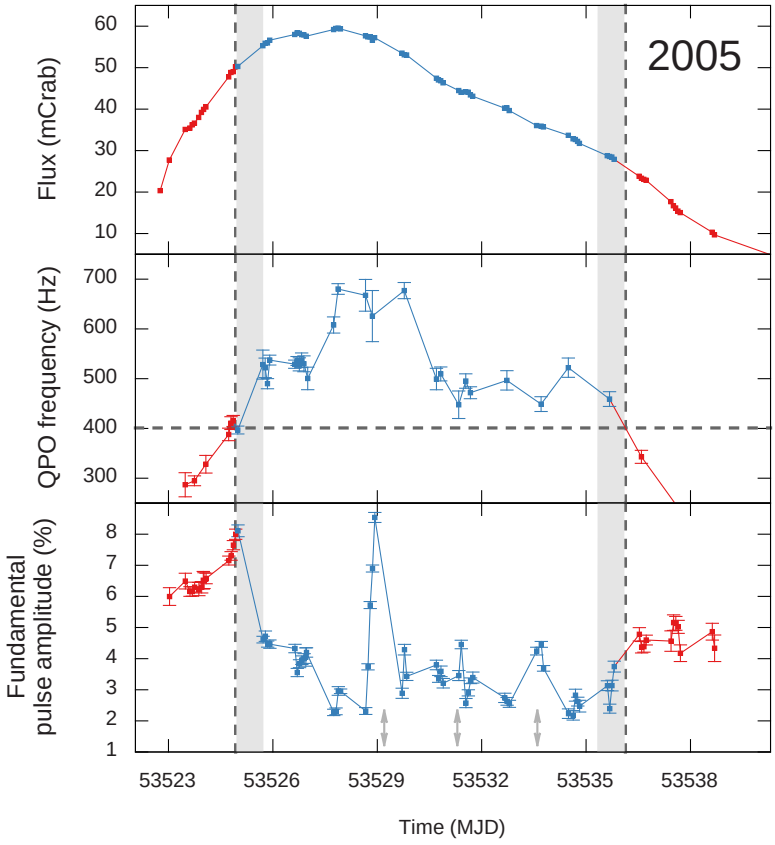

Figure 5.3: Overview of the 2005 outburst, showing the X-ray flux (*top frame*), the upper kHz QPO frequency (*middle frame*) and the fundamental pulse amplitude (*bottom frame*) as a function of time. Observations with the QPO frequency above and below the spin frequency are marked in blue and red, respectively. The dashed lines mark the spin-frequency passages and the gray bands show the extents of the transits between the two regimes. The double-headed arrows mark pulse amplitude excursions (see text). The other outbursts show similar trends.

from ~ 0.9 to $\sim 1.6\%$. The clustering of the brief excursions at high QPO frequencies is also clear among the points > 650 Hz.

The remaining data, at lower signal-to-noise, show behavior consistent with that in the three transitions reported above. When in 2005 at MJD 53536.1 the QPO moves from above to below 401 Hz, the pulse amplitude increases. In 1998 there is no transition; the QPO peak, while broad, is always entirely below 401 Hz. Consistent with this, the pulsations are strong and the second harmonic is weak. In 2011 kHz QPOs are detected only at frequencies > 401 Hz, so no transition is observed. In this outburst the pulse

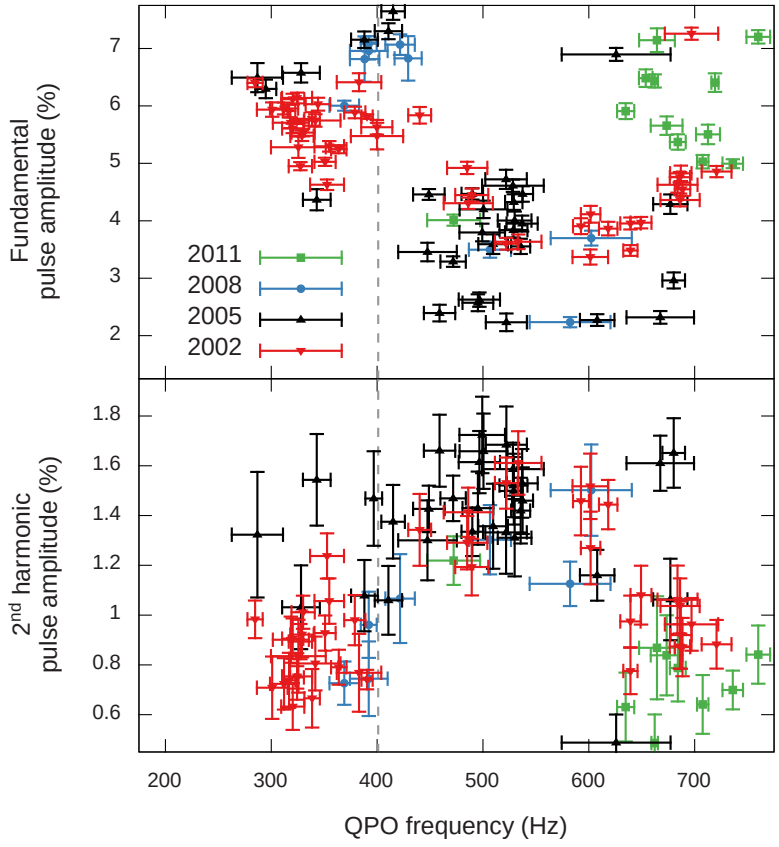

Figure 5.4: Fundamental (*top frame*) and second harmonic (*bottom frame*) pulse amplitudes as a function of the upper kHz QPO frequency of the outbursts as indicated. The dashed line marks the spin frequency.

amplitude is $\sim 4\%$ with, as expected, amplitude excursions of 2–3% on top of this.

5.4 Discussion

Our analysis establishes, for the first time, a direct effect of kHz QPOs on the millisecond pulsations: a large change in pulsation properties occurs when the upper kHz QPO frequency transits through the spin frequency, but reversely a change in pulse amplitude does not predict the QPO frequency. These findings point toward an origin of the upper kHz QPO in a process involving azimuthal motion in the accretion flow that makes the accreting plasma interact differently with the neutron-star magnetic field depending on whether the azimuthal motion is faster or slower than the spin. Although spin resonances

may play a role (see below), mechanisms relying on a resonance of the QPO frequency itself with the spin cannot explain our observations: the amplitude of such a resonance is largest when the QPO frequency is near 401 Hz and diminishes away from the resonant frequency. Instead, what is required is a step-wise change in the pulsations between QPO frequencies above and below the spin frequency.

Our observation that the pulse amplitude is sensitive to whether the QPO frequency is faster or slower than the spin immediately suggests an interpretation where the QPO is due to orbital motion and the key physics involved is the centrifugal force experienced by the accreting plasma as it enters the magnetosphere (Illarionov & Sunyaev 1975; Ghosh & Lamb 1978). In such a scenario, plasma outside the magnetosphere orbits in a Keplerian disk. Inside the magnetosphere the motions are dominated by the magnetic field and so the plasma is forced to corotate with the stellar spin. As long as the radius of the magnetosphere, $r_{\rm m}$, is larger than the corotation[2] radius $r_{\rm c}$, the plasma entering the magnetosphere speeds up and hence experiences a centrifugal force exceeding gravity, inhibiting lateral accretion. For a smaller magnetosphere no such centrifugal inhibition of the lateral accretion flow will occur and therefore a smaller fraction of the accreting plasma is available to flow out of the disk plane and toward the poles, causing the pulse amplitude to drop. Thus, if the QPO is due to orbital motion at the edge of the magnetosphere and hence the QPO frequency can be identified with the Keplerian frequency at $r_{\rm m}$, a very different accretion pattern is predicted for QPO frequencies above and below the spin frequency.

Another possible mechanism that can explain our result can apply to any model in which the QPO is due to an azimuthal motion at the inner edge of the disk. This motion could be Keplerian, but might also be, e.g., precessional, or that of an azimuthally propagating disk wave (van der Klis 2006, and references therein). As the inner edge of the disk moves inward it will pass through a resonance radius, $r_{\rm r}$, where the QPO frequency equals the spin frequency and a resonance may occur. For even smaller inner disk radii the QPO frequency increases further, but the resonance may continue to exist in the disk at $r_{\rm r}$. It is at least logically possible that such a resonance present in the disk flow at radius $r_{\rm r}$ leads to a different accretion pattern at radii inside $r_{\rm r}$. How precisely the resonance affects the pulse amplitude remains unspecified in this scenario, which in this generic sense could formally even work for an azimuthally symmetric QPO mechanism, and/or by interaction with the pulsar beam instead of the magnetic field.

In the above two scenarios, the accretion pattern changes when the inner edge of the disk passes through $r_{\rm c}$ or $r_{\rm r}$, respectively. A third possibility is that the relevant radius is $r_{\rm m}$. It has been suggested that it is possible for the Keplerian disk to penetrate the magnetosphere and continue its orbital motion inside $r_{\rm m}$, with the inner edge of the disk at $r_{\rm in}$ set by radiative stresses (Miller et al. 1998), so that $r_{\rm in}$ can be either larger or

[2]The corotation radius $r_{\rm c}$ is the radius where the Keplerian frequency equals the spin frequency: $r_{\rm c} \equiv \left[\sqrt{GM}/(2\pi\nu_s)\right]^{2/3} = 31$ km for an $M = 1.4M_\odot, \nu_s = 401$ Hz star, where M is the neutron-star mass and ν_s its spin frequency.

smaller than r_m. If the QPO originates from the inner edge of the disk, and its frequency is near the spin frequency as r_{in} passes through r_m, differences in magnetic coupling associated with r_{in} being larger or smaller than r_m might conceivably explain the change in the pulsations. For a QPO caused by Keplerian orbital motion these conditions might be fulfilled, as during outburst SAX J1808 may be near spin-equilibrium ($r_m \simeq r_c$, Hartman et al. 2008).

So, although some more complex explanations cannot formally be excluded, the interpretations discussed here predominantly point to a QPO that is produced by azimuthal motion at the inner edge of the accretion disk, most likely orbital motion, and a change in the interaction of the accreting plasma with the neutron star magnetic field near a QPO frequency equal to the spin frequency. The most straightforward scenario involves centrifugal inhibition of the accretion flow that sets in when the upper kHz QPO becomes slower than the spin. This scenario implies that the QPO is produced by orbital motion at the edge of the magnetosphere as it passes through 401 Hz.

5.A Additional figures

Here we present the evolution of the 2002, 2008 and 2011 outbursts, showing for each outburst the light curve, the upper kHz QPO frequency and the fundamental pulse amplitude. The outburst of 1998 has been omitted as it does not show a sufficiently coherent upper kHz QPO ($Q > 2$).

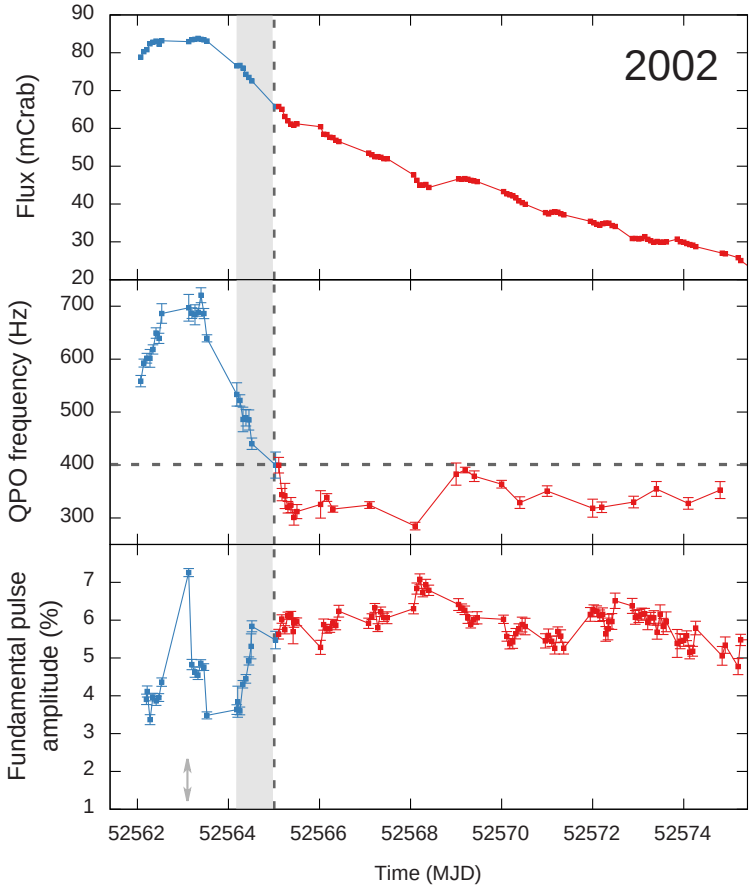

Figure 5.5: Overview of the 2002 outburst, see Figure 5.3 for details.

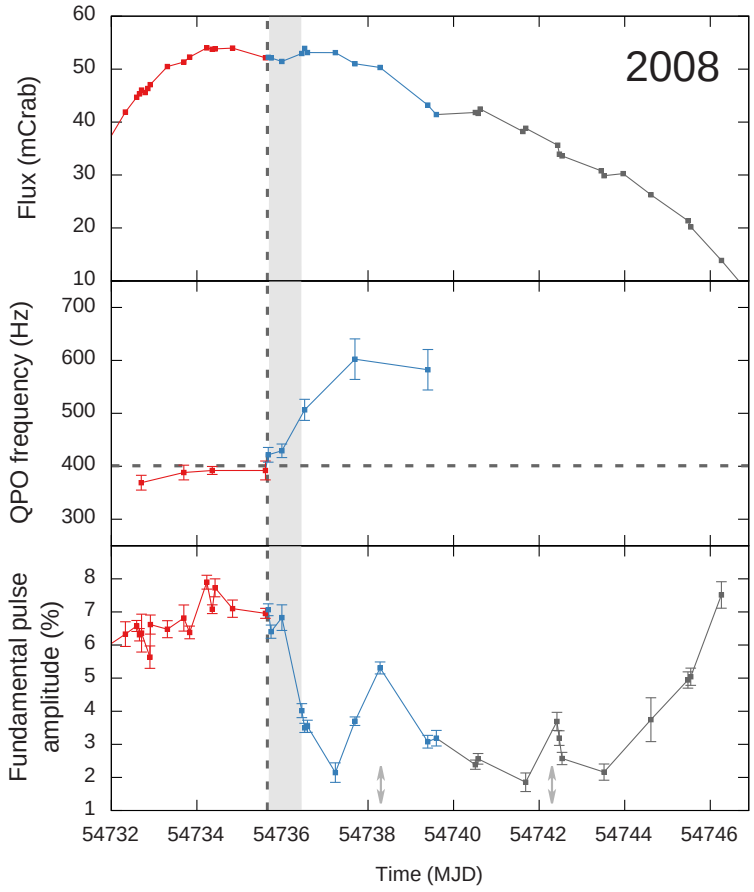

Figure 5.6: Overview of the 2008 outburst, with the grey points in the top and bottom frames indicating observations for which the upper kHz QPO is not sufficiently coherent or its frequency could not be measured. For further details see Figure 5.3.

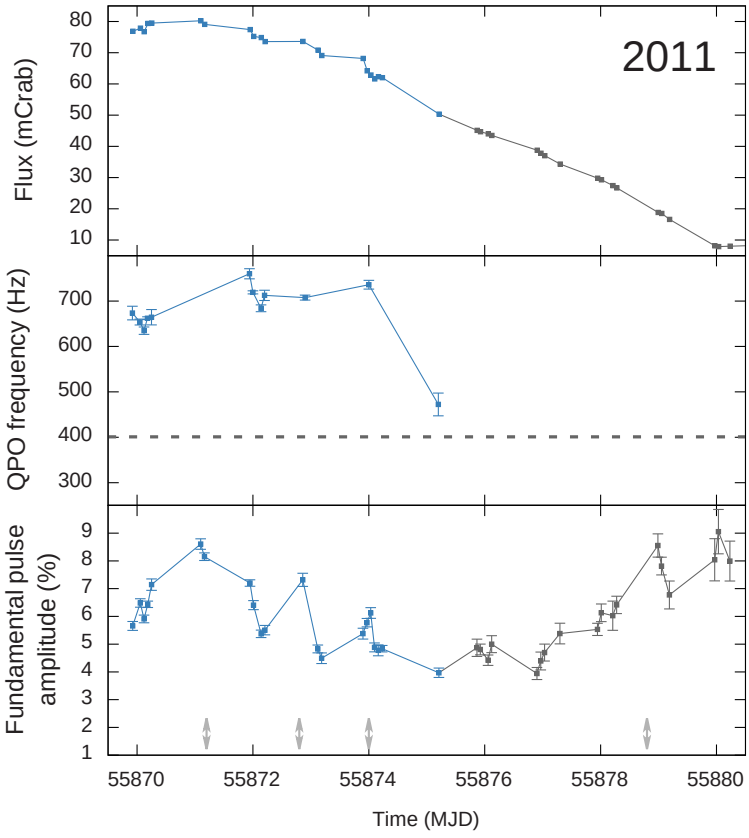

Figure 5.7: Overview of the 2011 outburst, see Figure 5.6 for details.

6 Coherent timing of the accreting millisecond pulsar NGC 6440 X-2

P. Bult, A. Patruno & M. van der Klis

The Astrophysical Journal, submitted

Abstract

We study the 205.9 Hz pulsations of the accreting millisecond X-ray pulsar NGC 6440 X-2 across all outbursts observed with the *Rossi X-ray Timing Explorer* over a period of 800 days. We find the pulsations are highly sinusoidal with a fundamental amplitude of $5\% - 15\%$ rms and a second harmonic that is only occasionally detected with amplitudes of $\lesssim 2\%$ rms. By connecting the orbital phase across multiple outbursts, we obtain an accurate orbital ephemeris for this source and constrain its 57 min orbital period to sub-ms precision. We do not detect an orbital period derivative to an upper limit of $|\dot{P}| \leq 8 \times 10^{-11}$ s s^{-1}. We investigate the possibility of coherently connecting the pulse phase across all observed outbursts, but find that due to the systematic uncertainties introduced by a flux-dependent bias in the pulse phase, multiple statistically acceptable phase-connected timing solutions exist.

6.1 Introduction

Accreting Millisecond X-ray Pulsars (AMXPs) are rapidly rotating neutron stars in low-mass X-ray binaries. These systems show coherent X-ray pulsations that arise when the accretion flow is magnetically channeled to the stellar surface. These pulsations offer a physical tracer of the neutron star and the inner accretion flow toward it, as their frequency gives a direct measure of the neutron star rotation rate, and the shape of the pulse waveform carries information on the accretion geometry and compactness of the neutron star (Poutanen & Gierliński 2003; Leahy et al. 2008; Psaltis et al. 2014). Tracking the pulse arrival times allows to measure the evolution of the neutron star spin and the binary orbit, thus offering insight into accretion torque theory (Psaltis et al. 1999), alternative torque mechanisms (Bildsten 1998a; Haskell & Patruno 2011) and the binary evolution of millisecond pulsars (Bildsten 2002; Nelson & Rappaport 2003; Patruno et al. 2012).

Among the currently known AMXPs (see Patruno & Watts 2012 for a review), the globular cluster source NGC 6440 X-2 is unique in its outburst behavior; it shows comparatively short, low luminosity outbursts, with peak X-ray luminosities of $L_X \lesssim 1.5 \times 10^{36}$ erg s^{-1} and outburst durations of $2-5$ days (Heinke et al. 2010). NGC 6440 X-2 was discovered with Chandra on July 28th, 2009 (Heinke et al. 2009) and seen in outburst again merely a month later with the *Rossi X-ray Timing Explorer* (*RXTE*), at which time the 205.9 Hz pulsations were discovered (Altamirano et al. 2009). The following two outbursts each occurred after a quiescent interval of about one month, establishing NGC 6440 X-2's recurrence time as the shortest of all AMXPs known to date. The coherent timing analysis of those first four outbursts was reported by Altamirano et al. (2010d), who found pulsations in three outbursts at fractional amplitudes of $\sim 7\%$ for the fundamental component.

After the fourth outburst, on October 28th, 2009, NGC 6440 X-2 remained in quiescence until new activity was observed in March, 2010 (Altamirano et al. 2010a). Subsequently, the source showed another three outbursts with a recurrence time of about 110 days, after which it remained quiescent for nearly 300 days until the last outburst was observed with *RXTE* in November, 2011 (Patruno & D'Angelo 2013).

In this work we present the results of a coherent timing analysis of NGC 6440 X-2 over the course of its complete outburst history as observed with *RXTE*. In Section 6.2 we describe our data reduction and analysis method. In Section 6.3 we present our results as we discuss how the high precision orbital ephemeris and pulse frequency evolution of NGC 6440 X-2 was obtained. Next, in Section 6.4, we briefly summarize and discuss our results.

Table 6.1: Outbursts of NGC 6440 X-2

ID	Date	T_{asc} (MJD)	ΔMJD (days)	ObsID	Exposure (s)	Pulse Amp. (% rms)
$\mathcal{O}2$	2009-07-28	55042.81		94044-04-01-00[b]	1900	12.9 ± 4.1
$\mathcal{O}3$	2009-08-30	55073.03	30.3	94044-04-02-00[c]	3200	9.0 ± 0.5
	...	...		94044-04-02-01	14000	5[a]
$\mathcal{O}4$	2009-10-01	55106.01	32.9	94044-04-03-00	2200	11.4 ± 1.9
	...	...		94044-04-04-00	3400	16[a]
$\mathcal{O}5$	2009-10-28	55132.90	27.0	94315-01-04-01	900	14.0 ± 1.8
	...	...		94315-01-04-02	900	10[a]
$\mathcal{O}6$	2010-03-21	55276.62	143.3	94315-01-12-00	2000	12.4 ± 0.7
	...	...		94315-01-12-01	2700	13.2 ± 1.0
	...	...		94315-01-12-02	1900	12.9 ± 1.1
$\mathcal{O}7$	2010-06-12	55359.47	83.2	94315-01-14-00	9900	7.6 ± 0.4
$\mathcal{O}8$	2010-10-04	55473.85	114.4	94315-01-25-00	1200	5.3 ± 0.6
$\mathcal{O}9$	2011-01-23	55584.71	110.9	96326-01-02-00	2100	6.0 ± 0.6
$\mathcal{O}10$	2011-03-21	55641.02	56.3	96326-01-10-00	2000	12.7 ± 1.9
$\mathcal{O}11$	2011-11-06	55871.23	231.9	96326-01-35-00	1200	6.3 ± 1.1
	...	55872.83		96326-01-40-00	3300	11.5 ± 2.3
	...	55873.31		96326-01-40-01	2400	9.8 ± 2.9

Note. Pulse amplitudes are that of the fundamental component and calculated per *RXTE* orbit ($\sim$ 3 ks intervals). ΔMJD gives the duration of the quiescent interval with respect to the last observed outburst. Reported ObsIDs refer to Event mode data unless otherwise specified.
[a] 95% c.l. upper limit
[b] GoodXenon
[c] SingleBit

6.2 Data reduction

We analyze all pointed *RXTE* observations of NGC 6440 X-2 (Altamirano et al. 2009; Heinke et al. 2010; Patruno & D'Angelo 2013). We use the 16-s time-resolution Standard-2 data to construct 2–16 keV light curves (see, e.g, van Straaten et al. 2003 for details). The flux is normalized to Crab and averaged per observation. We find one type I X-ray burst at MJD 55359.5, which we exclude from our further analysis.

For the timing analysis we use all high time resolution ($\leq 122\mu s$) SingleBit, Event and GoodXenon data. We correct the data to the Solar System barycenter using the FTOOL *faxbary* based on the Chandra X-ray position of Heinke et al. (2010). This tool also applies the *RXTE* fine clock corrections, allowing for an absolute timing precision of ~ 4 μs (Rots et al. 2004).

The observations are divided in $\sim$ 500 s segments, selecting only the events in the energy channels 5–37 ($\sim 2-16$ keV), which optimizes the pulse signal to noise ratio. We then compare the observed count rate with the background count rate estimated using the FTOOL *pcabackest*, and reject all observations for which the expected amplitude of

a 100% modulated source contribution cannot be detected above the noise amplitude expected from counting statistics.

The remaining observations are corrected for the orbital ephemeris, folded on the pulse period (see Section 6.3), and fit with a constant plus a sinusoid at the fundamental (ν) and second harmonic (2ν) pulse frequency. We consider a pulse harmonic to be significant if its amplitude exceeds a detection threshold, which we define as the noise amplitude for which there is only a small probability $1-\mathcal{C}$ that among all observations one or more exceed it by chance, with $\mathcal{C} = 99\%$ the confidence level of the detection. Once an episode of pulsations has been established we repeat the analysis for several different segment lengths ($100-3000$ s) to study the pulse properties on various timescales. Pulse amplitudes are reported in terms of fractional rms

$$r_i = \frac{1}{\sqrt{2}} \frac{A_i}{N_\gamma - B}, \tag{6.1}$$

where A_i is the measured sinusoidal amplitude of the i-th harmonic, N_γ the total number of counts in the segment and B the estimated background contribution (see, e.g. Patruno et al. 2010a).

We model the measured pulse arrival times per outburst using a circular orbit and constant pulse frequency. As such our timing model consists of four parameters, namely the orbital period P_b, the projected semi-major axis $A_x \sin(i)$, the time of the ascending node $T_{\rm asc}$, and the pulse frequency ν. Phase residuals are obtained by subtracting this timing model from the measured arrival times and analysed to refine the timing model. The details of this analysis are presented in the following section.

6.3 Results

Because of the short duration of its outbursts and its high recurrence rate, the coherent timing analysis of NGC 6440 X-2 requires careful consideration. In this section we describe our analysis of this source in detail. We start from a provisional timing solution based on the work of Altamirano et al. (2010d), and iteratively refine the timing model parameters until the final timing solution is obtained.

Initially we consider the outbursts of NGC 6440 X-2 separately (see Table 6.1 for details). We refer to i-th outburst as $\mathcal{O}i$, where we start counting outbursts from an archival *Swift* observation on the 4th of June, 2009 (MJD 54986), which is considered the earliest detection of this source (Heinke et al. 2010). For our preliminary timing solution we adopt the pulse frequency, projected semi-major axis and orbital period that Altamirano et al. (2010d) obtained for $\mathcal{O}3$. Because of the limited accuracy of their orbital period measurement ($P_b = 3438(33)$ s) we cannot reliably predict the time of ascending node for any of the other outbursts. Instead, for each outburst, we set this parameter by searching a grid of $T_{\rm asc}$ at a 5-second resolution and selecting the value that maximizes the pulse amplitude.

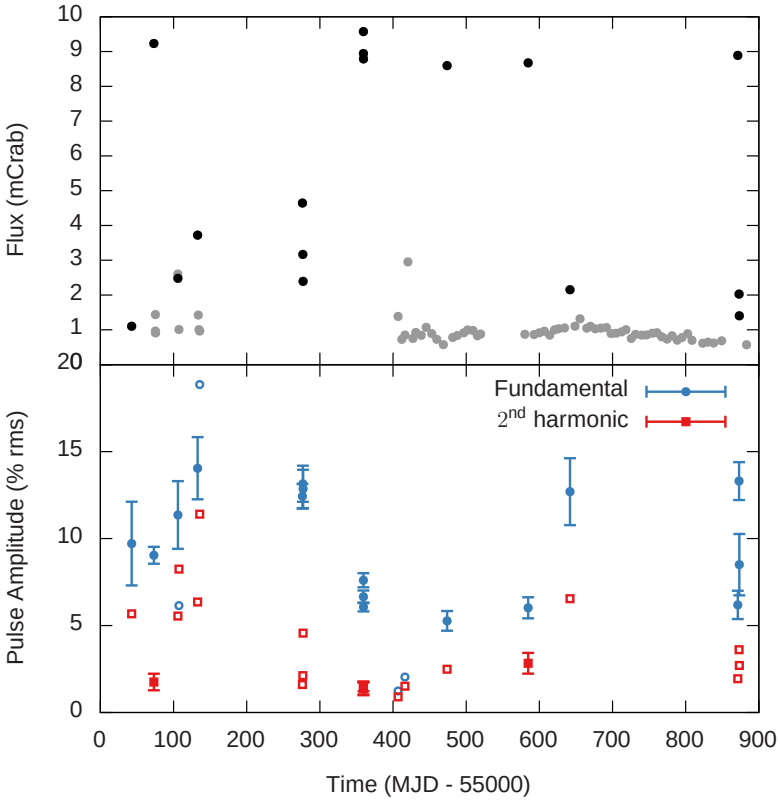

Figure 6.1: Top: light curve of NGC 6440 X-2 as observed with *RXTE*. Black points show observations with significantly detected pulsations, grey points show observations for which pulsations were not detected. Bottom: fundamental (blue circles) and second harmonic (red squares) fractional pulse amplitudes. Open symbols give 95% upper limits.

NGC 6440 X-2 has been reported to have shown nine outbursts observed with *RXTE* during the 800 day observational baseline (Patruno & D'Angelo 2013). We find pulsations during this baseline on ten occasions, adding one low-flux outburst ($\mathcal{O}10$) to the sample. Five of the observed outbursts reached a flux of ~ 9 mCrab, and six peaked at fluxes half that or lower (see Figure 6.1). The pulse profiles are highly sinusoidal, with typical fundamental pulse amplitudes of $5\% - 15\%$ rms and second harmonic amplitudes of $\sim 2\%$ detected for only three observations ($\mathcal{O}3$, $\mathcal{O}7$, $\mathcal{O}9$). We report the details of each outburst in Table 6.1.

Although NGC 6440 X-2 has shown many outbursts, only a few observations offer sufficient quality to place useful constraints on the timing model parameters. Many of the observations have a low signal to noise ratio due to the low count rate of the source.

Table 6.2: Per-outburst Timing Solutions

ID	ν (Hz)	$A_x \sin(i)$ (lt-ms)	P_b (s)	$T_{\rm asc}$ (MJD)
$\mathcal{O}3$	205.89217(14)	6.2(6)	3421(156)	55073.035(3)
$\mathcal{O}6$	205.8921768(2)	6.05(4)	3458.0(3)	55276.62545(3)
$\mathcal{O}7$	205.8921759(7)	6.14(2)	3458(1)	55359.51080(3)

Additionally, most outbursts are observed only for a single exposure of less than 3 ks, which is shorter than the orbital period of the binary. So, even if the phase could be measured on a sufficiently short timescale to allow for a fit to our 4-parameter timing model, the short exposures introduce strong correlations between ν, $T_{\rm asc}$ and P_b and hence cause a large uncertainty on all parameters.

For three outbursts of NGC 6440 X-2 the data is of sufficient quality to constrain the timing model. These are $\mathcal{O}3$, $\mathcal{O}6$ and $\mathcal{O}7$. The latter two are of particular use, as they consist of several consecutive exposures with separations of less than half a day. For these outbursts the data spans much more than a single orbital period, which breaks the correlation between the timing model parameters. We give the timing solutions for these outbursts in Table 6.2. While $\mathcal{O}11$ also consists of multiple exposures, we note that those observations are each about a day apart, and that, within the accuracy of the frequency measurement, the pulse phase cannot be uniquely propagated across that separation.

6.3.1 Orbital evolution

To refine the orbital period estimate, we consider the $T_{\rm asc}$ values measured locally for $\mathcal{O}3$, $\mathcal{O}6$ and $\mathcal{O}7$ and perform a phase-coherent analysis of the orbital evolution. Using the timing solution of $\mathcal{O}6$ we predict the $T_{\rm asc}$ at the time of $\mathcal{O}7$ to obtain a difference between the predicted and locally measured $T_{\rm asc}$ of $\Delta T = 0.002(8)$ days. Since the predicted $T_{\rm asc}$ and the local measurement are consistent, and the uncertainty is smaller than half the orbital period to within a 95% confidence level, we can coherently connect the orbital phase between these outbursts. Setting the estimated number of cycles between these outbursts, $N = (T_{\rm asc,7} - T_{\rm asc,6})/P_b$, to its nearest integer, then gives an accurate measurement of the orbital period of $P_b = 3457.892(2)$ s.

Using the phase-connected orbital period estimate we can describe all outbursts with a single orbital model. We therefore perform a joint-fit to the data using a timing model in which the orbital parameters are coupled, but the frequency is left free per outburst. This approach gives high accuracy measurements of the orbital parameters, which are presented in Table 6.3.

Table 6.3: Joint-fit Timing Solution

Parameter	Value	Statistical uncertainty	Systematic uncertainty
P_b (s)	3457.8929	7×10^{-4}	
$\lvert\dot{P}_b\rvert$ (s s^{-1})	$\leq 8 \times 10^{-11}$		
$A_x \sin(i)$ (lt-ms)	6.14	0.01	
$T_{\rm asc}$ (MJD)	55318.04809	2×10^{-5}	
ν_3 (Hz)	205.892177	3×10^{-6}	
ν_6 (Hz)	205.89217619	1.1×10^{-7}	2×10^{-6}
ν_7 (Hz)	205.8921758	7×10^{-7}	7×10^{-6}
ν_9 (Hz)	205.892185	1.7×10^{-5}	
ν_{10} (Hz)	205.89208	3×10^{-5}	
ν_{11a} (Hz)	205.89212	4×10^{-5}	
ν_{11b} (Hz)	205.89221	2×10^{-5}	
$\lvert\dot{\nu}\rvert$ (Hz s^{-1})	$\leq 5 \times 10^{-13}$		

Note. ν_i gives the frequency of the i-th outburst, with ν_{11a} referring to the first observation of $\mathcal{O}11$ and ν_{11b} to the second (also see Table 6.1).

6.3.2 Spin frequency analysis

Because in a joint-fit approach the orbital parameters are fit to all data, and only the frequency is measured locally per outburst, the correlation between the orbit and spin parameters that occurs for short observations is no longer an issue. This method therefore allows the frequency to be measured in additional outbursts. The frequency measurements, shown in Table 6.3, are consistent within their respective uncertainties, and place a 95% confidence level upper limit on the frequency derivative of $|\dot{\nu}| \lesssim 5 \times 10^{-13}$ Hz s^{-1}.

As was done for the orbital phase, we may also attempt to connect the pulse phase between outbursts. To do this we construct a single pulse profile using all data of an outburst, from which we measure an averaged pulse arrival time. Starting from $\mathcal{O}6$, which gives the most accurate frequency measurement, we then propagate the timing model to predict the pulse arrival time for the other outbursts. In this analysis, however, there are additional effects that contribute to the predicted phase or its uncertainty, which need to be accounted for.

The pulsations may show a frequency derivative that contributes to the phase difference between two outbursts. The spin derivative expected from standard accretion

theory is given as (Patruno & Watts 2012)

$$\dot{\nu} \simeq 4.2 \times 10^{-14}\ \mathrm{Hz\ s^{-1}}\ \gamma_B^{1/2} \left(\frac{\dot{M}}{2 \times 10^{-10}\ M_\odot\ \mathrm{yr^{-1}}}\right)^{6/7} \times \left(\frac{B}{10^8\ \mathrm{G}}\right)^{2/7} \left(\frac{M}{1.4\ M_\odot}\right)^{3/7} \left(\frac{R}{10\ \mathrm{km}}\right)^{6/7}, \tag{6.2}$$

where $\gamma_B \simeq 0.3 - 1$ parameterizes the uncertainty in the angular momentum at the inner edge of the accretion disk (Psaltis et al. 1999), $\dot{M}$ gives the mass accretion rate and M, R and B give the mass, radius and magnetic field strength of the neutron star, respectively. Assuming the pulse frequency derivative is of this order, it can cause a phase offset of ~ 1 cycle over the 80 day interval between $\mathcal{O}6$ and $\mathcal{O}7$, and so the possibility of a frequency derivative needs to be accounted for. As the frequency derivative is the second unknown contributing to the phase (the frequency being the first unknown) we need to consider the phase prediction for two outbursts to determine both parameters.

The phase residuals of the individual outbursts are subject to systematic uncertainties. As demonstrated by Patruno et al. (2009e), the pulse phase shows a correlation with X-ray flux in most AMXPs. This correlation can be understood as the instantaneous accretion rate causing an offset in the hotspot position and thus a bias in the phase residual. If the flux changes linearly in time, it introduces a linear trend in the phase residuals that the standard rms-minimization method corrects for by adjusting the pulse frequency. This effect is particularly relevant for $\mathcal{O}6$ and $\mathcal{O}7$, which both show a decay in flux. Because that flux decay is nearly linear we cannot constrain the potential effect of a phase-flux relation from the data of NGC 6440 X-2 alone. To still obtain an approximate estimate for the size of this uncertainty we consider that for most AMXPs the phase bias due to the flux is much less than one cycle (Patruno et al. 2009e) and adopt a maximum phase offset of $\delta\phi = 0.15$ cycles. The systematic uncertainty in frequency is then given as $\sigma_\nu = \delta\phi/\delta t$, where δt is the timespan of the considered outburst sampled by observations.

Due to the phase-flux relation the pulse phase measured for an outburst consists of the underlying spin phase and the flux-induced bias. The phase propagation based on the timing model, however, only applies to the part due to the neutron star spin, and not the bias. If the phase-flux relation is indeed introduced by a geometrical effect such as a drifting hotspot position, then we might expect that when averaging over an entire outburst, the bias will average to a mean value determined by the system accretion geometry which is the same for all outbursts. In other words; if the outburst is sufficiently well sampled, then we may be able to calibrate the flux-induced phase bias, such that we can calculate a reference phase that is stable between outbursts. For NGC 6440 X-2, however, the observational sampling of the outbursts is very poor, and consequently the measured pulse phase may be offset from the outburst-long average. Additionally, because other AMXPs, most notably SAX J1808.4–3658, have been observed to show different phase-flux relations for different outbursts (Patruno et al. 2009e), the size and direction of the bias are essentially unknown and cannot be trivially corrected for by

considering the flux difference between outbursts. As such, the flux-induced bias on the typical pulse phase of an outburst has considerable uncertainty. To get at least a rough estimate of this uncertainty we adopt the same $\delta\phi = 0.15$ cycles noted above. For $\mathcal{O}6$ this uncertainty is roughly 10 times larger than the statistical uncertainty on the averaged pulse arrival time.

Taking the noted considerations into account we can propagate the pulse phase from $\mathcal{O}6$ to $\mathcal{O}7$. We then find an uncertainty on the residual phase of $\sigma_\phi = 14.4$. The number of trials that we need to consider is then calculated as

$$n = 2(z\sigma_\phi + \varphi_{\dot{\nu}}) + 1, \tag{6.3}$$

where z gives the significance interval for the usual two-sided confidence level $\mathcal{C} = \mathrm{erf}\left(z/\sqrt{2}\right)$, $\varphi_{\dot{\nu}}$ gives the phase offset introduced by frequency derivative, the factor two accounts for the fact that the phase offset can be positive and negative, and the added one accounts for the central trial that has a phase offset of less than half a cycle. We then find that for a 95% confidence level, we need to consider 59 possible way to connect the phases between these outbursts. Similarly we propagate the pulse phase from $\mathcal{O}6$ to $\mathcal{O}5$ to find an uncertainty of $\sigma_\phi = 24.8$, implying we need to consider 100 possible ways to connect those phase measurements. Hence, there are 5900 combinations of ν and $\dot{\nu}$ that connect the phases of the three considered outbursts. To test these possible solutions we can propagate each trial solution to the other outbursts and calculate the χ^2 of the phase residuals to see which of them are statistically acceptable. However, due to the large phase uncertainty introduced by the phase bias we find that the accumulated error on phase residuals at the time of the other outbursts is larger than 0.5 cycles even for the closest outburst. As such we cannot test the different trial solutions and must conclude that all 5900 considered options are statistically acceptable.

It is clear that the systematic uncertainty due to the phase-flux relation plays an important role, and that in the case of NGC 6440 X-2, it becomes prohibitive in the analysis of the long term spin evolution. Future observations may be able to establish the phase-flux relation in this source, allowing the size of the flux dependent phase bias to be calibrated per outbursts, thereby reducing the systematic uncertainties or potentially eliminating them altogether. To investigate whether a coherent pulse phase connection would then be feasible, we consider the scenario that the phase bias is zero in NGC 6440 X-2. Then, by accounting only for the statistical uncertainty on the frequency measurements, the number of trials we need to consider drops drastically from 100×59 to $8 \times 6 = 48$. Additionally, without the phase uncertainty due the flux, the error on the residual phases accumulates much slower, such that the timing solution can be coherently extrapolated to $\mathcal{O}2$ and $\mathcal{O}10$. Comparing each of the 48 solutions to the outbursts $\mathcal{O}2$ through $\mathcal{O}10$, we find that there is only one combination of ν and $\dot{\nu}$ that provides an acceptable fit. Optimizing this solution by also refitting the orbital parameters and allowing for a second derivative on the pulse frequency, we find a pulse phase coherent timing solution that describes all data (including $\mathcal{O}11$). We then have

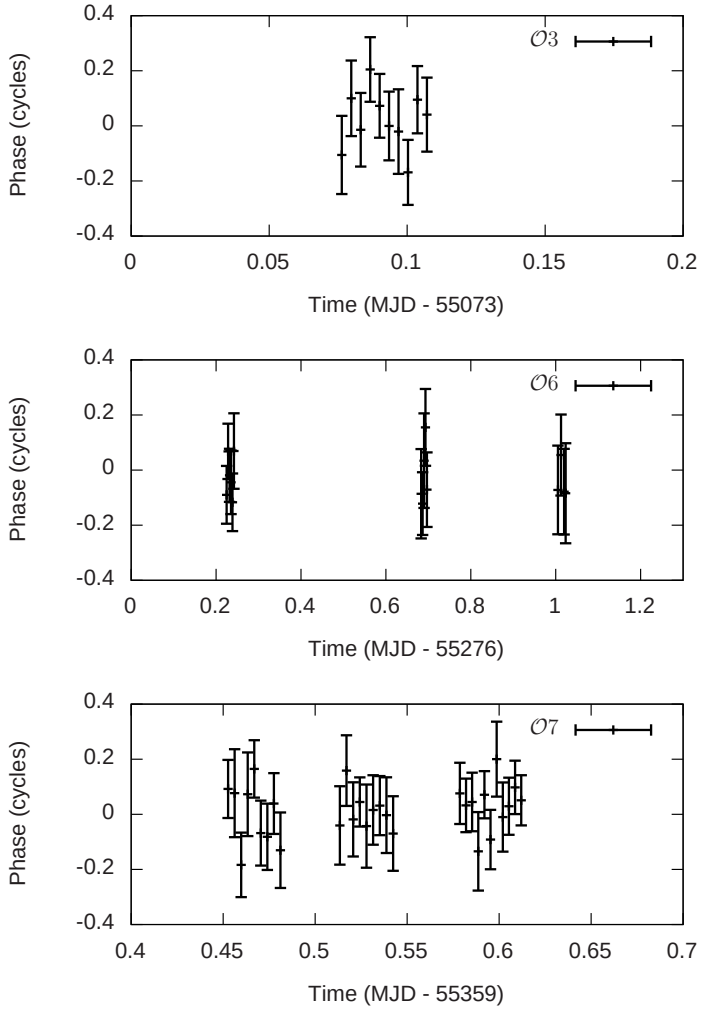

Figure 6.2: Phase residuals of the main outbursts for the phase connected timing solution assuming the the flux-induced phase bias is zero.

$\nu = 205.8921762261(3)$ Hz with $\dot{\nu} = 1.179(3) \times 10^{-14}$ Hz s^{-1} and a second pulse frequency derivative of $\ddot{\nu} = -3.7(1) \times 10^{-23}$ Hz s^{-2} (see Figure 6.2 for the phase residuals).

We stress that this result does not mean that the quoted solution gives the correct description of this system. What it shows is that if the flux-induced phase bias can be calibrated, the correct phase coherent solution can be found. The solution mentioned above then gives the timing solution if the phase bias can be shown to be zero for this source.

6.4 Discussion

We analysed the coherent pulsations of the accreting millisecond pulsar NGC 6440 X-2 for all outbursts observed with *RXTE*. We find that in the ten observed outbursts, the fundamental pulse amplitude varies from 5% to 15% rms, whereas the the second harmonic, if detected, has an amplitude of $\lesssim 2\%$ rms.

We have improved the orbital and spin parameter measurements of NGC 6440 X-2. Within the uncertainty of our measurements we find no evidence of a spin derivative to an upper limit of 5×10^{-13} Hz s^{-1}. This limit on the spin frequency derivative is larger than the expected spin-up or spin-down effects in AMXPs (see, e.g. Patruno & Watts 2012), and therefore does not constrain the neutron star spin evolution.

Through the coherent connection of the orbital phase, we measured the orbital period to high accuracy, but found no evidence of an orbital period derivative. These measurements are in line with expectations from binary evolution. As NGC 6440 X-2 is in an ultra-compact binary with a white dwarf companion star (Altamirano et al. 2010d), its orbital evolution is expected to be dominated by the loss of orbital angular momentum through the emission of gravitational waves (Kraft et al. 1962), with the evolution proceeding on a timescale of (Paczyński 1967)

$$\tau_{\rm GW} = 50 \text{ Gyr } \frac{\left(M + M_{\rm C}\right)^{1/3}}{M M_{\rm C}} P_b^{8/3}, \tag{6.4}$$

where M the neutron star mass, $M_{\rm C} \simeq 0.0076 M_\odot$ the companion star mass and P_b is expressed in days. Assuming a canonical $1.4 M_\odot$ neutron star we find a timescale of 1.4 Gyr, which implies an orbital derivate of $\dot{P} \sim 8 \times 10^{-14}$ s s^{-1}, much lower than the upper limit we find in this work.

The short recurrence time of NGC 6440 X-2 hints at the possibility that like the orbital phase, the pulse phase may also be coherently connected across outbursts. Such a coherent phase connection would allow the spin frequency evolution of this source to be measured to high accuracy. We investigated the possibility of such a pulse phase connection, and find that various systematic uncertainties introduced by the flux need to be taken into account. Unfortunately, these uncertainties are poorly constrained for NGC 6440 X-2 due to the sparse observational sampling of its outbursts.

Our analysis demonstrates the important role played by the systematic effects in pulse phase due to the X-ray flux when considering coherent timing of different outbursts. This applies not just to NGC 6440 X-2, but to any accreting millisecond pulsar. We also show that if future observations are able to accurately calibrate the phase bias a coherent phase connection will be possible, warranting a closer investigation of this interaction between pulse phase and instantaneous X-ray flux and the mechanism by which it arises.

7 The magnetic field strengths of accreting millisecond pulsars

D. Mukherjee, P. Bult, M. van der Klis & D. Bhattacharya

Monthly Notices of the Royal Astronomical Society, in press

Abstract

In this work we have estimated upper and lower limits to the strength of the magnetic dipole moment of all 14 accreting millisecond X-ray pulsars observed with the *Rossi X-ray Timing Explorer* (*RXTE*). For each source we searched archival *RXTE* data for the highest and lowest flux levels with a significant detection of pulsations. We assume these flux levels to correspond to the closest and farthest location of the inner edge of the accretion disk at which channeled accretion takes place. By estimating the accretion rate from the observed luminosity at these two flux levels, we place upper and lower limits on the magnetic dipole moment of the neutron star, using assumptions from standard magnetospheric accretion theory. Finally, we discuss how our field strength estimates can be further improved as more information on these pulsars is obtained.

7.1 Introduction

Magnetic field strengths of neutron stars span a wide range; from $\gtrsim 10^{14}$ G in magnetars via $\sim 10^{12}$ G in most radio pulsars down to $\sim 10^{8}$ G in millisecond pulsars. The millisecond pulsars are thought to attain their fast spin and low magnetic field strength through accretion in low-mass X-ray binaries (Alpar et al. 1982; Radhakrishnan & Srinivasan 1982; Bailes 1989). The discovery of accreting millisecond X-ray pulsars (AMXPs, Wijnands & van der Klis 1998a) and transitional millisecond pulsars (Papitto et al. 2013a) has lent strong support to this picture. However, a full understanding of the evolutionary scenario will only emerge through the comparison of both spin and magnetic field distributions of the LMXB neutron stars with those of transitional and millisecond radio pulsars. In this paper we undertake the task of estimating the magnetic field strengths of the AMXP population in a consistent approach.

Magnetic field strengths of neutron stars are estimated in a variety of ways. For non-accreting radio pulsars the field strengths are inferred from the spin-down rate due to electromagnetic torque (e.g. Ostriker & Gunn 1969; Beskin et al. 1984; Spitkovsky 2006). For anomalous X-ray pulsars, rough estimates of the field can also be obtained by modelling the non-thermal X-ray spectra with cyclotron and magnetic Compton scattering processes in the magnetosphere (Güver et al. 2007, 2008).

For accreting systems, the available methods for estimating the field strength are less robust. X-ray pulsars with high surface field strengths ($\gtrsim 10^{12}$ G), may show resonant electron cyclotron lines in their X-ray spectra, which give an estimate of the local field strength in the line formation region (Caballero & Wilms 2012). However, the location of this region is unclear, resulting in uncertainties in the measured dipole moment. For lower surface field strengths, as for AMXPs, cyclotron resonances move out of the X-ray band, leaving only indirect methods for estimating the field strength.

In this paper we estimate the magnetic field strength of AMXPs using X-ray observations obtained with the *Rossi X-ray Timing Explorer* (*RXTE*). We assume that the accretion disk is truncated at an inner radius that depends on the magnetic field strength and the accretion rate. Below the truncation radius the disk is disrupted and matter is forced to move along the magnetic field to the magnetic polar caps of the neutron star, creating localised hotspots responsible for X-ray pulsations (see, e.g., Poutanen & Beloborodov 2006). The detection of X-ray pulsations is taken to imply ongoing magnetically channeled accretion onto the neutron star, such that the highest and lowest flux levels with detected pulsations identify the range of luminosities (and hence accretion rates) over which accretion occurs. Assuming a disk-magnetic field interaction model, these measurements can then be used to constrain the surface dipole field strength of the neutron star.

To calculate the dipole moment from the set of flux levels, we consider the Ghosh & Lamb (1978, 1979b) model of disk-magnetic field interaction, applied in a manner akin

to that adopted by Psaltis & Chakrabarty (1999). We assume ongoing accretion to mean that the disk truncation radius is outside the neutron star surface, but smaller than the co-rotation radius (Pringle & Rees 1972; Illarionov & Sunyaev 1975), keeping in mind that these radii only set an approximate scale for the system. The accretion disk may not extend all the way down to the neutron star surface and channeled accretion may persist for a disk truncated outside the co-rotation radius (Spruit & Taam 1993; Rappaport et al. 2004; Bult & van der Klis 2015a, see Chapter 5). How this choice of radii affects our magnetic field strength estimates is discussed in Section 7.4.3.

We plan the paper as follows: in Section 7.2 we review the theory of accretion-disk/magnetic-field interaction, the details of our field strength estimation method and X-ray analysis; in Section 7.3 we describe the outburst history of the considered sources and the results of our analysis; in Section 7.4, we discuss the uncertainties in our method and how they affect our results; and finally in Section 7.5 we compare our results with previous estimates of the magnetic field strength. Technical details of the timing and spectral analysis are presented in Appendix 7.A and 7.B respectively.

7.2 Magnetic field strength estimation method

7.2.1 Theory of disk-stellar magnetic field interaction

For accretion in a steady state, the inner truncation radius depends on the balance between magnetic and material stresses. Equating the torque from the magnetic stresses and the angular momentum flux (Ghosh & Lamb 1979b; Rappaport et al. 2004)[1], one finds that

$$\frac{d(\dot{M} r^2 \Omega_K)}{dr} = B_\phi B_p r^2, \tag{7.1}$$

where $\dot{M}$ is the accretion rate, r the distance from the compact object, Ω_K the Keplerian angular velocity at r, and B_p and B_ϕ the respective poloidal and toroidal components of the magnetic field. For simplicity we calculate the torques at the truncation radius considering the spin axis to be aligned to the magnetic dipole, with the accretion disk being perpendicular to both axes. The toroidal field component is produced due to shearing of the poloidal fields. Its strength is an uncertain parameter as it depends on various poorly understood processes like turbulent diffusion and magnetic reconnection (Wang 1995). Another uncertain quantity is the radial extent of the accretion disk, Δr, over which matter couples to the stellar magnetic field and is channelled away from the disk. By expressing these uncertain quantities with the boundary layer parameter, $\gamma_B = (B_\phi / B_p)(\Delta r / r_t)$, the truncation radius r_t can be related to the poloidal magnetic field and hence the dipole moment as

$$B_p = \gamma_B^{-1/2} \left(G M \dot{M}^2 \right)^{1/4} r_t^{-5/4}, \tag{7.2}$$

[1] Viscous stresses at the truncation point have been ignored

where G is the gravitational constant and M the neutron star mass. Assuming a dipolar magnetic field, $B_p(r) = \mu/r^3$, with μ the magnetic dipole moment, the truncation radius is given as

$$r_t = \gamma_B^{2/7} \left(\frac{\mu^4}{GM\dot{M}^2} \right)^{1/7}. \tag{7.3}$$

The truncation radius is related to the classical Alfvén radius r_A as $r_t = \gamma_B^{2/7} 2^{1/7} r_A$, where

$$\begin{aligned} r_A &= (2G)^{-1/7} B_s^{4/7} M^{-1/7} \dot{M}^{-2/7} R_s^{12/7} \\ &= 31 \text{ km} \left(\frac{B_s}{10^8 \text{ G}} \right)^{4/7} \left(\frac{R_s}{10 \text{ km}} \right)^{12/7} \left(\frac{\dot{M}}{10^{16} \text{ g s}^{-1}} \right)^{-2/7} \left(\frac{M}{1.4 M_\odot} \right)^{-1/7}. \end{aligned} \tag{7.4}$$

Here $B_s = \mu/R_s^3$ is the magnetic field strength at the equator and R_s the neutron star radius.

At higher accretion rates the truncation radius will be closer to the neutron star surface. In this work we assume the disk to extend all the way down to the neutron star surface at the highest accretion rate. At the lowest accretion rate we assume the truncation radius to be at the co-rotation radius. Both radii are rough approximations as the true behaviour of the accretion disk truncation radius depends on uncertain aspects like disk/field coupling and the local magnetic field topology (Kulkarni & Romanova 2013; D'Angelo & Spruit 2012, 2010; Romanova et al. 2008). We discuss the effects and limitations of these assumptions in Section 7.4.3.

By identifying the highest and the lowest accretion rates with ongoing magnetic channelling (confirmed by the detection of pulsations), we estimate the magnetic field as outlined below.

For all sources we adopt the canonical neutron star mass of $M = 1.4\ M_\odot$ and radius $R_s = 10$ km. The value of γ_B is highly uncertain and depends on where the accretion disk is truncated. To be conservative we take γ_B to vary between a wide range of $0.01 - 1$ (Psaltis & Chakrabarty 1999).

- **Lower limit on μ:** At the highest accretion rates, to observe pulsations, the magnetic field must be at least high enough to truncate the accretion disk at or above the neutron star surface. Thus assuming $r_t = R_s$ we obtain the lower limit on the dipole moment as

$$\mu_{\min} = \gamma_B^{-1/2} (GM)^{1/4} \dot{M}_{\max}^{1/2} R_s^{7/4}, \tag{7.5}$$

  We assume the mass accretion rate can be estimated from the bolometric luminosity as $L = GM\dot{M}/R_s$, and estimate L from the observed luminosity in the X-ray band by applying a bolometric correction factor ($L = \epsilon_{\text{bol}} L_X$). The typical reported values of the bolometric correction factor have a range of $\epsilon_{\text{bol}} \sim 1 - 2$ (Gilfanov et al. 1998;

Galloway et al. 2002; Campana et al. 2003; Migliari & Fender 2006; Casella et al. 2008; Galloway et al. 2008). The mass accretion rate then follows as

$$\dot{M} = 10^{16}\ \mathrm{g\ s^{-1}} \left(\frac{\epsilon_{\mathrm{bol}} L_X}{1.87\times10^{36}\ \mathrm{erg\ s^{-1}}}\right)\left(\frac{M}{1.4\ M_\odot}\right)^{-1}\left(\frac{R_s}{10\ \mathrm{km}}\right). \tag{7.6}$$

Expressing the X-ray luminosity in terms of the observed X-ray flux and the assumed distance ($L_X = 4\pi d^2 F$), we obtain the lower limit on the magnetic moment

$$\begin{aligned}\mu_{\mathrm{min}} = {} & 9.36\times10^{24}\ \mathrm{G\ cm^{-3}} \left(\frac{\gamma_B}{1}\right)^{-1/2}\left(\frac{\epsilon_{\mathrm{bol}}}{1}\right)^{1/2} \\ & \times \left(\frac{F_{\mathrm{max}}}{10^{-10}\ \mathrm{erg\ cm^{-2}\ s^{-1}}}\right)^{1/2}\left(\frac{d}{10\ \mathrm{kpc}}\right) \\ & \times \left(\frac{M}{1.4\ M_\odot}\right)^{-1/4}\left(\frac{R_s}{10\ \mathrm{km}}\right)^{9/4},\end{aligned} \tag{7.7}$$

where F_{max} is the highest observed X-ray flux with pulsation and we adopted the boundary values of γ_B and ϵ_{bol} that give the lowest magnetic moment. For a detailed discussion of these assumptions we again refer to Section 7.4.

- **Upper limit on μ:** We assume magnetic channelling to be centrifugally inhibited if the accretion disk is outside the co-rotation radius

$$r_c = \left(\frac{\sqrt{GM}}{2\pi\nu_s}\right)^{2/3}, \tag{7.8}$$

where ν_s is the spin frequency. We then obtain an upper limit on the dipole moment by assuming that the truncation radius is at the co-rotation radius ($r_t = r_c$) for the lowest accretion rate with detected pulsations

$$\mu_{\mathrm{max}} = \gamma_B^{-1/2}(2\pi)^{-7/6}(GM)^{5/6}\dot{M}_{\mathrm{min}}^{1/2}\nu_s^{-7/6}. \tag{7.9}$$

By again substituting the expression for the mass accretion rate we obtain the upper limit on the magnetic dipole moment

$$\begin{aligned}\mu_{\mathrm{max}} = {} & 1.52\times10^{27}\ \mathrm{G\ cm^{-3}} \left(\frac{\gamma_B}{0.01}\right)^{-1/2}\left(\frac{\epsilon_{\mathrm{bol}}}{2}\right)^{1/2} \\ & \times \left(\frac{F_{\mathrm{min}}}{10^{-11}\ \mathrm{erg\ cm^{-2}\ s^{-1}}}\right)^{1/2}\left(\frac{d}{10\ \mathrm{kpc}}\right) \\ & \times \left(\frac{M}{1.4\ M_\odot}\right)^{1/3}\left(\frac{R_s}{10\ \mathrm{km}}\right)^{1/2}\left(\frac{\nu_s}{100\ \mathrm{Hz}}\right)^{-7/6},\end{aligned} \tag{7.10}$$

where F_{min} is the lowest observed X-ray flux with pulsation and we adopted the boundary values of γ_B and ϵ_{bol} that maximize the magnetic moment.

7.2.2 Data analysis

We analysed all AMXP outbursts observed with *RXTE*. The general structure of our analysis is as follows; for each *RXTE* observation we estimate the Crab normalized X-ray flux and then search for the presence of pulsations. We select the highest and lowest flux observations with detected pulsations, and from spectral analysis measure the source flux. Using these flux measurements and the best distance estimate from literature, we obtain limits on the magnetic dipole moment from eq. 7.7 and 7.10. These limits are expressed in terms of the magnetic dipole field strength at the equator ($B_p = \mu/r$), assuming a 10 km radius. The detailed procedure is outlined below.

7.2.2.1 Timing analysis

We initially estimate the 2–16 keV Crab normalised X-ray flux from the 16-second time-resolution Standard-2 data (see e.g. van Straaten et al. 2003 for details). To search for pulsations we consider the high time resolution GoodXenon or (122 μs) Event mode data of the same observation, selecting only those events in energy channels 5–37 ($\sim 2-16$ keV), which usually provides an optimal signal to noise ratio for the pulsations. The data were barycentred using the FTOOLS task *faxbary*, which also applies the *RXTE* fine clock corrections, thus allowing for timing analysis at an absolute precision of $\sim 4\mu s$ (Rots et al. 2004). We then take each ~ 3000 s continuous light curve (as set by the *RXTE* orbit), and fold it on the pulsar ephemeris (see appendix 7.A) to construct a pulse profile. For each profile we measure the amplitude at the fundamental frequency and that of its second harmonic (Hartman et al. 2008).

In standard procedures (see, e.g, Patruno & Watts 2012), a pulsation is usually said to be significant if the measured amplitude exceeds a detection threshold. This threshold is set as the amplitude for which there is only a small probability ϵ that one the of observations in an outburst exceeds it by chance. For observed amplitudes higher than this threshold we have a high confidence $\mathcal{C} = 1 - \epsilon$ that pulsations are detected ($\mathcal{C} = 99.7\%$). We can then consider the flux estimates associated with the significant pulse detections and straightforwardly select the observations of highest and lowest flux.

This approach is very conservative, as it sets a small joint false-alarm probability of detection for the entire outburst, in spite of the fact that we can be certain that pulsation are present in most observations. At the low flux end of the outburst, where the detection significance decreases with the count rate, this may cause us to miss pulsations.

To overcome this issue we first reduce the number of trials by comparing the observed total count rate of an observation with the X-ray background as estimated with the FTOOLS *pcabackest* (Jahoda et al. 2006). We then set a minimal count-rate threshold and reject all observation for which the pulse amplitude cannot be detected above the noise level assuming the expected source contribution is 100% modulated.

We then select all observations of an outburst that do not have significant pulsations according to the procedure described above. If the pulsar emission is indeed not present

in these observations, then the distribution of measured amplitudes and phases should correspond to the expected distribution of random noise, i.e. the phases should be uniform and the squared amplitude should follow a χ^2-distribution for two degrees of freedom. We compare the distributions using a KS-test, again with a 99.7% confidence level. If the data is not randomly distributed we take out the highest flux observation that has a significant pulse detection at the single trial level and whose phase is consistent with the expectation from the timing model, and iterate until the sample is consistent with being random. The last removed observation is then taken as the lowest observed flux with pulsations. We note that in practice the sensitivity of this iterative approach is limited by the small number of observations in the tail of an outburst and only rarely yields a lower flux pulse detection than through the initial procedure outlined above.

7.2.2.2 Spectral analysis

For the spectral analysis of selected observations we used HEASOFT version 6.12 and the calibration database (CALDB). Spectra were extracted from the Standard-2 data following the standard procedures outlined in the *RXTE* cookbook[2]. The background was again estimated using the FTOOLS task *pcabackest*. A dead-time correction was applied to the spectra following the prescription in the *RXTE* cookbook[3]. The spectral fits were done in the 3–20 keV energy range with XSPEC version 12.7.1.

From the measured flux we calculate the 3–20 keV X-ray luminosity and convert to the bolometric luminosity by multiplying with the correction factor $\epsilon_{\rm bol}$. The bolometric correction factor for a source depends on its spectral state, which in turn varies with accretion rate. The typical range of the bolometric correction factor is reported to be $\epsilon_{\rm bol} \sim 1-2$ (Gilfanov et al. 1998; Galloway et al. 2002; Campana et al. 2003; Migliari & Fender 2006; Casella et al. 2008; Galloway et al. 2008). To be conservative we use $\epsilon_{\rm bol} = 1$ when calculating $\mu_{\rm min}$ and $\epsilon_{\rm bol} = 2$ when calculating $\mu_{\rm max}$.

For many of the AMXPs considered here, there is considerable contaminating background emission in the observed X-ray flux, for instance from Galactic ridge emission. To estimate the background contamination, we also measured the bolometric luminosity for an observation in the tail of the outburst, where pulsations were not present and the light curve has asymptotically levelled off to a constant value. We assume that in such a state, accretion has ceased and the observed flux is purely due to background emission.

The details of the spectral fit parameters for different sources are presented in Appendix. 7.B.

[2] `http://heasarc.nasa.gov/docs/xte/recipes/cook_book.html`
[3] `http://heasarc.gsfc.nasa.gov/docs/xte/recipes/pca_deadtime.html`

Table 7.1: Flux range with pulsations of the analysed AMXPs in order of ascending spin frequency.

No	Name	Spin (Hz)	Maximum flux MJD	Maximum flux Flux (erg cm^{-2} s^{-1})	Minimum flux MJD	Minimum flux Flux (erg cm^{-2} s^{-1})	Background flux MJD	Background flux Flux (erg cm^{-2} s^{-1})
1	Swift J1756.9–2508	182	55026.1	6.30×10^{-10}	55032.5	1.99×10^{-10}	55037.0	4.07×10^{-11}
2	XTE J0929–314	185	52403.5	4.42×10^{-10}	52442.3	6.64×10^{-11}	–	–
3	XTE J1807.4–294	191	52697.6	8.19×10^{-10}	52808.7	3.51×10^{-10}	52816.8	7.25×10^{-11}
4	NGC 6440 X-2	206	55073.1	2.62×10^{-10}	55873.3	3.36×10^{-11}	55823.2	1.34×10^{-11}
5	IGR J17511–3057	245	55088.8	8.65×10^{-10}	55124.0	1.00×10^{-10}	55118.2	6.96×10^{-11}
6	XTE J1814–338	314	52814.3	4.41×10^{-10}	52844.1	6.00×10^{-11}	52852.9	1.00×10^{-12}
7	HETE J1900.1–2455	377	53559.5	1.15×10^{-9}	53573.8	3.84×10^{-10}	–	–
8	SAX J1808.4–3658	401	52563.2	1.85×10^{-9}	50936.8	2.82×10^{-11}	50935.1	1.21×10^{-11}
9	IGR J17498–2921	401	55789.6	1.13×10^{-9}	55818.3	4.44×10^{-10}	55826.4	4.23×10^{-10}
10	XTE J1751–305	435	52368.7	1.50×10^{-9}	52377.5	3.97×10^{-10}	52380.7	6.51×10^{-11}
11	SAX J1748.9–2021	442	55222.5	4.13×10^{-9}	52198.3	2.96×10^{-9}	55254.6	1.88×10^{-11}
12	Swift J1749.4–2807	518	55300.9	5.24×10^{-10}	55306.7	2.67×10^{-10}	55307.7	2.41×10^{-10}
13	Aql X-1	550	50882.0	8.74×10^{-9}	50882.0	8.74×10^{-9}	50939.8	1.34×10^{-11}
14	IGR J00291+5934	599	53342.3	9.70×10^{-10}	53352.9	1.09×10^{-10}	53359.5	5.76×10^{-11}

Note. For each source we give the minumum and maximum flux with pulsations. We also give the corresponding 3–20 keV background flux used in calculating the magnetic dipole moment and the MJD of the analysed observations.

Table 7.2: The magnetic field strength estimates (equatorial surface field) of all considered AMXPs.

No	Name	Spin (Hz)	Distance (kpc)	Background corrected	$B_{\rm min}$ (10^8 G)	$B_{\rm max}$ (10^8 G)	$B_{\rm K,max}$ (10^8 G)	B_L (10^8 G)	ref.
1	Swift J1756.9–2508	182	8	y	0.18	24.1	7.2	$0.4-9$	a
2	XTE J0929–314	185	6	n	0.12	11.5	3.4	–	
3	XTE J1807.4–294	191	4.4	n	0.11	18.6	5.4	–	
4	NGC 6440 X-2	206	8.2	y	0.12	7.6	2.1	–	
5	IGR J17511–3057	245	7	n	0.19	11.8	3.1	–	
6	XTE J1814–338	314	8	y	0.16	7.8	1.8	$\lesssim 5-10$	b
7	HETE J1900.1–2455	377	5	n	0.16	10.0	2.1	–	
8	SAX J1808.4–3658	401	3.5	n	0.14	1.77	0.36	$0.7-1.5$	c
9	IGR J17498–2921	401	8	n	0.20	16.0	3.2	–	
10	XTE J1751–305	435	7	y	0.25	11.0	2.1	$3.3-4.7$	d
11	SAX J1748.9–2021	442	8.2	y	0.49	37.8	7.2	–	
12	Swift J1749.4–2807	518	6.7	n	0.11	7.7	1.4	–	
13	Aql X-1	550	5	y	0.44	30.7	5.3	$\lesssim 9$	e
14	IGR J00291+5934	599	3	n	0.085	1.9	0.31	$1.5-2.0$	f

(a) Patruno et al. (2010a), (b) Watts et al. (2008); Papitto et al. (2007); Haskell & Patruno (2011), (c) Patruno et al. (2012), (d) Riggio et al. (2011a), (e) Di Salvo & Burderi (2003), (f) Patruno (2010).

Note. The values $B_{\rm min}$ and $B_{\rm max}$ correspond to field strengths estimated using eq. 7.7 and eq. 7.10. The values $B_{\rm K}$ are upper limits to the field strength computed using eq. 7.12 following the modified expression of truncation radius as obtained by Kulkarni & Romanova (2013) (see Sec. 7.4.3). B_L are field strength measurements from literature (see references). The background correction column indicates if the background estimate (Table 7.1) was used when calculating the upper limit on the magnetic field estimate (see, e.g, Sec. 7.3.3).

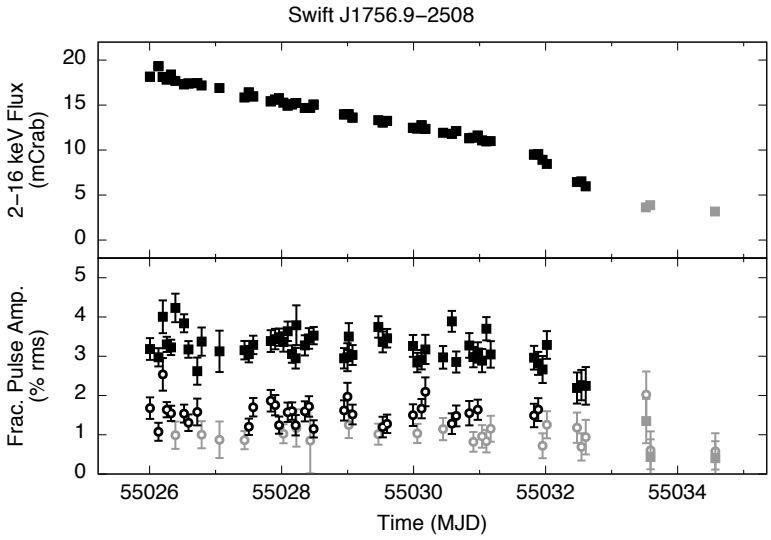

Figure 7.1: Upper panel: Light curve of the 2009 outburst of Swift J1756.9–2508 normalised to mCrab. Lower panel: pulse amplitude of the fundamental (squares) and the second harmonic (open circles). The observations with a significant detection (with 99.7% confidence limit) of pulsations are marked with black, observations without a significant detection of pulsations are shown in grey.

7.3 Results

In the following sections we present the magnetic field estimates we obtained from the timing and spectral analysis of all AMXPs observed with *RXTE*. For each source we briefly describe the outburst history, distance estimates and discuss specific details of our analysis. All results are summarized in Tables 7.1 and 7.2.

7.3.1 Swift J1756.9–2508

Swift J1756.9–2508 was first discovered with *Swift* in June 2007 (Krimm et al. 2007b,a), and 182 Hz pulsations were found with follow-up *RXTE* observations (Markwardt et al. 2007). The source showed a second outburst in July 2009 (Patruno et al. 2009b, 2010a).

We find both the highest and lowest flux with pulsations to occur during the 2009 outburst (Fig. 7.1), with a detection of pulsation for the outburst peak luminosity at MJD 55026.1 and lowest flux detection on MJD 55032.5, just before the light curve decays to the background level. The background contribution was measured from the last observation on MJD 55037.0.

The distance to the source is not known, but considering its close proximity to the

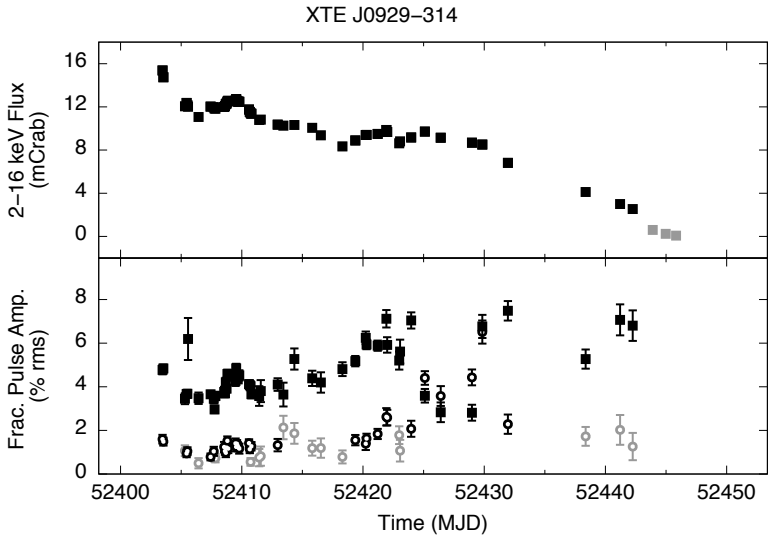

Figure 7.2: Light curve of the 2002 outburst of XTE J0929–314. Legends are same as in Figure 7.1.

Galactic centre (Krimm et al. 2007b), we assume a distance of 8 kpc. We then obtain a magnetic field range of 1.8×10^7 G $< B < 2.4 \times 10^9$ G.

7.3.2 XTE J0929–314

XTE J0929–314 was discovered in April 2002 with *RXTE*, and the 185 Hz pulsations were immediately detected (Remillard 2002; Remillard et al. 2002). The source has been detected in outburst only once, with the light curve shown in Figure 7.2.

XTE J0929–314 is significantly away from the Galactic plane (Galactic coordinates: $260.1^\circ, 14.2^\circ$) and shows a low neutral hydrogen column density ($\sim 7.6 \times 10^{20}$ cm^{-2}, Juett et al. 2003). The background contribution for this source is therefore negligibly low, and indeed could not be measured as the non-pulsating observations at the end of the outburst, which have too few counts to constrain the spectrum.

There are no good estimates of the distance to the source, with the only constraint claiming $d \gtrsim 6$ kpc based on estimates of average accretion rate Galloway et al. (2002). Using this distance we obtain a magnetic field range of 1.2×10^7 G $< B < 1.2 \times 10^9$ G.

7.3.3 XTE J1807.4–294

XTE J1807.4–294 was discovered in February 2003 (Markwardt et al. 2003) and the 191 Hz pulsations were immediately found with the *RXTE* observations. The source has been in outburst only once. We find the highest and lowest flux with pulsations to occur on MJD 52697.6 and MJD 52808.7, respectively (Fig. 7.3).

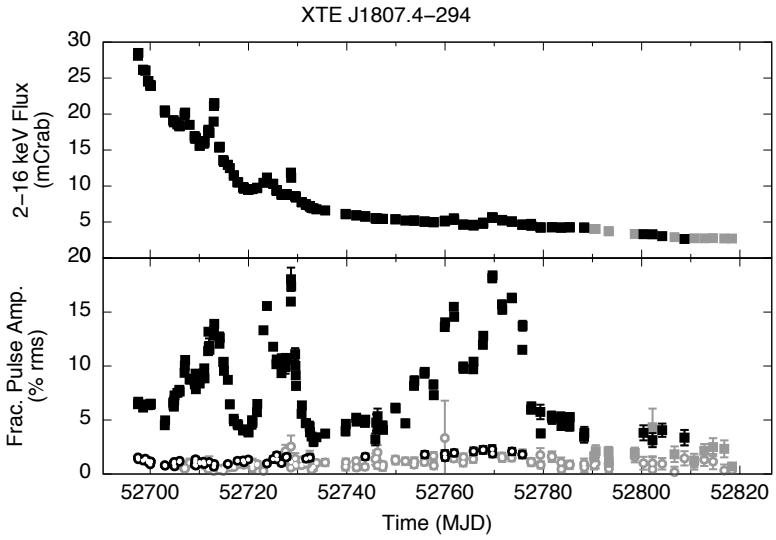

Figure 7.3: Light curve of the 2003 outburst of XTE J1807.4–294. Legends are same as in Figure 7.1.

We measured the background contribution on MJD 52816.8, but note that this background level is similar to the lowest flux with pulsations, such that the uncertainty in the background estimation is larger than the apparent source contribution. To be conservative we calculate the upper limit to the magnetic moment without adjusting for the background. This implies that we take the low flux observation as an upper limit to the true lowest flux at which pulsations are present. If the presence of pulsations can be established at a lower flux level, the upper limit will decrease, thus tightening the allowed magnetic field range.

There are no well defined estimates for the distance to this source. Some authors assume the source is near the Galactic centre (Falanga et al. 2005b; Campana et al. 2003), and take the distance to be $\sim$ 8 kpc. Others, however, estimate the distance at $\sim$ 4.4 kpc (Riggio et al. 2008), by comparing the observed flux to the accretion rate inferred from the pulse timing analysis. Lacking a more robust estimation of the distance, we adopt a distance of 4.4 kpc. We then arrive at a magnetic field range estimate of 1.1×10^7 G $< B < 1.9 \times 10^9$ G.

7.3.4 NGC 6440 X-2

NGC 6440 X-2 is located in the globular cluster NGC 6440 and was detected serendipitously with *Chandra* in July 2009 (Heinke et al. 2009, 2010). Pulsations at 206 Hz were discovered from subsequent *RXTE* observations (Altamirano et al. 2009, 2010d).

The outburst behaviour of NGC 6440 X-2 is atypical, as it shows brief outbursts of

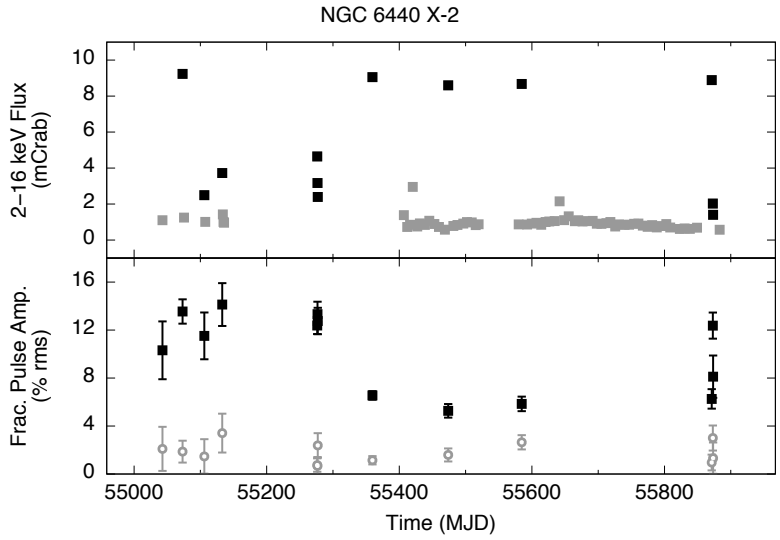

Figure 7.4: Light curve of NGC 6440 X-2 from July, 2009 to November, 2011. Legends are same as in Figure 7.1.

a few days with a recurrence time as short as one month (see Figure 7.4). Due to the high-cadence monitoring of this globular cluster, the background level is well established between MJD 55700–55850. We estimate the background flux on MJD 55823.2.

The distance to the cluster NGC 6440 is well constrained to $d = 8.2$ kpc (Valenti et al. 2007), and gives a magnetic field range of 1.2×10^7 G $< B < 7.6 \times 10^8$ G.

7.3.5 IGR J17511–3057

IGR J17511–3057 was discovered with *INTEGRAL* in September 2009 (Baldovin et al. 2009), with subsequent *RXTE* observations discovering 245 Hz pulsations (Markwardt et al. 2009b).

The outburst light curve shows a notable flare after MJD 55110 (Fig. 7.5) which is attributed to simultaneous activity of XTE J1751–305 (Falanga et al. 2011). Pulsations are observed throughout the outburst, and reoccur on MJD 55124.0, some 10 days after the source appears to have reached the background level. We select this observation as the lowest flux observation with pulsations, and select the observation on MJD 55118.2 for the background flux. Since the flux difference between these observations is very small (Table 7.1, we consider the low flux observation to be background dominated and, like in Section 7.3.3, neglect the background measurement in calculating the upper limit on the magnetic moment to obtain a more conservative estimate of the magnetic field strength.

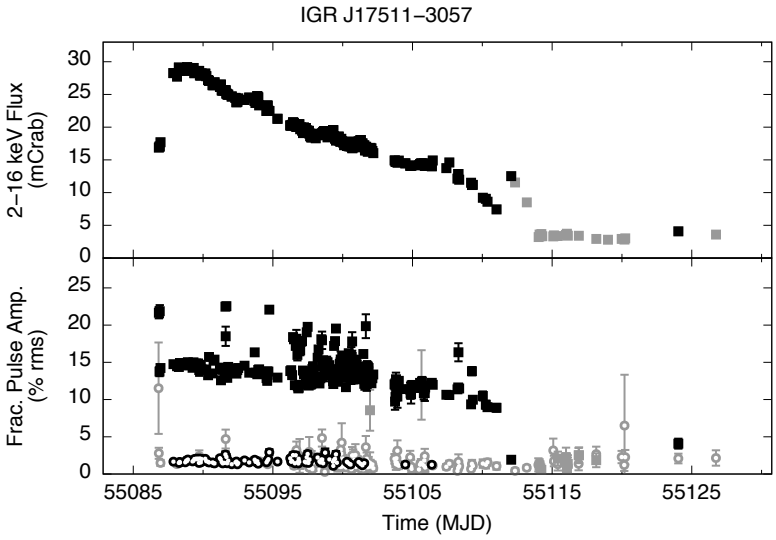

Figure 7.5: Light curve of the 2009 outburst of IGR J17511–3057. Legends are same as in Figure 7.1.

The distance to this source is estimated at $\lesssim 7$ kpc, derived by assuming the type I X-ray bursts are Eddington limited (Altamirano et al. 2010b; Papitto et al. 2010). Adopting this distance we obtain a magnetic field range of 1.9×10^7 G $< B < 1.2 \times 10^9$ G.

7.3.6 XTE J1814–338

XTE J1814–338 was discovered in June 2003 with *RXTE* and immediately recognized as a 314 Hz pulsar (Markwardt & Swank 2003). It has been detected in outburst only once, and shows pulsations throughout its outburst (Fig. 7.6).

We measured the background flux from the observation on MJD 52852.9, one of the last *RXTE* observations of the outburst.

The distance to the source is estimated at $\lesssim 8$ kpc, by assuming the measured luminosity during the type I X-ray burst is Eddington limited (Strohmayer et al. 2003). The resulting magnetic field range is 1.6×10^7 G $< B < 7.8 \times 10^8$ G.

7.3.7 HETE J1900.1–2455

HETE J1900.1–2455 was discovered through a bright type I X-ray burst observed with the *High Energy Transient Explorer 2* (*HETE-2*) in June, 2005 (Vanderspek et al. 2005) and 377 Hz pulsations were observed with *RXTE* quickly thereafter (Morgan et al. 2005; Kaaret et al. 2006). Unlike the other AMXPs, which show outbursts that last for weeks to months, HETE J1900.1–2455 has been active since discovery and is yet to return to

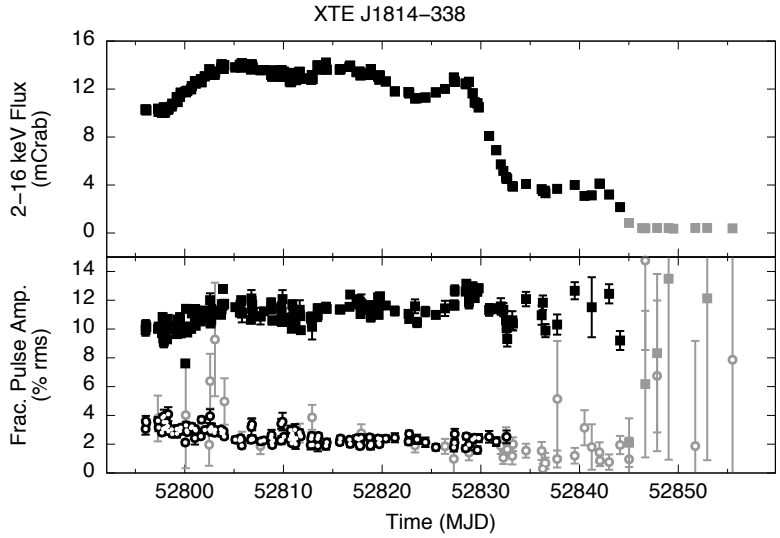

Figure 7.6: Light curve of the 2003 outburst of XTE J1814–338. Legends are same as in Figure 7.1.

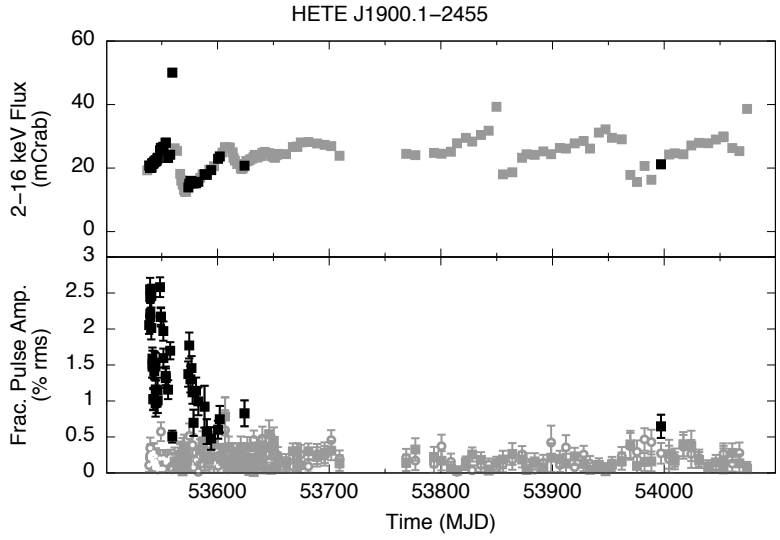

Figure 7.7: Light curve of HETE J1900.1–2455 from June 2005 to January 2007. Legends are same as in Figure 7.1. Note that there are additional pulse detections beyond ∼ 54000, however, these are tentative (Patruno 2012) and do not change the measured flux range.

quiescence. Persistent pulsations have been reported to occur during the first 20 days of the outburst, after which only intermittent pulsations have been seen (Patruno 2012).

We have analysed all archival *RXTE* observations of this source and find that the observations of highest and lowest flux with pulsations are on MJD 53559.5 and MJD 53573.8, respectively.

Since the source has shown continuous activity since its discovery, there is no observation during quiescence from which the background flux can be estimated. However, as the source is well away from the Galactic centre (Galactic coordinates: $l = 11.3°, b = -12.9°$), the background flux is expected to be comparatively small. We therefore neglect the background contribution for this source, noting again that this leads us to slightly overestimate the source flux, which yields a less stringent constraint on $\mu_{\max}$.

The distance to the source is taken to be $d \sim 5$ kpc, based on photospheric radius expansion of a type I X-ray burst (Kawai & Suzuki 2005). The magnetic field range obtained is 1.6×10^7 G $< B < 1.0 \times 10^9$ G.

7.3.8 SAX J1808.4–3658

SAX J1808.4–3658 was discovered with *BeppoSax* in in 1996 (in 't Zand et al. 1998) and the detection of 401 Hz pulsations in 1998 with *RXTE* made it the first known AMXP (Wijnands & van der Klis 1998a). SAX J1808.4–3658 has been observed in outbursts with *RXTE* six times (Bult & van der Klis 2015b, see Chapter 4).

We find the highest flux with pulsations to be in the 2002 outburst on MJD 52563.2 and the lowest flux with pulsations in the 1998 outburst on MJD 50936.8. The lowest flux with pulsations is observed toward the end of the 1998 outburst (Fig. 7.8). Although the flux of this observation is only slightly higher than that of the background observations, the pulse detection is very significant and yields a phase that is consistent with the timing model of this outburst. If pulsations are still present at the same amplitude in the other low flux observations, we would not be able to detect them due to the low count rate. We therefore consider the low flux observation with pulsations to be background dominated.

The distance to SAX J1808.4–3658 is $d = 3.5$ kpc, and was derived from photospheric radius expansion in type I X-ray bursts Galloway & Cumming (2006). With this distance we obtain a magnetic field range of 1.4×10^7 G $< B < 1.8 \times 10^8$ G.

7.3.9 IGR J17498–2921

IGR J17498–2921 was discovered in August, 2011 with *INTEGRAL* (Gibaud et al. 2011), following which pulsations at 401 Hz were reported by Papitto et al. (2011b). The light curve of this outburst is shown in Figure 7.9.

Since the source is close to the Galactic centre (Galactic coordinates: $l = 0.16°, b = -1°$), the observations have a large X-ray background contamination, with the lowest observed flux with pulsations again background dominated.

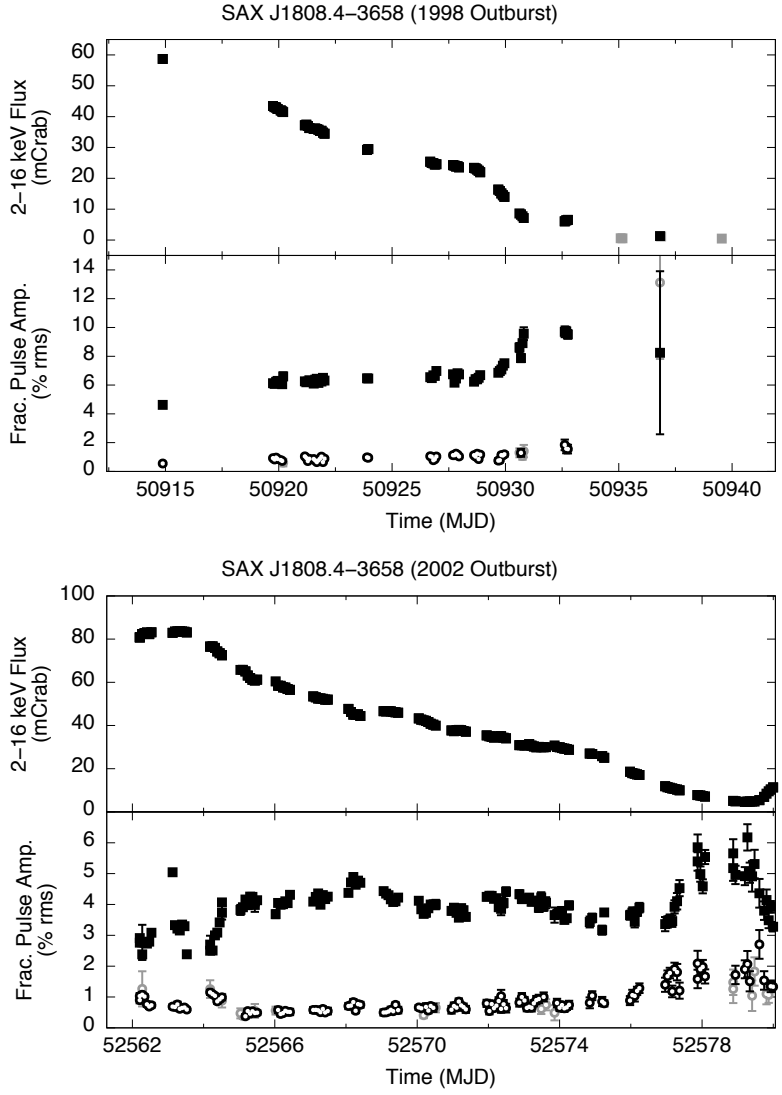

Figure 7.8: Light curve of the 1998 and 2002 outbursts of SAX J1808.4–3658. Legends are same as in Figure 7.1.

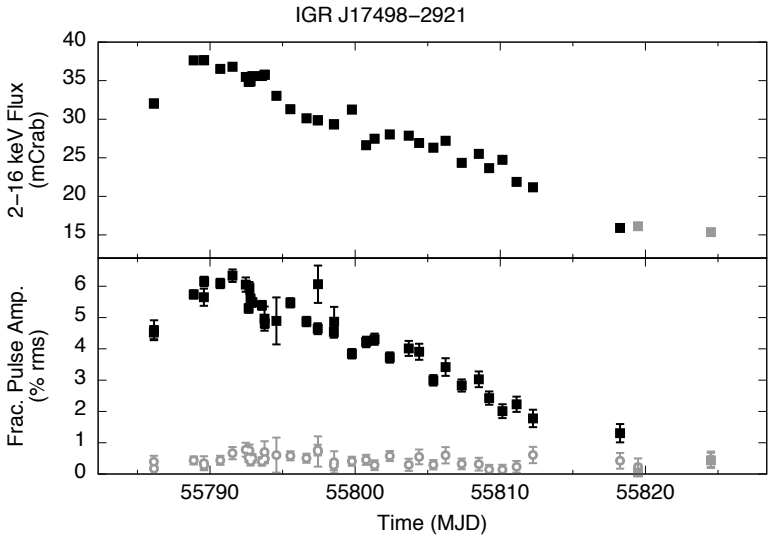

Figure 7.9: Light curve of the 2011 outburst of IGR J17498–2921. Legends are same as in Figure 7.1.

The distance to IGR J17498–2921 is estimated at ~ 8 kpc, based on photospheric radius expansion during a type I X-ray burst (Falanga et al. 2012). We then find a magnetic field range of 2.0×10^7 G $< B < 1.6 \times 10^9$ G.

7.3.10 XTE J1751–305

XTE J1751–305 and its 435 Hz pulsations were discovered with *RXTE* in April 2002 (Markwardt et al. 2002a). A brief second outburst was detected in 2009 (Markwardt et al. 2009a), which was coincident with on-going activity of IGR J17511–3057 in the same field of view. Since *RXTE* is not an imaging detector, the flux contribution of these two sources cannot be separated, so we restricted our analysis to the 2002 outburst of XTE J1751–305 only.

We estimate the background from the last *RXTE* observation on MJD 52380.7, when the pulsations were no longer detected (see Figure 7.10).

The distance to this source is not well-defined. Markwardt et al. (2002a) constrain the distance to $\gtrsim 7$ kpc by equating predicted mass transfer rates (Rappaport et al. 1983; King et al. 1997) to values inferred from X-ray observations. Papitto et al. (2008) instead compare the spin-frequency derivative to models for angular momentum exchange (Rappaport et al. 2004), and so constrain the distance to 6.7−8.5 kpc. For our analysis, we take a distance of 7 kpc, which results in a magnetic field range of 2.5×10^7 G $< B < 1.1 \times 10^9$ G.

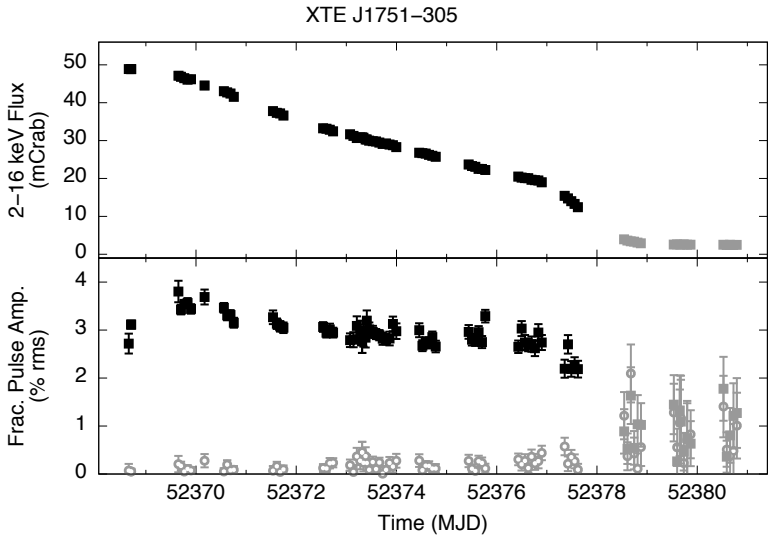

Figure 7.10: Light curve of the 2002 outburst of XTE J751–305. Legends are same as in Figure 7.1.

7.3.11 SAX J1748.9–2021

SAX J1748.9–2021 is located in the globular cluster NGC 6440 (in 't Zand et al. 1999), and was observed in outburst by *RXTE* in 1998, 2001, 2005 and 2010 (in 't Zand et al. 1999; in 't Zand et al. 2001; Markwardt & Swank 2005; Patruno et al. 2010c). Among these outbursts 442 Hz intermittent pulsations have been detected in 2001, 2005 and 2010 (Gavriil et al. 2007; Altamirano et al. 2008a; Patruno et al. 2010c).

We find that the highest flux with pulsations occurs during the 2010 outburst on MJD 55222.5, while the lowest flux with pulsations is seen in the 2001 outburst on MJD 52198.3 (light curves shown in Figure 7.11).

As the source is associated with a globular cluster, its distance is comparatively well constrained to 8.2 kpc (Valenti et al. 2007). We find a magnetic field range of 4.9×10^7 G $< B < 3.8 \times 10^9$ G.

7.3.12 Swift J1749.4–2807

Swift J1749.4–2807 was first detected in June 2006 (Schady et al. 2006), but its 518 Hz pulsations were not found until the second outburst in April, 2010 (Altamirano et al. 2010c, 2011). We find both the highest and lowest flux with pulsations occur in this second outburst on MJD 55300.9 and 55306.7, respectively.

The source is located close to the Galactic centre and has a strong contaminating X-ray background flux. The absence of pulsations (Fig. 7.12) indicate that the source was no longer accreting for the last three *RXTE* observations (> MJD 55307), which

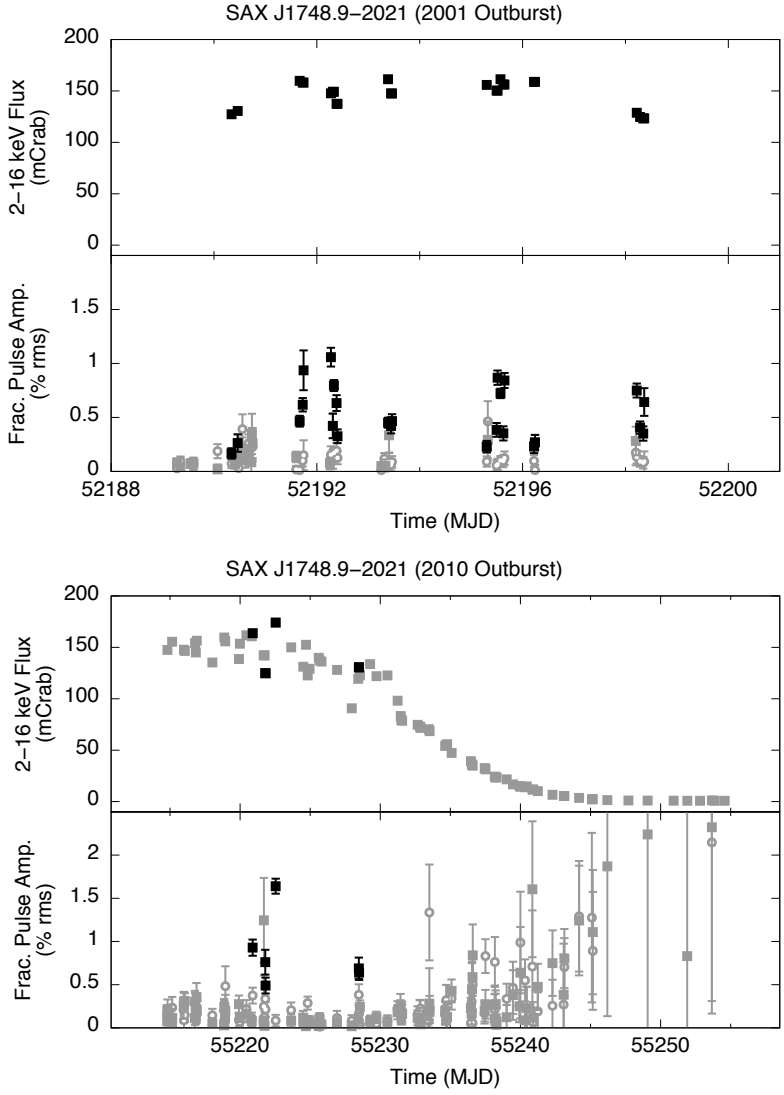

Figure 7.11: Light curves of the 2001 and 2010 outbursts of SAX J1748.9–2021. Legends are same as in Figure 7.1.

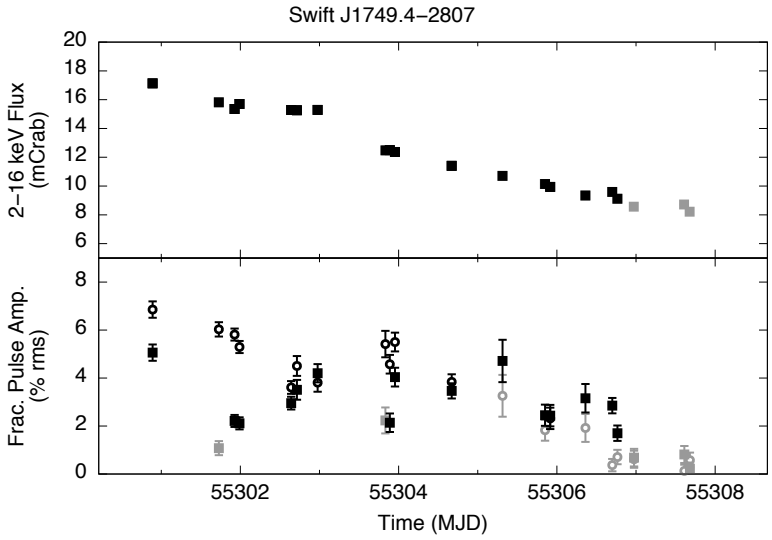

Figure 7.12: Light curve of the 2010 outburst of Swift J1749.4–2807. Legends are same as in Figure 7.1.

is confirmed by a source non-detection with both *Swift* and *INTEGRAL* (Ferrigno et al. 2011). We therefore use the last *RXTE* observation to measure the background flux. As this background flux is comparable to the lowest observed flux with pulsations, we cannot confidently estimate the source contribution and to be conservative we again calculate the upper limit on the magnetic field without using the background.

The distance to the source is $d = 6.7 \pm 1.3$ kpc, which was inferred from the luminosity of a suspected type I X-ray burst (Wijnands et al. 2009). Adopting the central value for the distance and the measured flux we obtain a magnetic field range of 1.1×10^7 G $< B < 7.7 \times 10^8$ G.

7.3.13 Aql X-1

In 18 outbursts across $\sim$ 15 years, Aql X-1 has shown its 550 Hz pulsations only for a single episode of about 150 seconds (Casella et al. 2008; Messenger & Patruno 2015). Hence we cannot measure a flux range for the presence of pulsations for this source. Instead we calculate both lower and upper limits on the magnetic field from the same measured flux, thus obtaining a very conservative estimate of the allowed magnetic field range.

The distance to the source is $4.4 - 5.9$ kpc and was obtained from a photospheric radius expansion during a type I X-ray (Jonker & Nelemans 2004). For a distance of 5 kpc and the measured flux we obtain a magnetic field range of 4.4×10^7 G $< B < 3.1 \times 10^9$ G.

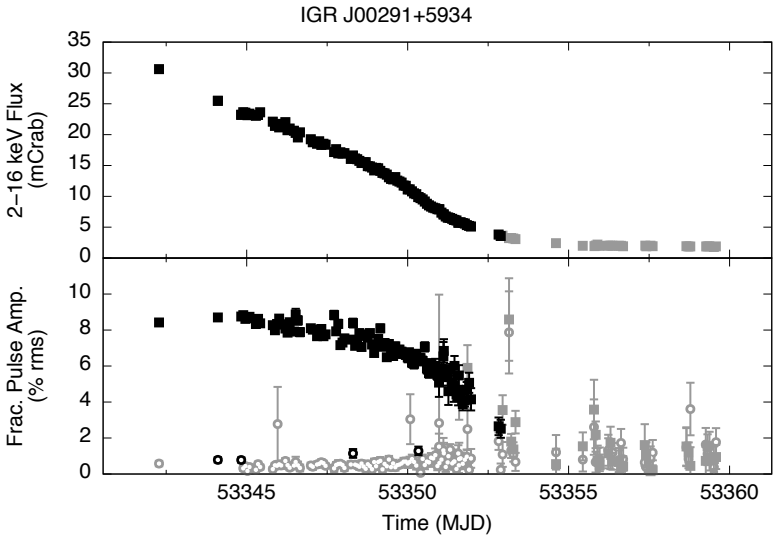

Figure 7.13: Light curve of the 2004 outburst of IGR J00291+5934. Legends are the same as in Figure 7.1.

7.3.14 IGR J00291+5934

IGR J00291+5934 was discovered with *INTEGRAL* in December 2004 (Eckert et al. 2004; Shaw et al. 2005) and its 599 Hz pulsations were detected in follow-up *RXTE* observations (Markwardt et al. 2004). Outbursts were detected again in August and September 2008 (Chakrabarty et al. 2008; Lewis et al. 2008). We find both the highest and the lowest flux with pulsations occur in the 2004 outburst.

It is evident from the light curve (Fig. 7.13) that the source gradually decays to the background level, which is due to an intermediate polar in the same field of view (Falanga et al. 2005a). Because the lowest flux with pulsations is again comparable to the estimated background flux, we assume the low flux observation is background dominated to get a more conservative magnetic field estimate.

The distance to IGR J00291+5934 has been estimated in several ways. From the long term average accretion rate, Galloway et al. (2005) constrain the distance to $\lesssim$ 4 kpc. Comparing the observed quiescent flux to that of SAX J1808.4–3658, Jonker et al. (2005) estimate the distance to be $2 - 3.6$ kpc. Similar estimates were also obtained by Torres et al. (2008), who report $d = 1.8 - 3.8$ kpc by modeling the light curve. In this work we adopt the central distance of $d = 3$ kpc, which gives a magnetic field range of 8.5×10^6 G $< B < 1.9 \times 10^8$ G.

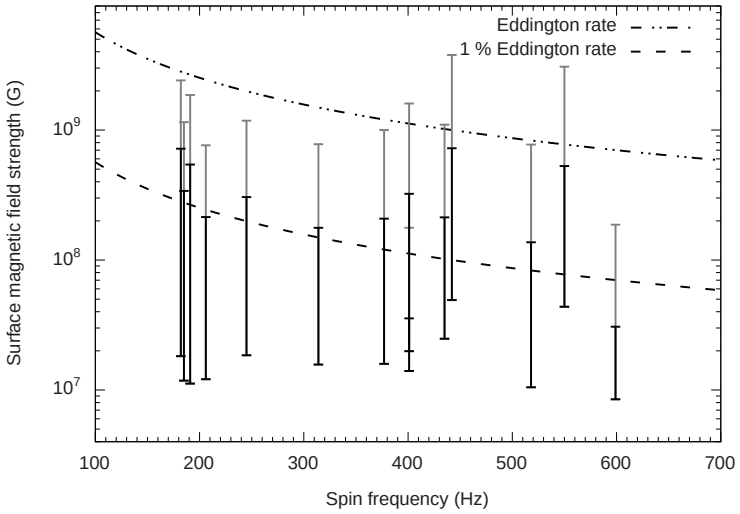

Figure 7.14: Magnetic field vs spin frequency for AMXPs analysed in this work. The grey lines show the range of estimated field strengths of the sources from Table. 7.2. The black lines represent the revised upper limits following eq. 7.11 which gives tighter constraints of the field strength estimates. The dashed and dashed-dotted curves show the equilibrium spin rate for two different accretion rates.

7.4 Discussion

In this section we discuss the various sources of uncertainty involved in the magnetic field estimates presented in this work.

7.4.1 Distance estimates

The largest uncertainties in our field estimates are due to poor constraints on the distance. Errors in the distance affect the luminosity estimates and cause a systematic uncertainty that scales both the upper and lower limit by the same factor ($B_{\mathrm{min/max}} \propto d$). The sources associated with globular clusters are not greatly affected by this uncertainty as they have well measured distances. Some AMXPs exhibit thermonuclear bursts with photospheric radius expansion, which allows for tight constraints on the distance. For the remaining sources, however the distance measurements are less certain and the resulting systematic uncertainty has a more prominent role. In Table 7.2 we explicitly report the distances used in calculating the upper and lower limits, such that our estimates can be easily adjusted should a more accurate measure distance be obtained for one of these sources.

7.4.2 Masses and radii of AMXPs

Currently there are no reliable estimates available for the masses or radii of AMXPs. In calculating the field strengths presented in Table 7.2 we assumed the neutron stars to be of canonical mass $M \sim 1.4 M_\odot$ and radius ~ 10 km. However, theoretical calculations of mass-radii relations (e.g. Lattimer & Prakash 2001; Lattimer 2014) predict that both parameters may vary over a wide range of $M \sim 0.2 - 2.9 M_\odot$ and $R \sim 10 - 15$ km.

For a more massive neutron star of $\sim 2 M_\odot$ the upper limit on the magnetic dipole moment will increase by $\sim 12.6\%$ ($\mu_{\rm max} \propto M^{1/3}$), whereas the lower limit will decrease by 8.2% ($\mu_{\rm min} \propto M^{-1/4}$) from the values reported in Table 7.2, resulting in a broadening of the estimated range.

For a neutron star of larger radius, e.g. ~ 15 km, the upper limit on the magnetic dipole moment will scale as $\mu_{\rm max} \propto R^{1/2}$, causing an increase of 22.5% with respect to the values we report. The lower limit to the magnetic dipole moment scales with radius as $\mu_{\rm min} \propto R^{9/4}$, such that assuming a 15 km radius increases the lower limit by 149%. For a $R = 15$ km neutron star we then find that the allowed range of magnetic field strength moves to higher values and covers a slightly broader range[4].

7.4.3 Disk-magnetosphere interaction

In this paper we made the assumption that the neutron star magnetic field is dipolar in nature, which may not be valid. Near the truncation radius the pressure the disk exerts on the magnetosphere can affect the field geometry, and near the neutron star surface this may be further complicated by higher multipole moments that could dominate over the dipole component. We parametrized the effect of the field shape with the factor γ_B (see eq. 7.3), which we assumed to vary over a wide range of $0.01 - 1$ to account for such uncertainties. This range is consistent with the results of numerical simulations, which suggest the largest range of truncation radii is $r_t \sim (0.5 - 1.2) r_A$ (Zanni & Ferreira 2009; Romanova et al. 2008), implying $\gamma_B \simeq 0.06 - 1.3$.

- Recent MHD simulations (Zanni & Ferreira 2013; Kulkarni & Romanova 2013; Long et al. 2008; Romanova et al. 2008) have confirmed that complex field topologies arise at the inner edge of the disk. Kulkarni & Romanova (2013) show that if the truncation radius is in the range $2.5 R_s < r_t < 5 R_s$, the non-dipolar field structure results in a modified expression of the truncation radius

$$r_t = 1.06 R_s \left(\frac{\mu^4}{G M \dot{M}^2 R_s^7} \right)^{1/10} \tag{7.11}$$

  This modification is relevant when estimating the upper limit to the magnetic field, for which we take the disk to be truncated at the co-rotation radius, which normally falls

[4] The field strength range covers more than an order of magnitude, so despite the large fractional change, the absolute shift of the lower limit is smaller than that of the upper limit.

within the range of radii where eq. 7.11 is applicable. Using this expression for the truncation radius we obtain a modified boundary layer parameter as

$$\widetilde{\gamma}_B = 0.0616 \left(\frac{\nu_s}{100\ \mathrm{Hz}}\right) \left(\frac{M}{1.4\ M_\odot}\right)^{-1/2} \left(\frac{R_s}{10\ \mathrm{km}}\right)^{3/2} \tag{7.12}$$

which, instead of conservatively assuming 0.01, may be used in eq. 7.10 to obtain a more constraining upper limit on the magnetic dipole moment.

- Near the neutron star surface higher multipole moments of the magnetic field may be stronger than the dipole component. As shown in numerical studies (Long et al. 2007, 2008) such complex non-dipolar field configurations strongly affect the inner accretion geometry, but the effect on γ_B is not well established. If further theoretical considerations can constrain γ_B to a smaller value than our conservative assumption of $\gamma_B = 1$, then this could be used to tighten the lower limit on the magnetic field strength ($B_{\mathrm{min}} \propto \gamma_B^{-1/2}$).

In Figure 7.14 we plot the conservative ranges of the surface field strength following the analysis in Section 7.2.1 in grey and present the more constraining estimates based on eq. 7.12 in black. The dashed lines represent the equilibrium spin (Alfvén radius at co-rotation) for a mean long term accretion rate

$$\nu_{\mathrm{eq}} = 441\ \mathrm{Hz} \left(\frac{B_s}{10^9\ \mathrm{G}}\right)^{-6/7} \left(\frac{R_s}{10\ \mathrm{km}}\right)^{-18/7} \left(\frac{\dot{M}}{\dot{M}_E}\right)^{3/7} \left(\frac{M}{1.4\ M_\odot}\right)^{5/7} \tag{7.13}$$

where $\dot{M}_E = 1.5 \times 10^{-8}\ M_\odot\ \mathrm{yr}^{-1}$ is the Eddington accretion rate.

- In our analysis we assumed that channeled accretion onto the neutron star can only take place when the disk is truncated inside the co-rotation radius. However, the large range of X-ray luminosities, and accordingly mass accretion rates, observed for AMXPs suggests that mass accretion onto the neutron star might persist even when the inner edge of the disk moves outside the co-rotation radius (see e.g. Rappaport et al. 2004), which indeed appears to be confirmed by observation (Bult & van der Klis 2015a, see Chapter 5).

  As pointed out by Spruit & Taam (1993) the inner edge of the disk must have receded to $r_t \sim 1.3\ r_c$ before the centrifugal force is strong enough to accelerate matter beyond the escape velocity and thus drive an outflow. If we consider the possibility that accretion may still occur for radii up-to $1.3\ r_c$, then we find that the upper limit to the magnetic field strength increases by 58% ($B_{\mathrm{max}} \propto (r_t/r_c)^{7/4}$) at most. The lower limit, being independent of the co-rotation radius, is unaffected.

7.4.4 Observational sampling

- In order to determine the upper limit to the magnetic field strength we consider the lowest observed flux for which pulsations are significantly detected. However, as the

flux decays, the signal-to-noise ratio also decreases, such that the non-detection of pulsations could be due to limited statistics. That is, the pulsations may persist below our detection limit. This concern is particularly relevant to XTE J1807.4–294, IGR J17498–2921, and IGR J17511–3057 in which pulsations are detected at approximately the same flux as the background level. If pulsations are still present at a very low level, and accretion is ongoing at even lower luminosities, then our estimates for these sources are overly conservative as we are overestimating the upper limit to the magnetic field strength. Since $B_{\rm max} \propto L^{1/2}$, a future detection of pulsations at a lower luminosity than reported in this work can therefore be used to further constrain the range of magnetic field strengths. This is especially relevant for other X-ray satellites that have better sensitivity and a lower background contamination such as XMM-Newton, or for a future ASTROSAT (Agrawal 2006; Singh et al. 2014) or LOFT (Feroci et al. 2012) mission.

- For the lower limit to the magnetic field strength we use the highest observed flux for which pulsations are detected. As we note in Section 7.2 the pulsations are expected to disappear at high flux when the disk extends to the neutron star surface, yet this is never observed. For all sources the highest observed flux considered always shows pulsations, which implies that the inner edge of the disk never extends down to the neutron star surface. Indeed some of the better sampled AMXPs (e.g. SAX J1808.4–3658 and IGR J00291+5934) show peak luminosities that vary by a factor of 2 between outbursts. If a future outburst reaches a higher peak luminosity than considered in this work, it will increase the lower limit as $B_{\rm min} \propto L^{1/2}$ and thus further constrain the allowed range of magnetic field strength.

7.4.5 Luminosity estimates

- To calculate the flux we consider the 3–20 keV X-ray band, which we convert to the bolometric flux by applying a correction factor (Gilfanov et al. 1998; Casella et al. 2008; Galloway et al. 2002; Campana et al. 2003). To be conservative in our estimates of the field strength we used a $\epsilon_{\rm bol} = 2$ for the upper limit and $\epsilon_{\rm bol} = 1$ for the lower limit. However, if the correction factor is well constrained then this approach is overly pessimistic. For many accretion powered pulsars the correction factor tends to be within $\sim 10\%$ of 2 (Galloway et al. 2008), such that the error introduced in the magnetic field estimate is only $\sim 2\%$ ($B_{\rm max} \propto (\epsilon_{\rm bol}/2)^{1/2}$, $B_{\rm min} \propto (\epsilon_{\rm bol}/1)^{1/2}$). If we adopt the same bolometric correction factor for the lower limit also, it we find the our estimates can improve by up-to $\lesssim 30\%$.

- Another source of uncertainty comes from the background contribution to the measured flux. We estimate the background contribution from the *RXTE* observations at the end of an outburst, when the source no longer shows pulsations and has presumably returned to quiescence. If this estimate contains residual source emission, or the

background contribution itself is variable, then this approach introduces an error in our field strength limits.

Because the highest observed flux with pulsations is always much higher than the background the lower limit to the magnetic field strength will not be greatly affected by the uncertainty in the background estimate. The lowest observed flux with pulsations, however, is often comparable to the background contribution, so the effect on the upper limit needs to be considered carefully.

For some sources the background flux is sufficiently lower than the minimum pulsating flux (as shown in Table 7.1) that the effect of the background correction amounts to only a small change in the field estimates (e.g. $\sim$ 8% for XTE J1814–38, $\sim$ 12% for Swift J1756.9–2508). For sources where background flux could not be measured (HETE J1900.1–2455 and XTE J0929–314) the error introduced by neglecting the background is expected to similarly be only a few percent.

The remaining sources have a comparatively high background contribution, such that the estimated background flux is a large fraction of the minimum pulsating flux. For these AMXPs we conservatively took the lowest observed flux with pulsations as an upper limit to the real flux at which pulsations and thus accretion stops. We then calculated the upper limit on the magnetic field strength without adjusting for the background. Accounting for the background would lower the source flux estimate by up-to a factor of two, and thus improve our estimates by roughly $\lesssim$ 40%. Further improvement might be achievable with more sensitive instrumentation (as noted in the previous section).

- To convert the observed flux to the source luminosity we assumed an isotropic emission process, however, the flux includes contributions from the hotspot, which may have a significant anisotropy (Poutanen & Beloborodov 2006; Viironen & Poutanen 2004; Poutanen & Gierliński 2003).

  The effect of anisotropic emission is not at all clear. The degree of anisotropy of the hotspot emission depends on assumptions of the emission process and can vary by a factor of $\sim$ 2 (Poutanen & Beloborodov 2006). Furthermore, what fraction of the total flux is affected by this will depend on the size, shape and position of the hotspot and is subject to considerable uncertainty. At best this effect applies only to the pulsed component of the emission ($\sim$ 10%) and thus introduces a systematic error in our estimates of only a few percent. At worst most of the observed flux originates from a large hotspot that has a slightly beamed emission pattern. In that case the allowed magnetic field range may show a systematic shift of up-to $\sim$ 40%.

7.5 Comparison with previous works

In this work we estimated upper and lower limits to the magnetic field strength of all accreting millisecond X-ray pulsars (AMXPs) observed with *RXTE*. We assume that the detection of X-ray pulsations signifies ongoing magnetically channelled accretion. Thus, by associating the range of luminosity for which pulsations are detected with the expected extent of the disk truncation radius, we have constrained the magnetic dipole moment of the neutron star. The obtained equatorial surface magnetic field strengths of the 14 AMXPs analysed are presented in Table 7.2.

Our magnetic field strength estimates are subject to a number of uncertainties, which were discussed in the previous section. We note that we have chosen most of the uncertain parameters such that we obtained a conservative range for the magnetic moment. If parameters such as γ_B or $\epsilon_{\rm bol}$ can be established more accurately, they will tighten the constraints further. Errors in other parameters, such as the distance to the source, introduce a systematic shift in our results. Refinement in the measurement of these parameters would affect both the upper and the lower limits the same way.

For 5 of the 14 considered AMXPs (Swift J1749.4–2807, IGR J17511–3057, NGC 6440 X-2, XTE J1807.4–294 and IGR J17498–2921) we obtain constraints on the magnetic field strength for the first time. For the other 9 AMXPs field strength estimates have been previously reported. Below we discuss some of the techniques used to obtain those estimates and how they compare with limits we report here.

- *Vacuum dipole radiation in quiescence:* For some AMXPs the spin frequency has been measured for successive outbursts that are months or years apart. Measurements of spin-down during the intervening periods of quiescence, can then be used to estimate the magnetic field strength by assuming the spin-down is due to magnetic dipole emission. Such estimates have been obtained for IGR J00291+5934 (Patruno 2010; Hartman et al. 2011), XTE J1751–305 (Riggio et al. 2011a), SAX J1808.4–3658 (Hartman et al. 2008, 2009; Patruno et al. 2012) and Swift J1756.9–2508 (Patruno et al. 2010a). While the radio emission associated with magnetic braking has not yet been detected in any of these sources, the recent discovery of millisecond neutron stars pulsating alternately in X-rays and radio (Papitto et al. 2013a; Archibald et al. 2015; Papitto et al. 2015) provides some evidence that this interpretation of measured spin-down is correct.

  Our magnetic field strength estimates appear to be systematically lower than those obtained through quiescent spin down, although we note that given the systematic uncertainties discussed in the previous section, the results of these two approaches are roughly consistent.

- *Quiescent luminosity estimates:* For some LMXBs e.g. SAX J1808.4–3658, Aql X-1 (Di Salvo & Burderi 2003), KS 1731–260 (Burderi et al. 2002) and XTE J0929–314 (Wij-

nands et al. 2005), limits to the magnetic field strength have been inferred from measurements of the quiescent X-ray luminosity. However, given the very low count rates in the quiescent phase, and a poor understanding of which physical mechanism governs the radiation process, these methods offer less reliable constraints on the dipole moment compared to other approaches. While for Aql X-1 no other independent confirmation of the upper limits exists, the upper limits for SAX J1808.4–3658 and XTE J0929–314 obtained through quiescent luminosity methods are comparable to the upper limits we report here.

- *Accretion induced spin down estimates:* For some systems the magnetic field strength has been estimated by comparing observed rate of spin down during ongoing accretion to theoretical estimates of magnetic torque. For example, for XTE J1814–338 Papitto et al. (2007) assume that observed pulse frequency variations are caused by spin down due to the torque applied by an accretion disk that is truncated near the co-rotation radius. Following theoretical calculations of accretion induced spin down torques (Rappaport et al. 2004), the authors estimate the surface magnetic field to be $\sim 8 \times 10^8$ G, which is comparable our conservative upper limit to the field, and significantly higher than the upper limit we obtain using eq. 7.12. However, given their simplifying assumptions regarding the magnetic field topology at the Alfvén radius, and the considerable uncertainty in interpreting pulse frequency variations as spin variations (Patruno et al. 2009e), accretion induced spin down estimates are less robust than those we obtain.

- *Burst oscillations* In some accreting pulsars the phase of burst oscillations in type I X-ray bursts is locked to the phase of the accretion powered pulsations (XTE J1814–338 Watts et al. 2008, IGR J17480–2446 Cavecchi et al. 2011). Cavecchi et al. (2011) argue that if this phase-locking is due to magnetic confinement of the flame propagation front, then it would require a field strength of $\gtrsim 5 \times 10^9$ G. Even given the systematic uncertainties that enter in our estimates, such a large magnetic field strength would be difficult to reconcile with the lower upper limit we obtain for XTE J1814–338.

- *Spectral state transitions in LMXBs:* In another approach, spectral state transitions have been used to identify the onset of the propeller regime (Matsuoka & Asai 2013; Asai et al. 2013). These authors argue that a spectral change and a fast decline of luminosity towards the end of an outburst indicates the onset of the propeller regime and thus an accretion disk that is truncated at the co-rotation radius. Such spectral state transitions have been investigated for only a handful of LMXBs (e.g. Aql X-1, 4U 1608–52, XTE J1701–462), but give limits on the magnetic field strength of Aql X-1 that are tighter than those we obtained. However, there is no clear evidence that these transitions are indeed caused by a propeller effect. In fact, the observation of similar state transitions in black hole binaries seems to suggest otherwise (Jonker et al. 2004).

To conclude, the magnetic field estimates we obtain agree with most of the other indirect methods to within an order of magnitude. The large uncertainties on many parameters, as well as the uncertainty in the underlying assumptions, introduce a significant spread in the range of field strengths inferred via each approach, with no single technique being more robust than the others. Nonetheless, all alternative methods discussed in this section require that the AMXP be observed during a specific state of its outburst (e.g during quiescence or a spectral state transition). Since observations of such special states are not available, or may not even exist, for all sources, these methods are not suitable for studying the population. By contrast, the method used in this work applies to any AMXP, making it more reliable for comparing the field strengths of the population and understanding the evolutionary processes which lead to the formation of AMXPs.

7.A Details of the timing analysis

7.A.1 Swift J1756.9–2508:

The two outbursts of Swift J1756.9–2508 were observed with *RXTE* under program IDs P92050 & P93065 (2007) and P94065 (2009). We barycenter this data using the best known coordinates of Krimm et al. (2007a). For the timing solution we adopt the ephemeris of Patruno et al. (2010a).

7.A.2 XTE J0929–314:

We correct the *RXTE* data (program ID P70096) to the Solar system barycenter using the Chandra source position of Juett et al. (2003). The data was folded using the timing solution of Iacolina et al. (2009).

7.A.3 XTE J1807.4–294:

The *RXTE* data of the outburst of XTE J1807.4–294 is given by program IDs P70134 and P80(145/419). We use the Chandra coordinates of Markwardt et al. (2003) to barycenter the data. We use the system ephemeris of Riggio et al. (2008) to fold the data.

7.A.4 NGC 6440 X-2:

The nine short outbursts of NGC 6440 X-2 that were observed with *RXTE* are given by program IDs P94044, P94315 and P95040 (Patruno & D'Angelo 2013). We correct the data to the Solar System barycenter using the Chandra position of Heinke et al. (2010). The timing solution for the first outburst is given by Altamirano et al. (2010d). This timing solution is also used the later outbursts, but with the locally optimized time of ascending node values given in Table 7.3.

7.A.5 IGR J17511–3057:

The *RXTE* data of the 2009 outburst of IGR J17511–3057 is given by program ID P940(41/42). We barycenter the data using the Chandra position given by Nowak et al. (2009). The timing solution of this source is given by Riggio et al. (2011b).

7.A.6 XTE J1814–338:

The *RXTE* data of XTE J1814–338 is given by program IDs P80(138/145/418) and P92054. The optical position used to barycenter the data is given by Krauss et al. (2005) and the timing solution is taken from Papitto et al. (2007).

Table 7.3: Adopted T_{asc} values for the outbursts of NGC 6440 X-2.

NGC 6440 X-2	
Outburst	T_{asc}
Outburst 1	55042.817
Outburst 2	55073.034
Outburst 3	55106.012
Outburst 4	55132.907
Outburst 5	55276.625
Outburst 6	55359.470
Outburst 7	55473.854
Outburst 8	55584.714
Outburst 9	55871.231

7.A.7 HETE J1900.1–2455:

The source HETE J1900.1–2455 has a long history of activity and thus its *RXTE* data is spread over many program IDs: P910(15/57/59), P91432, P92049, P93(030/451), P940(28/30), P95030 and P96030. For source coordinates we use the optical position of Fox (2005). The timing solution is given by Patruno (2012).

7.A.8 SAX J1808.4–3658:

The *RXTE* program IDs for SAX J1808.4–3658 are given by P30411 (1998), P40035 (2000), P70080 (2002), P91056 & P91418 (2005), P93027 & P93417 (2008) and P96027 (2011). When considering the outbursts of SAX J1808.4–3658 we exclude the prolonged outburst tail which represents an unusual disk state (Patruno et al. 2009d, 2015), so the outburst of 2000 is entirely omitted from the analysis. Source coordinates for barycentering are taken from Hartman et al. (2008). For the ephemeris we adopt the solutions of Hartman et al. (2008, 2009) and Patruno et al. (2012) for the respective outbursts of 1998, 2002 and 2005; 2008; and 2011.

7.A.9 IGR J17498–2921:

RXTE data for IGR J17498–2921 is given by program ID P96435. For the source position we adopt the Chandra coordinates of Chakrabarty et al. (2011). The timing solution is given by Papitto et al. (2011c).

7.A.10 XTE J1751–305:

We only analyze the *RXTE* data of the 2002 outburst (see main text for details) which is given by programs P70131 and P70134. To barycenter the data we use the Chandra position of Markwardt & Dobrzycki (2002). For the orbital ephemeris we use the timing solution of Markwardt et al. (2002b).

7.A.11 SAX J1748.9–2021:

The *RXTE* data of SAX J1748.9–2021 is given by programs P30425, P60035 & P60084 (2001), P91050 (2005) and P94315 (2010). We use the Chandra position of in 't Zand et al. (2001) for barycentering the data. The timing solution of Patruno et al. (2009a) was used to fold the data of the 1998, 2001 and 2005 outbursts and that of Patruno et al. (2010c) for the 2010 outburst.

7.A.12 Swift J1749.4–2807:

We use the data of *RXTE* program P95085. For barycentering we adopt the X-ray coordinates of Wijnands et al. (2009), obtained with XMM-Newton. We use the ephemeris of Altamirano et al. (2011) to fold the data.

7.A.13 IGR J00291+5934:

We use *RXTE* data from programs P90052 and P90425 for the 2004 outburst and program P93013 and P93435 for the 2008 outburst. We use radio coordinates of Rupen et al. (2004) to barycenter the data. The timing solution of Patruno (2010) was used to fold the data.

Table 7.4: Spectral fit parameters of Swift J1756.9–2508.

	Swift J1756.9–2508		
	High flux	Low flux	Background
ObsIDs	94065-02-01-05	94065-06-02-03	94065-06-03-02
$N_H (10^{22}$ cm$^{-2})$	5.4 (fixed)	5.4 (fixed)	5.4 (fixed)
$T_{\rm BB}$ (keV)	–	0.49 ± 0.08	–
$\rm Norm_{bb}$	–	$10^{+6}_{-2} \times 10^{-4}$	–
Γ	1.970 ± 0.014	2.24 ± 0.06	2.67 ± 0.11
χ^2/d.o.f.	45.66/37	40.39/41	34.68/36
Flux (erg cm^{-2} s^{-1})	$6.30 \pm 0.04 \times 10^{-10}$	$1.990 \pm 0.017 \times 10^{-10}$	$4.07 \pm 0.15 \times 10^{-11}$

Note. N_H is the column density of neutral hydrogen for the *tabs* model, $T_{\rm bb}$ is the black body temperature, $\rm Norm_{bb}$ is the normalisation of the *bbody* model, Γ is the power-law index. The first column represents the highest flux (HF) with pulsations, the second column gives the lowest flux (LF) with pulsations and the third column gives the observation used to measure the background emission (BE).

7.B Details of the spectral analysis

For the spectral analysis we extracted the data of all Xenon layers of PCU2, and for observations with a poor signal to noise ratio we combined data from all active PCUs. Due to poor signal to noise some spectral fits at low flux have a reduced-χ^2 of much less than 1. As our work does not focus on obtaining the most accurate spectral model, but rather on measuring the flux, our final results will not be significantly affected by the model uncertainty of these fits.

Our analysis of the *RXTE/PCA* data was performed for the $3 - 20$ keV energy range using XSPEC version 12.7.1. The Galactic absorption was modelled with the *TBABS* model (Wilms et al. 2000). Since *RXTE* instruments cannot properly constrain the Galactic absorption due to neutral hydrogen in the lower energy range, we fix N_H to values obtained from literature. The errors quoted are for a 95% confidence limit.

7.B.1 Swift J1756.9–2508:

For ObsIDs 94065-02-01-05 (high flux with pulsations, HF) and 94065-06-02-03 (low flux with pulsations, LF) data were extracted from PCU2 whereas for 94065-06-03-02 (background estimate, BE), data from PCU 0, 2 and 4 were combined for the spectral analysis. The HF and BE spectra were fit with a simple absorbed power-law model XSPEC (Arnaud 1996). The LF spectrum was fit with a power-law continuum and a thermal black body component. The hydrogen column density accounting for Galactic absorption was fixed to $N_H = 5.4 \times 10^{20}$ cm^{-2} (Krimm et al. 2007a). A Gaussian emission component centred at ~ 6.5 keV (width fixed to 10^{-3} keV) was required to obtain statistically acceptable fits. The results of the spectral analysis are presented in Table 7.4.

Table 7.5: Spectral fit parameters of XTE J0929–314, see Table 7.4 for details.

	XTE J0929–314		
	High flux	Low flux	Background
ObsIDs	70096-03-02-00	70096-03-14-00	–
$N_H(10^{22}$ cm$^{-2})$	0.0076 (fixed)	0.0076 (fixed)	–
$T_{\rm BB}$ (keV)	0.82 ± 0.04	0.53 ± 0.05	–
$\rm Norm_{bb}$	$3.5 \pm 0.5 \times 10^{-3}$	$1.9 \pm 0.4 \times 10^{-3}$	–
Γ	1.80 ± 0.04	1.90 ± 0.11	–
χ^2/d.o.f.	36.33/42	26.11/42	–
Flux (erg cm^{-2} s^{-1})	$4.42 \pm 0.02 \times 10^{-10}$	$6.64 \pm 0.14 \times 10^{-11}$	–

Table 7.6: Spectral fit parameters of XTE J1807.4–294, see Table 7.4 for details.

	XTE J1807.4–294		
	High flux	Low flux	Background
ObsIDs	70134-09-02-01	80145-01-17-02	80419-01-01-01
$N_H(10^{22}$ cm$^{-2})$	0.56 (fixed)	0.56 (fixed)	0.56 (fixed)
Γ	1.90 ± 0.03	2.19 ± 0.04	2.16 ± 0.04
$T_{\rm BB}$ (keV)	$1.46^{+0.33}_{-0.19}$	–	–
$\rm Norm_{bb}$	$4.9 \pm 0.2 \times 10^{-4}$	–	–
χ^2/d.o.f.	49.87/42	31.07/44	34.69/44
Flux (erg cm^{-2} s^{-1})	$8.19 \pm 0.04 \times 10^{-10}$	$3.51 \pm 0.07 \times 10^{-10}$	$7.25 \pm 0.15 \times 10^{-11}$

7.B.2 XTE J0929–314:

For ObsID 70096-03-02-00 (HF) data were extracted from PCUs 0, 2, 3 & 4 whereas for 70096-03-14-00 (LF) they were extracted from PCUs 0, 2, 4. The spectra were fit with a power-law continuum and thermal blackbody component. The hydrogen column density was fixed to $N_H = 7.6 \times 10^{20}$ cm^{-2} (Juett et al. 2003). The results are presented in Table 7.5.

7.B.3 XTE J1807.4–294:

For ObsIDs 70134-09-02-01 (HF) and 80145-01-17-02 (LF) the data were extracted from PCU2 whereas for 80419-01-01-01 (BE) data were extracted from PCUs 0, 2 and 3. The HF spectrum was fit with a power-law continuum and thermal blackbody component whereas the LF and BE spectra were fit with a simple power-law model. The hydrogen column density was fixed to $N_H = 5.6 \times 10^{21}$ cm^{-2} (Falanga et al. 2005b). The resulting fit parameters are presented in Table 7.6.

Table 7.7: Spectral fit parameters of NGC 6440 X-2, see Table 7.4 for details.

	NGC 6440 X-2		
	High flux	Low flux	Background
ObsIDs	94044-04-02-00	96326-01-40-01	96326-01-36-00
$N_H (10^{22}$ cm$^{-2})$	0.59 (fixed)	0.59 (fixed)	0.59 (fixed)
Γ	1.83 ± 0.02	$2.36^{+0.21}_{-0.12}$	2.3 ± 0.4
Γ (Cutoffpl)	–	1.1 ± 0.8	–
$E_{\rm cut}$	–	5.5^{+9}_{-2}	–
χ^2/d.o.f.	34.38/38	45/35	36.77/44
Flux (erg cm^{-2} s^{-1})	$2.62 \pm 0.03 \times 10^{-10}$	$3.4 \pm 0.2 \times 10^{-11}$	$1.3 \pm 0.2 \times 10^{-11}$

Note. $E_{\rm cut}$ is the high energy cutoff for a cutoff power-law model.

Table 7.8: Spectral fit parameters of IGR J17511–3057, see Table 7.4 for details.

	IGR J17511–3057		
	High flux	Low flux	Background
ObsIDs	94041-01-01-02	94042-01-03-04	94042-01-02-05
$N_H \times 10^{22}$ cm^{-2}	1 (fixed)	1 (fixed)	1 (fixed)
$T_{\rm BB}$ (keV)	1.10 ± 0.16	–	–
Norm$_{\rm bb}$	$6 \pm 3 \times 10^{-4}$	–	–
Γ	1.70 ± 0.04	2.02 ± 0.04	2.37 ± 0.06
χ^2/d.o.f.	44.81/39	39.89/41	36.71/44
Flux (erg cm^{-2} s^{-1})	$8.65 \pm 0.05 \times 10^{-10}$	$1.000 \pm 0.018 \times 10^{-10}$	$6.960 \pm 0.018 \times 10^{-11}$

7.B.4 NGC 6440 X-2:

For ObsIDs 94044-04-02-00 and 96326-01-36-00 data was extracted from PCU2 whereas for ObsID 96326-01-40-01 data was taken from PCU 1 and 2. The hydrogen column density was fixed to $N_H = 5.9 \times 10^{21}$ cm^{-2} (Harris 1996). The data were fit with a simple absorbed power-law for all ObsIDs. The fit parameters are presented in Table 7.7.

7.B.5 IGR J17511–3057:

For ObsID 94041-01-01-02 (HF) the data were extracted from PCU 2. For ObsIDs 94042-01-03-04 (LF) and 94042-01-02-05 (BE) spectral analysis was performed by combining data from PCUs 2, 3 and PCUs 2, 4 respectively. The hydrogen column density was fixed to $N_H = 1 \times 10^{22}$ cm^{-2} (Papitto et al. 2010; Paizis et al. 2012). The HF was well described with a power-law continuum and thermal blackbody component, whereas the LF and BE spectra were fit with a simple absorbed power law. A Gaussian feature at $\sim$ 6.5 keV

Table 7.9: Spectral fit parameters of XTE J1814–338, see Table 7.4 for details.

	XTE J1814–338		
	High flux	Low flux	Background
ObsIDs	80418-01-03-08	80418-01-07-08	80418-01-09-00
$N_H(10^{22}$ cm$^{-2})$	0.167 (fixed)	0.167 (fixed)	0.167 (fixed)
$T_{\rm BB}$ (keV)	$1.21 \pm +0.06$	–	–
$\rm Norm_{bb}$	$1.7 \pm 0.4 \times 10^{-3}$	–	–
Γ	1.55 ± 0.04	1.96 ± 0.03	2.4 ± 0.3
$\Delta\chi^2$/d.o.f.	63.99/42	23.2/43	28.17/44
Flux (erg cm^{-2} s^{-1})	$4.41 \pm 0.03 \times 10^{-10}$	$6.00 \pm 0.10 \times 10^{-11}$	$1.00 \pm 0.16 \times 10^{-11}$

was added to the HF and BE spectra to improve the fits. The resulting parameters are presented in Table 7.8.

7.B.6 XTE J1814–338:

Since the observed count rate of XTE J1814–338 is small (< 40ct s^{-1} for the entire outburst), data from all available PCUs were combined for all spectra. For ObsID 80418-01-03-08 (HF) the data were extracted from PCU 0, 2 and 3. For 80418-01-07-08 (LF) data from PCUs 0, 1, 2 and 3 and for 80418-01-09-00 (BE) PCUs 0, 1 and 2 were used. The hydrogen column density was fixed to $N_H = 1.67 \times 10^{21}$ cm^{-2} (Krauss et al. 2005).

The HF spectrum was fit with a power-law continuum and a blackbody component, whereas the LF and BE spectra were fit with a simple absorbed power-law model. The details of the fit parameters are presented in Table 7.9.

7.B.7 HETE J1900.1–2455:

The data were extracted from all layers of PCU2 for the considered ObsIDs. The hydrogen column density was fixed to $N_H = 1 \times 10^{21}$ cm^{-2} (Papitto et al. 2013b). We obtain the HF spectrum from ObsID 91015-01-06-00 with fit with *tbabs*cutoffpl*. We found a large excess at ~ 6 keV, which was modelled with a Gaussian centred at ~ 6.2 keV with a width of ~ 1 keV. The resulting fits were statistically acceptable.

The ObsID 91059-03-02-00 (LF) was fit with *tbabs(bbody+powerlaw)*. A weak Gaussian feature at ~ 6.5 keV was added to improve the fits. The results are presented in Table 7.10.

A background estimate is not available for this source.

Table 7.10: Spectral fit parameters of HETE J1900.1–2455, see text and Table 7.4 for further details.

	HETE J1900.1–2455		
	High flux	Low flux	Background
ObsIDs	91015-01-06-00	91059-03-02-00	–
$N_H(10^{22}$ cm$^{-2})$	0.1 (fixed)	0.1 (fixed)	–
$T_{\rm BB}$ (keV)		0.74 ± 0.10	–
$\rm Norm_{bb}$		$8 \pm 2 \times 10^{-4}$	–
Γ (cutoffpl)	0.9 ± 0.1		–
$E_{\rm cut}$	4.0 ± 0.2		–
Γ		1.83 ± 0.07	–
χ^2/d.o.f.	42.74/40	25.26/40	–
Flux (erg cm^{-2} s^{-1})	$1.15 \pm 0.05 \times 10^{-9}$	$3.84 \pm 0.03 \times 10^{-10}$	–

Table 7.11: Spectral fit parameters of SAX J1808.4–3658.

	SAX J1808.4–3658		
	High flux	Low flux	Background
ObsIDs	70080-01-01-04	30411-01-11-00	30411-01-11-02
$N_H(10^{22}$ cm$^{-2})$	0.2 (fixed)	0.2 (fixed)	0.2 (fixed)
Γ (Powerlaw)	–	2.24 ± 0.05	2.23 ± 0.11
$T_{\rm bb}$ (keV)	1.25 ± 0.07	–	–
$\rm Norm_{bb}$	$9.2 \pm 1.4 \times 10^{-3}$	–	–
$T_{\rm disk}$ (keV)	0.45 ± 0.06	–	–
$\rm Norm_{disk}$	$8.7^{+18}_{-5} \times 10^3$	–	–
E_1 (keV)	6.2 (fixed)	–	–
σ_1 (keV)	1.04 ± 0.15	–	–
Γ (NTHCOMP)	2.3 ± 0.1	–	–
T_e (keV)	100 (fixed)	–	–
χ^2/d.o.f.	33.37/35	50.18/45	35.47/43
Flux (erg cm^{-2} s^{-1})	$1.850 \pm 0.007 \times 10^{-9}$	$2.82 \pm 0.07 \times 10^{-11}$	$1.21 \pm 0.08 \times 10^{-11}$

Note. $T_{\rm disk}$ is the temperature of the inner radius of the accretion disk, and $\rm Norm_{disk}$ is the normalisation of the *diskbb* model. The fluorescent iron line is fit with a Gaussian component, such that E_1 is the line energy and σ_1 the width of the line. Similarly E_2 and σ_2 are the line energy and width of a Gaussian component needed to model an excess at ~ 5.4 keV. See text and Table 7.4 for further details.

Table 7.12: Spectral fit parameters of IGR J17498–2921, see Table 7.4 for details.

	IGR J17498–2921		
	High flux	Low flux	Background
ObsIDs	96435-01-02-01	96435-01-06-04	96435-01-07-01
$N_H(10^{22}$ cm$^{-2})$	2.87 (fixed)	2.87 (fixed)	2.87 (fixed)
$T_{\rm BB}$ (keV)	1.51 ± 0.05	1.93 ± 0.15	1.76 ± 0.08
$\rm Norm_{bb}$	$1.9 \pm 0.2 \times 10^{-3}$	$1.41^{+0.2}_{-0.08} \times 10^{-3}$	$2.2 \pm 0.2 \times 10^{-3}$
Γ	1.93 ± 0.02	$2.39^{+0.1}_{-0.06}$	2.3 ± 0.1
χ^2/d.o.f.	52.76/39	28.90/38	32.39/38
Flux (erg cm^{-2} s^{-1})	$1.130^{+0.003}_{-0.006} \times 10^{-9}$	$4.44 \pm 0.04 \times 10^{-10}$	$4.23 \pm 0.04 \times 10^{-10}$

7.B.8 SAX J1808.4–3658:

For ObsID 70080-01-01-04 (HF) the data were extracted from the top layers of PCU2. The hydrogen column density was fixed to $N_H = 2 \times 10^{21}$ cm^{-2} (Papitto et al. 2009; Cackett et al. 2009; Patruno et al. 2009c). The continuum was modelled with the thermal comptonisation *NTHCOMP* of Zdziarski et al. (1996); Życki et al. (1999). A blackbody and diskblackbody component were also required to model the continuum. A broad excess at ~ 6.2 keV was seen in the residuals, reminiscent of a relativistically broadened iron line reported in other works (Papitto et al. 2009; Patruno et al. 2009c; Cackett et al. 2009). However, owing to the poor spectral resolution of RXTE, we have not employed the sophisticated relativistic models like *diskline* and instead modelled the feature with a broadened Gaussian. The central energy of the Gaussian was fixed to 6.2 keV.

Data for ObsIDs 30411-01-11-00 (LF) and 30411-01-11-02 (BE) was extracted from all PCUs and combined for spectral analysis. The data fit well with a simple power-law model. The results are presented in Table 7.11.

7.B.9 IGR J17498–2921:

Data for all ObsIDs viz. 96435-01-02-01 (HF), 96435-01-06-04 (LF) and 96435-01-07-01 (BE) were extracted from all layers of PCU 2. All three spectra were fit with a simple power-law continuum model and a thermal blackbody component. A narrow Gaussian component centred at ~ 6.5 keV (most likely a feature from background emission) was required to obtain a statistically acceptable fit. The hydrogen column density was fixed to $N_H = 2.87 \times 10^{22}$ cm^{-2} (Torres et al. 2011). The results are presented in Table 7.12.

We note that flux measured from the LF and BE observations are the same within error, indicating that the lowest flux with pulsations is background dominated.

Table 7.13: Spectral fit parameters of XTE J1751–305, see Table 7.4 for details.

	XTE J1751–305		
	High flux	Low flux	Background
ObsIDs	70134-03-01-00	70131-01-09-000	70131-02-04-00
$N_H(10^{22}$ cm$^{-2})$	1 (fixed)	1 (fixed)	1 (fixed)
$T_{\rm bb}$ (keV)	1.95 ± 0.16	–	–
$\rm Norm_{bb}$	$2.1 \pm 0.3 \times 10^{-3}$	–	–
$T_{\rm disk}$ (keV)	–	–	–
$\rm Norm_{disk}$	–	–	–
Γ	1.77 ± 0.03	2.070 ± 0.007	2.32 ± 0.03
χ^2/d.o.f.	47.59/40	38.07/35	56.08/40
Flux (erg cm^{-2} s^{-1})	$1.500^{+0.006}_{-0.01} \times 10^{-9}$	$3.97 \pm 0.01 \times 10^{-10}$	$6.51 \pm 0.08 \times 10^{-11}$

Table 7.14: Spectral fit parameters of SAX J1748.9–2021, see Table 7.4 for details.

	SAX J1748.9–2021		
	High flux	Low flux	Background
ObsIDs	94315-01-06-07	60035-02-03-02	94315-01-11-02
$N_H(10^{22}$ cm$^{-2})$	0.59 (fixed)	0.59 (fixed)	0.59 (fixed)
$T_{\rm bb}$ (keV)	2.11 ± 0.14	$0.63^{+0.06}_{-0.11}$	–
$\rm Norm_{bb}$	$1.30 \pm 0.19 \times 10^{-2}$	$6.5^{+2.9}_{-1.7} \times 10^{-3}$	–
Γ (cutoffpl)	1.00 ± 0.16	$0.39^{+0.15}_{-0.23}$	–
$E_{\rm cut}$ (keV)	4.1 ± 0.6	$3.36^{+0.16}_{-0.21}$	–
Γ (power law)	–	–	2.2 ± 0.2
χ^2/d.o.f.	45.41/41	36.21/33	28.23/43
Flux (erg cm^{-2} s^{-1})	$4.13 \pm 0.01 \times 10^{-9}$	$2.960 \pm 0.005 \times 10^{-9}$	$1.9 \pm 0.2 \times 10^{-11}$

7.B.10 XTE J1751–305:

For all ObsIDs viz. 70131-03-01-00 (HF), 70131-01-09-000 (LF) and 70131-02-04-00 (BE), data was extracted from PCU2. For the HF and BE, the spectra were fit with *tbabs(powerlaw+bbody)*. The LF spectrum was fit with a simple absorbed powerlaw. Additionally, a narrow Gaussian component centred at ~ 6.5 keV was required for the low flux observations. The neutral hydrogen column density was fixed to $N_H = 1 \times 10^{22}$ cm^{-2} (Miller et al. 2003; Gierliński & Poutanen 2005). The results are presented in Table 7.13.

Table 7.15: Spectral fit parameters of Swift J1749.4–2807, see Table 7.4 for details.

	Swift J1749.4–2807		
	High flux	Low flux	Background
ObsIDs	95085-09-01-00	95085-09-02-05	95085-09-02-10
$N_H(10^{22}$ cm$^{-2})$	3 (fixed)	3 (fixed)	3 (fixed)
$T_{\rm bb}$ (keV)	–	1.67 ± 0.11	1.8 ± 0.2
$\rm Norm_{bb}$	–	$7.94 \pm 1.2 \times 10^{-4}$	$5.8 \pm 1.2 \times 10^{-4}$
Γ	1.89 ± 0.02	1.78 ± 0.08	1.90 ± 0.09
χ^2/d.o.f.	43.21/41	54.01/33	39.77/39
Flux (erg cm^{-2} s^{-1})	$5.24 \pm 0.06 \times 10^{-10}$	$2.67 \pm 0.02 \times 10^{-10}$	$2.41 \pm 0.03 \times 10^{-10}$

7.B.11 SAX J1748.9–2021:

For ObsID 94315-01-06-07 (HF) and 60035-02-03-02 (LF) the data were extracted from PCU 2, whereas for 94315-01-11-02 (BE) the combined spectra from PCU 0 and 2 were used. The HF and LF spectra fit with *tabs(bbody+cutoffpl)*. The BE spectrum was fit using an absorbed power-law. The hydrogen column density was fixed to $N_H = 5.9 \times 10^{21}$ cm^{-2} (Harris 1996). A Gaussian emission feature centred at ~ 6.5 keV was used to improve statistics of the LF spectrum fit. The results are presented in Table 7.14.

7.B.12 Swift J1749.4–2807:

The data were extracted from PCU2 for all ObsIDs (HF: 95085-09-01-00, LF: 95085-09-02-07, BE: 95085-09-02-10). There was an eclipse during the observation in 95085-09-01-00 (Markwardt & Strohmayer 2010; Ferrigno et al. 2011), so for the spectral analysis of that observation we considered only the data from the initial 990 s when the source was visible. The spectra were fit with power-law continuum model. The neutral hydrogen column density was fixed to $N_H = 3 \times 10^{22}$ cm^{-2} (Ferrigno et al. 2011; Wijnands et al. 2009). For the LF and BE an additional blackbody component was required. The results are presented in Table 7.15.

7.B.13 Aql X-1:

Since the pulsations of Aql X-1 have been detected only once (ObsID 30188-03-05-00), we use this observation as both the HF and LF. We extract the data from PCU2 and fit the spectrum with a *tbabs(cutoffpl+Gaussian+bbody)* model. The background emission is evaluated from ObsID 30073-06-01-00, which was fit with a simple absorbed power-law. Our results are shown in Table 7.16.

Table 7.16: Spectral fit parameters of Aql X-1, see Table 7.4 for details.

	Aql X-1	
	High/Low flux	Background
ObsIDs	30188-03-05-00	30073-06-01-00
$N_H(10^{22}$ cm$^{-2})$	0.4 (fixed)	0.4 (fixed)
$T_{\rm bb}$ (keV)	$0.81^{+0.44}_{-0.09}$	–
$\rm Norm_{bb}$	$1.2^{+2.1}_{-0.6}$	–
Γ	–	1.92 ± 0.02
Γ (cutoffpl)	$0.7^{+0.2}_{-0.4}$	–
$E_{\rm cut}$ (keV)	3.4 ± 0.4	–
E_1 (keV)	$6.32^{+0.18}_{-0.38}$	–
σ_1 (keV)	1.0 ± 0.3	–
χ^2/d.o.f.	45.95/38	45.39/43
Flux (erg cm^{-2} s^{-1})	$8.74 \pm 0.01 \times 10^{-9}$	$1.34 \pm 0.05 \times 10^{-11}$

Table 7.17: Spectral fit parameters of IGR J00291+5934, see Table 7.4 for details

	IGR J00291+5934		
	High flux	Low flux	Background
ObsIDs	90052-03-01-00	90425-01-02-01	90425-01-03-06
$N_H(10^{22}$ cm$^{-2})$	0.46 (fixed)	0.46 (fixed)	0.46 (fixed)
Γ	1.50 ± 0.04	1.73 ± 0.04	1.50 ± 0.03
$T_{\rm BB}$ (keV)	1.14 ± 0.06	–	–
$\rm Norm_{bb}$	$1.05 \pm 0.03 \times 10^{-3}$	–	–
χ^2/d.o.f.	48.81/42	22.92/35	30.55/41
Flux (erg cm^{-2} s^{-1})	$9.7 \pm 0.05 \times 10^{-10}$	$1.09 \pm 0.02 \times 10^{-10}$	$5.76 \pm 0.09 \times 10^{-11}$

7.B.14 IGR J00291+5934:

For the ObsID 90052-03-01-00 (HF) data from PCU2 were used for spectral analysis. For 90425-01-02-01 (LF) and 90425-01-03-06 (BE) data from all active PCUs (PCU 0, 2 and PCU 0, 2, 3 respectively) were combined to improve the photon statistics.

The HF spectrum was fit with the thermal blackbody and power-law models. The LF and BE spectra were fit with a simple absorbed power law. The neutral hydrogen column density was fixed to $N_H = 0.46 \times 10^{22}$ cm^{-2} based on measurements from *XMM-Newton* and *Chandra* observations (Torres et al. 2008; Paizis et al. 2005). A gaussian emission feature was required to improve the fits of the LF and BE spectra. The fit results are given in Table 7.17.

Summary

Connecting the coherent and stochastic X-ray variability of accreting millisecond pulsars

Accreting millisecond pulsars are rapidly rotating neutron stars in low-mass X-ray binary systems. In these systems a low-mass companion star acts as a mass donor and matter is transferred from the companion to the neutron star. As it flows toward the neutron star, this matter will enter an orbit around it, form a disk structure, and through the release of gravitational energy it will heat-up as it spirals in. The bulk of the energy released through the accretion process originates from close to the neutron star, where the disk will have a temperature of about 10^7 Kelvin and its thermal emission will be bright in the X-ray band.

The disk is expected to be turbulent, showing structures that propagate in and through the material flow, modulating the intensity of its thermal emission. Such variability in the X-ray emission thus gives the means to study these neutron stars and their surroundings. As the timescale of this variability decreases for matter closer to the neutron star, the fastest, millisecond variability that can be seen in such objects is of special interest.

In the case of accreting millisecond pulsars, the neutron star magnetic field plays a dynamically important role in the accretion process close to the neutron star. If the stellar magnetic field is strong enough, it may disrupt the structure of the accretion disk, forcing the accreting material to flow along the field lines toward the stellar magnetic poles. There, the impact of the accretion flow creates a local emission region, the hotspot, which through aspect variations gives rise to a periodic modulation of the emerging X-ray emission. As these periodic pulsations are strictly coherent and reveal the rotation rate of the neutron star, they offer a powerful diagnostic of the neutron star.

Since the discovery of the first accreting millisecond pulsar in 1998, a total of 15 of such objects have been found. The coherent pulsations of these sources have been extensively studied, yet the stochastic variability that may also be seen in such objects has received comparatively little attention. In this thesis I explored the X-ray variability of accreting millisecond pulsars, considering both the coherent pulsations and the stochastic emission. As the pulsations are powered by the variable accretion flow, it is expected that these two aspects of the X-ray variability share strong links. By connecting the coherent and stochastic variability we may therefore obtain a more complete view of the accretion process toward these pulsars and use the diagnostic power of the pulsations to gain a

better understanding of the variable flow and its magnetic connection to the neutron star.

In chapter 2 the coherent pulsations of the canonical accreting millisecond X-ray pulsar (AMXP) SAX J1808.4–3658 are studied during its 2011 outburst. This chapter represents a continuation of the study of the coherent emission from this AMXP, extending the observational baseline of the monitoring campaign to 14 years. In previous work on this source it was found that the neutron star shows a steady long-term spin down, and that the binary orbit is expanding. In the presented analysis we confirm that the long-term spin-down of this source remains stable. We also show that the expansion of the binary orbit is accelerating at a rapid rate. Such an accelerating expansion is difficult to understand in terms of the binary secular evolution, and instead suggests that some other mechanism is active in this system. We suggest that the acceleration can be interpreted as a short-term angular momentum exchange between the companion star and the binary orbit, possibly due to a spin-orbit coupling through the companion star's mass quadrupole.

In chapter 3 the pulsar SAX J1808.4–3658 is again considered, but now in terms of its aperiodic variability. In this chapter we report on the discovery of a peculiar flaring phenomenon that appears in the outbursts of 2008 and 2011 when the source luminosity is high. This flaring phenomenon is seen for a few days in each of these two outbursts, but is not seen in any of the earlier observations of this source. It shows a very similar phenomenology as another flaring variability observed in the outburst tails of this source, which occurs at a luminosity that is an order of magnitude lower. A clue on the origin of this new high luminosity flaring is obtained by looking at its relation with the coherent pulsations. We show that the pulse amplitude correlates with the luminosity variations due to the flaring and that this correlation is such that the fractional pulse amplitude remains constant throughout the flaring intensity variations. We interpret this correlation to mean that the flaring must originate from modulation of the accretion rate and suggest that is probably related to the magnetosphere. This type of flaring variability, if observed in other low-mass X-ray binaries, may therefore provide evidence of a magnetosphere, even in absence of pulsations.

In chapter 4 the aperiodic variability in SAX J1808.4–3658 is studied. This chapter provides an in-depth overview of the very rich phenomenology observed in this source. Two new instances of twin kilohertz quasi-periodic oscillations (kHz QPOs) are reported, allowing their frequency evolution to be measured for the first time in this source. Additionally, we consider the overal properties of the aperiodic variability components and study how their respective frequencies relate to one-another. Comparing the variability properties of pulsating and non-pulsating accreting neutron stars gives a sense of which phenomena are intrinsic to the accretion disk and which are related to the neutron star magnetosphere. Special attention is given to the enigmatic 410 Hz QPO, which so far remains unique to this accreting millisecond pulsar. We show that this QPO appears in only in a very narrow region of source luminosities and upper kHz QPO frequencies, thus

providing an indication of how to search for this phenomenon in future outbursts or other sources. Interpreting this QPO as a sideband of the 401 Hz pulsations, we suggest that the underlying 9 Hz component may be due to the same mechanism as the low-frequency QPO, which would then have to be retrograde with respect to the neutron star rotation direction.

In chapter 5 we report on the discovery of a direct connection between the kHz QPOs and the coherent pulsations. By considering the SAX J1808.4–3658 data, we show that every time the frequency of the upper kHz QPO drifts through the spin frequency, the amplitude of the pulsation shows a systematic jump. This result indicates that accretion flow toward the neutron star is somehow different depending on whether the kHz QPO frequency is faster of slower than the spin frequency of the neutron star and its magnetosphere. This result provides strong evidence that the QPO originates in azimuthal motion in the accretion flow. The most straightforward interpretation then suggests that the upper kHz QPO is due to orbital motion at the inner edge of the accretion disk and the centrifugal inhibition that sets in when that motion becomes slower than the spin frequency causes a qualitative change in how matter flows toward the neutron star.

In chapter 6 the coherent pulsations of the accreting millisecond pulsar NGC 6440 X-2 are analyzed. Compared to the population of AMXPs, this globular cluster source shows an intriguing and unique outburst pattern. Its outbursts are faint, and with durations of only a few days, very short. The recurrence time of the outbursts is similarly short, ranging from one to a few months. Through the analysis of the coherent pulsations the orbital evolution of this source is established. We investigate whether the rotational phase of the various outburst of this source can be coherently connected, as to obtain a single description of its spin and orbit evolution. We find that given the systematic uncertainties in the coherent timing analysis of this source, there is no unique way to obtain such a coherent phase connection.

Finally, in chapter 7 we present a population study of accreting millisecond pulsars. One of the key properties of a neutron star is the strength of its magnetic field. For accreting millisecond pulsars, however, the magnetic field strength is notoriously difficult to measure. All available methods are indirect and subject to various systematic uncertainties, which is problematic when trying to compare the field strengths within the accreting millisecond pulsar population or with to the field strengths of related classes of pulsars. In this chapter we estimate the magnetic field strength of an AMXP through the detection of its pulsations. By associating the range of luminosity over which pulsations are found with the range of accretion disk truncation radii over which channelled accretion onto the neutron star is expected, we derive an upper and lower limit on the magnetic field strength. Using this approach a magnetic field strength estimate is derived for each accreting millisecond pulsars observed with the *Rossi X-ray Timing Explorer*, yielding a systematic study of magnetic field strength for the population of AMXPs.

Samenvatting

De koppeling tussen de coherente en stochastische röntgenvariabiliteit van accreterende milliseconde pulsars

Accreterende milliseconde pulsars zijn snel roterende neutronensterren in lage massa röntgendubbelsterren. In dergelijke systemen fungeert de begeleidende ster als massadonor en wordt materie overgedragen van de begeleidende ster naar de neutronenster. Als deze materie richting de neutronenster stroomt, komt het in een baanbeweging rond de ster en vormt zodoende een gasschijf, welke door het vrijkomen van gravitationele energie opwarmt terwijl het materiaal via een spiraal naar binnen beweegt. Het merendeel van de energie die via het accretieproces vrijkomt, is afkomstig uit de nabije omgeving van de neutronenster, waar de schijf een temperatuur heeft ten orde van 10^7 Kelvin en de resulterende thermische emissie helder is in de röntgenband.

De schijf is turbulent en vertoont structuren die zich in en via de materiestroom voortbewegen, wat de intensiteit van de thermische emissie moduleert. Dergelijke variabiliteit in de röntgenemissie biedt daarmee de mogelijkheid om neutronensterren en hun directe omgeving te bestuderen. Aangezien de tijdschaal van deze variabiliteit afneemt naargelang materie zich dichterbij de neutronenster bevind, verdient de snelste milliseconde variabiliteit die van dergelijke objecten kan worden waargenomen speciale aandacht.

In het geval van accreterende milliseconde pulsars levert het magnetische veld van de neutronenster een dynamisch belangrijke bijdrage aan het accretieproces in de directe omgeving van de neutronenster. Als het magnetische veld sterk genoeg is kan het de schijfstructuur van het accreterende materiaal verstoren, de stroomrichting van de materie afbuigen en deze naar de magnetische polen van de ster leiden. De inslag van deze materiestroom creëert een lokaal emissie gebied op het steroppervlak, dat ten gevolge van aspect-variaties een periodieke modulatie van de uitgezonden röntgenstraling veroorzaakt. Aangezien deze periodieke pulsaties strikt coherent zijn en de rotatiesnelheid van de neutronenster weergeven, leveren ze een accuraat signaal waarmee de neutronenster bestudeerd kan worden.

Sinds de ontdekking van de eerste accreterende milliseconde pulsar in 1998 zijn er in totaal 15 van zulke systemen gevonden. De coherente pulsaties van deze objecten zijn uitvoerig bestudeerd, echter de stochastische variabiliteit heeft bij vergelijking veel minder aandacht gekregen. In dit proefschrift bestudeer ik de röntgenvariabiliteit van accreterende milliseconde pulsars, waarbij zowel de coherente pulsaties als de stochas-

tische variabiliteit in aanmerking worden genomen. Aangezien de coherente pulsaties worden gevoed door de variabele accretiestroom, is het redelijk te verwachten dat deze twee componenten van de röntgenvariabiliteit een sterke relatie vertonen. Door de coherente en stochastische variabiliteit te koppelen krijgen we een vollediger beeld van het accretieproces naar deze milliseconde pulsars en kunnen we de nauwkeurigheid van de pulsaties gebruiken om tot een een beter begrip te komen van de variabele accretiestroom en de magnetische verbinding met de neutronenster.

In hoofdstuk 2 worden de coherente pulsaties van de klassieke accreterende milliseconde röntgenpulsar (AMXP) SAX J1808.4–3658 tijdens de uitbarsting in 2011 bestudeerd. Dit hoofdstuk vertegenwoordigt de voortzetting van een langere studie naar de coherente pulsaties van deze bron en breidt het tijdspanne van de waarnemingen uit naar 14 jaar. In eerder werk is aangetoond dat de pulsaties op lange termijn een stabiele vertraging vertonen en dat de baanbeweging van het dubbelster systeem uitdijt. In deze nieuwe analyse bevestigen we dat de vertraging van de pulsaties stabiel is gebleven en tonen we aan dat de uitdijing van de baanbeweging versnelt. Een dergelijke versnelde uitdijing is moeilijk verklaarbaar in termen van de seculiere evolutie van het dubbelstersysteem, en suggereert dan er een ander mechanisme actief is dat de baanperiode beïnvloedt. We suggereren dat de versnelde uitdijing het gevolg is van kortdurende uitwisseling van impulsmoment tussen de begeleidende ster en de baanbeweging van het dubbelstersysteem, mogelijk via spin-baan koppeling in de massa quadrupool van de begeleidende ster.

In hoofdstuk 3 wordt wederom de pulsar SAX J1808.4–3658 bestudeerd, echter nu in termen van de aperiodieke variabiliteit. In dit hoofdstuk presenteren we de ontdekking van een opmerkelijk *flaring* fenomeen, dat wordt waargenomen in de uitbarstingen van 2008 en 2011 bij een hoge röntgenlichtkracht. Dit flaring-verschijnsel wordt gedurende enkele dagen waargenomen in deze twee uitbarstingen, maar is niet te zien in eerdere waarnemingen van deze bron. Het vertoont sterke overeenkomsten met een ander soort flaring-variabiliteit, die alleen in de staart van de uitbarstingen wordt waargenomen, bij een orde van grootte kleinere lichtkracht. Een aanwijzing voor de oorsprong van deze nieuwe hoge lichtkracht flaring-variabiliteit komt voort uit de relatie met de coherente pulsaties. We tonen aan dat de pulsamplitude correleert met de flaring, zodanig dat de fractionele amplitude van de pulsaties constant is tijdens de flaring-variaties. Volgens onze interpretatie betekent deze correlatie dat de flaring wordt veroorzaakt door een modulatie van de massa-accretiesnelheid, waarvan we suggereren dat die gerelateerd is aan de magnetosfeer. Indien dit soort flaring in andere lage massa röntgendubbelster systemen wordt waargenomen, dan levert dat bewijs voor het bestaan van een magnetosfeer, zelfs in de afwezigheid van pulsaties.

In hoofdstuk 4 wordt de aperiodieke variabiliteit van SAX J1808.4–3658 bestudeerd. In dit hoofdstuk presenteren we een gedetailleerd overzicht van de rijke fenomenologie van deze bron. Twee nieuwe waarnemingen van dubbele kilohertz quasi-periodieke oscillaties (kHz QPOs) worden gerapporteerd, waardoor, voor het eerst voor dit systeem,

hun relatieve frequentieverandering kan worden gemeten. Verder bestuderen we de verscheidene componenten van de aperiodieke varabiliteit en vergelijken we hun onderlinge relaties. We besteden uitgebreid aandacht aan de mysterieuze 410 Hz QPO, welke tot nu toe alleen in deze bron is waargenomen. Zo tonen we aan dat deze QPO alleen verschijnt voor een nauwe regio van lichtkracht en kHz QPO frequentie, wat een aanwijzing geeft over hoe er naar een dergelijke QPO gezocht kan worden in toekomstige uitbarstingen of observaties van andere systemen. Door deze QPO te interpreteren als een zijband van de 401 Hz pulsfrequentie, suggereren we dat de onderliggende 9 Hz component door hetzelfde mechanisme wordt veroorzaakt als de lage-frequentie QPO, welke dan retrograad ten aanzien van de pulsar moet bewegen.

In hoofdstuk 5 presenteren we de ontdekking van een directe relatie tussen de kHz QPOs en de milliseconde pulsaties. Aan de hand van de SAX J1808.4–3658 data tonen we aan dat elke keer dat the hogere kHz QPO frequentie door de spinfrequentie heen gaat, de amplitude van de pulsaties een systematische sprong laat zien. Dit resultaat geeft aan dat de binnenste accretiestroom anders is, afhankelijk van of de QPO frequentie sneller of trager is dan de rotatie van de neutronenster en de daaraan gekoppelde magnetosfeer. Dit resultaat levert een sterk bewijs dat de QPO ontstaat in een azimutale beweging van de accretiestroom. De meest voor de hand liggende verklaring is dan dat de QPO direct gegeven wordt door de baansnelheid aan de binnenrand van de accretieschijf en dat de centrifugaalkracht die relevant wordt wanneer die beweging trager is dan de rotatie van de ster de kwalitatieve verandering van de accretiestroom naar de neutronenster veroorzaakt.

In hoofdstuk 6 analyseren we de coherente pulsaties van de accreterende milliseconde pulsar NGC 6440 X-2. In vergelijking met de AMXP-populatie vertoont deze bolhoop-geassocieerde bron een uniek uitbarstingspatroon. De uitbarstingen zijn lichtzwak en, met een duur van enkele dagen, uitzonderlijk kort. De tijd tussen uitbarstingen is met één tot enkele maanden ook kort. Aan de hand van de coherent pulsaties bepalen we de baanevolutie van het dubbelstersysteem. We bestuderen tevens of de fase van de pulsaties tussen verschillende uitbarsten coherent verbonden kan worden, om zodoende de spin en baan evolutie van deze pulsar in een enkele oplossing uit te drukken. We vinder, echter, dat gegeven de systematische onzekerheden in de coherente analyse er geen unieke tijdsoplossing gevonden kan worden.

Ten slotte wordt in hoofdstuk 7 de populatie van accreterende milliseconde pulsars onderzocht. Een van de basiseigenschappen van een neutronenster is de sterkte van het magnetisch veld. Voor accreterende milliseconde pulsars is deze eigenschap echter lastig te meten; alle beschikbare methoden zijn indirect en bevatten verscheidene systematische onzekerheden. Dit is problematisch voor studies waarin de veldsterkte tussen systemen in de vergeleken moet worden, of de gehele populatie wordt vergeleken met andere soorten pulsars. In dit hoofdstuk schatten we de sterkte van het magnetische veld voor een AMXP aan de hand van de detectie van pulsaties. Door het bereik van lichtkracht waarvoor pulsaties waargenomen worden te associeren met het bereik van de binnenste

straal van de accretieschijf waarvoor pulsaties verwacht worden, kunnen we onder- en bovenlimieten op de veldsterkte afleiden. Deze methode wordt op elk van accreterende milliseconde pulsars die met met de *Rossi X-ray Timing Explorer* zijn waargenomen toegepast, om zodoende tot een systematische studie te komen van de magnetische veldsterkte in AMXPs.

Reference list

Below I summarize the bibliographic information of the chapters in this thesis. For each chapter the relative importance of the co-authors is indicated by the order of the author list.

Chapter 2: Accelerated orbital expansion of SAX J1808.4–3658
The Astrophysical Journal Letters, 2012, 746, L27
A. Patruno, P. Bult, A. Gopakumar, J. M. Hartman, R. Wijnands, M. van der Klis & D. Chakrabarty

Chapter 3: 1–5 Hz flaring in SAX J1808.4–3658
The Astrophysical Journal, 2014, 789, 99
P. Bult & M. van der Klis

Chapter 4: The aperiodic X-ray variability of SAX J1808.4–3658
The Astrophysical Journal, 2015, 806, 90
P. Bult & M. van der Klis

Chapter 5: Pulse amplitude depends on kHz QPO frequency
The Astrophysical Journal Letters, 2015, 798, L29
P. Bult & M. van der Klis

Chapter 6: Coherent timing of NGC 6440 X-2
The Astrophysical Journal, submitted
P. Bult, A. Patruno & M. van der Klis

Chapter 7: The magnetic field strengths of accreting millisecond pulsars
Monthly Notices of the Royal Astronomical Society, in press
D. Mukherjee, P. Bult, M. van der Klis & D. Bhattacharya
— D.M. and P.B. contributed equally to this work.

Bibliography

Agrawal, P. C. 2006, Advances in Space Research, 38, 2989

Alpar, M. A., Cheng, A. F., Ruderman, M. A., & Shaham, J. 1982, Nature, 300, 728

Alpar, M. A., & Psaltis, D. 2008, MNRAS, 391, 1472

Altamirano, D., Casella, P., Patruno, A., Wijnands, R., & van der Klis, M. 2008a, ApJ, 674, L45

Altamirano, D., Patruno, A., Heinke, C., et al. 2010a, The Astronomer's Telegram, 2500, 1

Altamirano, D., van der Klis, M., Méndez, M., et al. 2008b, ApJ, 685, 436

Altamirano, D., van der Klis, M., Méndez, M., et al. 2005, ApJ, 633, 358

Altamirano, D., Watts, A., Linares, M., et al. 2010b, MNRAS, 409, 1136

Altamirano, D., Strohmayer, T. E., Heinke, C. O., et al. 2009, The Astronomer's Telegram, 2182, 1

Altamirano, D., Wijnands, R., van der Klis, M., et al. 2010c, The Astronomer's Telegram, 2565, 1

Altamirano, D., Patruno, A., Heinke, C. O., et al. 2010d, ApJ, 712, L58

Altamirano, D., Cavecchi, Y., Patruno, A., et al. 2011, ApJ, 727, L18

Aly, J. J., & Kuijpers, J. 1990, A&A, 227, 473

Applegate, J. H. 1992, ApJ, 385, 621

Applegate, J. H., & Patterson, J. 1987, ApJ, 322, L99

Applegate, J. H., & Shaham, J. 1994, ApJ, 436, 312

Archibald, A. M., Stairs, I. H., Ransom, S. M., et al. 2009, Science, 324, 1411

Archibald, A. M., Bogdanov, S., Patruno, A., et al. 2015, ApJ, 807, 62

Arnaud, K. A. 1996, in Astronomical Society of the Pacific Conference Series, Vol. 101, Astronomical Data Analysis Software and Systems V, ed. G. H. Jacoby & J. Barnes, 17

Arons, J., & Lea, S. M. 1976, ApJ, 207, 914

Arzoumanian, Z., Fruchter, A. S., & Taylor, J. H. 1994, ApJ, 426, L85

Asai, K., Matsuoka, M., Mihara, T., et al. 2013, ApJ, 773, 117

Bachetti, M., Romanova, M. M., Kulkarni, A., Burderi, L., & di Salvo, T. 2010, MNRAS, 403, 1193

Bailes, M. 1989, ApJ, 342, 917

Balbus, S. A., & Hawley, J. F. 1991, ApJ, 376, 214

Baldovin, C., Kuulkers, E., Ferrigno, C., et al. 2009, The Astronomer's Telegram, 2196, 1

Belloni, T., Psaltis, D., & van der Klis, M. 2002, ApJ, 572, 392

Beskin, V. S., Gurevich, A. V., & Istomin, I. N. 1984, Ap&SS, 102, 301

Bevington, P. R., & Robinson, D. K. 2003, Data reduction and error analysis for the physical sciences (Boston: McGraw-Hill)

Bildsten, L. 1998a, ApJ, 501, L89

Bildsten, L. 1998b, in NATO ASI Series, Vol. 515, The Many Faces of Neutron Stars, ed. R. Buccheri, J. van Paradijs, & A. Alpar, 419

Bildsten, L. 2002, ApJ, 577, L27

Bildsten, L., & Chakrabarty, D. 2001, ApJ, 557, 292

Bisnovatyi-Kogan, G. S., & Komberg, B. V. 1974, Soviet Ast., 18, 217

Bult, P., & van der Klis, M. 2014, ApJ, 789, 99

Bult, P., & van der Klis, M. 2015a, ApJ, 798, L29

Bult, P., & van der Klis, M. 2015b, ApJ, 806, 90

Burderi, L., Di Salvo, T., Menna, M. T., Riggio, A., & Papitto, A. 2006, ApJ, 653, L133

Burderi, L., Riggio, A., di Salvo, T., et al. 2009, A&A, 496, L17

Burderi, L., Di Salvo, T., Stella, L., et al. 2002, ApJ, 574, 930

Caballero, I., & Wilms, J. 2012, Mem. Soc. Astron. Italiana, 83, 230

Cackett, E. M., Altamirano, D., Patruno, A., et al. 2009, ApJ, 694, L21

Campana, S., Ravasio, M., Israel, G. L., Mangano, V., & Belloni, T. 2003, ApJ, 594, L39

Campana, S., Stella, L., & Kennea, J. A. 2008, ApJ, 684, L99

Casella, P., Altamirano, D., Patruno, A., Wijnands, R., & van der Klis, M. 2008, ApJ, 674, L41

Cavecchi, Y., Patruno, A., Haskell, B., et al. 2011, ApJ, 740, L8

Chakrabarty, D., Markwardt, C. B., Linares, M., & Jonker, P. G. 2011, The Astronomer's Telegram, 3606, 1

Chakrabarty, D., & Morgan, E. H. 1998, Nature, 394, 346

Chakrabarty, D., Swank, J. H., Markwardt, C. B., & Smith, E. 2008, The Astronomer's Telegram, 1660, 1

Damour, T., & Taylor, J. H. 1991, ApJ, 366, 501

D'Angelo, C. R., & Spruit, H. C. 2010, MNRAS, 406, 1208

D'Angelo, C. R., & Spruit, H. C. 2012, MNRAS, 420, 416

Davidson, K., & Ostriker, J. P. 1973, ApJ, 179, 585

Deloye, C. J., Heinke, C. O., Taam, R. E., & Jonker, P. G. 2008, MNRAS, 391, 1619

Di Salvo, T., & Burderi, L. 2003, A&A, 397, 723
di Salvo, T., Burderi, L., Riggio, A., Papitto, A., & Menna, M. T. 2008, MNRAS, 389, 1851
Doroshenko, O., Löhmer, O., Kramer, M., et al. 2001, A&A, 379, 579
Dotani, T., Mitsuda, K., Makishima, K., & Jones, M. H. 1989, PASJ, 41, 577
Eckert, D., Walter, R., Kretschmar, P., et al. 2004, The Astronomer's Telegram, 352, 1
Falanga, M., Kuiper, L., Poutanen, J., et al. 2012, A&A, 545, A26
Falanga, M., Kuiper, L., Poutanen, J., et al. 2005a, A&A, 444, 15
Falanga, M., Bonnet-Bidaud, J. M., Poutanen, J., et al. 2005b, A&A, 436, 647
Falanga, M., Kuiper, L., Poutanen, J., et al. 2011, A&A, 529, A68
Feroci, M., Stella, L., van der Klis, M., et al. 2012, Experimental Astronomy, 34, 415
Ferrigno, C., Bozzo, E., Falanga, M., et al. 2011, A&A, 525, A48
Ford, E. C., & van der Klis, M. 1998, ApJ, 506, L39
Fox, D. B. 2005, The Astronomer's Telegram, 526, 1
Fragile, P. C., Blaes, O. M., Anninos, P., & Salmonson, J. D. 2007, ApJ, 668, 417
Galloway, D. K., Chakrabarty, D., Morgan, E. H., & Remillard, R. A. 2002, ApJ, 576, L137
Galloway, D. K., & Cumming, A. 2006, ApJ, 652, 559
Galloway, D. K., Markwardt, C. B., Morgan, E. H., Chakrabarty, D., & Strohmayer, T. E. 2005, ApJ, 622, L45
Galloway, D. K., Muno, M. P., Hartman, J. M., Psaltis, D., & Chakrabarty, D. 2008, ApJS, 179, 360
Gavriil, F. P., Strohmayer, T. E., Swank, J. H., & Markwardt, C. B. 2007, ApJ, 669, L29
Ghosh, P., & Lamb, F. K. 1978, ApJ, 223, L83
Ghosh, P., & Lamb, F. K. 1979a, ApJ, 232, 259
Ghosh, P., & Lamb, F. K. 1979b, ApJ, 234, 296
Gibaud, L., Bazzano, A., Bozzo, E., et al. 2011, The Astronomer's Telegram, 3551, 1
Gierliński, M., & Poutanen, J. 2005, MNRAS, 359, 1261
Gilfanov, M., Revnivtsev, M., & Molkov, S. 2003, A&A, 410, 217
Gilfanov, M., Revnivtsev, M., Sunyaev, R., & Churazov, E. 1998, A&A, 338, L83
Güver, T., Özel, F., Göğüş, E., & Kouveliotou, C. 2007, ApJ, 667, L73
Güver, T., Özel, F., & Göğüş, E. 2008, ApJ, 675, 1499
Harris, W. E. 1996, AJ, 112, 1487
Hartman, J. M., Galloway, D. K., & Chakrabarty, D. 2011, ApJ, 726, 26
Hartman, J. M., Patruno, A., Chakrabarty, D., et al. 2009, ApJ, 702, 1673
Hartman, J. M., Patruno, A., Chakrabarty, D., et al. 2008, ApJ, 675, 1468
Hasinger, G., & van der Klis, M. 1989, A&A, 225, 79
Haskell, B., & Patruno, A. 2011, ApJ, 738, L14

Heger, A., Cumming, A., & Woosley, S. E. 2007, ApJ, 665, 1311

Heinke, C. O., Jonker, P. G., Wijnands, R., Deloye, C. J., & Taam, R. E. 2009, ApJ, 691, 1035

Heinke, C. O., Altamirano, D., Cohn, H. N., et al. 2010, ApJ, 714, 894

Hobbs, G. B., Edwards, R. T., & Manchester, R. N. 2006, MNRAS, 369, 655

Homan, J., Jonker, P. G., Wijnands, R., van der Klis, M., & van Paradijs, J. 1999, ApJ, 516, L91

Iacolina, M. N., Burgay, M., Burderi, L., Possenti, A., & di Salvo, T. 2009, A&A, 497, 445

Ibragimov, A., & Poutanen, J. 2009, MNRAS, 400, 492

Illarionov, A. F., & Sunyaev, R. A. 1975, A&A, 39, 185

in 't Zand, J. J. M., Heise, J., Muller, J. M., et al. 1998, A&A, 331, L25

in 't Zand, J. J. M., van Kerkwijk, M. H., Pooley, D., et al. 2001, ApJ, 563, L41

in 't Zand, J. J. M., Verbunt, F., Strohmayer, T. E., et al. 1999, A&A, 345, 100

in 't Zand, J. J. M., Galloway, D. K., Marshall, H. L., et al. 2013, A&A, 553, A83

Ingram, A., & Done, C. 2010, MNRAS, 405, 2447

Ingram, A., & Done, C. 2012, MNRAS, 419, 2369

Ingram, A., Done, C., & Fragile, P. C. 2009, MNRAS, 397, L101

Jahoda, K., Markwardt, C. B., Radeva, Y., et al. 2006, ApJS, 163, 401

Jonker, P. G., Campana, S., Steeghs, D., et al. 2005, MNRAS, 361, 511

Jonker, P. G., Gallo, E., Dhawan, V., et al. 2004, MNRAS, 351, 1359

Jonker, P. G., & Nelemans, G. 2004, MNRAS, 354, 355

Jonker, P. G., van der Klis, M., Homan, J., et al. 2000, ApJ, 531, 453

Jonker, P. G., van der Klis, M., & Wijnands, R. 1999, ApJ, 511, L41

Juett, A. M., Galloway, D. K., & Chakrabarty, D. 2003, ApJ, 587, 754

Kaaret, P., Morgan, E. H., Vanderspek, R., & Tomsick, J. A. 2006, ApJ, 638, 963

Kajava, J. J. E., Ibragimov, A., Annala, M., Patruno, A., & Poutanen, J. 2011, MNRAS, 417, 1454

Kato, S. 2004, PASJ, 56, 559

Kawai, N., & Suzuki, M. 2005, The Astronomer's Telegram, 534, 1

King, A. R., Kolb, U., & Szuszkiewicz, E. 1997, ApJ, 488, 89

Klein-Wolt, M., Homan, J., & van der Klis, M. 2004, Nucl. Phys. B, 132, 381

Kluzniak, W., & Abramowicz, M. A. 2001, ArXiv e-prints, astro-ph/0105057, ads

Kluźniak, W., Abramowicz, M. A., Kato, S., Lee, W. H., & Stergioulas, N. 2004, ApJ, 603, L89

Kraft, R. P., Mathews, J., & Greenstein, J. L. 1962, ApJ, 136, 312

Krauss, M. I., Wang, Z., Dullighan, A., et al. 2005, ApJ, 627, 910

Krimm, H. A., Markwardt, C. B., Deloye, C. J., et al. 2007a, ApJ, 668, L147

Krimm, H. A., Barthelmy, S. D., Barbier, L., et al. 2007b, The Astronomer's Telegram, 1105, 1

Kulkarni, A. K., & Romanova, M. M. 2008, MNRAS, 386, 673

Kulkarni, A. K., & Romanova, M. M. 2009, MNRAS, 398, 701

Kulkarni, A. K., & Romanova, M. M. 2013, MNRAS, 433, 3048

Lai, D. 1998, ApJ, 502, 721

Lai, D. 1999, ApJ, 524, 1030

Lai, D., & Zhang, H. 2008, ApJ, 683, 949

Lamb, F. K., Boutloukos, S., Van Wassenhove, S., et al. 2009, ApJ, 705, L36

Lamb, F. K., & Miller, M. C. 2003, ArXiv e-prints, astro-ph/0308179, ads

Lamb, F. K., Pethick, C. J., & Pines, D. 1973, ApJ, 184, 271

Lattimer, J. M. 2014, General Relativity and Gravitation, 46, 1713

Lattimer, J. M., & Prakash, M. 2001, ApJ, 550, 426

Lazaridis, K., Verbiest, J. P. W., Tauris, T. M., et al. 2011, MNRAS, 414, 3134

Leahy, D. A., Darbro, W., Elsner, R. F., et al. 1983, ApJ, 266, 160

Leahy, D. A., Morsink, S. M., & Cadeau, C. 2008, ApJ, 672, 1119

Lewis, F. ., Linares, M., Russell, D. M., Wijnands, R., & Roche, P. 2008, The Astronomer's Telegram, 1726, 1

Lii, P. S., Romanova, M. M., Ustyugova, G. V., Koldoba, A. V., & Lovelace, R. V. E. 2014, MNRAS, 441, 86

Linares, M., van der Klis, M., Altamirano, D., & Markwardt, C. B. 2005, ApJ, 634, 1250

Linares, M., Wijnands, R., van der Klis, M., et al. 2008, ApJ, 677, 515

Long, M., Romanova, M. M., & Lovelace, R. V. E. 2007, MNRAS, 374, 436

Long, M., Romanova, M. M., & Lovelace, R. V. E. 2008, MNRAS, 386, 1274

Lorimer, D. R. 2008, Living Reviews in Relativity, 11, 8

Lovelace, R. V. E., & Romanova, M. M. 2007, ApJ, 670, L13

Markovic, D. 2000, ArXiv e-prints, astro-ph/0009450, ads

Markwardt, C. B., Altamirano, D., Strohmayer, T. E., & Swank, J. H. 2009a, The Astronomer's Telegram, 2237, 1

Markwardt, C. B., Altamirano, D., Swank, J. H., et al. 2009b, The Astronomer's Telegram, 2197, 1

Markwardt, C. B., & Dobrzycki, A. 2002, IAU Circ., 7876, 2

Markwardt, C. B., Krimm, H. A., & Swank, J. H. 2007, The Astronomer's Telegram, 1108, 1

Markwardt, C. B., Smith, E., & Swank, J. H. 2003, The Astronomer's Telegram, 122, 1

Markwardt, C. B., & Strohmayer, T. E. 2010, ApJ, 717, L149

Markwardt, C. B., Swank, J., Wijnands, R., & in't Zand, J. 2005, The Astronomer's Telegram, 505, 1

Markwardt, C. B., & Swank, J. H. 2003, IAU Circ., 8144, 1

Markwardt, C. B., & Swank, J. H. 2005, The Astronomer's Telegram, 495, 1

Markwardt, C. B., Swank, J. H., & Strohmayer, T. E. 2004, The Astronomer's Telegram, 353, 1

Markwardt, C. B., Swank, J. H., Strohmayer, T. E., in 't Zand, J. J. M., & Marshall, F. E. 2002a, ApJ, 575, L21

Markwardt, C. B., Swank, J. H., Strohmayer, T. E., in 't Zand, J. J. M., & Marshall, F. E. 2002b, ApJ, 575, L21

Markwardt, C. B., Palmer, D. M., Barthelmy, S. D., et al. 2011, The Astronomer's Telegram, 3733, 1

Marshall, F. E., Wijnands, R., & van der Klis, M. 1998, IAU Circ., 6876, 1

Matsuoka, M., & Asai, K. 2013, PASJ, 65, 26

Méndez, M., van der Klis, M., van Paradijs, J., et al. 1998, ApJ, 494, L65

Menna, M. T., Burderi, L., Stella, L., Robba, N., & van der Klis, M. 2003, ApJ, 589, 503

Merloni, A., Vietri, M., Stella, L., & Bini, D. 1999, MNRAS, 304, 155

Messenger, C., & Patruno, A. 2015, ApJ, 806, 261

Migliari, S., & Fender, R. P. 2006, MNRAS, 366, 79

Miller, J. M., Wijnands, R., Méndez, M., et al. 2003, ApJ, 583, L99

Miller, M. C., Lamb, F. K., & Psaltis, D. 1998, ApJ, 508, 791

Morgan, E., Kaaret, P., & Vanderspek, R. 2005, The Astronomer's Telegram, 523, 1

Morsink, S. M., & Leahy, D. A. 2011, ApJ, 726, 56

Nelson, L. A., & Rappaport, S. 2003, ApJ, 598, 431

Nice, D. J., Arzoumanian, Z., & Thorsett, S. E. 2000, in Astronomical Society of the Pacific Conference Series, Vol. 202, IAU Colloq. 177: Pulsar Astronomy - 2000 and Beyond, ed. M. Kramer, N. Wex, & R. Wielebinski, 67

Nowak, M., Rots, A. H., McCollough, M. L., et al. 2009, in Chandra's First Decade of Discovery, ed. S. Wolk, A. Fruscione, & D. Swartz, 171

Nowak, M. A. 2000, MNRAS, 318, 361

Ostriker, J. P., & Gunn, J. E. 1969, ApJ, 157, 1395

Paczyński, B. 1967, Acta Astron., 17, 287

Paizis, A., Nowak, M. A., Rodriguez, J., et al. 2012, ApJ, 755, 52

Paizis, A., Nowak, M. A., Wilms, J., et al. 2005, A&A, 444, 357

Papitto, A., Bozzo, E., Ferrigno, C., et al. 2011a, The Astronomer's Telegram, 3736, 1

Papitto, A., de Martino, D., Belloni, T. M., et al. 2015, MNRAS, 449, L26

Papitto, A., di Salvo, T., Burderi, L., et al. 2007, MNRAS, 375, 971

Papitto, A., Di Salvo, T., D'Aì, A., et al. 2009, A&A, 493, L39

Papitto, A., Ferrigno, C., Bozzo, E., et al. 2011b, The Astronomer's Telegram, 3556, 1

Papitto, A., Menna, M. T., Burderi, L., di Salvo, T., & Riggio, A. 2008, MNRAS, 383, 411

Papitto, A., Riggio, A., di Salvo, T., et al. 2010, MNRAS, 407, 2575

Papitto, A., Bozzo, E., Ferrigno, C., et al. 2011c, A&A, 535, L4

Papitto, A., Ferrigno, C., Bozzo, E., et al. 2013a, Nature, 501, 517

Papitto, A., D'Aì, A., Di Salvo, T., et al. 2013b, MNRAS, 429, 3411

Patruno, A. 2010, ApJ, 722, 909

Patruno, A. 2012, ApJ, 753, L12

Patruno, A., Altamirano, D., Hessels, J. W. T., et al. 2009a, ApJ, 690, 1856

Patruno, A., Altamirano, D., & Messenger, C. 2010a, MNRAS, 403, 1426

Patruno, A., Bult, P., Gopakumar, A., et al. 2012, ApJ, 746, L27

Patruno, A., & D'Angelo, C. 2013, ApJ, 771, 94

Patruno, A., Hartman, J. M., Wijnands, R., Chakrabarty, D., & van der Klis, M. 2010b, ApJ, 717, 1253

Patruno, A., Maitra, D., Curran, P. A., et al. 2015, ArXiv e-prints, arXiv:1504.05048, ads

Patruno, A., Markwardt, C. B., Strohmayer, T. E., et al. 2009b, The Astronomer's Telegram, 2130, 1

Patruno, A., Rea, N., Altamirano, D., et al. 2009c, MNRAS, 396, L51

Patruno, A., Watts, A., Klein Wolt, M., Wijnands, R., & van der Klis, M. 2009d, ApJ, 707, 1296

Patruno, A., & Watts, A. L. 2012, in Timing neutron stars: pulsations, oscillations and explosions, ed. T. Belloni, M. Mendez, & C. M. Zhang (in press)

Patruno, A., Wijnands, R., & van der Klis, M. 2009e, ApJ, 698, L60

Patruno, A., Altamirano, D., Watts, A., et al. 2010c, The Astronomer's Telegram, 2407, 1

Patruno, A., Yang, Y., Altamirano, D., et al. 2010d, The Astronomer's Telegram, 2672, 1

Poutanen, J., & Beloborodov, A. M. 2006, MNRAS, 373, 836

Poutanen, J., & Gierliński, M. 2003, MNRAS, 343, 1301

Pringle, J. E., & Rees, M. J. 1972, A&A, 21, 1

Psaltis, D., Belloni, T., & van der Klis, M. 1999, ApJ, 520, 262

Psaltis, D., & Chakrabarty, D. 1999, ApJ, 521, 332

Psaltis, D., Özel, F., & Chakrabarty, D. 2014, ApJ, 787, 136

Radhakrishnan, V., & Srinivasan, G. 1982, Current Science, 51, 1096

Rappaport, S., Verbunt, F., & Joss, P. C. 1983, ApJ, 275, 713

Rappaport, S. A., Fregeau, J. M., & Spruit, H. 2004, ApJ, 606, 436

Remillard, R. A. 2002, IAU Circ., 7888, 2

Remillard, R. A., Swank, J., & Strohmayer, T. 2002, IAU Circ., 7893, 1

Richman, H. R., Applegate, J. H., & Patterson, J. 1994, PASP, 106, 1075

Riggio, A., Burderi, L., di Salvo, T., et al. 2011a, A&A, 531, A140

Riggio, A., Di Salvo, T., Burderi, L., et al. 2008, ApJ, 678, 1273

Riggio, A., Papitto, A., Burderi, L., et al. 2011b, A&A, 526, A95

Romanova, M. M., Kulkarni, A. K., & Lovelace, R. V. E. 2008, ApJ, 673, L171

Romanova, M. M., Ustyugova, G. V., Koldoba, A. V., & Lovelace, R. V. E. 2013, MNRAS, 430, 699

Rots, A. H., Jahoda, K., & Lyne, A. G. 2004, ApJ, 605, L129

Rupen, M. P., Dhawan, V., & Mioduszewski, A. J. 2004, The Astronomer's Telegram, 364, 1

Schady, P., Beardmore, A. P., Marshall, F. E., et al. 2006, GRB Coordinates Network, 5200, 1

Shakura, N. I., & Sunyaev, R. A. 1973, A&A, 24, 337

Shaw, S. E., Mowlavi, N., Rodriguez, J., et al. 2005, A&A, 432, L13

Shirakawa, A., & Lai, D. 2002, ApJ, 564, 361

Singh, K. P., Tandon, S. N., Agrawal, P. C., et al. 2014, in Society of Photo-Optical Instrumentation Engineers (SPIE) Conference Series, Vol. 9144, 1

Spitkovsky, A. 2006, ApJ, 648, L51

Spruit, H. C., Stehle, R., & Papaloizou, J. C. B. 1995, MNRAS, 275, 1223

Spruit, H. C., & Taam, R. E. 1993, ApJ, 402, 593

Srinivasan, G., & van den Heuvel, E. P. J. 1982, A&A, 108, 143

Stella, L., & Vietri, M. 1998, ApJ, 492, L59

Stella, L., & Vietri, M. 1999, Physical Review Letters, 82, 17

Strohmayer, T. E., Markwardt, C. B., Swank, J. H., & in't Zand, J. 2003, ApJ, 596, L67

Strohmayer, T. E., Zhang, W., Swank, J. H., et al. 1996, ApJ, 469, L9

Sunyaev, R. A., & Shakura, N. I. 1977, Pisma v Astronomicheskii Zhurnal, 3, 262

Tauris, T. M. 2012, Science, 335, 561

Tauris, T. M., Langer, N., & Kramer, M. 2012, MNRAS, 425, 1601

Tauris, T. M., & van den Heuvel, E. P. J. 2006, in Compact stellar X-ray sources, ed. W. H. G. Lewin & M. van der Klis (Cambridge: Cambridge University Press), 623

Torres, M. A. P., Madej, O., Jonker, P. G., et al. 2011, The Astronomer's Telegram, 3638, 1

Torres, M. A. P., Jonker, P. G., Steeghs, D., et al. 2008, ApJ, 672, 1079

Uzdensky, D. A. 2004, Ap&SS, 292, 573

Valenti, E., Ferraro, F. R., & Origlia, L. 2007, AJ, 133, 1287

van den Heuvel, E. P., van Paradijs, J. A., & Taam, R. E. 1986, Nature, 322, 153

van der Klis, M. 1989, in NATO ASI Series, Vol. 262, Timing Neutron Stars, ed. H. Ögelman & E. P. J. van den Heuvel (Dordrecht: Kluwer), 27

van der Klis, M. 1995, in NATO ASI series, Vol. 450, The Lives of the Neutron Stars, ed. M. A. Alpar, U. Kiziloglu, & J. van Paradijs (Dordrecht: Kluwer), 301

van der Klis, M. 2006, in Compact stellar X-ray sources, ed. W. H. G. Lewin & M. van der Klis (Cambridge: Cambridge University Press), 39

van der Klis, M., Chakrabarty, D., Lee, J. C., et al. 2000, IAU Circ., 7358, 3

van der Klis, M., Swank, J. H., Zhang, W., et al. 1996, ApJ, 469, L1

van Straaten, S., van der Klis, M., di Salvo, T., & Belloni, T. 2002, ApJ, 568, 912

van Straaten, S., van der Klis, M., & Méndez, M. 2003, ApJ, 596, 1155

van Straaten, S., van der Klis, M., & Wijnands, R. 2005, ApJ, 619, 455

Vanderspek, R., Morgan, E., Crew, G., Graziani, C., & Suzuki, M. 2005, The Astronomer's Telegram, 516, 1

Viironen, K., & Poutanen, J. 2004, A&A, 426, 985

Wang, Y.-M. 1995, ApJ, 449, L153

Watts, A. L., Krishnan, B., Bildsten, L., & Schutz, B. F. 2008, MNRAS, 389, 839

Wijnands, R. 2004, Nucl. Phys. B, 132, 496

Wijnands, R., Homan, J., Heinke, C. O., Miller, J. M., & Lewin, W. H. G. 2005, ApJ, 619, 492

Wijnands, R., Méndez, M., Markwardt, C., et al. 2001, ApJ, 560, 892

Wijnands, R., Rol, E., Cackett, E., Starling, R. L. C., & Remillard, R. A. 2009, MNRAS, 393, 126

Wijnands, R., & van der Klis, M. 1998a, Nature, 394, 344

Wijnands, R., & van der Klis, M. 1998b, ApJ, 507, L63

Wijnands, R., & van der Klis, M. 1999, ApJ, 514, 939

Wijnands, R., van der Klis, M., Homan, J., et al. 2003, Nature, 424, 44

Wilms, J., Allen, A., & McCray, R. 2000, ApJ, 542, 914

Zanni, C., & Ferreira, J. 2009, A&A, 508, 1117

Zanni, C., & Ferreira, J. 2013, A&A, 550, A99

Zdziarski, A. A., Johnson, W. N., & Magdziarz, P. 1996, MNRAS, 283, 193

Zhang, C. 2004, A&A, 423, 401

Zhang, W., Jahoda, K., Swank, J. H., Morgan, E. H., & Giles, A. B. 1995, ApJ, 449, 930

Życki, P. T., Done, C., & Smith, D. A. 1999, MNRAS, 309, 561

Acknowledgements

Let me be brief. I would like to thank all those who, in whatever way, helped shape this work; be it by direct contributions, through helpful discussions and explanations, or simply by offering support or, perhaps unknowingly, inspiration in these past years.

Finally I would like to explicitly mention my supervisors. Firstly, to Michiel, thank you for offering me this opportunity and allowing me the freedom of doing things in my own stubborn way. Always challenged to try and meet your incredible attention to detail, I have learned a great deal from you. Secondly to Ale, thanks for your help and always very enthusiastic comments along the way, which have always been very motivational. I've greatly enjoyed working with you both, and hope we can continue our collaboration for years to come.

This book was written using 100% recycled words
– Terry Pratchett